

Three-dimensional Numerical Model for Seabed Foundation Stability around Breakwaters



Lin Cui

BEng (Hon)

School of Engineering and Built Environment
Griffith University

Submitted in fulfilment of the requirements of the degree of
Doctor of Philosophy

March 2020

To my family

Abstract

With the increasing demand for coastal zones from human activities, a growing number of breakwaters have been constructed around the main beach and major estuaries to defend against wave erosion and damage. The vulnerability of the breakwater foundation can be associated with dynamic soil responses in the vicinity of structure when subjects to the consecutive ocean wave loading. For the severe situations, soil liquefaction may occur around the breakwater foundation, which is considered as a significant cause of catastrophic failures of many marine structures. Therefore, understanding and predicting soil responses and liquefaction potential around breakwaters have become one of the main concerns when design and maintain these marine structures.

The traditional models used to analyse the soil responses and liquefaction potential in the neighbourhood of breakwaters were mostly limited to two-dimensional (2D) frameworks, in which only the middle cross-section of the breakwaters under perpendicular waves can be investigated. However, the natural environment is three-dimensional (3D) that involves much more complicated fluid-seabed-structure interactions, which requires a 3D model. What's more, most of the existing models assumed the seabed foundation as poro-elastic medium, which only the oscillatory soil responses and momentary liquefaction can be studied. Nevertheless, the residual soil responses and liquefaction within the poro-elastoplastic soil are more significant and can cause more severe damage to the marine structure foundations. Another deficiency of the traditional models is the lack of advanced Computational Fluid Dynamic (CFD) model to accurately simulate more realistic conditions, for example, including the interactions of ocean currents.

According to the gaps in previous literature, the main objective of this thesis is defined as numerically predicting the soil responses and examining the breakwater foundation stability (i.e., liquefaction potential) under combined waves and currents loading within both poro-elastic and poro-elastoplastic seabed foundation from both two- and three-dimensional perspectives for different engineering conditions. One of the main novel contributions of this study is to develop the integrated numerical model that make up for the deficiency of the

fluid-seabed-structure interactions problems mentioned above: the wider application ranges including complicated 3D situations; the consideration of poro-elastoplastic soil behaviour and corresponding soil liquefaction; the inclusion of an advanced flow model to precisely predict the hydrodynamic behaviour around the structures. In the future, the models can be further developed and applied to practical engineering analyses, providing preliminary results for the design of the projects.

The integrated numerical model consists of the flow sub-model, the seabed sub-model and the coupling module between two sub-models. The flow model is developed based on the Finite Volume Method (FVM) by solving the Volume-Averaged Reynolds Averaged Navier-Stokes (VARANS) equations for simulating the two incompressible phases (i.e., water and air) inside and outside the porous medium. The seabed model is governed by the dynamic Biot's equations known as the $u - p$ approximations, in which the relative displacements of pore fluid to soil particles are ignored and the acceleration of pore fluid and solid particles is included. Two constitutive models: poro-elastic model for oscillatory soil responses and momentary liquefaction; and poro-elastoplastic model for residual soil responses and residual liquefaction, are incorporated into the seabed model. An integration module is developed between flow sub-model and seabed sub-model through pressure continuity on the common faces. A set of validation works have been done to prove the capability of simulating the fluid-seabed-breakwater interactions in an accurate way.

By adopting the integrated numerical model, three numerical studies have been conducted in this thesis, including one 2D study (soil responses around submerged breakwaters with Bragg reflection) and two 3D studies (seabed foundation stability around breakwaters at river mouth; seabed foundation stability around offshore detached breakwaters). A series of results, including the hydrodynamic properties of flow domain, variation of pore pressure, effective stresses and soil displacements, and characteristics of soil liquefaction within both poro-elastic and poro-elastoplastic seabed foundation have been obtained. Numerical results revealed that the construction of breakwaters can dramatically change the flow pattern and stress state in the vicinity, which will further affect the assessment of foundation stability. Besides, compared to the poro-elastic seabed foundation, the liquefaction is much easier to occur in the poro-elastoplastic seabed foundation and usually will develop to a much more significant level, which can cause critical failure of the structures. Furthermore, the effects of wave characteristics and soil properties on the breakwater foundation stability have been examined through parametric studies: the soil liquefaction is more serious within the loosely deposited seabed with poor drainage conditions under large wave height and wave period. It was also found that the currents have remarkable effects on foundation stability that aggravate with the increase of currents velocity.

Declaration

This work has not previously been submitted for a degree or diploma in any university. To the best of my knowledge and belief, the thesis contains no material previously published or written by another person except where due reference is made in the thesis itself.

Signed:

Lin Cui

March 2020

Acknowledgements

This thesis would not have been possible without the help, support and guidance from many people. I would like to take this opportunity to show my appreciations to those people.

I would like to sincerely express my gratitude to my supervisor Professor Dong-Sheng Jeng for his continuous support, valuable guidance and constant feedback throughout all stages of my PhD study. His patience, motivation, and immense knowledge helped me through the most difficult time in my doctoral study. I could not have imagined having a better supervisor and mentor for my PhD study.

At the same time, I gratefully thank my co-supervisor Hong Zhang for her kind help during my study. I also owe my deep gratitude to Professor Xiaobo Qu, I always remember your help and encouragement, especially during the period of applying for the PhD. Thank you for introducing me to Professor Dong-Sheng Jeng, which makes me having the honour to be a member of his research group.

My sincere thanks must also goes to my parents for their endless love, support and encouragement throughout my life. I am so grateful for your emotional and financial support, that helps me to chase my dreams. My elder sister, who always believes in me and wants the best for me, deserves my wholehearted thanks as well. To my girlfriend, thank you for all the love and persistent support.

I want to extend my thanks to each member of our research group: Zhengxu Li, Shuang Han, Zuodong Liang, Sheng Wu and Xiaoxiao Wang, without whom, my PhD journey would be much less fun. We have established deep friendships that I cherish very much. Thank each of you for bringing all the happy memories to me. In addition, I would like to show my greatest appreciation to all my friends outside the research group, I cannot thank you enough for making me smile everyday. Special thanks to one of my closest friends Bo Wen, your unconditional support and encouragement always give me a warm feeling in my heart.

Last but not least, I am very thankful for the financial support from Griffith University Postgraduate Research Scholarship (GUPRS) and Griffith University International Postgradu-

ate Research Scholarship (GUIPRS). I also gratefully appreciate the support from the Griffith University eResearch Services team and the use of the Griffith University Gowanda High Performance Computing Cluster to complete this research.

Publication list

1. Cui, L., & Jeng, D. S. (2018, November). Integrated model for fluid-soil interactions around submerged breakwaters on a poro-elastoplastic seabed with Bragg effects. In *The Thirteenth ISOPE Pacific/Asia Offshore Mechanics Symposium*. International Society of Offshore and Polar Engineers.
2. Cui, L., & Jeng, D. S. (2018). Numerical study for soil response around submerged breakwaters with Bragg Reflection. *International Journal of Ocean and Coastal Engineering*, 1(04), 1850005.
3. Cui, L., & Jeng, D. S. (2020). Numerical study for foundation stability around breakwater heads at a river mouth. Submitted to *Coastal Engineering*.
4. Cui, L., & Jeng, D. S. Wave/current induced soil response and liquefaction around offshore detached breakwaters. Prepare to submit to *Ocean Engineering*.

Table of contents

List of figures	xiii
List of tables	xxi
List of symbols	xxii
1 Introduction	1
1.1 Background	1
1.2 Research objectives	3
1.3 Outline of this thesis	4
2 Literature Review	5
2.1 Fluid-Seabed Interactions	5
2.1.1 Decoupled models	5
2.1.2 Coupled models for the wave-induced oscillatory soil responses . .	7
2.1.3 Coupled models for the wave-induced residual soil responses	18
2.2 Fluid-Seabed-Breakwaters Interactions	20
2.2.1 Models for the oscillatory soil responses	21
2.2.2 Models for the residual soil responses	24
2.2.3 The impact of currents	25
2.2.4 Breakwater foundation instability	27
2.3 Summary	29

3	Theoretical Models	31
3.1	Flow sub-model	31
3.1.1	Governing equations: VARANS equations	33
3.1.2	Free surface modelling	34
3.1.3	Turbulence models	35
3.2	Seabed sub-model	37
3.2.1	Governing equations: $u - p$ approximation	37
3.2.2	Constitutive models	39
3.3	Integration of flow and seabed sub-models	43
3.4	Model validations	44
3.4.1	Comparison with Umeyama (2010)'s experiments: regular wave with uniform following current travelling over a rigid bottom	45
3.4.2	Comparison with Qi et al. (2019)'s flume observations: combined wave and current induced excess pore pressure in a sandy seabed . .	48
3.4.3	Comparison with Mizutani et al. (1998)'s experiments: submerged rubble mound breakwater	50
3.4.4	Comparison with Mostafa et al. (1999)'s experiments: caisson-type composite breakwater	56
3.4.5	Comparison with Sassa and Sekiguchi (1999)'s geotechnical cen- trifuge test: build-up of pore pressure	61
3.4.6	Comparison with Hsu and Jeng (1994)'s analytical solution	63
3.5	Summary	63
4	2D Numerical Study: Soil responses around Submerged Breakwaters with Bragg Reflection^{1*}	66
4.1	Introduction	66
4.2	Computational domain, boundary conditions and input parameters	68
4.3	Flow field around multiple submerged breakwaters	69
4.4	Consolidation of the seabed foundation	76

4.5	Wave/current induced dynamic soil responses	78
4.6	Liquefaction in the seabed foundation	84
4.7	Parametric study	90
4.8	Summary	93
5	3D Numerical Study I: Seabed Foundation Stability around Breakwaters at River Mouth^{2*}	101
5.1	Introduction	101
5.1.1	Engineering background	101
5.1.2	Computational domain, boundary conditions and input parameters .	103
5.2	Flow field around breakwaters	108
5.2.1	Wave profile and surface elevation	108
5.2.2	Velocity field	110
5.2.3	Hydrodynamic pressure	114
5.3	Consolidation of the porous seabed foundation	114
5.4	Dynamic soil response in the seabed foundation	116
5.4.1	Time series of dynamic soil responses	118
5.4.2	Spatial distribution of dynamic soil responses	123
5.5	Soil liquefaction in the seabed foundation	131
5.5.1	Momentary liquefaction	131
5.5.2	Residual liquefaction	133
5.6	Parametric study	137
5.6.1	Effect of soil properties	138
5.6.2	Effect of fluid characteristics	140
5.7	Summary	143
6	3D Numerical Study II: Seabed Foundation Stability around Offshore Detached Breakwaters^{3*}	145
6.1	Introduction	145

Table of contents

6.2	Problem set-up	147
6.3	Flow field around breakwaters	150
6.4	Stress state after consolidation process	150
6.5	Liquefaction potential in the seabed foundation	152
6.5.1	Effect of seabed properties	152
6.5.2	Effect of wave characteristics	157
6.6	Liquefaction zones in the seabed foundation	161
6.7	Summary	169
7	Conclusions and Future Works	171
7.1	Conclusions	171
7.2	Future works	173
	References	175

List of figures

2.1	Zones of applicability of Biot's models (Zienkiewicz et al., 1980).	17
2.2	Boundary lines of applicability of Biot's models (Jeng and Cha, 2003). . . .	18
2.3	Regions of applicability of Biot's models (Ulker et al., 2009).	19
3.1	The coupling process of integrated model.	44
3.2	The set-up of Umeyama (2010)'s experiments (units: m).	46
3.3	The comparison of water surface elevation between the simulation results and Umeyama (2010)'s experimental results.	47
3.4	The sketch of Qi et al. (2019)'s flume tests for combined wave-current induced excess pore pressure in a sandy seabed.	48
3.5	The comparison between the simulation results and Qi et al. (2019)'s experi- mental results for the surface elevation.	50
3.6	The comparison between the simulation results and Qi et al. (2019)'s experi- mental results for the excess pore pressure.	51
3.6	The comparison between the simulation results and Qi et al. (2019)'s experi- mental results for the excess pore pressure (cont.).	52
3.7	The set-up of Mizutani et al. (1998)'s experiments (units: cm).	53
3.8	The application range for various water wave theories (Le Méhauté, 1976). .	54
3.9	The comparison between the simulation results and Mizutani et al. (1998)'s experimental results for the surface elevation.	55
3.10	The comparison between the simulation results and Mizutani et al. (1998)'s experimental results for the wave induced dynamic pore pressure.	57

3.11	The set-up of Mostafa et al. (1999)'s experiments (units: cm).	58
3.12	The comparison of surface elevation between the simulation results and Mostafa et al. (1999)'s experimental results.	59
3.13	The comparison of wave induced dynamic pore pressure between the simulation results and Mostafa et al. (1999)'s experimental results.	60
3.14	The sketch of Sassa and Sekiguchi (1999)'s centrifuge test under progressive wave loading.	61
3.15	The comparison between the simulation results and Sassa and Sekiguchi (1999)'s centrifuge test results for excess pore pressure in sandy seabed. . .	64
3.16	The comparison between the simulation results and Hsu and Jeng (1994)'s analytical solution for vertical distribution of maximum wave induced oscillatory soil response including pore pressure, effective stress and shear stress.	65
4.1	The computational domain of the 2D numerical study.	68
4.2	Time series of surface elevation at three typical locations (a: $x = -8$ m, b: $x = 32$ m and c: $x = 112$ m) for the cases with one ($N = 1$), two ($N = 2$) and three breakwaters ($N = 3$).	72
4.3	Time series of surface elevation at four typical locations (a: $x = -8$ m, b: $x = 32$ m, c: $x = 72$ m and d: $x = 112$ m) for the cases under following currents ($U_0 = 1$ m/s), no currents ($U_0 = 0$ m/s) and opposing currents ($U_0 = -1$ m/s). .	73
4.4	Time series of surface elevation at two typical locations (a: $x = -8$ m and d: $x = 112$ m) for the cases with different spacing between two adjacent breakwaters ($L = 40, 80$ and 30 m).	74
4.5	Distribution of the horizontal velocity field at $t = 240$ s for cases with different spacing between two adjacent breakwaters: (a) $L = 40$ m; (b) $L = 80$ m and (c) $L = 30$ m.	75
4.6	Distribution of pore pressure (p_s), effective normal stress (σ'_z) and shear stress (τ_{xz}) in the seabed foundation after the consolidation process is completed. .	77
4.7	Time series of wave/current induced soil responses including build-up of pore pressure (p_s) and reduction of effective normal stress (σ'_z) and shear stress (τ_{xz}) at (a) location A ($x = -1$ m, $z = -4$ m) and (b) location D ($x = 105$ m, $z = -4$ m) in a sandy seabed foundation.	80

4.7	Time series of wave/current induced soil responses including build-up of pore pressure (p_s) and reduction of effective normal stress (σ'_z) and shear stress (τ_{xz}) at (a) location A ($x=-1$ m, $z=-4$ m) and (b) location D ($x=105$ m, $z=-4$ m) in a sandy seabed foundation(cont.).	81
4.8	Distribution of wave/current induced dynamic soil responses in the (a) poro-elastoplastic seabed foundation and (b) poro-elastic seabed foundation. . . .	83
4.9	Time series of wave/current induced horizontal and vertical displacement at three typical locations ($x=-1$ m, $z=-4$ m; $x=52$ m, $z=-4$ m; $x=105$ m, $z=-4$ m) in a poro-elastoplastic seabed foundation.	85
4.10	Time series of wave/current induced horizontal and vertical displacement at three typical locations ($x=-1$ m, $z=-4$ m; $x=52$ m, $z=-4$ m; $x=105$ m, $z=-4$ m) in a poro-elastic seabed foundation.	86
4.11	Time series of liquefaction potential ($L_{potential}$) within an poro-elastoplastic seabed foundation at typical locations ($x=-1$ m; $x=32$ m; $x=52$ m; $x=105$ m) around breakwaters from two depth: (a) $z=-4$ m and (b) $z=-6$ m.	88
4.12	Wave/current induced liquefaction zones in a poro-elastoplastic seabed foundation at $t=100, 200$ and 300 s in the cases with one ($N=1$), two ($N=2$) and three breakwaters ($N=3$).	89
4.13	Wave/current induced liquefaction zones in a poro-elastic seabed foundation in one wave period from $t=17.6$ s to $t=20$ s.	91
4.14	Effects of currents (U_0) on vertical distribution of liquefaction potential ($L_{potential}$) for $x=-1.5$ m at $t=20, 40, 150$ and 250 s.	92
4.15	Effects of soil permeability (k_s) on vertical distribution of liquefaction potential ($L_{potential}$) for $x=-1.5$ m at $t=20, 40, 150$ and 250 s.	94
4.16	Effects of degree of saturation (S_r) on vertical distribution of liquefaction potential ($L_{potential}$) for $x=-1.5$ m at $t=20, 40, 150$ and 250 s.	95
4.17	Effects of the relative density (D_r) on vertical distribution of liquefaction potential ($L_{potential}$) for $x=-1.5$ m at $t=20, 40, 100$ and 120 s.	96
4.18	Effects of wave period (T) on vertical distribution of liquefaction potential ($L_{potential}$) for $x=-1.5$ m at $t=20, 40, 150$ and 250 s.	97
4.19	Effects of wave height (H) on vertical distribution of liquefaction potential ($L_{potential}$) for $x=-1.5$ m at $t=20, 40, 100$ and 150 s.	98

4.20	Effects of water depth (d) on vertical distribution of liquefaction potential ($L_{potential}$) for $x = -1.5$ m at $t = 20, 40, 150$ and 250 s.	99
5.1	The Southport Spit, Gold Coast, QLD (Figure retrieved from https://haveyoursay.dsdmip.qld.gov.au/the-spit).	102
5.2	The computational domain of the 3D numerical study I.	104
5.3	The sketch of the cross section of the composite breakwater.	104
5.4	The three-view drawings of the computational domain of the 3D numerical study I.	105
5.5	The free surface around the breakwaters at $t = 300$ s, 302 s, 304 s and 306 s.	109
5.6	Time series of surface elevation at location A, B, C, D and E in the case: (a) with river currents and (b) without river currents.	111
5.7	The velocity field in y – direction around breakwaters at $t = 100$ s, 200 s, 300 s and 400 s.	112
5.8	The velocity field in x – direction around breakwaters at $t = 100$ s, 200 s, 300 s and 400 s.	113
5.9	The hydrodynamic pressure acting on the seabed surface around breakwaters at $t = 300$ s, 302 s, 304 s and 306 s.	115
5.10	Distribution of pore pressure (p_s), effective stresses (σ'_x , σ'_y and σ'_z) and shear stresses (τ_{xy} , τ_{yz} and τ_{zx}) on plane $y = 30$ m after consolidation process.	117
5.11	Time series of the dynamic soil responses, including pore pressure (p_s), effective stresses (σ'_x , σ'_y and σ'_z) and shear stresses (τ_{xy} , τ_{yz} and τ_{zx}) at location A ($x = -10$ m, $y = 15$ m, $z = -6$ m) near to first breakwater head.	120
5.12	Time series of the dynamic soil responses, including pore pressure (p_s), effective stresses (σ'_x , σ'_y and σ'_z) and shear stresses (τ_{xy} , τ_{yz} and τ_{zx}) at location C ($x = 10$ m, $y = 52$ m, $z = -6$ m) in front of first breakwater.	121
5.13	Time series of the dynamic soil responses, including pore pressure (p_s), effective stresses (σ'_x , σ'_y and σ'_z) and shear stresses (τ_{xy} , τ_{yz} and τ_{zx}) at location D ($x = 45$ m, $y = 52$ m, $z = -6$ m) between two breakwaters.	122

5.14	Time series of displacements in x - direction (u_s), y - direction (v_s) and z - direction (w_s) at location A ($x = -10$ m, $y = 15$ m, $z = -6$ m), C ($x = 10$ m, $y = 52$ m, $z = -6$ m) and D ($x = 45$ m, $y = 52$ m, $z = -6$ m) within the poro-elastoplastic seabed foundation.	124
5.15	Time series of displacements in x - direction (u_s), y - direction (v_s) and z - direction (w_s) at location A ($x = -10$ m, $y = 15$ m, $z = -6$ m), C ($x = 10$ m, $y = 52$ m, $z = -6$ m) and D ($x = 45$ m, $y = 52$ m, $z = -6$ m) within the poro-elastic seabed foundation.	125
5.16	Spatial distribution of oscillatory pore pressure (p_s) and stress field (effective stresses: σ'_x ; σ'_y ; σ'_z and shear stresses: τ_{xy} ; τ_{yz} ; τ_{zx}) within an elastic seabed foundation around the breakwaters at $t = 300$ s.	127
5.17	Accumulation of the residual pore pressure within a poro-elastoplastic seabed foundation at $t = 50$ s, 200 s, 300 s and 350 s.	129
5.18	Vertical distribution of (a) the maximum dynamic oscillatory pore pressure within the poro-elastic seabed foundation; and (b) the residual dynamic pore pressure at $t = 400$ s within the poro-elastoplastic seabed foundation at location A, C and D.	130
5.19	Distribution of the dynamic pore pressure on a circular area around two breakwater heads at $t = 375$ s.	132
5.20	The predicted momentary liquefaction zones around the breakwaters in a typical wave period from $t = 300$ s to $t = 306$ s, based on Tsai (1995)'s liquefaction criteria.	134
5.21	The predicted residual liquefaction zones around breakwaters from $t = 50$ s to $t = 350$ s based on Jeng and Seymour (1997b)'s liquefaction criteria.	135
5.22	Time series of residual liquefaction potential at location A, B, C, D and E within the poro-elastoplastic seabed foundation around the breakwaters under combined wave and current loading.	137
5.23	Vertical distribution of the wave/current induced liquefaction potential at location A, B, C, D and E within (a) poro-elastoplastic seabed foundation; and (b) poro-elastic seabed foundation at $t = 350$ s.	138
5.24	The development of residual liquefaction zones at $t = 300$ s showed in three typical slides ($y = 0$ m, $y = 25$ m and $y = 50$ m) with different soil permeability ($k_s = 10^{-7}$ m/s, $k_s = 10^{-5}$ m/s and $k_s = 10^{-3}$ m/s).	139

5.25	The development of residual liquefaction zones at $t = 300$ s showed in three typical slides ($y = 0$ m, $y = 25$ m and $y = 50$ m) with different soil degree of saturation ($S_r = 98\%$, $S_r = 95\%$ and $S_r = 93\%$).	140
5.26	The development of residual liquefaction zones at $t = 300$ s showed in three typical slides ($y = 0$ m, $y = 25$ m and $y = 50$ m) within the loosely packed seabed foundation and densely packed seabed foundation.	141
5.27	The development of residual liquefaction zones at $t = 300$ s showed in three typical slides ($y = 0$ m, $y = 25$ m and $y = 50$ m) with different wave height ($H = 1$ m, $H = 2$ m and $H = 2.5$ m).	142
5.28	The development of residual liquefaction zones at $t = 300$ s showed in three typical slides ($y = 0$ m, $y = 25$ m and $y = 50$ m) with different wave period ($T = 6$ s, $T = 5$ s and $T = 4$ s).	142
5.29	The development of residual liquefaction zones at $t = 300$ s showed in three typical slides ($y = 0$ m, $y = 25$ m and $y = 50$ m) with different river currents velocity ($U_0 = 0$ m/s, $U_0 = 1$ m/s, $U_0 = 0.8$ m/s and $U_0 = 0.6$ m/s).	143
6.1	The shore-paralleled detached breakwater at Sea Palling, Norfolk (Figure retrieved from http://pcwww.liv.ac.uk/civilCRG/leacoast/studyarea.htm). . .	146
6.2	The computational domain of the 3D numerical study II.	147
6.3	The three-view drawings of the computational domain of the 3D numerical study II.	148
6.4	Time series of surface elevation at location A, B, C and D in the case: (a) with currents; and (b) without currents.	151
6.5	The distribution of pore pressure (p_s), effective stresses (σ'_x , σ'_y and σ'_z) and shear stresses (τ_{xy} , τ_{yz} and τ_{xz}) after consolidation process.	153
6.6	Vertical distribution of the liquefaction potential ($L_{potential}$) for various soil permeability ($k_s = 10^{-4}$ m/s, $k_s = 10^{-5}$ m/s, $k_s = 10^{-6}$ m/s and $k_s = 10^{-8}$ m/s) at location A ($x = 55$ m, $y = 70$ m), B ($x = 65$ m, $y = 70$ m), C ($x = 60$ m, $y = 90$ m) and D ($x = 60$ m, $y = 50$ m) within the poro-elastoplastic seabed foundation at $t = 350$ s.	155

6.7	Vertical distribution of the liquefaction potential ($L_{potential}$) for various degree of saturation ($S_r = 99\%$, $S_r = 98\%$ and $S_r = 97\%$) at location A ($x = 55$ m, $y = 70$ m), B ($x = 65$ m, $y = 70$ m), C ($x = 60$ m, $y = 90$ m) and D ($x = 60$ m, $y = 50$ m) within the poro-elastoplastic seabed foundation at $t = 350$ s.	156
6.8	Vertical distribution of the maximum liquefaction potential ($L_{potential}$) for various soil permeability ($k_s = 10^{-4}$ m/s, $k_s = 10^{-5}$ m/s and $k_s = 10^{-6}$ m/s) at location A ($x = 55$ m, $y = 70$ m), B ($x = 65$ m, $y = 70$ m), C ($x = 60$ m, $y = 90$ m) and D ($x = 60$ m, $y = 50$ m) within the poro-elastic seabed foundation. . .	158
6.9	Vertical distribution of the maximum liquefaction potential ($L_{potential}$) for various degree of saturation ($S_r = 99\%$, $S_r = 98\%$ and $S_r = 97\%$) at location A ($x = 55$ m, $y = 70$ m), B ($x = 65$ m, $y = 70$ m), C ($x = 60$ m, $y = 90$ m) and D ($x = 60$ m, $y = 50$ m) within the poro-elastic seabed foundation.	159
6.10	Vertical distribution of the liquefaction potential ($L_{potential}$) at location A ($x = 55$ m, $y = 70$ m), B ($x = 65$ m, $y = 70$ m), C ($x = 60$ m, $y = 90$ m) and D ($x = 60$ m, $y = 50$ m) within the loosely deposited poro-elastoplastic seabed foundation and densely deposited poro-elastoplastic seabed foundation at $t = 350$ s.	160
6.11	Vertical distribution of the liquefaction potential ($L_{potential}$) for various long-shore currents conditions ($U_0 = -0.6$ m/s, $U_0 = 0$ m/s and $U_0 = -0.3$ m/s) at location A ($x = 55$ m, $y = 70$ m), B ($x = 65$ m, $y = 70$ m), C ($x = 60$ m, $y = 90$ m) and D ($x = 60$ m, $y = 50$ m) within the poro-elastoplastic seabed foundation at $t = 350$ s.	162
6.12	Vertical distribution of the maximum liquefaction potential ($L_{potential}$) for various longshore currents conditions ($U_0 = -0.6$ m/s, $U_0 = 0$ m/s and $U_0 = -0.3$ m/s) at location A ($x = 55$ m, $y = 70$ m), B ($x = 65$ m, $y = 70$ m), C ($x = 60$ m, $y = 90$ m) and D ($x = 60$ m, $y = 50$ m) within the poro-elastic seabed foundation.	163
6.13	Vertical distribution of the liquefaction potential ($L_{potential}$) for various wave height ($H = 2.4$ m, $H = 2.05$ m and $H = 1.7$ m) at location A ($x = 55$ m, $y = 70$ m), B ($x = 65$ m, $y = 70$ m), C ($x = 60$ m, $y = 90$ m) and D ($x = 60$ m, $y = 50$ m) within the poro-elastoplastic seabed foundation at $t = 350$ s.	164
6.14	Vertical distribution of the liquefaction potential ($L_{potential}$) for various wave period ($T = 4.5$ s, $T = 4.0$ s and $T = 3.5$ s) at location A ($x = 55$ m, $y = 70$ m), B ($x = 65$ m, $y = 70$ m), C ($x = 60$ m, $y = 90$ m) and D ($x = 60$ m, $y = 50$ m) within the poro-elastoplastic seabed foundation at $t = 350$ s.	165

6.15	Vertical distribution of the maximum liquefaction potential ($L_{potential}$) for various wave height ($H = 2.4$ m, $H = 2.05$ m and $H = 1.7$ m) at location A ($x = 55$ m, $y = 70$ m), B ($x = 65$ m, $y = 70$ m), C ($x = 60$ m, $y = 90$ m) and D ($x = 60$ m, $y = 50$ m) within the poro-elastic seabed foundation.	166
6.16	Vertical distribution of the maximum liquefaction potential ($L_{potential}$) for various wave period ($T = 4.5$ s, $T = 4.0$ s and $T = 3.5$ s) at location A ($x = 55$ m, $y = 70$ m), B ($x = 65$ m, $y = 70$ m), C ($x = 60$ m, $y = 90$ m) and D ($x = 60$ m, $y = 50$ m) within the poro-elastic seabed foundation.	167
6.17	Liquefaction zones within a loosely packed poro-elastoplastic seabed foundation around breakwaters at $t = 250, 300$ and 350 s for three typical slices: $x = 54, 60$ and 66 m.	168
6.18	Liquefaction depth within a densely packed seabed foundation at $t = 300$ s. .	169

List of tables

3.1	Parameters used in Umeyama (2010)'s experiments.	46
3.2	Parameters used in Qi et al. (2019)'s tests and numerical simulations	49
3.3	Parameters used in Mizutani et al. (1998)'s experiments	53
3.4	Parameters used in Mostafa et al. (1999)'s experiments	58
3.5	Parameters for verification with Sassa and Sekiguchi (1999)'s centrifuge test.	62
3.6	Parameters for validation with Hsu and Jeng (1994)'s analytical solution . .	63
4.1	The input parameters used in the 2D numerical study.	70
5.1	The input parameters used in the 3D numerical study I.	107
6.1	The input parameters used in the 3D numerical study II.	149

List of symbols

α	volume fraction indicator function
α_g, α_f	parameters related to dilatancy of the soil
β	compressibility of pore fluid
$\dot{\epsilon}_s^e$	elastic deviatoric strain
$\dot{\epsilon}_v^e$	elastic volumetric strain
ε	turbulence energy dissipation rate
ε_s	volume strain
η	ratio between the deviatoric and mean effective stress
η_u	stress ratio from which the unloading takes place
η_w	water surface elevation
γ_U	material constant
γ_w	unit weight of water
γ_{DM}	degradation constant
λ	wave number
λ'	Lame's constant
$\langle \rangle$	Darcy's volume averaging operator
$\langle \rangle^f$	intrinsic averaging operator
μ	molecular dynamic viscosity

μ_s	Poisson's ratio
μ_{eff}	efficient dynamic viscosity
∇	Laplace operator
ν_{turb}	turbulent kinetic viscosity
ϕ	porosity of porous material in fluid domain
ϕ'	residual friction angle of sand measured when $\theta = 30^\circ$
Φ_{water}, Φ_{air}	any property of water and air
ρ	density of the fluid in the fluid domain
ρ'	averaged density of porous seabed
ρ_f	density of pore fluid
ρ_s	density of the solid
$\sigma'_x, \sigma'_y, \sigma'_z$	wave/current induced effective stresses
σ_{ij}	wave/current induced total stresses
$\sigma'_{x0}, \sigma'_{y0}, \sigma'_{z0}$	initial effective stresses in the x -, y -, z - direction
$\tau_{xy}, \tau_{yz}, \tau_{xz}$	wave/current induced shear stresses
θ	Lode's angle
ξ	accumulated deviatoric plastic strain
$C_\mu, C_1, C_2, \sigma_k, \sigma_\varepsilon$	empirical constants used in turbulence model
C_{ijkl}^e	elastic compliance tensor
$d\varepsilon_s$	increment of deviatoric strain
$d\varepsilon_v$	increment of volumetric strain
$d\varepsilon_{ij}^e$	elastic strain increment
$d\varepsilon_{ij}^p$	plastic strain increment
$d\sigma_{kl}$	effective stresses increment

d	water depth
D_r	relative density of soil
d_{50}	mean size of sand grains in seabed
d_{50}	medium grain diameter of the porous material in fluid domain
D_{ijkl}^e	elastic tensor
E	Young's modulus
e	void ratio
G	shear modulus
g_i	acceleration of gravity
G_{es0}	shear modulus of soil under p'_0
G_{es}	shear modulus of soil depending on the confined stress
H	wave height
h	seabed foundation thickness
H_0, H_{U0}	parameter that scales the plastic modulus
$H_{L/U}$	plastic modulus for the loading or unloading stage
k	turbulence kinetic energy
K_0	lateral compression coefficient of soil
K_s	bulk modulus of the solid
k_s	permeability of porous medium
K_w	true bulk modulus of pore fluid
K_{ev0}	elastic bulk modulus of soil under p'_0
K_{ev}	bulk modulus of soil depending on the confined stress
KC	Keulegan Carpenter number
L	space between two adjacent breakwaters

L_w	wave length
L_{depth}	liquefaction depth of soil
$L_{potential}$	wave/current induced liquefaction potential in seabed foundation
M_g	slope of critical state line in $p' - q'$ plane
m_{ij}	plastic flow direction tensor
N	number of breakwaters
n_s	porosity of porous medium
n_{ij}	loading or unloading direction tensor
p^*	pseudo-dynamic pressures
p'	mean effective stress
p_0	hydrodynamic wave pressure calculated by linear wave theory
p'_0	mean effective stress used to measure the elastic parameter of soil
p_b	wave/current induced pressure on the seabed surface
p'_f	size parameter for the yield surface function
p'_g	size parameter for the plastic potential surface function
p_s	wave/current induced pore pressure
P_{cr}	critical value when soil becomes liquefied
p_{w0}	absolute water pressure
q'	deviatoric stress
S_r	degree of saturation
T	wave period
T_0	period of the oscillation
U_0	velocity of current
u_i	flow velocity

u_m	maximum oscillating velocity
u_s, v_s, w_s	soil displacement in the x –, y – and z – direction
V	total volume
V_c	velocity of the compressive wave
V_f	volume of fluid

Chapter 1

Introduction

1.1 Background

Coastal zones have been in increasingly strong demands for human activities such as port trade, marine transport, tourism, agricultural and fishery production. While these demands bring immeasurable economic benefits, they also directly lead to the rapid development of the coastal areas focusing on the shoreline management and protection. Many coastal protection structures, such as breakwaters, groynes, artificial headlands, seawalls and bulkheads, have been constructed around the main beaches and major estuaries as the critical defences against ocean wave effects such as beach erosion and damage. Breakwaters have been commonly constructed due to their low construction costs and environmental impacts, high performance and convenience for later quality control and maintenance. Breakwaters also have wide ranges of application coverage according to their designed functions and characteristics, for example, providing an artificial harbour by blocking the wave actions and redirecting the rivers and streams.

While protecting the shoreline, breakwaters are also exposed to the harsh marine environment. Significant changes of pore pressure, effective stresses and soil deformation will occur in the seabed when waves propagate over seabed surface. These changes due to rapidly applied ocean loading are referred to as excess pore pressures, dynamic effective stresses and soil displacements. With the reduction of effective stresses, soil liquefaction may occur around the structure foundation, which is considered as a significant cause of catastrophic failures of marine structures.

In general, depending on how the excess pore pressure is generated, two types of soil response mechanisms have been classified based on field measurements (Zen and Yamazaki,

1991) or laboratory experiments (Nago et al., 1993; Zen and Yamazaki, 1990a), namely (1) transient/oscillatory soil responses and (2) residual soil responses. For the wave induced transient/oscillatory soil responses, the pore water pressure and effective stresses in the seabed fluctuate periodically in accordance with the propagation of waves. In general, the soil behaviour of the poro-elastic seabed under small-amplitude waves is dominated by transient/oscillatory soil response mechanism since there is no permanent deformation occurs. The wave-induced residual soil responses are always accompanied by the build-up of pore pressure in seabed. This kind of pore pressure build-up is caused by permanent seabed deformation due to the compaction of soil particles under long-term of cyclic wave loading. Therefore, the residual mechanism is dominant for a poro-elastoplastic seabed, in which the soil particles are relatively loose. The corresponding soil liquefaction caused by the above two mechanisms are defined as transient/momentary liquefaction and residual liquefaction, respectively.

The vulnerability of breakwater foundations can be associated with dynamic soil responses in the vicinity of the structure when subject to cyclic ocean wave loading (Oumeraci, 1994). As reported in the literature, numerous damages of breakwaters were caused by wave-induced seabed foundation instability rather than from the structural deficiencies (Lundgren et al., 1989; Sumer, 2014). Some examples of breakwater failures caused by the foundation liquefaction have been reported in the literature (del Campo and Vicente, 2011; Lundgren et al., 1989; Oumeraci, 1994; Puzrin et al., 2010). Therefore, a better understanding the foundation responses and accurately predicting the potential liquefaction in the neighbourhood of breakwaters under cyclic ocean loading, especially in the cases with complex loading conditions and foundation geometries, have become one of the main factors involved in the design and maintenance of these marine structures of their long term behaviour.

Numerous investigations with respect to the fluid-seabed-structure interactions have been carried out, in which analytical approximations were normally adopted in the early stage, with marine structure being simplified as an impermeable line without width and weight due to the limitation of analysis. On the other hand, numerical simulations on the fluid-seabed-breakwater interactions have been developed in the last two decades with the improving of computing resources and the development of advanced integrated numerical model to include both wave transformations and soil responses. Among the existing numerical works, following limitations are identified: (1) most the previous works have been limited to wave-induced oscillatory soil responses and associated momentary liquefaction using the linear poro-elastic theory for the soil skeleton. The wave induced residual soil responses are also significant, actually, the residual liquefaction that caused by pore pressure build-up in the poro-elastoplastic seabed foundation is much easier to occur and can cause more severe

damage to the foundation of marine structures than the momentary liquefaction in the poro-elastic soil; (2) the vast majority of the previous studies have been limited to two-dimensional (2D) frameworks, in which only the middle cross-section of breakwaters under perpendicular incident waves can be studied. In the practical engineering environment, there are many situations that involve much more complicated fluid-seabed-structure interactions, which requires three-dimensional (3D) numerical models to fully provide insight into both fluid and soil dynamics; (3) many previous works simplified the flow field by only considering the wave loading, some even simplified the flow pressure as an analytical approximation. However, in the real marine environment, in addition to the propagating waves, there are often other components such as ocean/river currents. The actual environment is more complex and the resulting soil response is often different. A more advanced flow model is required to incorporate into the integrated numerical model to handle more realistic conditions.

1.2 Research objectives

One of the main novel contributions of this study is the development of the efficient integrated numerical model with the capability of modelling the problems of fluid-seabed-structures interactions, which overcomes the above-mentioned shortcomings, including considering the poro-elastoplastic soil behaviour, more complicated 3D engineering situations and more accurate and realistic hydrodynamic actions. This integrated model includes a flow sub-model, a seabed sub-model and an integrated module between two sub-models. The flow sub-model is governed by the Volume-Averaged Reynolds Averaged Navier-Stokes (VARANS) equations with $k - \varepsilon$ turbulence model, which has the capability of efficiently and accurately simulating the local hydrodynamic process around the breakwaters. The seabed sub-model is governed by the Biot's $u - p$ approximation equations, which is embedded with both poro-elastic soil constitutive model for the oscillatory soil response and momentary liquefaction and poro-elastoplastic soil constitutive model for the residual soil response and residual liquefaction. The integration of flow and seabed sub-models are through pressure continuity on the common faces, including the surface of seabed and surface of breakwaters. The main objective of this thesis is to use the model to numerically examine the breakwater foundation stability by predicting and assessing the dynamic soil responses and liquefaction potential around the breakwaters in different engineering conditions. More specific project objectives are outline as below:

1. Validation of the integrated model with existing laboratory experiments data, centrifuge wave test data or analytical solutions available in the literature;

2. Analysis of flow field, wave/current induced soil response and liquefaction potential around multiple submerged breakwaters with Bragg effect in 2D condition;
3. Evaluation of the seabed foundation stability around the breakwaters at a river mouth in 3D condition;
4. Assessment of the seabed foundation stability around the coast-paralleled detached breakwaters in 3D condition.

1.3 Outline of this thesis

This thesis consists of seven chapters. In addition to Chapter 1, Chapter 2 is the literature review, in which a detailed review of previous works with respect to the fluid-seabed interactions and fluid-seabed-breakwater interactions is provided. Chapter 3 describes the detailed mathematical framework involved in the integrated numerical model, including the flow sub-model, seabed sub-model and the integrated process between two sub-models, followed by a set of comprehensive model validations by the existing laboratory experiments data or analytical solutions. Chapter 4 presents the first numerical study conducted in 2D condition, the soil response and liquefaction potential around multiple submerged breakwater with Bragg effect under combine wave and current loading. Chapter 5 conducts the investigation of seabed foundation stability around the breakwater at a river mouth that involves the interactions between waves, river current and breakwaters in 3D condition. In this case, time and spatial series of oscillatory soil responses and residual soil responses and associated momentary liquefaction and residual liquefaction are examined. Chapter 6 presents another 3D numerical study of seabed foundation stability around the coast-paralleled detached breakwaters, considering the effect of soil properties and wave characteristics on the liquefaction potential in the seabed foundation. Last, Chapter 7 concludes the key findings of this thesis and provides the possible applications of the present work in the future.

Chapter 2

Literature Review

In this chapter, a detailed literature review will be presented to summarise the achievement and limitation of the previous work available in the literature. Based on the literature, the research gaps between the existing knowledge and the proposed study can be identified.

2.1 Fluid-Seabed Interactions

2.1.1 Decoupled models

At the early stage of the sea floor dynamic theory development, the soil skeleton was assumed to be incompressible. The flow in the voids has no effect on soil skeleton, that is, the pore fluid and soil particles are not coupled. These models are called decoupled models, which have been well solved analytically. However, only wave-induced pore pressure is considered in these models. If the pore fluid is treated as incompressible medium, the model is governed by Laplace's equation, which is called Laplace model. Compared with Laplace model, if the compressibility of pore fluid is considered, the model is subjected to diffusion equation and it is called Diffusion model. Both models ignore the accelerations of pore fluid and soil particles.

Laplace model

The governing equation of Laplace model can be expressed as:

$$\nabla^2 p_s = \frac{\partial^2 p_s}{\partial x^2} + \frac{\partial^2 p_s}{\partial y^2} + \frac{\partial^2 p_s}{\partial z^2} = 0 \quad (2.1)$$

where $x - y - z$ is the coordinate system; ∇^2 is the Laplace operator ($\nabla^2 = \frac{\partial^2}{\partial x^2} + \frac{\partial^2}{\partial y^2} + \frac{\partial^2}{\partial z^2}$); p_s is the wave-induced pore pressure in seabed.

Based on the assumption of incompressible soil skeleton and pore fluid, Putnam (1949) presented an analytical solution for an isotropic seabed with finite thickness using linear wave theory. Putnam (1949) found that the wave energy loss when propagating over the porous sandy seabed mainly comes from the percolation process of viscous fluid within the seabed. He also pointed out that pore pressure only depends on the geometry of seabed and wave characteristics above seabed, not related to soil properties. In fact, the soil properties have huge impact on the distribution of pore pressure within seabed. Putnam (1949)'s work was further extended by Sleath (1970) for the wave-induced pore pressure in rigid seabed with finite thickness and anisotropic permeability, and by Liu (1973) for considering the viscous effect of boundary layer and energy balance. Sleath (1970) also conducted experiments aiming at verifying his analytical results, however, the experimental results were inconsistent with his theoretical results due to the limited assumptions of his theoretical approach. Through Sleath (1970)'s experiments, an unexpected result of the phase lag (less than 10 degrees) of wave-induced pore pressure in vertical direction in sandy seabed was found. The results of Liu (1973)'s study showed that the pore pressure is unrelated to permeability, while fluid velocity is depended on the porosity and permeability. Later, Liu (1977) further extended his work to a two-layered porous seabed, and found that the pore pressure is slightly related to both permeability and thickness of the upper layer. Due to the fact that the Laplace model is a fast drainage model that assumes the soil is rigid and the pore fluid is incompressible, the Laplace model is only suitable for gravel and coarse sandy seabed with very large soil permeability.

Diffusion model

The governing equation of Diffusion model can be expressed as:

$$\nabla^2 p_s - \frac{\gamma_w n_s \beta}{k_z} \frac{\partial p_s}{\partial t} = 0 \quad (2.2)$$

where γ_w is the unit weight of water; n_s is the porosity; β is the compressibility of pore fluid that is defined in equation, (2.7); and the k_z is Darcy's permeability in z - direction.

Nakamura et al. (1973) first studied the vertical distribution of the pore pressure within a fine sandy seabed. The compressibility of pore fluid was included in Nakamura et al. (1973)'s model, the soil skeleton was still treated as a rigid medium. As a result, this is another type of decoupled model, Diffusion model. Using their model, Nakamura et al. (1973) compared the theoretical results of pore pressure with laboratory experiments in fine and coarse sandy seabed. They found that the Diffusion model can better describe the vertical distribution of pore pressure in a fine sandy seabed with a phase lag identified. For a coarse sandy seabed, no phase lag was found in laboratory results, which the distribution of pore pressure agreed well with Laplace model. However, the analytical results from Diffusion model did not match the laboratory results near the seabed surface. Yamamoto et al. (1978) explained that it might due to the local liquefaction occurred near the seabed surface that caused by steep wave used in their experiments. Møshagen and Tørum (1975) studied the motion characteristics of pore fluid within a non-deformable seabed, and pointed out that the inclusion of compressibility of pore fluid can significantly alter the seepage force on the soil skeleton.

The above-mentioned decoupled models have great limits of application. Laplace model is only applicable to a coarse gravel sandy seabed with large soil permeability, while Diffusion model is suitable for a fine sandy seabed with small soil permeability. In addition, such decoupled models only consider the pore pressure distribution, which does not provide information for key variables of marine soil mechanics such as effective stresses and soil displacements.

2.1.2 Coupled models for the wave-induced oscillatory soil responses

With the development of sea floor dynamics theory, many scholars realised that the decoupled models are not sufficient to simulate real seabed conditions in most cases because the deformation of soil skeleton and the motion of pore fluid simultaneously exist. To overcome the shortcoming of the decoupled models, the coupled models which treat both soil skeleton and pore fluid as compressible medium were proposed. The soil-pore fluid interaction has been considered in the coupled models, which is a more accurate way to describe the mechanical properties of porous medium.

In the rest of this chapter, the coupled models for wave-induced oscillatory soil responses and residual soil responses will be reviewed. Most coupled models are based on Biot's theory. Depending on whether the acceleration of soil particles and pore fluid motion is included,

Biot's theory can be classified into three categories: Biot's consolidation model, dynamic model and $u - p$ approximation.

Biot's consolidation model

The Biot's consolidation model can be expressed in forms of forces equilibrium:

$$G\nabla^2 u_s + \frac{G}{1-2\mu_s} \frac{\partial \epsilon_s}{\partial x} = \frac{\partial p_s}{\partial x} \quad (2.3)$$

$$G\nabla^2 v_s + \frac{G}{1-2\mu_s} \frac{\partial \epsilon_s}{\partial y} = \frac{\partial p_s}{\partial y} \quad (2.4)$$

$$G\nabla^2 w_s + \frac{G}{1-2\mu_s} \frac{\partial \epsilon_s}{\partial z} = \frac{\partial p_s}{\partial z} \quad (2.5)$$

and mass conservation of pore fluid:

$$\frac{k_x}{k_z} \frac{\partial^2 p_s}{\partial x^2} + \frac{k_y}{k_z} \frac{\partial^2 p_s}{\partial y^2} + \frac{\partial^2 p_s}{\partial z^2} - \frac{\gamma_w n_s \beta}{k_z} \frac{\partial p_s}{\partial t} = \frac{\gamma_w}{k_z} \frac{\partial \epsilon_s}{\partial t} \quad (2.6)$$

where G is the shear modulus of soil; u_s , v_s and w_s are the displacements of soil in the x -, y - and z - direction, respectively; μ_s is the Poisson's ratio; ϵ_s is the volume strain, defined as $\epsilon_s = \partial u_s / \partial x + \partial v_s / \partial y + \partial w_s / \partial z$; p_s is the pore pressure; γ_w is the unit weight of water; n_s is the porosity of soil; k_x , k_y and k_z are the Darcy's permeability coefficients in the x -, y - and z - direction, respectively; β is the compressibility of pore fluid defined as:

$$\beta = \frac{1}{K_w} + \frac{1-S_r}{P_{w0}} \quad (2.7)$$

where K_w is the true bulk modulus of pore water that is taken as $K_w = 1.95 \times 10^9$ Pa (Yamamoto et al., 1978); S_r is the degree of saturation; p_{w0} is the absolute water pressure.

For the two-dimensional Biot's consolidation model, the terms related to y - axis should be ignored.

The Biot's consolidation model has limitations in application due to some assumptions made in Biot (1941)'s work. First, the soil is considered as homogeneous and isotropic. Then, the stress-strain relation is reversible (i.e, linear elastic), which only the small deformation

cases are applicable. Furthermore, the water flows within the porous medium are considered as steady. Therefore, Darcy's law is used as the governing equation. It is also worth noting that the accelerations of solid and fluid are ignored in Biot's consolidation equations. As the result, consolidation equations are suitable for consolidation process with small permeability or low-frequency loading.

To solve the Biot's consolidation equations, three methodologies have been mainly adopted in the literature: analytical solution, boundary-layer approximation and numerical modelling.

At the early stage, analytical solution was the most widely used method to solve the wave-seabed interaction problems due to the insufficient development of computer technology. Based on Biot (1941)'s consolidation theory, Yamamoto et al. (1978) obtained the exact closed-form solutions for the wave-induced pore water pressures, the displacements of soil and the effective stresses in an elastic isotropic infinite porous bed induced. Their solution showed that the seabed response is dependent on the permeability, the stiffness of the porous medium, and the compressibility of the pore fluid. Moreover, they found that the previous solutions presented by Putnam (1949), Nakamura et al. (1973) and Mørshagen and Tørum (1975) are extreme cases of their solution. When the stiffness of the porous medium is much smaller than that of the pore fluid (i.e., saturated soft soils), Yamamoto et al. (1978)'s solution approaches the solution by Putnam (1949) that is independent of permeability and no phase lag, when the stiffness of the porous medium is much larger than that of the pore fluid (i.e., partially saturated dense sands), it approaches the solution by Nakamura et al. (1973) and Mørshagen and Tørum (1975) that the pressure attenuates rapidly and the phase lag increases linearly as the distance from the bed surface increasing. Yamamoto (1981) further extended his analytical solution from an isotropic infinite seabed to a non-homogeneous layered seabed with finite thickness, along with a comprehensive validation using the data obtained from Mississippi Delta. However, the solution is semi-analytical without a closed form.

Madsen (1978) also developed a solution of wave-induced seabed response based on the Biot's consolidation theory. He treated the infinite seabed as hydraulically anisotropic and partially saturated. It was found that the effect of anisotropy of the soil has an appreciable effect on the nature of the wave-induced effective stresses only in a coarse sand. The effect of partial saturation may be significant for all soils.

Using Biot's consolidation theory and a compatibility condition for elasticity, Okusa (1985) proposed a simple method to solve the wave-induced pore pressure and effective stresses in a poro-elastic seabed based on plane-stress conditions. The governing equation is a fourth-order partial differential linear equation. From his study, Okusa found that for

the unsaturated seabed, the wave-induced pore pressure and effective stresses consist of two parts. One part is only dependent on the wave length and the other part depends on both sediment and wave characteristics. For saturated sediment, the wave-induced pore pressures and effective stresses are almost unrelated to the sediment properties and are only dependent on the wave height and wave length.

Within the framework of Biot's consolidation theory, Rahman et al. (1994) summarised the previous work with a general semi-analytical analysis. In his work, the response of homogeneous seabed with finite thickness under a plane progressive wave was studied. An extension for the case of a layered seabed was also studied. A three-dimensional response of seabed was also developed for a general wave field which provides the analysis for soil responses around a structure.

In a natural seabed, the permeability of seabed is usually not isotropic, which most of the aforementioned studies are based on. The soil permeability generally decreases with depth as the effect of consolidation. Seymour et al. (1996) developed a new theory for the wave-induced response in an unsaturated and anisotropic seabed with variable permeability. The results of their study showed that the effect of variable permeability on the response of seabed can be significant, in particular to coarser seabed and unsaturated sandy soils. Furthermore, Jeng and Seymour (1997b) and Jeng and Seymour (1997a) developed the analytical solutions for wave-induced soil responses in both finite and infinite thickness seabed with variable permeability.

The elastic properties of a cross-anisotropic material could be defined by five independent elastic parameters while it only needs two independent constants to characterise an isotropic elastic material. Many investigations show that significant errors may occur with assumptions of isotropic materials. For instance, Jeng (1996b) pointed out that a simplified anisotropic model based on three parameters caused the error in prediction of strain by 30 % to 40 %, compared with the prediction from isotropic model. Gatmiri (1992) might be the first to study the wave-induced response in a cross-anisotropic seabed using the numerical method (finite element method), without giving the analytical solution. Jeng (1996b) was the first one who derived the analytical solution for wave-seabed interaction with a cross-anisotropic seabed. Based on Jeng's solution, the maximum liquefaction potential can be estimated. Jeng also found that, in his study, the isotropic solution underestimates the wave-induced pore pressure, and overestimates the maximum potential liquefaction depth.

The analytical solution could provide a very accurate result for the wave-induced seabed response. However, it contains complicated mathematical expressions which makes it inconvenient for engineering applications. This kind of shortcoming is even more obvious when

the seabed is finite thickness or layered. On account of this issue, another methodology to solve the governing equations of Biot's consolidation model, the boundary layer approximation, was first proposed by Mei and Foda (1981). The solution from the boundary-layer approximation method has a much simpler form compared with analytical solution because only the inner part of soil requires a full solution, while for the outer part, a simplified solution is sufficient. However, it may lose accuracy for all soil in unsaturated condition and for coarse sand under saturated conditions. The boundary-layer approximation proposed by Mei and Foda (1981) is restricted only to low frequency waves. Huang and Chwang (1990) found three uncoupled Helmholtz equations to represent all three kinds of waves which are applicable for complete range of wave frequencies.

With the development of computer technology, more and more researchers have chosen to use numerical simulation to study the wave-seabed interactions. The numerical modelling has many advantages compared with analytical solutions and boundary-layer approximations. It can solve more complex problem more easily and its operability makes it more suitable for engineering applications.

Madga (1990) developed a one-dimensional finite difference model for analysing wave-induced pore pressure in a highly saturated sandy bed. The finite difference analysis was adopted in Zen and Yamazaki (1990b)'s work to examine the oscillatory pore pressure in porous seabed induced by ocean waves in the context of the wave-induced liquefaction. The experimental model tests were also performed and a good agreement between the finite difference solutions and the measurement was found. Cheng et al. (2001) developed a numerical solution using finite difference method to simplify the Biot's consolidation equation. Their model was to investigate the wave-induced accumulation of pore pressure in marine sediments. The results of their study showed that the solution for deep soil conditions is sensitive to the shear stress in the top thin layer of the soil.

Gatmiri (1990) developed a finite element program (COHET) to investigate the effects of different variables on the wave-induced pore pressures and effective normal stresses and shear stresses in finite thickness isotropic seabed. This study provided a numerical solution of the generalised Biot's formulation based on theory of finite deformation of saturated porous seabed under transient dynamic loading. Also, a comparative study was made for the finite element program with infinite depth solution given by Yamamoto et al. (1978) and Madsen (1978). For a homogeneous isotropic, linear elastic porous bed saturated with an incompressible pore water, there exists a critical bed thickness about 0.2 times of wave length (i.e., $d_s = 0.2L$) that the horizontal movement of sea floor is maximum and the most unstable stress state occurs. For the response of an inhomogeneous seabed, the effect of

a soft layer near the sea-soil interface is very important. Gatmiri (1992) further extended his program to study the effect of cross-anisotropic seabed on the distribution of wave-induced pore pressure and effective stresses. The solution of his model showed that the elastic anisotropic parameters have significant influence on the wave-induced soil responses. However, Jeng (2003) has found that a possible error in Gatmiri (1990) and Gatmiri (1992) caused by implementing invalid boundary condition. Thomas (1989, 1995) derived the finite element formulation of the differential equations governing wave-induced soil responses for a two-layered unsaturated seabed. Then, a series of 1D finite element models have been developed for the wave-induced seabed response in a nonhomogeneous seabed (Jeng and Lin, 1996, 1997; Lin and Jeng, 1996, 1997). The results of their 1D models are validated by previous 2D experimental data and analytical solutions. On the one hand, these 1D finite element models have advantages like computationally efficient. On the other hand, the case with a structure within the seabed cannot be analysed under one-dimensional condition, these 1D finite element models become invalid for this kind of case. As a result, Jeng et al. (1998) and Lin and Jeng (2000) proposed a 2D finite element model, based on the concept of repeatability.

Raman-Nair and Sabin (1991) studied the effect of wave forces on the stability of a sloping seabed using linear wave theory and Biot's consolidation theory. They applied the boundary element method to compute the wave forces on the slope, the wave-induced effective stresses and pore pressure. The results of their investigation indicated that the stability of a slope under waves is strongly dependent on the initial stress distribution.

Wang et al. (2004) established a model to analyse the wave-induced transient response of seabed soils by using Radial Point Interpolation Mesh-free Method (RPIM), which probably was the first one who applied the mesh-free method to coastal engineering. Wang et al. (2004)'s study is based on the Biot's consolidation theory, in which the seabed is assumed to be linear and elastic. The results of their study were validated by comparing with two typical solutions for the wave-induced response of the seabed, Madsen (1978) and Hsu and Jeng (1994)'s closed-form solutions and FEM results. The results of pore water pressure at a point near seabed surface were compared, mesh-free method results agree well with Hsu and Jeng (1994)'s closed-form solutions, while have a little difference at the location near bottom compared to Madsen (1978)'s solution. This is because he developed the solution based on the infinite thickness seabed while Hsu and Jeng based on finite thickness. The mesh-free Method also agreed well with the FEM method results.

Fully dynamic model

The Biot's fully dynamic model can be expressed in forms of stress equilibrium equation, momentum equilibrium equation and continuity equation, respectively, as (in the tensor form)

$$\sigma_{ij,j} + \rho' g_i = \rho' \ddot{u}_{si} + \rho_f (\ddot{w}_{fi} + \dot{w}_{fj} \dot{w}_{fi,j}) \quad (2.8)$$

$$-p_{,i} + \rho_f g_i = \rho_f \ddot{u}_{si} + \frac{\rho_f}{n_s} (\ddot{w}_{fi} + \dot{w}_{fj} \dot{w}_{fi,j}) + \frac{\rho_f g}{k_{ij}} \dot{w}_{fj} \quad (2.9)$$

$$\dot{\epsilon}_{ii} + \dot{w}_{fi,i} + \frac{1}{Q} \dot{p}_s = 0 \quad (2.10)$$

where σ_{ij} is the total stresses; ρ' is the average density of porous seabed, defined as $\rho' = \rho_f n_s + \rho_s (1 - n_s)$ in which ρ_f is the density of pore water and ρ_s is the density of the solid; g_i is the gravity; $(u_s)_i$ and $(w_f)_i$ are the displacements of solid and the relative displacements of fluid to solid, respectively; Q is defined as:

$$\frac{1}{Q} = n_s \beta + \frac{1 - S_r}{K_s} \quad (2.11)$$

in which K_s is the bulk modulus of the solid.

Biot (1955, 1956a) extended the Biot's consolidation model to the general cases of a porous anisotropic solid and a porous viscoelastic anisotropic solid, respectively. After that, Biot further extended the theory to dynamic forms by introducing the inertia terms of solid and fluid in low-frequency range (Biot, 1956b) and in high-frequency range (Biot, 1956c). Then, Biot (1962) presented a general set of fully coupled equations governing the behaviour of a saturated linear elastic porous seabed for consolidation and dynamic problems. Compared with Biot's consolidation model, the acceleration of solid and the relative acceleration of pore fluid to solid are involved in the fully dynamic model.

Within the same framework as Zienkiewicz et al. (1980), Jeng and Rahman (2001) investigated the effects of dynamic soil behaviour on the wave-induced soil responses through a two-dimensional analysis. The solution of their model provided a better prediction of the soil responses. However, their model is difficult to be applied in engineering practice due to its lengthy mathematical expression.

Based on boundary-layer approximation, Huang and Song (1993), Chen et al. (1997) and Hsieh et al. (2001) developed a series of analytical solutions for dynamic response of poro-elastic bed to water waves. Both linear and nonlinear wave loading were considered.

A simpler formulation was provided by their approximation compared to the close-form solutions.

Alternatively, based on the governing equations derived by Mei and Foda (1981), Yuhi and Ishida (1998) presented the analytical solution for wave-induced seabed response, rather than using boundary-layer approximation. In their study, the seabed was considered to be infinite thickness.

$u - p$ approximation

The $u - p$ approximation model was first proposed by Zienkiewicz et al. (1980) by neglecting the terms involving the second time derivatives of the relative fluid displacement (i.e., the relative acceleration of pore fluid to soil skeleton) in Biot (1962)'s fully dynamic model. Since the primary variables are now displacement $\vec{u} = (u_x, v_s, w_x)$ and pore pressure (p_s), the model is called the $u - p$ approximation. The governing equations for $u - p$ approximation can be presented as:

$$G\nabla^2 u_s + \frac{G}{1-2\mu_s} \frac{\partial \epsilon_s}{\partial x} = \frac{\partial p_s}{\partial x} + \rho' \frac{\partial^2 u_s}{\partial t^2} \quad (2.12)$$

$$G\nabla^2 v_s + \frac{G}{1-2\mu_s} \frac{\partial \epsilon_s}{\partial y} = \frac{\partial p_s}{\partial y} + \rho' \frac{\partial^2 v_s}{\partial t^2} \quad (2.13)$$

$$G\nabla^2 w_s + \frac{G}{1-2\mu_s} \frac{\partial \epsilon_s}{\partial z} = \frac{\partial p_s}{\partial z} + \rho' \frac{\partial^2 w_s}{\partial t^2} \quad (2.14)$$

$$\frac{k_x}{k_z} \frac{\partial^2 p_s}{\partial x^2} + \frac{k_y}{k_z} \frac{\partial^2 p_s}{\partial y^2} + \frac{\partial^2 p_s}{\partial z^2} - \frac{\gamma_w n_s \beta}{k_z} \frac{\partial p_s}{\partial t} + \rho_f \frac{\partial^2 \epsilon_s}{\partial t^2} = \frac{\gamma_w}{k_z} \frac{\partial \epsilon_s}{\partial t} \quad (2.15)$$

The above equations are in 3D situation, for the 2D situation, the terms related to y- axial should be ignored. The acceleration of pore fluid/soil skeleton itself is still included in the $u - p$ model, which can be seen from the inertia terms in governing equations compared with Biot's consolidation model. On the one hand, the $u - p$ model is computational economically and conveniently in the case with small permeability where the relative acceleration of pore fluid to soil skeleton is apparently small. On the other hand, this simplified form will certainly affect the solution accuracy to some extent. The application range of these approximations will be discussed in the later Section.

Sakai et al. (1988) examined the effects of inertia of pore fluid and solid in seabed and gravity on seabed response under the ocean waves. Using Mei and Foda (1981)'s

Boundary-layer approximation, taking into account the effect of inertia, an analytical solution of pore water pressure under small amplitude waves was obtained. It was found that in their investigation the effect of inertia on pore water pressure is several percent in a seabed of clay or silt ($G = 1.5 \times 10^7 \text{ N/m}^2$) under small amplitude waves. They also reported that the effect of inertia is large under a breaking wave. Then, they modified the Biot's consolidation equations to include gravity terms and solved the equations numerically using finite element method for the pore water pressure and solid displacement in a seabed of small pore water bulk modulus under small amplitude. The effect of gravity was found negligibly small even in a seabed with small pore water bulk modulus. Later, Sakai et al. (1991) further considered the effect of wave-induced bottom shear stress using boundary layer approximation in surf zone.

Jeng et al. (1999) examined the influence of inertia forces on the wave-induced seabed response in a condition of two-dimensional waves over a porous seabed. They presented the first closed-form analytical solution to the governing equation for such a condition. It was found in their study that the inertia forces cannot be ignored in a soft seabed. The relative differences between the case considering inertia forces and the case without considering inertia forces may reach 5 % of the amplitude of pressure under certain combination of wave and soil conditions. Jeng et al. (1999)'s study was based on the assumption that the seabed thickness is infinite. However, seabed thickness significantly affects the evaluation of seabed response. Later, Jeng and Rahman (2000) further examined the influences of inertia forces on the wave-induced seabed response in a seabed with finite thickness. They presented a new semi-analytical solution in this case and found that the relative differences between the case with inertia items and the case without inertia items may reach up to 17 % of the amplitude of pressure under certain combination of wave and soil conditions. They also found that the inertia forces do not only affect the magnitudes of the wave-induced seabed response, but also cause a phase lag in the distribution of the wave-induced seabed response.

Chan (1988) developed a two-dimensional finite element model (SWANDYNE II), in which the $u - p$ approximation was used as the governing equations. SWANDYNE II has ability to analyse problems with static, consolidating and dynamic conditions under drained and undrained situations. SWANDYNE II was initially for the problems of earthquake induced soil liquefaction, but was later applied to wave-induced soil liquefaction. For instance, Dunn et al. (2006) numerically studied the liquefaction of seabed around a buried pipeline under wave action by adopting the finite element model SWANDYNE II. More recently, Ye and Jeng (2012) used the elastic model of SWANDYNE II as the seabed model to examine the seabed response under combined wave and current loading. However, DIANA-SWANDYNE II is limited to two-dimensional numerical simulations while most of the

problems in practical engineering could only be solved in three-dimension. For example, in most cases, structures under three-dimensional ocean loading involves different component of waves (i.e., incident, reflected and diffracted waves), which will further induce the three-dimensional soil response around the structures. Therefore, Ou (2009) further extended the SWANDYNE II program to a three-dimensional model (DYNE3WAC) and applied the model to perform analysis for soil responses and liquefaction around a breakwater head (Jeng and Ou, 2010). Later, Jeng and Ou (2010) applied DYNE3WAC to investigate the wave-induced pore pressure near breakwater heads. However, the 3D wave loading around breakwater heads is adopted as analytical solution proposed by Stoker (1957) and they did not consider the actual breakwater heads structure but the breakwater's influence on the wave field.

Application range of Biot's models

It is important to identify the applicability of Biot's models for practical engineering. In general, the fully dynamic model is capable to describe all quasi-static and dynamic problems. However, it costs huge time to solve quasi-static problems using dynamic models. Using the simplified forms of Biot's models, the $u - p$ approximation and Biot's consolidation model, to solve certain problems with relatively high accuracy is a more reasonable choice. Three main works on identifying the applicable ranges of validity of three types of Biot's models will be reviewed in this section.

The first attempt to investigate the appropriate domain of applicable range of Biot's models was made by Zienkiewicz et al. (1980), who conducted an analytical study of a soil layer under periodic surface loading with same boundary conditions. The comparative results of their study are shown in Figure 2.1 that is divided into three zones (I, II and III) based on the soil permeability and loading frequency. Zienkiewicz et al. (1980) concluded that the fully dynamic model can be used in all three zones; the $u - p$ approximation can be used in zone I and II with the largest applicable frequency approximately at 1000 Hz; the Biot's consolidation model only can be used in zone I, which is the low soil permeability and low loading frequency zone. Figure 2.1 can only provide a rough approximation as the results were based on one-dimensional analysis with single soil layer, assuming that the compressive wave velocity was 1000 m/s. Jeng and Cha (2003) pointed out that the speed of compressive wave is significantly related to the saturation of soil and the water depth.

The second study was conducted by Jeng and Cha (2003) using their analytical solution for two-dimensional wave seabed interaction problems. They plotted boundary lines (Figure 2.2) to determine the conditions when the fully dynamic model and $u - p$ approximation must

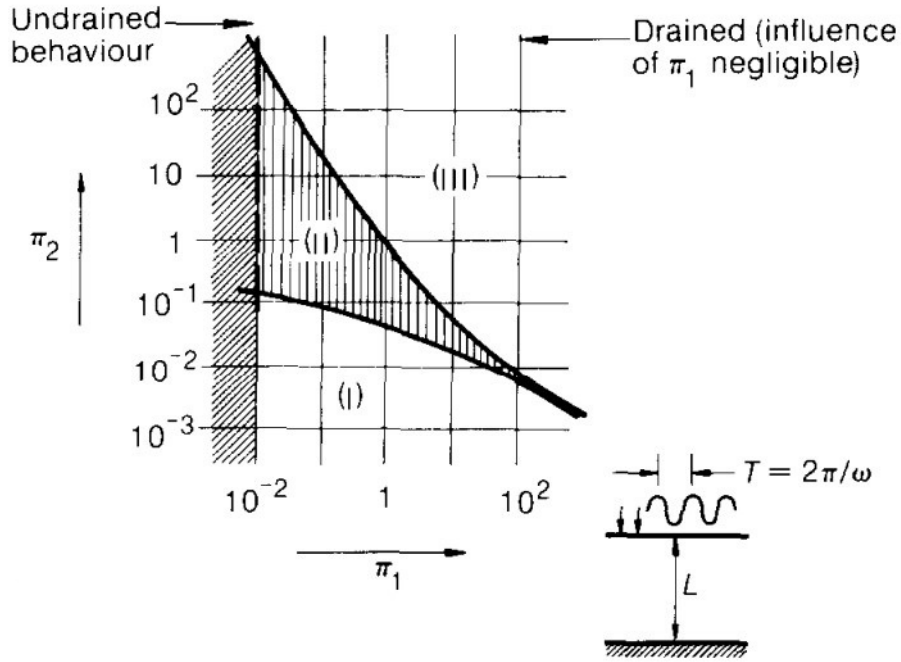


Figure 2.1 Zones of applicability of Biot's models (Zienkiewicz et al., 1980).

be adopted and the conditions when Biot's consolidation model can be use after conducting a series of parametric studies with various wave characteristics and soil properties. They concluded that the fully dynamic model or the $u - p$ approximation must be adopted for the case where the point (Π_1, Π_2) is located above the boundary line. For the case where the point (Π_1, Π_2) is located below the line, Biot's consolidation model can be used. The abscissa Π_1 and the longitudinal coordinates Π_2 are two non-dimensional parameters characterise most wave and soil properties, defined as:

$$\Pi_1 = \frac{k_s V_c^2 \lambda^2}{\rho_f g \omega} \quad \text{and} \quad \Pi_2 = \frac{\rho_f \omega^2}{\left(\frac{G}{1-2\mu_s} + \frac{1}{n_s \beta}\right) \lambda^2} \quad (2.16)$$

in which λ is the wave number and V_c is the velocity of the compressive wave that is defined by:

$$V_c^2 = \frac{\frac{G}{1-2\mu_s} + \frac{1}{n_s \beta}}{\rho_f} \quad (2.17)$$

The third work was conducted by Ulker et al. (2009) and Ulker and Rahman (2009). They proposed a graph (Figure 2.3) to show the applicable ranges of three different models for different types of soil. In Figure 2.3, QS, PD and FD are abbreviations of quasi-static, partly

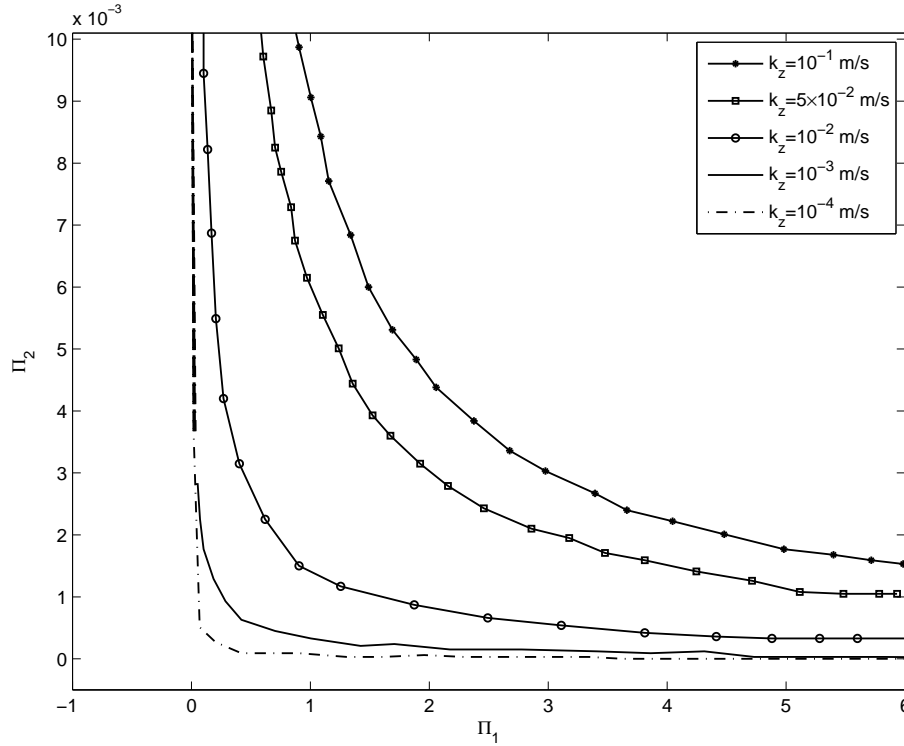


Figure 2.2 Boundary lines of applicability of Biot's models (Jeng and Cha, 2003).

dynamic and fully dynamic, which sequentially correspond to Biot's consolidation model, $u - p$ approximation and Biot's fully dynamic model. m and S in this figure are the spatial variation of the loading and saturation, respectively. It can be seen that Biot's consolidation model is suitable for clay soils and some silts; the $u - p$ approximation is sufficient for most silts and some sandy soils; the fully dynamic model has to be used for gravel soils.

2.1.3 Coupled models for the wave-induced residual soil responses

As mentioned previously, there are two types of mechanisms for the wave-induced sea floor dynamics: oscillatory mechanism and residual mechanism. A detailed review of wave-induced oscillatory soil responses has been covered in the previous section. In this section, the literature considering the other mechanism that is related to residual soil responses will be presented. All these works can be classified into two categories: the inelastic models that still is base on poro-elasticity theory and the poro-elastoplastic models that use more advanced constitutive models.

Numerous inelastic models have been developed. McDougal et al. (1989) proposed the analytical solutions for the accumulation of excess pore water pressure in a uniform

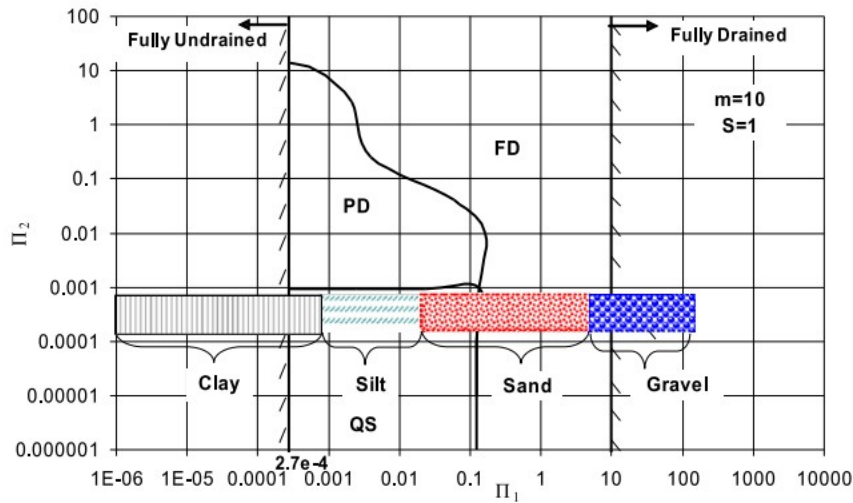


Figure 2.3 Regions of applicability of Biot's models (Ulker et al., 2009).

layer of soil by adding two different source terms into the governing equations based on the one-dimensional consolidation theory. Cheng et al. (2001) corrected the errors in McDougal et al. (1989)'s derivation and performed an error analysis based on the results of their analytical solution. Sumer and Cheng (1999) and Sumer and Fredsøe (2002) further studied the phenomenon of pore water pressure accumulation in the soil by using analytical approximations. Jeng et al. (2007) divided the seabed soil into shallow foundation, deep foundation and finite-depth foundation according to relative seabed thickness and gave the corresponding soil responses for each case. Jeng and Seymour (2007) proposed a curve (J-S curve) that gives the maximum liquefaction depth within the marine soil under the action of waves based on the engineering practice. Guo et al. (2014) presented the revised J-S curve for the wave-induced maximum liquefaction depth in a shallow seabed by introduced a weighting factor that include both oscillatory and residual pore pressure in the liquefaction criteria. Jeng and Zhao (2015) further developed a two-dimensional pore water pressure accumulation model by introducing a new definition of source term. In addition to the analytical works, Seed and Rahman (1978) developed a one-dimensional finite element model to simulate the residual soil responses under wave action. Their model considered the cyclic shear stress within the soil foundation generated by the wave cyclic load and the accumulation of pore water pressure that mainly depends on the relative density of the soil, the cyclic shear stress rate and the current pore water pressure value.

The inelastic models are based on poro-elasticity theory, which means these models can only handle the small deformation problems. However, the poro-elastoplastic soil behaviours such as permanent deformation under long-term cyclic wave loading are not

able to be determined by using such models. Therefore, the inclusion of a more advanced elasto-plastic constitutive model is desired for engineering problems. Due to the complexity of elasto-plastic model, not many literature can be found in the problem of wave-seabed interaction.

Sekiguchi et al. (1995) may have been the first to derive a closed-form poro-elastoplastic solution for the wave-induced pore pressure in the seabed soil. Their solution consists of two parts: elastic part and plastic part, which considered the accumulative contraction of cohesion-less soils under cyclic loading. They demonstrated the difference between the elasto-plastic model and the elastic model and verified their theory by comparing with centrifuge experiments. Sassa and Sekiguchi (1999) further explained the Sekiguchi et al. (1995)'s theory and conducted a range of centrifuge wave tank tests to examine the behaviour of loosely packed, fine-grained sandy seabed under the progressive- or standing-wave loading. Based on the same theory, Sassa et al. (2001) investigated the post-liquefaction process using the method of moving-boundary between the liquefied soil and sub-liquefied soil, in which they treated the completely liquefied soil as an inviscid fluid and the underlying sub-liquefied soil as poro-elastoplastic material. Their results were compared with the experimental data and concluded that the proposed theoretical model is capable of predicting the progressive nature of liquefaction as observed in centrifuge wave tank tests. Based on Sassa and Sekiguchi (1999)'s work, Sassa and Sekiguchi (2001) added the effect of the principal stress rotation on the soil responses by adopting the modified version of PZIII model (Pastor et al., 1990; Zienkiewicz et al., 1999). Li et al. (2002) also developed a poro-elastoplastic model to analyse stationary discontinuities and fluttery instabilities for wave propagating over seabed. More recently, Liao et al. (2015b) numerically analysed the liquefaction of the soil surface under the action of waves based on the analysis of the wave pressure distribution on the surface of a poro-elastoplastic seabed.

2.2 Fluid-Seabed-Breakwaters Interactions

Breakwater is one of the most common offshore structures constructed for the purpose of protecting the coastal line from the wave action. Coastal Engineers mainly focused on the design of the breakwaters based on the evaluation of the wave loading acting on the structures, and generally simplified the seabed foundation into a solid wall. However, the Offshore Geotechnical Engineers are more concerned with the stability of the seabed foundation around the structures. In fact, as reported in the literature, numerous damages of breakwaters were caused by wave-induced seabed instability rather than from the construction deficiencies

(Sumer, 2014). With the development of the theoretical knowledge and computer technology, the soil responses under oceanic loading have become a hot research topic. A large amount of research work has been conducted in the past two decades.

2.2.1 Models for the oscillatory soil responses

Similar to the problems of fluid-seabed interactions, the fluid-seabed-breakwater interactions were first solved by analytical approximation due to its simplicity. However, there are many limitations on account of the assumptions of these analytical solutions. For example, the breakwater is simplified as impermeable lines without weight. Therefore, the effect of breakwater weight could not be considered. Hsu et al. (1993) analytically derived the solution of pore pressure and effective stresses in a porous seabed with infinite thickness under a three-dimensional short-crested waves caused by a vertical wall. Their work has been further extended to the unsaturated seabed with finite thickness (Hsu and Jeng, 1994) and the unsaturated layered seabed (Hsu et al., 1995). The two-dimensional standing waves and three-dimensional short-crested waves will be produced when progressive waves normally and obliquely reflected from a breakwater respectively. These two kinds of wave systems are likely to cause instability in the seabed foundation. Based on Hsu et al. (1993), the analytical solutions for soil responses within a porous seabed in front of the breakwater were obtained under the standing wave loading by Tsai and Lee (1995) and under the partial short-crested wave loading by Tsai (1995). Tsai and Lee (1995) also conducted a wave flume test and compared the results with Hsu et al. (1993)'s analytical solution. The overall agreement was good for small wave heights, however, the difference was relatively large in the case of large wave height. The reason could be that the seabed was assumed to be infinite in the analytical work and finite in the experiment. Later, considering the effect of diffracted wave components, Jeng (1996a) presented an analytical solution for the wave-induced soil responses and evaluated the liquefaction potential within an unsaturated finite seabed around the tip of a breakwater. Jeng (1998) also proposed an analytical solution of wave-induced soil responses in a cross-anisotropic seabed. Tsai et al. (2000) considered the effect of wave non-linearity on the liquefaction potential in front of a breakwater. A standing-wave theory to a second-order approximation was applied and found to agree better with the experimental results compared to the linear solution. Oh et al. (2002) conducted the similar work, but the seabed foundation was under the non-linear short-crested wave system. Kumagai and Foda (2002) also proposed an analytical solution to investigate the interaction between waves, composite breakwater and seabed foundation.

2.2 Fluid-Seabed-Breakwaters Interactions

Another analytical way to solve the soil responses around breakwater is by means of boundary-layer approximation. Mynett and Mei (1982) used boundary-layer method to analytically solve the distribution of pore water pressure and effective stresses under the bottom of a caisson in a saturated poro-elastic seabed. Later, also by using the boundary-layer approximation, Tsai et al. (1990) investigated the response of a finite poro-elastic seabed around a composite breakwater, which contains a upper caisson structure and a bottom rubble bedding layer.

All the aforementioned works were conducted by the means of analytical method, whose application range is limited to structures with simple geometries. With the development of the computer technology, numerical method has become the main way to solve the problem of fluid-seabed-breakwater interactions, especially for the complicated conditions. A large amount of numerical simulations have been conducted in recent years. Coastal Engineers have intensively studied the fluid-breakwater interactions, which the seabed foundation is generally simplified as a solid wall without considering the soil responses of seabed. Another type of research usually involves the upper fluid model and lower seabed model, mainly focusing on the study of foundation stability around the structure by solving the Biot's equations.

For the research works involving the seabed model, in the early stage, the wave loading is solved analytically based on the potential flow theory, then is applied to the numerical seabed model to solve the soil responses. For example, Mase et al. (1994) developed a numerical model to study wave-induced pore water pressure and effective stresses in an isotropic sand seabed and rubble mound foundation of a composite breakwater, in which the analytical solution of linear standing waves was used as the boundary condition at the surface of seabed and breakwater. Later, Jeng et al. (2000) proposed a finite element seabed model to simulate the distribution of pore water pressure in a cross-anisotropic seabed around a caisson-type breakwater. Using the same method, Jeng et al. (2001) investigated the wave-induced soil responses around a composite breakwater. Ulker et al. (2010) also investigated the standing wave-induced soil responses around a caisson breakwater using finite element model. By comparing the distribution of stress and pore pressure underneath the breakwater from different formulations (i.e., fully dynamic, partly dynamic and quasi-static), they found that the fully dynamic formulation give the most accurate solution. Further applying their finite element model, Ulker et al. (2012) investigated the breaking wave-induced dynamic response and instability of seabed around a caisson breakwater. All above mentioned works were using analytical solution of the flow field which is very different from actual situation.

2.2 Fluid-Seabed-Breakwaters Interactions

As mentioned previously, the computational dynamics (CFD) models have been well developed for simulating the interaction between fluid and structure. Researchers have developed numerous integrated numerical models, in which the fluid field is solved by the Navier-Stokes equations using CFD tools. Mizutani et al. (1998) developed a Boundary Element Method-Finite Element Method (BEM-FEM) model to study the nonlinear dynamic interactions among waves, submerged permeable breakwater and finite thickness seabed. In their model, the flow field was governed by the modified the Navier-Stokes equations and the poro-elastic media was governed by Biot's equations. They also conducted experiments to record the free water surface around breakwater and dynamic pore pressure inside the breakwater and foundation. One year later, they further experimentally and numerically investigated the nonlinear dynamic interaction among waves, composite breakwater and a sandy finite seabed foundation using the same model (Mostafa et al., 1999). Adopting the open source platform OpenFOAM®, Liu and García (2006) and Liu et al. (2007) developed a three-dimensional Finite Volume Method (FVM) numerical model to study the seabed foundation response under free surface waves. The Navier-Stokes equations were solved in free surface wave field using CFD model and the Biot's consolidation equations were solved using FVM model. Two models are coupled together through pressure and stress condition on the common boundaries.

Later, based on the Volume Averaged Reynolds Averaged Navier Stokes (VARANS) equations and Biot's poro-elastic equations, an integrated model (PORO-WSSI II) was proposed by Zhang et al. (2011) to investigate the wave-breakwater-seabed interactions. The breakwater and seabed were both considered as porous media in their model, Therefore, the wave-induced soil response in both breakwater and seabed could be obtained. The free surface elevation and pore water pressure inside breakwater and seabed predicted by their model agreed well with Mizutani et al. (1998)'s experimental results. Using the similar method, Zhang et al. (2012b) studied the solitary wave transformation around a permeable submerged breakwater. Zhang et al. (2012a) investigated the wave motion and seabed response around multiple submerged breakwater considering the effect of Bragg reflection. However, the seabed foundation in their study was considered as poro-elastic medium, so only the transient soil responses can be observed. Based on the two-dimensional model (PORO-WSSI II), Zhang et al. (2012c) and Zhao et al. (2013) presented a three-dimensional model to investigate the wave-induced pore pressure within a porous seabed around breakwater heads.

Based on the wave model COBRAS (Hsu et al., 2002; Lin and Liu, 1999) and seabed model SWANDYNE II (Chan, 1988), Ye et al. (2014) applied the integrated numerical model PORO-WSSI 2D to examine the liquefaction in the seabed foundation around a composite breakwater under the breaking wave loading. Ye et al. (2017) extended the two-dimensional

model to three-dimensional model (FSSI-CAS 3D) and investigate the dynamic soil responses in a poro-elastic seabed foundation around a caisson breakwater under wave loading. These studies were all limited to porous elastic seabed foundation. More recently, Liao et al. (2018) numerically studied the wave-induced oscillatory pore pressure and liquefaction around impermeable slope breakwater head using an integrated three-dimensional model. Their model was based on finite volume method CFD program OpenFOAM[®] and finite element method software COMSOL scripts. Adopting an integrated FVM-FEM scheme, Zhao et al. (2018) investigated the oscillatory soil responses around a submerged rubble mound breakwater. In their work, they considered the influence of currents on the hydrodynamic properties and the resulting seabed responses.

2.2.2 Models for the residual soil responses

All the aforementioned studies regarding to the fluid-seabed-breakwaters interactions were limited to poro-elastic seabed foundation, which only the transient soil responses could be captured. In order to reproduce the residual soil responses and residual soil liquefaction around the breakwater, some more advanced models were developed in the past one decade. Since the process of reproducing the non-linear soil behaviour around the breakwater is more complicated compared to the linear elastic soil responses, only limited literature could be found.

Jeng and Ou (2010) developed a three-dimensional poro-elastoplastic finite element program (DYNE3WAC) to investigate the foundation instability near breakwater heads, which is capable to simulate both oscillatory and residual soil responses simultaneously. In their study, the wave field was analytically solved, the soil-pore fluid interaction was governed by $u - p$ approximation of Biot formulation and the plastic soil behaviour under cyclic wave loading was described by generalised plasticity model PZIII (Pastor et al., 1990; Zienkiewicz et al., 1999). They compared the pore water pressure and liquefaction development in both elastic model and elasto-plastic model and the results showed that plasticity has a greater influence on soil with lower permeability, in which the effect of residual pore pressure is greater than the oscillatory pore pressure. They concluded that the elastic model will underestimate the size of liquefaction zone around breakwater heads. It is also worth noting that, in their model, only the breakwater's influence on the wave field was considered rather than including the actual breakwater structure.

Zhao and Jeng (2015) developed an integrated model to investigate the wave-induced accumulation of residual pore pressure within a sloping seabed in the vicinity of breakwater.

They considered the seabed foundation as poro-elastic medium and used the phase-resolved absolute shear stress as the source term for the pore pressure build-up. In this way, they linked the oscillatory and residual mechanism simultaneously. Based on their parametric studies, they found that the soil liquefaction is more likely to happen in a steep slop, low density and low permeability seabed. They also found that the permeability of breakwater can greatly affect the liquefaction potential underneath the breakwater. Zhao et al. (2017) developed another integrated model to study the foundation instability for a loosely deposited sandy seabed around caisson-type breakwater. A two-dimensional poro-elastoplastic model was applied to reproduce the residual soil responses under cyclic shearing. Their model is capable to examine the pore pressure build-up and resulting liquefaction under combined actions of both wave and structure rocking motions.

Based on the previous two-dimensional poro-elastic model (PORO-WSSI 2D) (Ye et al., 2014), Ye et al. (2015) developed an integrated numerical model (FSSI-CAS 2D) by incorporating an poro-elastoplastic constitutive model PZIII (Pastor et al., 1990; Zienkiewicz et al., 1999) that is used to describe the plastic soil behaviour under wave loading. Used this model, they investigated the dynamic responses of a composite breakwater and the seabed foundation. After that, Ye et al. (2017) further extended their model to three-dimensional (FSSI-CAS 3D) and studied the 3D wave, caisson breakwater and loosely deposited seabed foundation interactions. Zhang et al. (2016) also developed an integrated model to investigate the soil responses around submerged breakwaters under combined wave and current loading. The seabed foundation is considered as an inelastic porous medium where pore pressure accumulated.

2.2.3 The impact of currents

In the natural ocean environments, waves and currents co-exist and always interact with each other. The presence of currents could significantly change the hydrodynamic properties of flow field and further affect the dynamic responses within the seabed foundation. The impact of ocean currents on the marine engineering structures foundation stability cannot be ignored. Since 1960s, scholars and engineers paid their attention to the problems of wave-current interactions, and there is a large amount of literature on the development of wave-current interactions (Hughes and Stewart, 1961; Longuet-Higgins and Stewart, 1960, 1961, 1964; Phillips, 1966; Umeyama, 2010; Zhang et al., 2014a). These studies mainly focused on the deformation of linear and non-linear waves under the action of currents with different directions.

2.2 Fluid-Seabed-Breakwaters Interactions

Then, the studies have been extended to wave-current-seabed interactions, which involves the soil responses by coupling the flow and seabed model. Research on this topic has just been developed in recent years. Ye and Jeng (2012) are the first to include currents in their model to study seabed responses and liquefaction. In their work, the third-order approximation of non-linear wave-current interaction was used to determine the dynamic pressure acting on the surface of the seabed foundation, and the $u - p$ approximation theory was adopted in the seabed model. Using their model, they examined the soil responses and the development of oscillatory liquefaction within the seabed foundation under the action of both following and opposing current. Other researchers further conducted some work on wave-current-seabed interactions (Liao et al., 2015a; Liu et al., 2014; Wen and Wang, 2013; Zhang et al., 2013b). The above flow models for the wave-current interaction all adopted analytical solution. With the improvement of computational capacity, wave-current-seabed interactions are gradually solved by the method of numerical simulation (Tong et al., 2019; Zhang et al., 2013a, 2014b). However, the above studies were all limited to 2D conditions. In addition to the theoretical study, some flume tests were also performed. For example, Qi and Gao (2014b); Qi et al. (2019) conducted the indoor flume tests which can generate the wave and current (following and opposing current) simultaneously. The pore water pressure sensors were installed in the seabed foundation to monitor the wave current induced excess pore pressure changes in real time. The flume observations show that the pore pressure increases for the following currents cases, but reduces for the opposing currents cases. They also compared their experimental results with existing analytical solutions and found that the distribution of the excess pore pressure in the flume observations is consistent with analytical solutions.

Later on, researchers focused on the soil responses around structures under combined wave and current loading. Due to the complicated interactions at the boundaries of structures, numerical simulation was often adopted in such cases. Most of the existing investigations are aimed at structures such as pipelines or mono-pile. For example, Wen et al. (2012), Zhou et al. (2014) and Foo et al. (2019) considered the buried pipeline in their model. Although the structures are involved in their studies, the pipelines are buried inside the seabed foundation and have no effects on waves and currents. Qi and Gao (2014a) physically examined the scouring around a large-diameter mono-pile in combined waves and current. As for the breakwaters, as discussed in the previous section, only the effect of wave loading was considered while ignoring the impact of currents. Only very few works could be found in the literature.

Zhang et al. (2016) proposed a two-dimensional inelastic model to investigate the wave/current induced seabed responses around submerged breakwaters. Zhao et al. (2018) further numerically studied the dynamic soil responses around a submerged breakwater

under combined wave and current loading using a two-dimensional elastic model. Their two-dimensional models can only cover the scenario with perpendicularly incident wave at the middle section of the breakwater. However, in practice, the incident waves could be oblique with breakwaters and the currents could come from another direction that interact with waves and breakwater. This will cause a complicated interactions, especially at the area around breakwater heads. Therefore, in order to consider the 3D effects, three-dimensional model is required. In addition, their elastic or inelastic models are only valid for small strain conditions. Such models are not able to predict the poro-elastoplastic soil behaviours such as permanent deformation under long-term cyclic wave loading. Hence, it is also desired to include a more advanced elasto-plastic constitutive theory into the seabed model.

2.2.4 Breakwater foundation instability

Under the wave/current loading, the foundation instability mechanisms mainly include scouring, shear failure and liquefaction. Sumer and Fredsøe (1997) and Sumer et al. (2001) conducted a systematic literature review on the scouring of seabed foundation around marine structures. The shear failure refers to the instability of the soil caused by the wave/current induced shear stress within the seabed foundation that exceeds the soil shear strength, which mainly causes the horizontal displacement of the soil. Since the present study is focusing on the liquefaction around breakwater foundation, these two foundation instability mechanisms will not be discussed in detail here. Liquefaction refers to the state of soil where the effective stresses between the individual grains vanish, soil lose all its strength and acts like fluid. If the liquefaction occurs, the seabed foundation loses its bearing capacity, which might cause the failure of the structure built on it. In general, there are two types of liquefaction mechanisms. The first mechanism is momentary liquefaction, which has a very short duration. It only occurs under the passage of the wave troughs, where the upward transient seepage forces occur. The momentary liquefaction usually happens in a poro-elastic seabed foundation. The second mechanism is residual liquefaction, which is caused by the accumulation of the pore pressure within the seabed foundation under a long period of wave loading. It usually happens in a poro-elastoplastic seabed foundation.

Numerous liquefaction criteria have been proposed based on the “effective stress” or “excess pore pressure”. The “effective stress criterion” deems soil is liquefied if the wave-induced dynamic effective stress (i.e., the effective stress caused by the wave cyclic loading) is greater than the initial effective stress (i.e., the effective stress after the consolidation process) of the seabed foundation. Its one-dimensional liquefaction criteria is firstly proposed

by Okusa (1985):

$$-(\gamma_s - \gamma_w)z \leq \sigma'_z \quad (2.18)$$

in which γ_s and γ_w are the unit weight of soil and unit weight of water, respectively; z is the depth; σ'_z is the effective stress in z -direction. The left-hand-side represents the initial vertical effective stress and the right-hand-side is the dynamic vertical effective stress induced by the wave loading. Later, based on the concept of mean effective normal stress, Tsai (1995) extended Okusa (1985)'s theory to the three-dimensional seabed:

$$-(\gamma_s - \gamma_w)\left(\frac{1+2K_0}{3}\right)z \leq \frac{1}{3}(\sigma'_x + \sigma'_y + \sigma'_z) \quad (2.19)$$

in which K_0 is the lateral compression coefficient of soil. Similarly, the left-hand-side represent the mean initial effective stress and the right-hand-side represent the mean dynamic effective stress induced by the wave loading.

For the other one, the “excess pore pressure criterion” deems soil is liquefied if the wave-induced excess pore pressure is greater than the initial effective stress. Based on the “excess pore pressure criterion”, Zen and Yamazaki (1990b) proposed a one-dimensional liquefaction criteria:

$$-(\gamma_s - \gamma_w)z \leq p_{excess} \quad (2.20)$$

in which the right-hand side represents the excess pore pressure caused by the wave loading. Then, Jeng and Seymour (1997b) extended Zen and Yamazaki (1990b)'s theory to a three-dimensional condition by employing the mean effective stress that similar to that in Equation (2.19) proposed by Tsai (1995):

$$-(\gamma_s - \gamma_w)\left(\frac{1+2K_0}{3}\right)z \leq p_{excess} \quad (2.21)$$

It is worth noting that, under the liquefaction criteria based on “excess pore pressure”, the calculation method of the wave-induced excess pore pressure is different due to the different mechanisms of momentary liquefaction and residual liquefaction. As for the momentary liquefaction, since it is caused by the pore pressure attenuation and phase delay along the seabed depth (i.e., the pore pressure gradient), the wave-induced excess pore pressure is obtained by subtracting the wave pressure acting on the seabed surface (p_b) from the wave-induced dynamic pore pressure (p_s) in the seabed. In contrast, the residual liquefaction is caused by the weakening in the contact force between the soil particles due to the build-up of

the pore pressure. Hence, the right-hand side term of the criteria should be considered as the accumulative value of the pore pressure induced by wave loading.

Another thing to note is that all the above liquefaction criteria could only be applied to the seabed foundation without the structures. In the real environment, the seabed foundation with structures built on it generally undergoes a consolidation process. Due to the compression effect of the structure, the initial effective stresses in the seabed foundation around the structure will significantly change. Therefore, in this case, the left-hand side term of the the liquefaction criteria should be replaced by the stress state that is determined after consolidation process instead of as shown in the equations.

2.3 Summary

A vast amount of studies have been conducted on the problem of fluid-seabed interactions and fluid-seabed-breakwater interactions over the past three decades. With the continuous development of theoretical knowledge and improvement of computational capability, a series of analytical solutions and numerical models have been proposed to investigate the mechanism of wave-induced soil dynamics. However, some limitations of previous studies have been identified and the present study aims to fill these research gaps by developing a more advanced 3D model. Some of the limitations are discussed as following:

- The majority of previous models were limited to 2D model, 3D numerical models in the field of fluid-seabed-breakwater interactions have been few and not as well developed as 2D models, some examples include Jeng and Ou (2010), Zhao et al. (2013) and Ye et al. (2017). Nevertheless, These models were subjected to analytical linear wave loading or restricted to elastic soil behaviour. Since many practical engineering problems related to soil responses around breakwaters can be only solved in 3D condition, it is worth further developing a 3D numerical model.
- Most of the previous studies focused on the wave-induced oscillatory soil responses and momentary liquefaction that occurs in the poro-elastic seabed foundation based on the theory of poro-elasticity. The studies about wave-induced residual soil responses and residual liquefaction in a poro-elastoplastic seabed foundation are still relatively rare. In this study, the wave-induced residual soil responses and residual liquefaction (i.e., liquefaction potential and liquefaction zones) within the poro-elastoplastic seabed foundation near to breakwaters will be investigated by using an advanced plastic constitutive model (PZIII).

- In most of previous models, the effect of ocean current on the dynamic soil responses was not considered. A few studies that considered ocean currents are available, however, they were either limited to analytical approximation or 2D situations. Their model could only cover some simple scenarios. In practice, the ocean current could travel in any direction and interact with incident waves and breakwaters, which usually causes complicated 3D loading on the seabed surface. Therefore, a more advancing 3D numerical model is essentially needed to simulate the strong non-linear wave/current-seabed-breakwater interactions.

Chapter 3

Theoretical Models

In this study, the integrated model is developed to examine the seabed foundation stability around breakwaters by numerically simulating fluid-structures-seabed interactions. The integrated model consists of the flow and seabed sub-models, which are coupled together by the hydrodynamic pressure boundary condition on the common interface. The flow sub-model is developed by using open-source CFD toolbox OpenFOAM[®] (Open Field Operation and Manipulation). The seabed sub-model is based on the finite element program DIANA-SWANDYNE II (Dynamic Interaction And Nonlinear Analysis-SWANsea DYNamic version II) (Chan, 1988; Zienkiewicz et al., 1999), and its extended three-dimensional version, DYNE3WAC (Dynamic Earthquake Analysis Program 3D Window Version for Academic applications) (Ou, 2009). Two soil constitutive models are adopted, one is the poro-elastic model for the momentary soil response and the other one is the poro-elastoplastic model for the residual soil response.

3.1 Flow sub-model

The flow model that used to simulate the wave-current-breakwaters interaction is based on one of the solvers in OpenFOAM[®], OlaFlow, which is an evolution of IHFOAM (Higuera, 2015). OlaFlow is developed within the frame of an open source Computational Fluid Dynamics (CFD) source code under the GNU General Public License (GPL), OpenFOAM[®]. OpenFOAM[®] has been developed for high versatility as a CFD tool. However, its application to coastal engineering that related to wave dynamics is limited due to insufficient modulus for wave generation/absorption and porous media flow. In order to overcome these limitations, within the framework of OpenFOAM[®], Higuera et al. (2014a), Higuera et al. (2014b) and

Higuera (2015) developed an advanced numerical model for coastal engineering based on the three-dimensional Volume Averaged Reynolds Averaged Navier-Stokes (VARANS) equations using finite volume discretization and volume of fluid (VOF) method. The solving algorithm used in his model is PIMPLE, which is a combination of PISO (Pressure Implicit with Splitting of Operators) and SIMPLE (Semi-Implicit Method for Pressure-Linked Equations) algorithms.

The wave generation boundary conditions along with the active wave absorption are implemented within the OlaFlow solver. As the wave generation is the start point for the coastal engineering simulation, an accurate wave generation is critical for obtaining the results that are matched with realistic situation. OlaFlow has ability to realistically generate waves at the boundaries with a number of wave theories, including: Stokes I, II, III and V, cnoidal and streamfunction theory, solitary wave, first to second order irregular waves and piston wave maker emulation. Moreover, the active wave absorption is adopted, which has the advantages of enhancing simulation stability on long-term running (Higuera et al., 2013). Compared with the passive wave absorption, the active wave absorption can significantly reduce the computational domain while providing more accurate results. For passive wave absorption, at least two wave length of wave damping region, usually porous media such as dissipative beaches has to be included, which is not efficient for a large domain.

OlaFlow is also capable to handle flow through the porous media. The porous media flow is important for the present study, as most of the breakwaters have to be treated as porous structures. For examples, the armour layers of the rubble mound breakwaters and the porous foundation of the caisson type of breakwaters. The Reynolds-Averaged Navier-Stokes (RANS) model is one of the most advanced method in numerical modelling for simulating the wave-structure interaction, which is an Eulerian approach that treats the fluids as continuous in space. Numerous researches using RANS equations to deal with wave-coastal structures interactions could be found in literature (Lara et al., 2006; Lin and Liu, 1999). In order to characterise the flow inside porous media, the volume averaging technique is applied to modify RANS equation, which aims at obtaining a mean behaviour of flow inside the porous media by integrating the RANS equations over the control volume. There are more than one way to simulate the flow through the porous media. Since the focus of present study is on the global effects rather than obtaining the detailed solution within the complex internal of material, the Volume Averaged RANS (VARANS) equations are adopted which could save a lot of computing resources while providing sufficiently precise simulating results of flow field inside and outside of porous structures.

3.1.1 Governing equations: VARANS equations

The VARANS equations, including the mass conservation (3.1) and momentum conservation (3.2) equations, are the governing equations for two incompressible phases (i.e., water and air) in a domain with porous structures. The mathematical formulations are expressed as following:

$$\frac{\partial \langle u_i \rangle}{\partial x_i} = 0 \quad (3.1)$$

$$\frac{\partial \rho \langle u_i \rangle}{\partial t} + \frac{\partial}{\partial x_j} \left[\frac{1}{\phi} \rho \langle u_i \rangle \langle u_j \rangle \right] = -\phi \frac{\partial \langle p^* \rangle^f}{\partial x_i} + \phi \rho g_i + \frac{\partial}{\partial x_j} \left[\mu_{eff} \frac{\partial \langle u_i \rangle}{\partial x_j} \right] - [CT] \quad (3.2)$$

where u_i is the so-called extended averaged or Darcy velocity; ρ is the density of the fluid in flow domain, computed by $\rho = \alpha \rho_{water} + (1 - \alpha) \rho_{air}$, in which α is the indicator function defined in Equation (3.7); ϕ is the porosity; p^* is the pseudo-dynamic pressures; g_i is the gravitational acceleration; μ_{eff} is the efficient dynamic viscosity, defined as $\mu_{eff} = \mu + \rho \nu_{turb}$, in which μ is the molecular dynamic viscosity and ν_{turb} is the turbulent kinetic viscosity, given by the chosen turbulence model.

The symbols $\langle \rangle$ and $\langle \rangle^f$ are Darcy's volume averaging operator and the intrinsic averaging operator, respectively, which are defined as:

$$\langle a \rangle = \frac{1}{\forall} \int_{\forall_f} a \, d\forall \text{ and } \langle a \rangle^f = \frac{1}{\forall_f} \int_{\forall_f} a \, d\forall \quad (3.3)$$

where a is a given field; \forall is the total (fixed) averaging volume and \forall_f is the portion of \forall containing the fluid. Here, the total volume \forall consists of only the volume of fluid and the volume of solid. Therefore, the porosity is defined as the ratio of the volume of fluid to the total volume, $\phi = \frac{\forall_f}{\forall}$. For the clear fluid region, $\forall_f = \forall$ ($\phi = 1$). While for a region inside a solid obstacle, $\forall_f = 0$ ($\phi = 0$). This new variable establish a relationship between the Darcy's volume averaging operator and the intrinsic averaging operator as:

$$\langle a \rangle = \phi \langle a \rangle^f \quad (3.4)$$

The last term in Equation (3.2) describes the flow through porous media by considering the resistance (i.e., drag forces) generated by the porous material, which can be expressed as:

$$[CT] = A \langle u_i \rangle + B |\langle u \rangle| \langle u_i \rangle + C \frac{\partial \langle u_i \rangle}{\partial t} \quad (3.5)$$

where these three terms correspond to the linear, non-linear and unsteady flow within the porous media, respectively. A , B and C are three friction parameters, which need to be calibrated based on the porous material properties and flow regime. The coefficient C has proven to be less significant to factors A and B and a value of $C = 0.34 [kg/m^3]$ is often applied by default (del Jesus, 2011). As for values of coefficients A and B , Engelund (1953)'s formulas, as applied in Burcharth and Andersen (1995), are employed in the present model as:

$$A = E_1 \frac{(1 - \phi)^3}{\phi^2} \frac{\mu}{d_{50}^2}, \text{ and } B = E_2 \left(1 + \frac{7.5}{KC} \right) \frac{1 - \phi}{\phi^2} \frac{\rho}{d_{50}} \quad (3.6)$$

in which d_{50} is the medium grain diameter of the materials; KC is the Keulegan Carpenter number, which is defined as $KC = \frac{u_m T_0}{\phi d_{50}}$, in which u_m is the maximum oscillating velocity and T_0 is the period of the oscillation; E_1 and E_2 are parameters that characterise the linear and non-linear friction terms. As mentioned before, these two parameters can be calibrated from physical tests. For cases where there is no experimental data for the simulation, the sensitivity analysis of these parameters on the solutions can be carried on. The start point of the sensitivity analysis should be the default values of these parameters ($E_1 = 50$ and $E_2 = 1.2$) (Higuera, 2015).

3.1.2 Free surface modelling

The Volume Of Fluid (VOF) method (Hirt and Nichols, 1981) is adopted in present model to track the free surface location. Since, generally, there are only two phases (e.g., water and air) considered in numerical coastal engineering simulations, each cell in the computational domain can be considered as a mixture of two-phase fluid. Therefore, only one indicator phase function (α) is needed, which is defined as the quantity of water per unit of volume in each cell:

$$\alpha = \begin{cases} 1 & \text{water} \\ 0 & \text{air} \\ 0 < \alpha < 1 & \text{free surface} \end{cases} \quad (3.7)$$

where $\alpha = 1$ indicates the cell is full of water, while $\alpha = 0$ means the cell is full of air, and for the value of α between 0 and 1, these cells belong to the free surface. Any spatial variation of fluid properties, such as density and viscosity, can be represented using the indicator function α considering the mixture properties:

$$\Phi = \alpha \Phi_{water} + (1 - \alpha) \Phi_{air} \quad (3.8)$$

where Φ_{water} and Φ_{air} are any properties of water and air respectively.

In order to describe the movement of the phases, the VOF advection equation has to be included. The start point of this equation is a classic advection equation:

$$\frac{\partial \alpha}{\partial t} + \nabla \cdot u \alpha = 0 \quad (3.9)$$

OpenFOAM[®] applied an artificial compression term ($\nabla \cdot u_c \alpha (1 - \alpha)$) to the solution of this equation in order to make the final results physical, which includes limiting the α value to a range of 0 to 1 and keeping the interface as thin as possible. The final expression of this equation is:

$$\frac{\partial \alpha}{\partial t} + \nabla \cdot u \alpha + \nabla \cdot u_c \alpha (1 - \alpha) = 0 \quad (3.10)$$

where u_c is the relative velocity field, calculated as $|u_c| = \min[c_\alpha |u|, \max(|u|)]$, in which the default value of c_α is 1. However, the user can specify a greater value to enhance the compression of the interface, or zero to eliminate it.

For the sake of implementing the VOF advection equation into the olaFlow solver, the volume-averaging process need to be applied. The final equation that including the compression term is expressed as:

$$\frac{\partial \alpha}{\partial t} + \frac{1}{\phi} \frac{\partial \langle u_i \rangle \alpha}{\partial x_i} + \frac{1}{\phi} \frac{\partial \langle u_{ci} \rangle \alpha (1 - \alpha)}{\partial x_i} = 0 \quad (3.11)$$

3.1.3 Turbulence models

The water flow patterns are determined by the Reynolds number, which is a dimensionless parameter of the ratio between inertial forces to viscous forces. The water flow will transform from laminar flow to turbulent flow when the Reynolds number is large enough. The turbulent flow has effects such as randomness, non-linearity, diffusivity and vorticity. For the present study, the interactions between waves, currents and structure generally involves

in a significant amount of turbulence generated in the vicinity of breakwaters. Hence, it is required to predict the effect of turbulence induced by the porous structure in the numerical simulation by adopting the turbulence model.

The turbulence model is a common method to take turbulence into account in RANS simulation, which usually consists of a set of independent differential equations. Two types of turbulence models are included in olaFlow solver: Reynolds-averaged simulation (RAS) modelling and large-eddy simulation (LES) modelling. The RAS modelling is generally adopted for practical engineering calculations for its computational advantages as compared to other turbulence models, while providing results of acceptable accuracy. The LES approach requires large computer resources to resolve the energy-containing turbulence eddies. In this study, the $k - \varepsilon$ RAS turbulence model is adopted to model the turbulent viscosity ν_{turb} as:

$$\nu_{turb} = \frac{C_\mu k^2}{\varepsilon} \quad (3.12)$$

where C_μ is an empirical constant; k and ε are the turbulence kinetic energy and the turbulence energy dissipation rate, respectively. The approximated version of $k - \varepsilon$ equations that involving only the most important terms is shown as below:

$$\frac{Dk}{Dt} = \frac{\partial}{\partial x_j} \left(\frac{\nu_{turb}}{\sigma_k} \frac{\partial k}{\partial x_j} \right) + \nu_{turb} \frac{\partial \bar{u}_i}{\partial x_j} \left(\frac{\partial \bar{u}_i}{\partial x_j} + \frac{\partial \bar{u}_j}{\partial x_i} \right) - \varepsilon \quad (3.13)$$

$$\frac{D\varepsilon}{Dt} = \frac{\partial}{\partial x_j} \left(\frac{\nu_{turb}}{\sigma_\varepsilon} \frac{\partial \varepsilon}{\partial x_j} \right) + C_1 \nu_{turb} \frac{\varepsilon}{k} \frac{\partial \bar{u}_i}{\partial x_j} \left(\frac{\partial \bar{u}_i}{\partial x_j} + \frac{\partial \bar{u}_j}{\partial x_i} \right) - C_2 \frac{\varepsilon^2}{k} \quad (3.14)$$

the constants appear in the above equations are empirically determined as: $C_\mu = 0.09$; $C_1 = 1.44$; $C_2 = 1.92$; $\sigma_k = 1.0$; $\sigma_\varepsilon = 1.3$.

similarly, the implementation of the $k - \varepsilon$ model in olaFlow involves a volume-averaged procedure in order to account for the turbulence enhancement within the porous media. The final expression of volume-averaged $k - \varepsilon$ model for the porous flow inside porous medium is:

$$\begin{aligned} \frac{\partial \langle k \rangle}{\partial t} + \nabla \cdot \left(\frac{1}{\phi} \langle k \rangle \langle u \rangle \right) - \nabla \cdot \left[\left(\nu + \frac{1}{\phi} \frac{\langle \nu_{turb} \rangle}{\sigma_k} \right) \nabla \langle k \rangle \right] + \langle \varepsilon \rangle \\ = \frac{2}{\phi^2} \langle \nu_{turb} \rangle \left| \frac{\nabla \langle u \rangle + (\nabla \langle u \rangle)^t}{2} \right|^2 + [CT]_k \end{aligned} \quad (3.15)$$

$$\begin{aligned}
 \frac{\partial \langle \varepsilon \rangle}{\partial t} + \nabla \cdot \left(\frac{1}{\phi} \langle \varepsilon \rangle \langle u \rangle \right) - \nabla \cdot \left[\left(v + \frac{1}{\phi} \frac{\langle v_{turb} \rangle}{\sigma_k} \right) \nabla \langle \varepsilon \rangle \right] + C_{\varepsilon 2} \frac{\langle \varepsilon \rangle^2}{\langle k \rangle} \\
 = \frac{2C_{\varepsilon 1}}{\phi^2} \left\langle v_{turb} \frac{\langle \varepsilon \rangle}{\langle k \rangle} \right\rangle \left| \frac{\nabla \langle u \rangle + (\nabla \langle u \rangle)^t}{2} \right|^2 + [CT]_{\varepsilon}
 \end{aligned} \tag{3.16}$$

The definition and determination of the parameters and terms in Equation (3.15) and (3.16) could be referred to Higuera (2015).

3.2 Seabed sub-model

3.2.1 Governing equations: $u - p$ approximation

The $u - p$ approximations proposed by Zienkiewicz et al. (1980) are used as the governing equations for the interactions between solid skeleton and pore fluid in a porous seabed, in which the relative displacements of pore fluid to soil particles are ignored and the acceleration of pore fluid and solid particles is included. The soil skeleton displacement u and pore pressure p are used as the field variables. The detailed review of $u - p$ approximations has been included in Section 2.1.2. The $u - p$ approximation comprise equilibrium equation and continuity equation, which can be expressed as:

For two-dimensional situations:

$$\frac{\partial \sigma'_x}{\partial x} + \frac{\partial \tau_{xz}}{\partial z} = -\frac{\partial p_s}{\partial x} + \rho' \frac{\partial^2 u_s}{\partial t^2} \tag{3.17}$$

$$\frac{\partial \tau_{xz}}{\partial x} + \frac{\partial \sigma'_z}{\partial z} + \rho' g = -\frac{\partial p_s}{\partial z} + \rho' \frac{\partial^2 w_s}{\partial t^2} \tag{3.18}$$

$$k_s \nabla^2 p_s - \gamma_w n_s \beta \frac{\partial p_s}{\partial t} + k_s \rho_f \frac{\partial^2 \varepsilon_s}{\partial t^2} = \gamma_w \frac{\partial \varepsilon_s}{\partial t} \tag{3.19}$$

For three-dimensional situations:

$$\frac{\partial \sigma'_x}{\partial x} + \frac{\partial \tau_{xy}}{\partial y} + \frac{\partial \tau_{xz}}{\partial z} = -\frac{\partial p_s}{\partial x} + \rho' \frac{\partial^2 u_s}{\partial t^2} \tag{3.20}$$

$$\frac{\partial \tau_{xy}}{\partial x} + \frac{\partial \sigma'_y}{\partial y} + \frac{\partial \tau_{yz}}{\partial z} = -\frac{\partial p_s}{\partial y} + \rho' \frac{\partial^2 v_s}{\partial t^2} \quad (3.21)$$

$$\frac{\partial \tau_{xz}}{\partial x} + \frac{\partial \tau_{yz}}{\partial y} + \frac{\partial \sigma'_z}{\partial z} + \rho' g = -\frac{\partial p_s}{\partial z} + \rho' \frac{\partial^2 w_s}{\partial t^2} \quad (3.22)$$

$$k_s \nabla^2 p_s - \gamma_w n_s \beta \frac{\partial p_s}{\partial t} + k_s \rho_f \frac{\partial^2 \epsilon_s}{\partial t^2} = \gamma_w \frac{\partial \epsilon_s}{\partial t} \quad (3.23)$$

where σ'_x , σ'_y and σ'_z are the effective stresses in the x -, y - and z - directions, respectively; τ_{xy} , τ_{yz} and τ_{xz} are the shear stresses; p_s is the pore pressure; u_s , v_s and w_s are soil displacements in the x -, y - and z - directions, respectively; n_s is the porosity of seabed soil; $\rho' = \rho_f n_s + \rho_s (1 - n_s)$ is the average density of porous seabed, in which ρ_f is fluid density and ρ_s is soil density; g is the gravitational acceleration; k_s is Darcy's permeability; γ_w is the unit weight of water; β and ϵ_s are the compressibility of pore fluid and volume strain respectively, which are defined as below:

$$\beta = \frac{1}{K_f} + \frac{1 - S_r}{p_{w0}} \quad (3.24)$$

$$\begin{aligned} \epsilon_s &= \frac{\partial u_s}{\partial x} + \frac{\partial w_s}{\partial z} && \text{for 2D situations} \\ \epsilon_s &= \frac{\partial u_s}{\partial x} + \frac{\partial v_s}{\partial y} + \frac{\partial w_s}{\partial z} && \text{for 3D situations} \end{aligned} \quad (3.25)$$

where S_r is the degree of saturation; p_{w0} is the absolute static pressure and K_f is bulk modulus of pore fluid, generally, $K_f = 1.95 \times 10^9$ N/m² for pore water (Yamamoto et al., 1978).

For the numerical implementation of the above governing equations, the finite element discretization has to be performed. The spatial discretization is achieved by replacing the variables u and p by the relevant shape functions \mathbf{N}^u and \mathbf{N}^p , respectively. The temporal discretization is conducted using the GNPj time integration scheme (Generalised Newmark p^{th} order interpolation scheme for j^{th} order differential equation) (Katona and Zienkiewicz, 1985; Newmark, 1959).

3.2.2 Constitutive models

The stress-strain relationship for the soil under the wave/current loading is determined by the constitutive models incorporated within the seabed model. There are many different constitutive models, however, no model can predict the perfect results for all soil conditions. Whether a model is suitable for practical engineering analysis depends on the feasibility for implementation of the model, including whether the parameters of the model can be easily determined from standard laboratory experiments, under the premise of being able to give relatively accurate results under a certain condition.

For the soil with high relative density and high elastic compressibility, the linear elastic constitutive relationship based on Hooke's law is usually applied due to its simplicity. In such a model, the soil is treated as elastic medium and the strain is reversible. The elastic strain increment can be obtained through the relation as below:

$$d\epsilon_{ij}^e = C_{ijkl}^e d\sigma_{kl} \quad (3.26)$$

in which $d\sigma_{kl}$ is the effective stresses increment; C_{ijkl}^e is the elastic compliance tensor, which is the inverse of the elastic tensor D_{ijkl}^e , expressed as:

$$D_{ijkl}^e = \lambda' \delta_{ij} \delta_{kl} + 2G \delta_{ik} \delta_{jl} \quad (3.27)$$

where λ' is the Lamé's constant and G is the shear modulus.

However, the linear elastic constitutive model is not able to simulate the plastic soil behaviour which irreversible soil contraction occurs under the long-term cyclic loading, such as loosely deposited sand seabed whose relative density and elastic compressibility are low. Therefore, a large number of plastic constitutive models based on classical plastic theory were proposed (Drucker, 1957; Drucker and Prager, 1952; Roscoe et al., 1958). However, the plasticity of soil could not be obtained by these models when subject to small amplitudes cyclic loading like wave loading due to that the load-unload cycle may belong to the yield surface interior where the soil behaviour is still assumed to be elastic. As a consequence, Zienkiewicz and Morz (1984) proposed the generalised plasticity theory, in which no yield or plastic potential surface are explicitly defined. Then, based on the framework of the generalised plasticity theory, Pastor-Zienkiewicz-Mark-III (PZIII) model (Pastor et al., 1990) was developed, which is suitable for the dynamic analysis of the cyclic behaviour of loosely packed soil under wave/current loading. Instead of yield surface, the plastic flow potential or

the hardening rule, PZIII model only needs the plastic modulus, the direction of plastic flow and a tensor indicating the loading/unloading direction to simulate the plastic soil behaviour.

In the PZIII model, the strain increment is decomposed into two components:

$$d\epsilon_{ij} = d\epsilon_{ij}^p + d\epsilon_{ij}^e \quad (3.28)$$

where $d\epsilon_{ij}^p$ is the plastic component accounting for the irreversible strain and $d\epsilon_{ij}^e$ is the elastic component accounting for the reversible strain. The elastic part is still governed by the Hooke's law as Equation (3.26). The elastic volumetric strain-rate and deviatoric strain-rate are considered separately as:

$$\dot{\epsilon}_v^e = \frac{\dot{p}'}{K_{ev}} \quad \text{and} \quad \dot{\epsilon}_s^e = \frac{\dot{q}'}{G_{es}} \quad (3.29)$$

where $\dot{\epsilon}_v^e$ and $\dot{\epsilon}_s^e$ are the elastic volumetric strain and deviatoric strain respectively; K_{ev} and G_{es} are the bulk modulus of the soil and shear modulus respectively; p' and q' are the mean effective stress and deviatoric stress respectively:

$$p' = \frac{1}{3} (\sigma'_{11} + \sigma'_{22} + \sigma'_{33})$$

$$q' = \sqrt{\frac{(\sigma'_{11} - \sigma'_{22})^2 + (\sigma'_{11} - \sigma'_{33})^2 + (\sigma'_{22} - \sigma'_{33})^2 + 6(\sigma_{12}^2 + \sigma_{23}^2 + \sigma_{31}^2)}{3}} \quad (3.30)$$

In PZIII model, the bulk modulus of the soil K_{ev} and the shear modulus G_{es} are dependent on mean effective stress, which can be written as:

$$K_{ev} = K_{ev0} \frac{p'}{p'_0} \quad \text{and} \quad G_{es} = G_{es0} \frac{p'}{p'_0} \quad (3.31)$$

where p'_0 is the mean effective stress used to measure the elastic parameter of soil; K_{ev0} and G_{es0} are the elastic bulk modulus and shear modulus of soil under p'_0 .

The plastic part of the strain increment is expressed as:

$$d\epsilon_{ij}^p = \frac{1}{H_{L/U}} m_{ij} n_{ij} d\sigma_{ij} \quad (3.32)$$

where m_{ij} and n_{ij} are the plastic flow direction tensor and the loading or unloading direction tensor respectively. The loading and unloading status are defined by following expressions:

$$\begin{aligned} \text{if } n_{ij}d\sigma_{ij} > 0 & \quad \text{Loading} \\ \text{if } n_{ij}d\sigma_{ij} = 0 & \quad \text{Neutral-loading} \\ \text{if } n_{ij}d\sigma_{ij} < 0 & \quad \text{Unloading} \end{aligned} \quad (3.33)$$

The following expressions should be used instead if in a softening situation since plastic strain can be developed under loading condition even when stress decrease.

$$\begin{aligned} \text{if } n_{ij}d\sigma_{ij}^e > 0 & \quad \text{Loading} \\ \text{if } n_{ij}d\sigma_{ij}^e = 0 & \quad \text{Neutral-loading} \\ \text{if } n_{ij}d\sigma_{ij}^e < 0 & \quad \text{Unloading} \end{aligned} \quad (3.34)$$

$H_{L/U}$ stands for the plastic modulus for the loading or unloading stage. The material is hardening when $H_{L/U}$ is positive, while the material is softening and stress is reducing when $H_{L/U}$ is negative.

There are several basis assumptions made in PZIII model. Firstly, the dilatancy relation of soil proposed by Nova and Wood (1982) is adopted in PZIII model:

$$d_g = \frac{d\epsilon_v}{d\epsilon_s} = (1 + \alpha') (M_g - \eta) \quad (3.35)$$

where $d\epsilon_v$ and $d\epsilon_s$ are the total increment of volumetric and deviatoric strain respectively; M_g is the slope of critical state line in $p' - q'$ plane; α' is a constant; η is the deviatoric and mean effective stress ratio:

$$\eta = \frac{q'}{p'} \quad (3.36)$$

The expressions of the plastic potential surface and the yield/bounding surface functions can be derived from the following dilatancy relation as:

$$\begin{aligned} g &= q' - M_g p' \left(1 + \frac{1}{\alpha_g}\right) \left[1 - \left(\frac{p'}{p'_g}\right)^{\alpha_g}\right] = 0 \\ f &= q' - M_f p' \left(1 + \frac{1}{\alpha_f}\right) \left[1 - \left(\frac{p'}{p'_f}\right)^{\alpha_f}\right] = 0 \end{aligned} \quad (3.37)$$

where p'_g and p'_f are size parameters for the plastic potential surface function and yield surface function respectively; α_g and α_f are the parameters related to dilatancy of the soil; M_f is a constant, whose initial approximation is suggested to be given by:

$$\frac{M_f}{M_g} = D_r \quad (3.38)$$

in which D_r is the relative density of soil, defined as:

$$D_r = \frac{e - e_{min}}{e_{max} - e_{min}} \quad (3.39)$$

where e is the void ratio.

A smoothed Mohr-Coulomb criterion is assumed in the PZIII model to generalise the critical state line to three-dimensional stress state:

$$M_g = \frac{6\sin\phi'}{3 - \sin\phi'\sin3\theta} \quad (3.40)$$

where θ is the Lode's angle and ϕ' is the residual friction angle of sand measured when $\theta = 30^\circ$.

Another basic assumption made in PZIII model is that the ratio between the plastic increment of volumetric strain $d\varepsilon_v^p$ and deviatoric strain $d\varepsilon_s^p$ is approximately the same as the ratio between the total increment of volumetric strain $d\varepsilon_v$ and deviatoric strain $d\varepsilon_s$:

$$\frac{d\varepsilon_v^p}{d\varepsilon_s^p} \cong \frac{d\varepsilon_v}{d\varepsilon_s} = (1 + \alpha') (M_g - \eta) \quad (3.41)$$

Then, the plastic modulus at loading/unloading stage are needed to reproduced the plastic soil behaviour. In the PZIII model, the plastic modulus at loading stage is defined as:

$$H_L = H_0 p' \left(1 - \frac{q'/p'}{\eta_f}\right)^4 \left[1 - \frac{q'/p'}{M_g} + \beta_0 \beta_1 \exp(-\beta_0 \xi)\right] \left(\frac{q'/p'}{\eta_{max}}\right)^{-\gamma_{DM}} \quad (3.42)$$

H_0 is a parameter that scales the plastic modulus; The term $\left(1 - \frac{q'/p'}{\eta_f}\right)$ shows the fact that the plastic strain increment increases as the stress ratio increases, and the stress ratio cannot exceed η_f where $\eta_f = M_f(1 + 1/\sigma_0)$. The term $\left(1 - \frac{q'/p'}{M_g}\right)$ accounts for the influence of volumetric hardening, which will approach zero when the stress ratio reaches the critical state line, which implies that sand will fail when the stress ratio reaches the critical state

line. The term $(\beta_0 \beta_1 \exp(-\beta_0 \xi))$ stands for the influence of deviatoric strain hardening, in which β_0 and β_1 are constants valuing from 1.5 to 5.0 and 0.1 to 0.2 respectively; ξ is the accumulated deviatoric plastic strain. The term $\left(\frac{q/p'}{\eta_{max}}\right)^{-\gamma_{DM}}$ stands for the plastic modulus in the reloading stage, which shows that the plastic deformation is inversely proportional to the stress ratio; η_{max} is the largest value of stress ratio that the soil reaches and γ_{DM} is a degradation constant.

The plastic modulus at unloading stage is given as:

$$H_U = \begin{cases} H_{U0} \left(\frac{M_g}{\eta_u}\right)^{\gamma_U} & \text{for } \left|\frac{M_g}{\eta_u}\right| > 1 \\ H_{U0} & \text{for } \left|\frac{M_g}{\eta_u}\right| \leq 1 \end{cases} \quad (3.43)$$

where H_{U0} is the parameter which scale the plastic modulus; η_u is the stress ratio from which the unloading takes place and γ_U is the material constant controlling the influence of it.

3.3 Integration of flow and seabed sub-models

A one-way coupling algorithm is adopted between the flow and seabed sub-models through the pressure continuity on the common faces (i.e., the surface of seabed and structures) for the integration of numerical model. The detailed coupling process between the flow model and seabed model is illustrated in Figure 3.1. The flow model is responsible for generating and propagating of waves/current over the seabed foundation, as well as the porous flow inside porous medium if the porous structures applied. Based on the input parameters including wave/current characteristics and structures properties, the output results including velocity field, free surface elevation and the hydrodynamic pressure at the interface between fluid domain and solid domain can be obtained by solving the VARANS equations and Volume of Fluid equations. While the seabed model is responsible for the soil behaviour around the structures. The hydrodynamic pressure extracted from the flow model will be applied to the surface of the seabed and structures as the external loading through the developed data exchange port. Along with the soil/structures properties and other input parameters, seabed model time dependently solves the $u - p$ approximation equations to obtain the soil response, such as dynamic pore pressure, effective stresses and soil displacement, etc.

To achieve the numerical stability, the time step and the mesh scheme are usually much smaller in the flow model than that in the seabed model. In the OlaFlow solver, the time

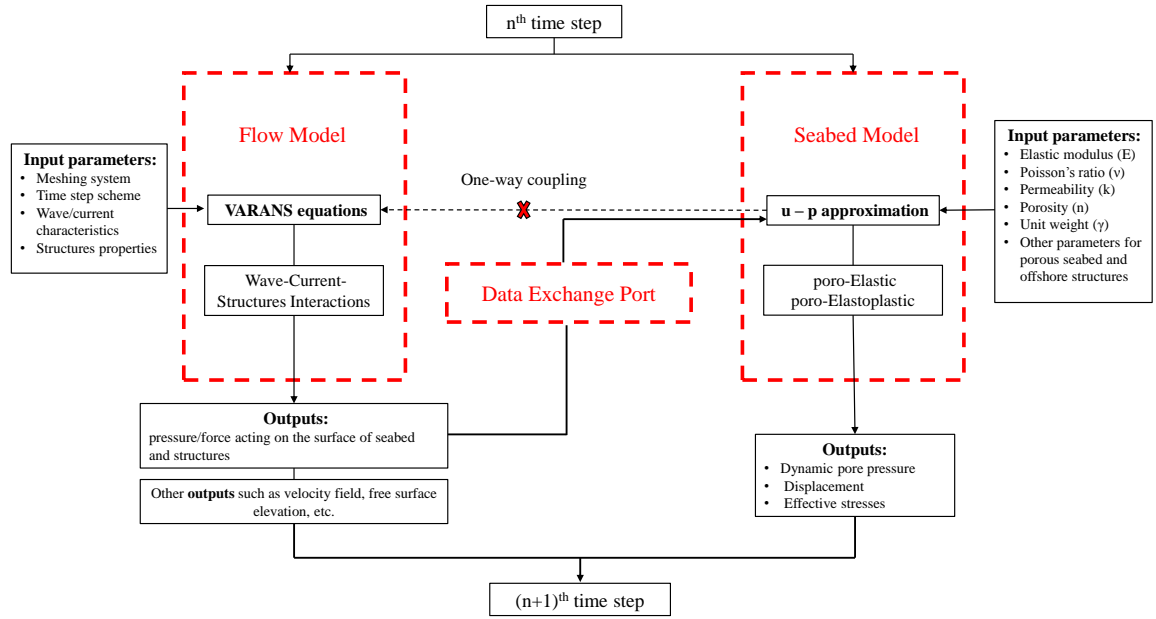


Figure 3.1 The coupling process of integrated model.

interval automatically adjusts to satisfy the Courant-Friedrichs-Lewy (CFL) condition with a range from 0.001 s to 0.005 s, while the time interval for the seabed model is generally larger, for example 0.2 s. The size of the meshing element in the flow model is quite small in order to capture the complicated wave motion, especially when there are structures involved, which causing the turbulence around the structures. However, the meshing size in the seabed model can reach 5 to 10 times that of the flow model. If the same timing scheme and meshing scheme are adopted in both the flow and seabed model, a large amount of computational resources will be wasted. Therefore, in the present model, only the hydrodynamic pressure selected based on the seabed model time interval from the flow model is adopted, and it is interpolated to the grid point on the surface of seabed and structures in the seabed model.

3.4 Model validations

In this section, the accuracy of the proposed integrated model to simulate the wave-current interaction (case 1), oscillatory soil response under combined wave and current loading (case 2), wave-breakwater-seabed interaction (case 3 & 4) and residual soil response (case 5) will be validated by the existing laboratory experiments and centrifugal wave test from available literature. In addition, since there is no 3D experimental data available, the 3D numerical

model will be validated by the analytical solutions proposed by Hsu and Jeng (1994) (case 6). Details of all cases are listed as following:

1. Umeyama (2010): regular wave with uniform following current travelling over a rigid bottom;
2. Qi et al. (2019): combined wave and current induced excess pore pressure in a sandy seabed;
3. Mizutani et al. (1998): nonlinear regular wave, submerged breakwater and seabed dynamic interaction;
4. Mostafa et al. (1999): nonlinear wave, composite breakwater and seabed dynamic interaction;
5. Sassa and Sekiguchi (1999): wave induced residual soil response of a sandy seabed in centrifugal wave test;
6. Hsu and Jeng (1994): analytical solution of wave induced soil response.

3.4.1 Comparison with Umeyama (2010)'s experiments: regular wave with uniform following current travelling over a rigid bottom

Ocean wave and current is commonly existed in the real ocean environment. Therefore, validating the ability of the flow model to simulate the interactions between wave and current is crucial. In this section, the water surface elevation is compared between the numerical results and experimental results from Umeyama (2010)'s experiments, under the conditions of wave loading only and combined wave and current loading.

Umeyama (2010) conducted a series of experiments to study the kinematic aspects of surface waves propagating with or without a steady current. The sketch of his experimental apparatus is shown in figure 3.2. A recirculating wave tank with length of 25.0 m, width of 0.7 m and depth of 1.0 m was used in his experiments. A piston-type wave paddle was installed on the right hand side of the tank to generate waves. On the other side, a wave absorber that consists of vinylidene chloride mat was installed to avoid reflected waves. A steady current with the depth-average velocity of $U_0 = 8.0$ cm/s that flows in the same direction as the waves was generated by recirculating the water via an 8-cm-diameter pipe under the tank. A probe was located at 14.0 m from the wave paddle to record the water surface elevation. The water depth was 30 cm and the wave period (T) was 1.0 s during

Table 3.1 Parameters used in Umeyama (2010)'s experiments.

	W1	W2	W3	WC1	WC2	WC3
Depth average velocity (cm/s)	0.0	0.0	0.0	-8.0	-8.0	-8.0
Wave height (cm)	1.03	2.34	3.61	0.91	2.02	3.09
Wave period (s)	1.0	1.0	1.0	1.0	1.0	1.0
Water depth (cm)	30.0	30.0	30.0	30.0	30.0	30.0

all the tests. Runs W1 to W3 are cases for wave loading only, while WC1 to WC3 are for combined wave and current loading. All the parameters used in these cases are list in Table 3.1.

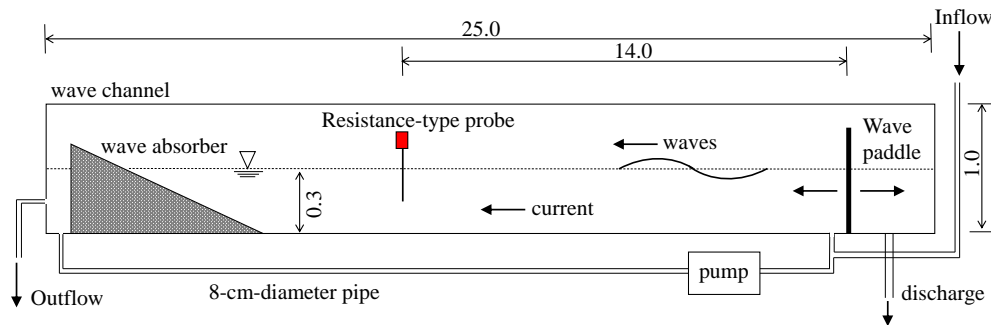


Figure 3.2 The set-up of Umeyama (2010)'s experiments (units: m).

Figure 3.3 shows the comparison of phase-averaged water surface elevation between the numerical results and Umeyama (2010)'s experimental results in the wave alone cases (i.e., W1, W2 and W3) and combined wave-current cases (i.e., WC1, WC2 and WC3). Although the measured water surface elevation at the wave trough is slightly steeper than the simulation results for case 2 and case 3, overall, the agreement between numerical and experimental results is good. This demonstrates that the flow model is capable to simulate the interactions between wave and current. What's more, it can be seen from the figure that the wave height is attenuated in the wave-current cases compared with the original wave only cases. As pointed out by Umeyama (2010), the presence of the following current could decrease wave height by 13 – 15 % for the same wave-paddle motion. He also pointed out that the greater the wave steepness becomes, the more the wave attenuates.

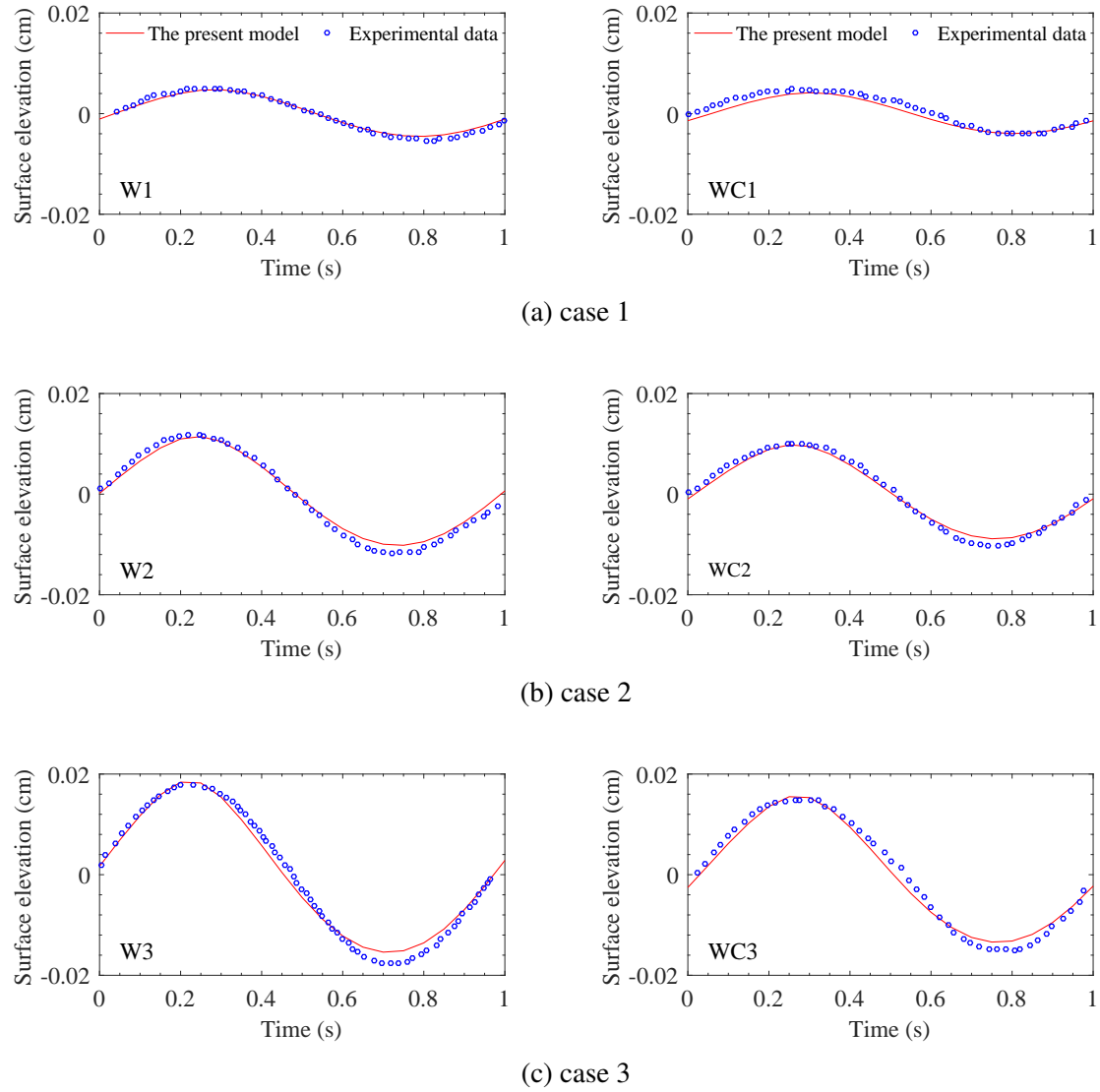


Figure 3.3 The comparison of water surface elevation between the simulation results and Umeyama (2010)'s experimental results.

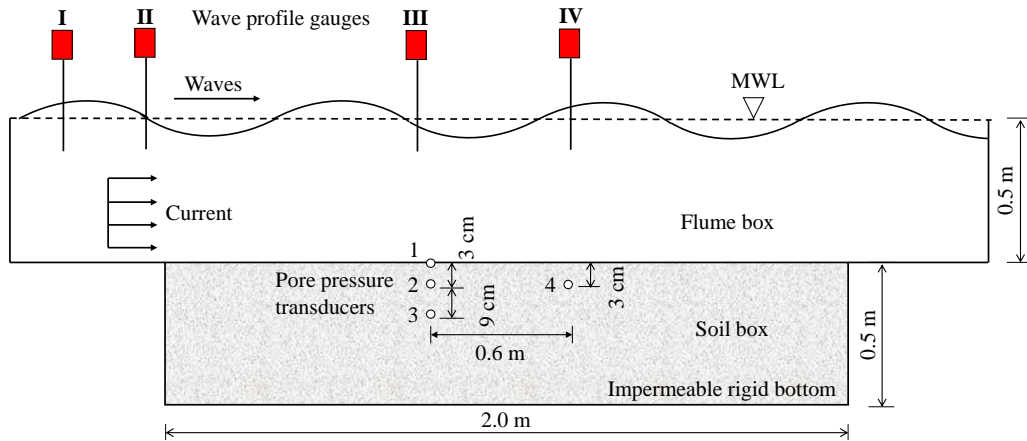


Figure 3.4 The sketch of Qi et al. (2019)'s flume tests for combined wave-current induced excess pore pressure in a sandy seabed.

3.4.2 Comparison with Qi et al. (2019)'s flume observations: combined wave and current induced excess pore pressure in a sandy seabed

Umeyama (2010)'s experiments were based on a rigid bottom without considering the fluid-seabed interactions, only the wave-current interactions reproduced by flow model was validated. The ability of the integrated model to simulate the seabed response under combined wave-current loading still needs further validation. To do this, in this section, the present model will be used to reproduce the Qi et al. (2019)'s flume observations.

Qi et al. (2019) conducted a series of flume tests to investigate the combined wave and current induced excess pore pressure in a sandy seabed. The specially-designed flume has the ability to concurrently generate periodic waves and following/opposing current, whose sketch has been presented in Figure 3.4. The flume box is 52.0 m in length, 1.0 m in width and 1.5 m in depth, which was used for the wave-current interactions. Four wave height gauges (WHGs) were utilised to measure the wave height and calculate the wave length in real time. Among them, No. I and II WHGs were at the far-field to ensure the accuracy of the incident waves and No. III and IV were at the middle part of the flume box. A soil box of 2.0 m in length, 1.0 m in width and 0.5 m in depth was placed under the middle of flume box for the sandy seabed simulation. Four miniature pore pressure transducers (PPTs) were installed right below the No. III and IV WHGs to measure the wave/current induced pore pressure within the sandy seabed.

A set of tests runs with different current conditions were conducted in Qi et al. (2019)'s work. Among them, the experimental observations from run number 1 and run number 9 are chosen to validate the present numerical model, which are the conditions with wave

Table 3.2 Parameters used in Qi et al. (2019)'s tests and numerical simulations

	Parameters	Values
Wave parameters	mean water depth d (m)	0.5
	wave period T (s)	1.2
	wave height H (cm)	9.5
	current velocity U_0 (m/s)	0/0.25
Physical properties of test sands	mean size of sand grains d_{50} (mm)	0.38
	void ratio e	0.771
	relative density D_r	0.352
	buoyant unit weight of soil γ' (kN/m ³)	9.32
Input parameters for numerical soil model	Young's modulus E (Pa)	2.6×10^6
	Poisson's ratio μ_s	0.3
	soil permeability k_s (m/s)	1.88×10^{-4}
	void ratio e	0.771
	degree of saturation S_r	0.995

loading only (run 1) and waves with a 0.25 m/s following current (run 9), respectively. All the other wave parameters are identical in both tests: the mean water depth (d) is 0.5 m, the wave period (T) is 1.2 s, the wave height (H) is 9.5 cm. The sandy seabed in Qi et al. (2019)'s experiments was prepared by means of sand-raining technique, whose main physical properties could be found in Table 3.2. A set of input parameters for the numerical soil model that best matches the experimental results is also listed in Table 3.2.

Qi et al. (2019) firstly examined the effect of a current on the surface elevation. The free surface elevation was measured with WHG III for run number 1 and run number 9 under wave-only and waves with a following current, respectively. The comparison results are shown in Figure 3.5. As can be seen from the figure, the wave steepness (i.e., wave height/wave length) is slightly decreased in the case of wave with following current compared to the case of wave loading only. The numerical results from the flow model can accurately capture this difference and is consistent with the experimental results.

Then, Qi et al. (2019) measured and calculated the corresponding excess pore pressure with PPT1, PPT2 and PPT3 for both runs. Figure 3.6 shows the comparison results between the simulation results and Qi et al. (2019)'s experimental results for the excess pore pressure. The numerical results are consistent with the experimental results, which indicates that the present model has the ability to accurately predict the seabed response under combined wave and current loading. The figure also indicates that, compared to the wave loading only case, the pore pressure amplitudes induced by combined wave and following current loading

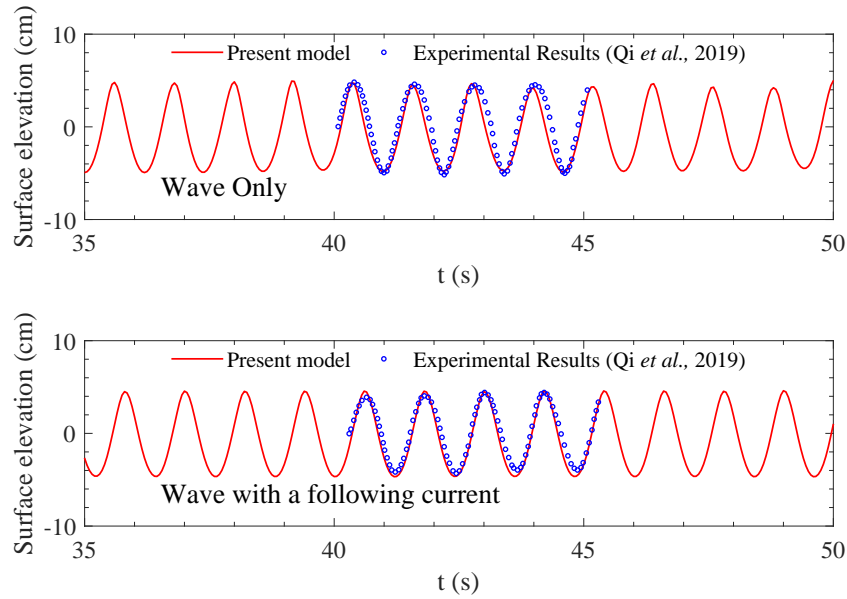


Figure 3.5 The comparison between the simulation results and Qi et al. (2019)'s experimental results for the surface elevation.

slightly increases. The flume observations from Qi et al. (2019)'s work have also found that such wave-current combination effect becomes significant for shorter wave periods.

3.4.3 Comparison with Mizutani et al. (1998)'s experiments: submerged rubble mound breakwater

Neither of the aforementioned two cases includes the structures. The presence of the structures will significantly change the nearby flow field and further induce the dramatically different soil response. Apart from this, one of the most important objectives of present study is to evaluate the stability of the seabed foundation around the offshore structure. Therefore, it is still necessary to validate the ability of the numerical model to simulate the wave-seabed-structure interaction. In this section, the experiment of nonlinear regular wave, submerged breakwater and seabed dynamic interaction conducted by Mizutani et al. (1998) will be adopted in the validation process.

A series of wave flume experiments were carried out by Mizutani et al. (1998) using a two-dimensional wave tank at Nagoya University. The set-up of their experiments is shown in Figure 3.7. The sand seabed is 360.0 cm long and 19.0 cm thick. A trapezoid wooden step was placed on the left side of sandy bed and a wave absorber was placed on the other side of seabed. The rubble mound breakwater with a 2:1 (horizontal:vertical) side slop was

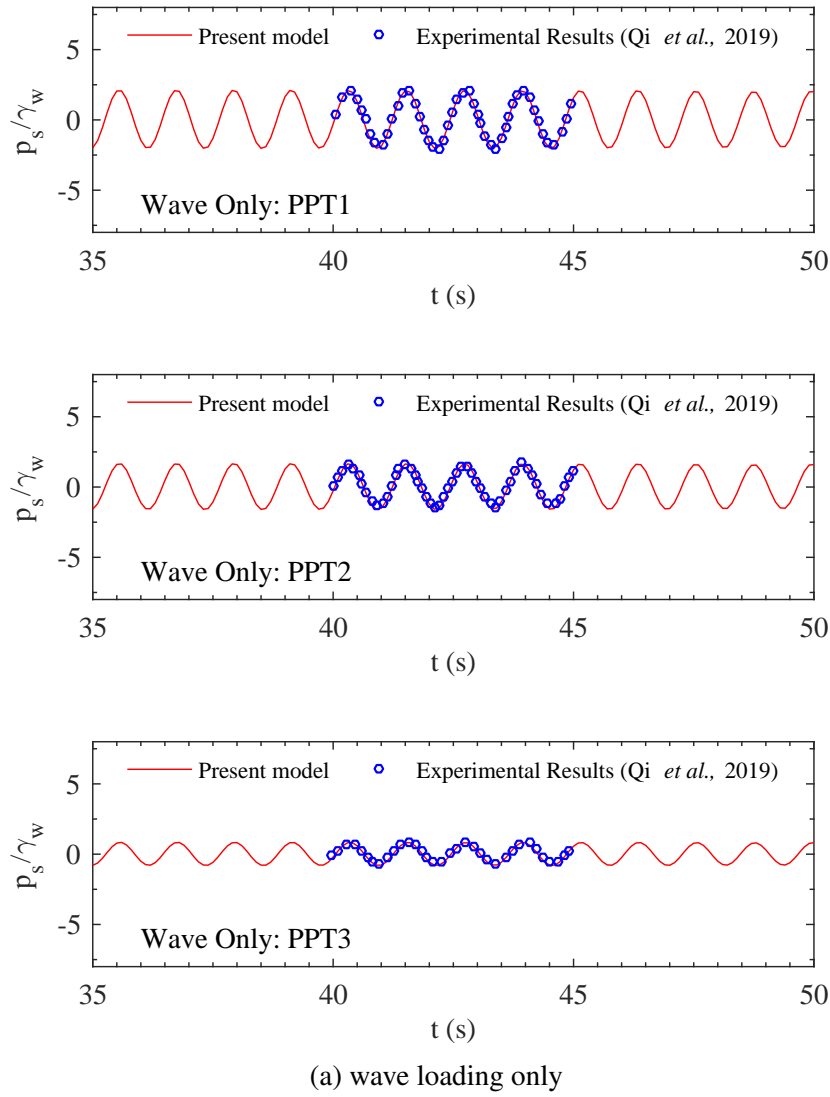


Figure 3.6 The comparison between the simulation results and Qi et al. (2019)'s experimental results for the excess pore pressure.

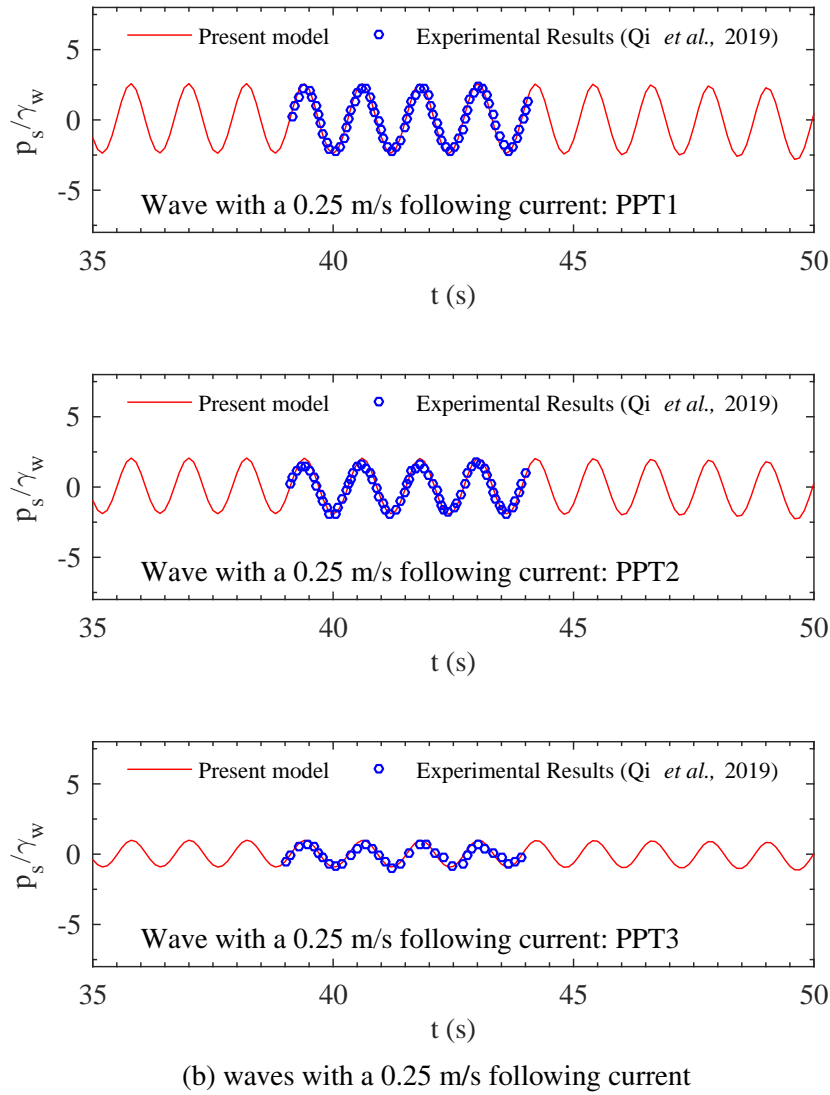


Figure 3.6 The comparison between the simulation results and Qi et al. (2019)'s experimental results for the excess pore pressure (cont.).

Table 3.3 Parameters used in Mizutani et al. (1998)'s experiments

	Parameters	Values
Wave parameters	water depth d (m)	0.3
	wave period T (s)	1.4
	wave height H (cm)	3
Seabed properties	shear modulus G (N/m ²)	1×10^8
	Poisson's ratio μ_s	0.33
	permeability k_s (m/s)	2.2×10^{-3}
	porosity n_s	0.3
	saturation S_r	0.99
Rubble mound breakwater	shear modulus G (N/m ²)	1×10^9
	Poisson's ratio μ_s	0.24
	permeability k_s (m/s)	1.8×10^{-1}
	porosity n_s	0.33
	saturation S_r	0.99

placed on the top middle of the sandy bed. The crown of the permeable breakwater is 105.0 cm long and 21.0 cm high. Four wave meters were installed at point a, b, c and d in order to monitor the surface elevation around and over the breakwater and four pressure gauges were installed in the porous medium with one in breakwater (point A) and the other three in sandy bed (points B, C and D) to record the wave induced pore pressure. The parameters used in the experiments are listed in Table 3.3.

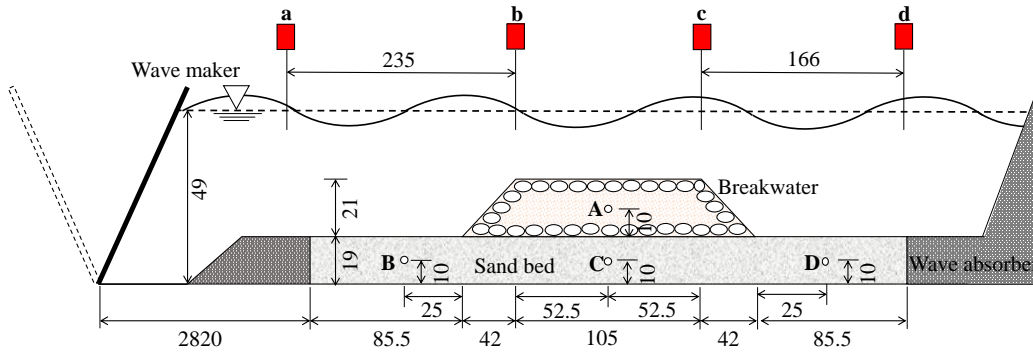


Figure 3.7 The set-up of Mizutani et al. (1998)'s experiments (units: cm).

The present model is validated by comparing the surface elevation at points a, b, c and d and dynamic pore pressure at points A, B, C and D with Mizutani et al. (1998)'s experimental results. First, the wave-submerged breakwater interaction is simulated using the flow model. Since the water depth is 30.0 cm, the wave height is 3.0 cm and the wave period is 1.4 s,

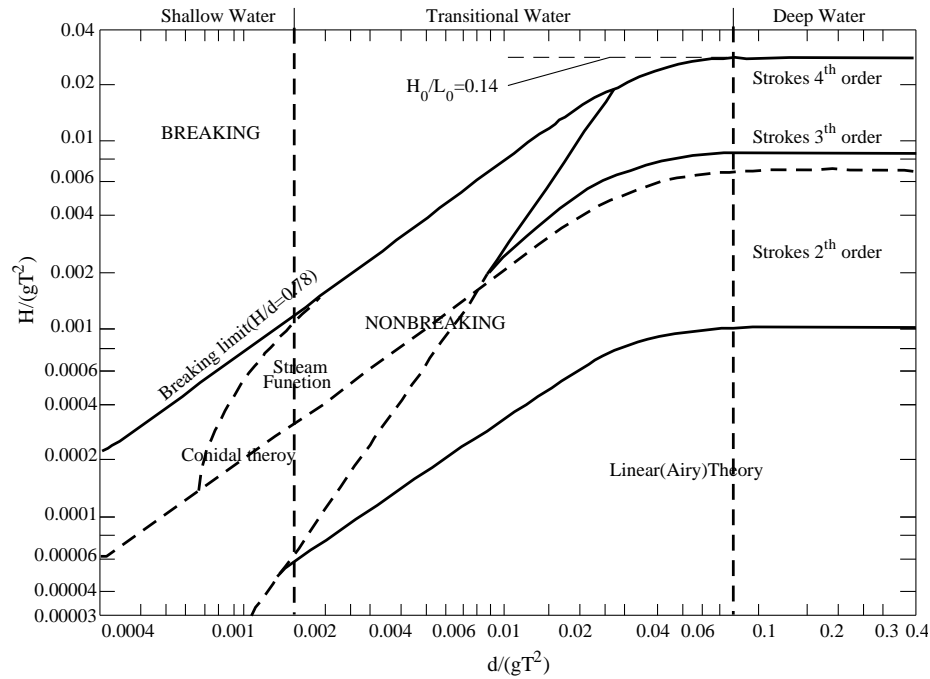
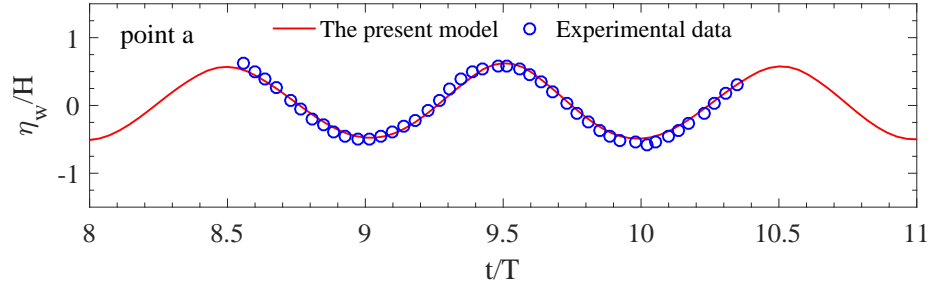


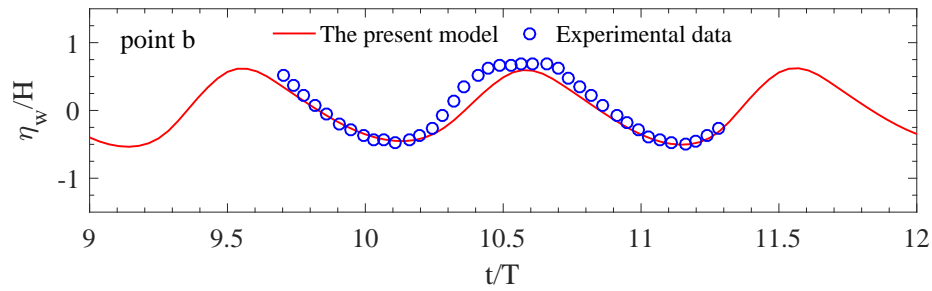
Figure 3.8 The application range for various water wave theories (Le Méhauté, 1976).

by using the classic graph provided by Le Méhauté (1976) (Figure 3.8), the second-order wave theory is chosen to generate waves at the boundary. The breakwater is considered as a porous medium with a porosity of 0.24 in the flow model. A comparison of the surface elevation between the simulation results and Mizutani et al. (1998)'s experimental results is shown in Figure 3.9. Point a is 235 cm away from offshore of the breakwater; point b is over the offshore crown corner of the breakwater; point c is over the onshore crown corner of the breakwater; point d is 166cm away from onshore of the breakwater. As can be seen from the figure, the simulation results agree very well with Mizutani et al. (1998)'s experimental results at all points both in front of the breakwater and behind the breakwater. The wave model can capture the surface elevation with a relative high accuracy, even the non-linearity and wave damping that happen after interaction with breakwater.

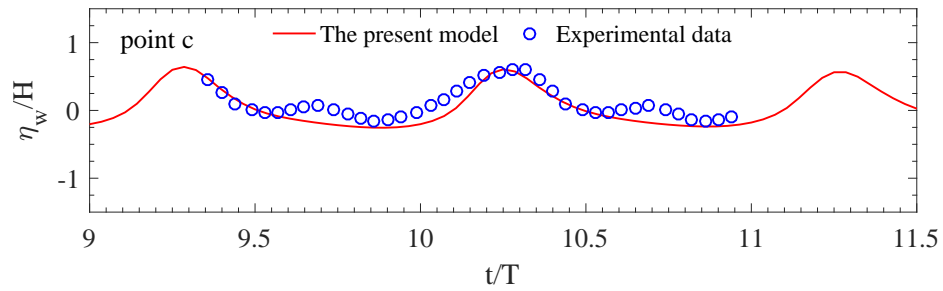
Then, the seabed model is adopted to simulate the dynamic response of seabed foundation. In the procedure of preparing Mizutani et al. (1998)'s experiments, sandy soil was firstly used to fill the tank, then the breakwater was constructed on the top of the sandy bed, after that, the tank was filled with water to the specific depth. The prepared sandy seabed consolidated for several days under the self weight of breakwater and hydrostatic pressure. In order to make the predicted results as accurate as possible, this consolidation process will be reproduced in the numerical simulation. After the completion of the consolidation process, the initial



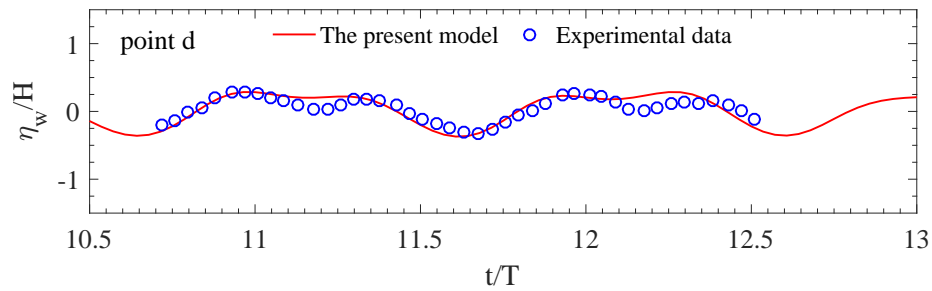
(a) Point a



(b) Point b



(c) Point c



(d) Point d

Figure 3.9 The comparison between the simulation results and Mizutani et al. (1998)'s experimental results for the surface elevation.

condition for the dynamic analysis is obtained. Along with the hydrodynamic pressure extracted from the flow model at the interface between the solid domain and wave domain, dynamic analysis was conducted. Figure 3.10 shows the comparison for the wave induced dynamic pressure at points A, B, C and D between the simulation results and Mizutani et al. (1998)'s experimental results. It is clear that the comparison is quite consistent which indicates that the integrated model is capable of simulating problems of wave-seabed-porous breakwater interaction.

3.4.4 Comparison with Mostafa et al. (1999)'s experiments: caisson-type composite breakwater

Similar to Mizutani et al. (1998)'s work, Mostafa et al. (1999) conducted the experiments to study the interaction between wave, composite breakwater and sandy seabed foundation in the same laboratory. The experimental set-up is shown in Figure 3.11. As can be seen from the figure, the composite breakwater consists of two parts: a rubble base and an impermeable wooden caisson. The wooden caisson was built over the rubble base to reflect the wave back to the wave maker. Four wave gauges were installed to record the water surface elevations (two of them were in front of the breakwater and other two were behind the breakwater). Three pressure gauges were installed at points A, B and C to monitor the pore pressure. The parameters used in Mostafa et al. (1999)'s experiments are list in Table 3.4.

Again, the numerical model will be verified by comparing the surface elevation in fluid domain and dynamic pore pressure in solid domain with Mostafa et al. (1999)'s experimental results. Firstly, the second order wave was adopted according to Figure 3.8 to simulate the wave generation, propagation and reflection in fluid domain. In the flow model, the rubble base is treated as a permeable medium and the wooden caisson is treated as an impermeable structure. Figure 3.12 shows that the predicted results of water surface elevations at all four points agree very well with the measured results, both at onshore and offshore of the breakwater. It also can be seen that, due to the blockage and reflected effect of the impermeable wooden caisson, a partial standing wave is formed in front of the composite breakwater at point b. Only a little part of the wave is transmitted to its leeward side through the rubble base. Furthermore, at point a, a secondary wave crest is formed which indicate that higher harmonics exist in the wave filed around the composite breakwater.

Figure 3.13 shows the comparison of wave induced pore pressure at three locations (A, B, C) between the computed results and measure results. It is found that the predicted dynamic pore pressure inside the rubble base (point A) and the foundation (points B and C) agree

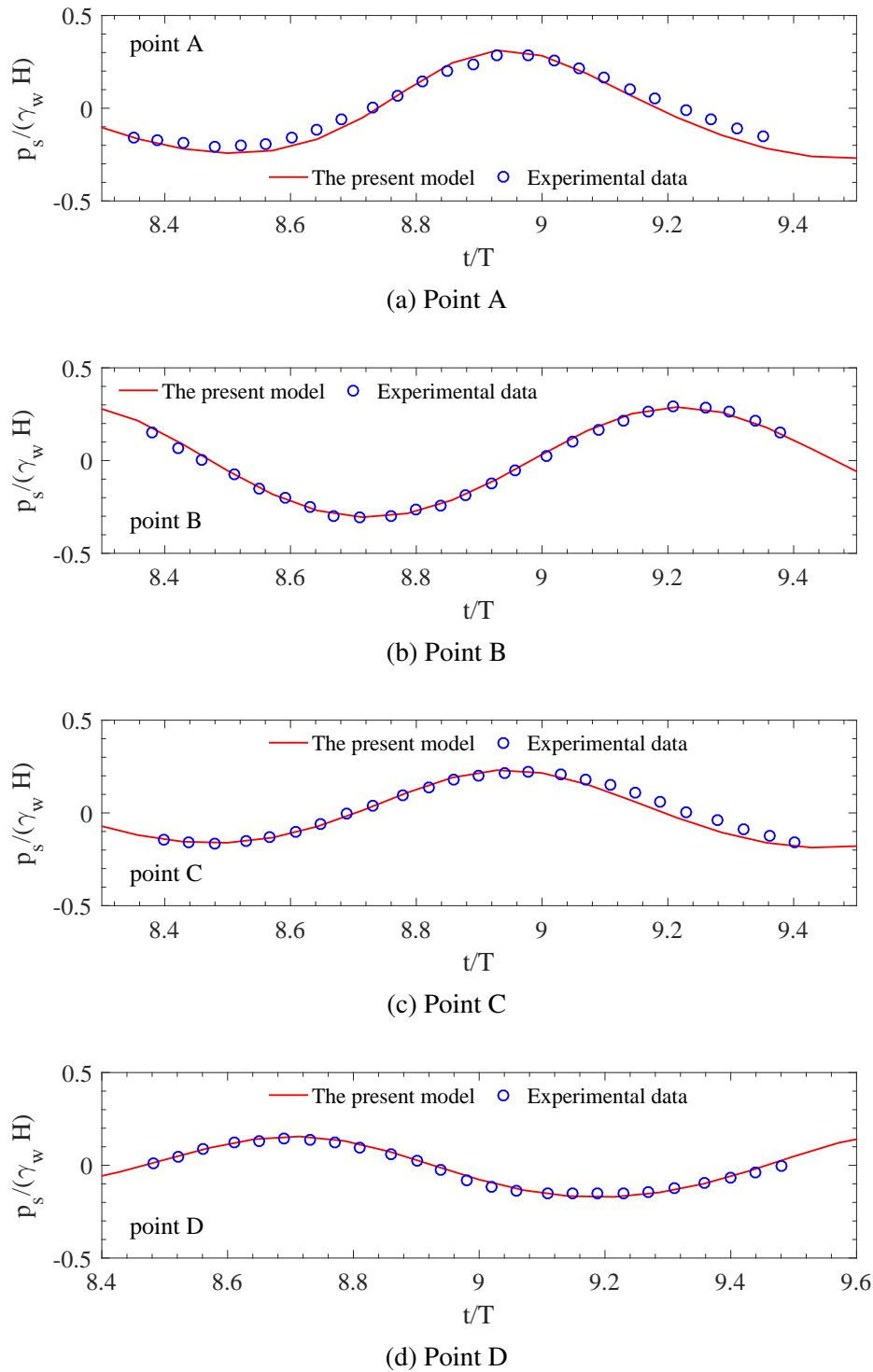


Figure 3.10 The comparison between the simulation results and Mizutani et al. (1998)'s experimental results for the wave induced dynamic pore pressure.

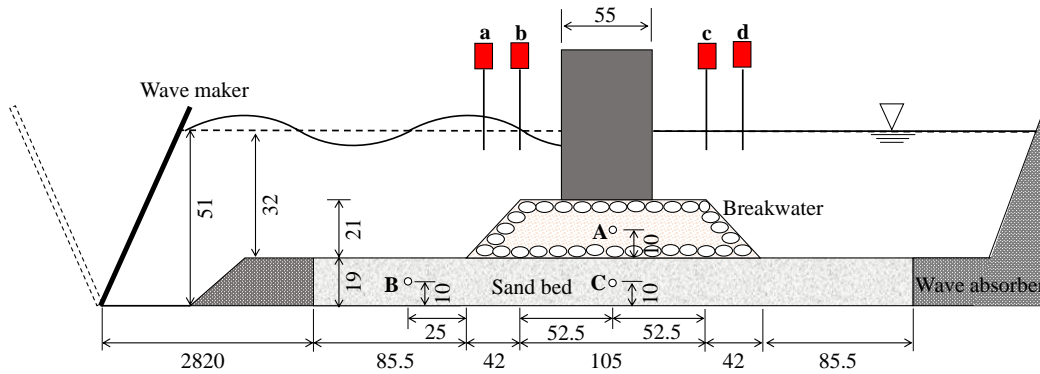
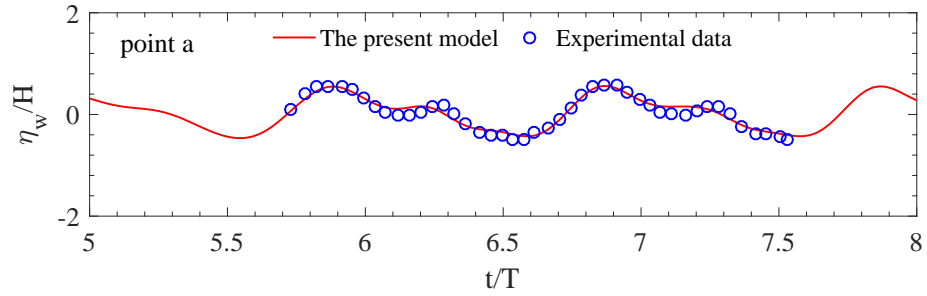


Figure 3.11 The set-up of Mostafa et al. (1999)’s experiments (units: cm).

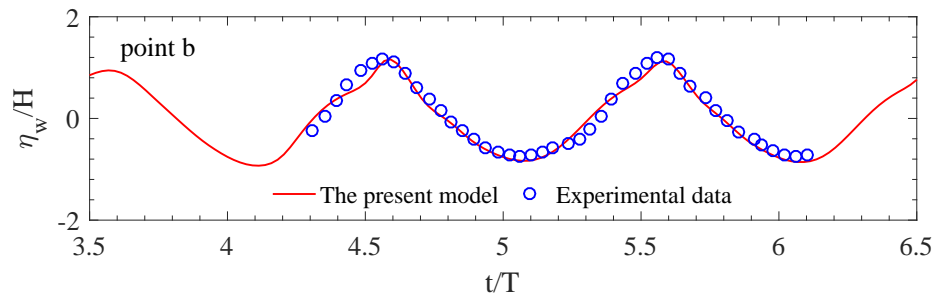
Table 3.4 Parameters used in Mostafa et al. (1999)’s experiments

	Parameters	Values
Wave parameters	water depth d (m)	0.32
	wave period T (s)	2.2
	wave height H (cm)	5
Seabed properties	shear modulus G (N/m ²)	1×10^8
	Poisson’s ratio μ_s	0.33
	permeability k_s (m/s)	2.3×10^{-3}
	porosity n_s	0.3
	saturation S_r	0.99
Rubble mound breakwater	shear modulus G (N/m ²)	1×10^9
	Poisson’s ratio μ_s	0.24
	permeability k_s (m/s)	1.6×10^{-1}
	porosity n_s	0.33
	saturation S_r	0.99
Caisson	shear modulus G (N/m ²)	1×10^{10}
	Poisson’s ratio μ_s	0.25
	permeability k_s (m/s)	0.0
	porosity n_s	0.0
	saturation S_r	0.0

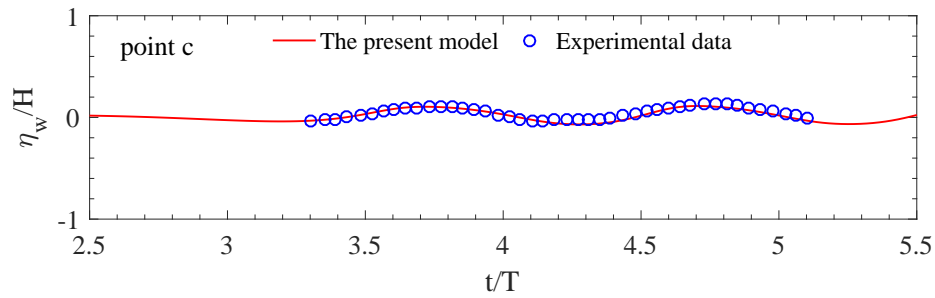
well with the results from Mostafa et al. (1999)’s physical model, which indicates that the numerical model is capable to model the problem of wave-seabed-composite breakwater interactions.



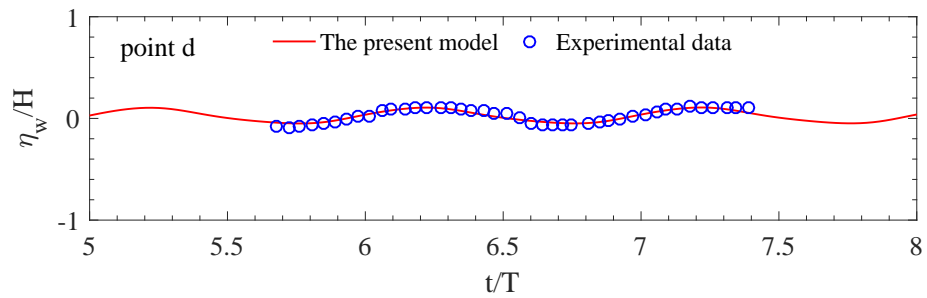
(a) Point a



(b) Point b



(c) Point c



(d) Point d

Figure 3.12 The comparison of surface elevation between the simulation results and Mostafa et al. (1999)'s experimental results.

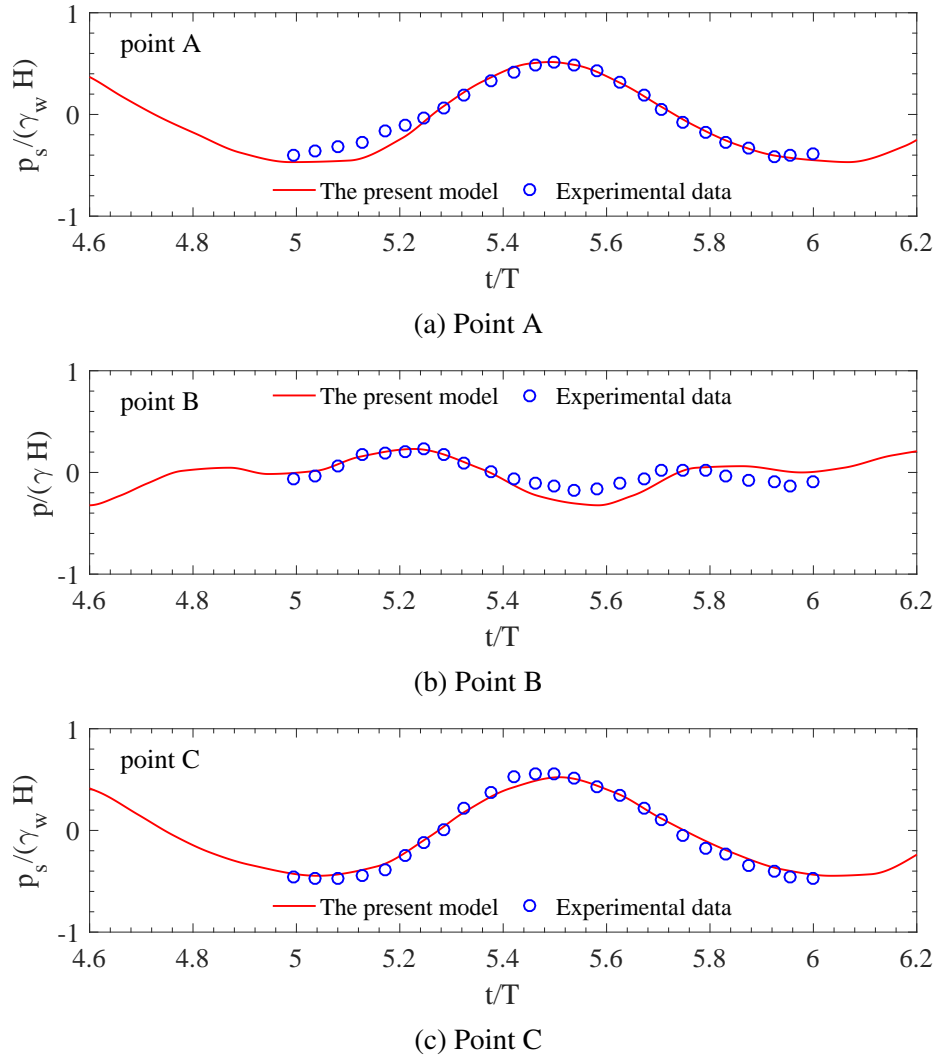


Figure 3.13 The comparison of wave induced dynamic pore pressure between the simulation results and Mostafa et al. (1999)'s experimental results.

3.4.5 Comparison with Sassa and Sekiguchi (1999)'s geotechnical centrifuge test: build-up of pore pressure

All previous cases have used the poro-elastic soil model to simulate the oscillatory soil response. While numerous studies regarding to wave induced residual soil response were reported in the past few decades. It is necessary to validate the capability of the present model to reproduce the residual soil response under cyclic waves loading, where the build-up of pore pressure takes place. Sassa and Sekiguchi (1999) performed three sets of centrifuge wave tank tests, including progressive- and standing-wave loading, with viscous scaling to investigate wave induced liquefaction within loosely packed, fresh deposited sandy bed. In this section, one of Sassa and Sekiguchi (1999)'s centrifuge tests (wave test P5-1) is used to verify the present model. The test was carried out under a steady-state centrifugal acceleration of 50 g. The silicone oil with a viscosity of 50 cSt was used as fluid. A sketch of Sassa and Sekiguchi (1999)'s test is shown in Figure 3.14. Four pore pressure sensors were placed in a vertical array in the centre line of the soil bed with the distance from the seabed surface as 0 mm, 10 mm, 40 mm and 91 mm, respectively.

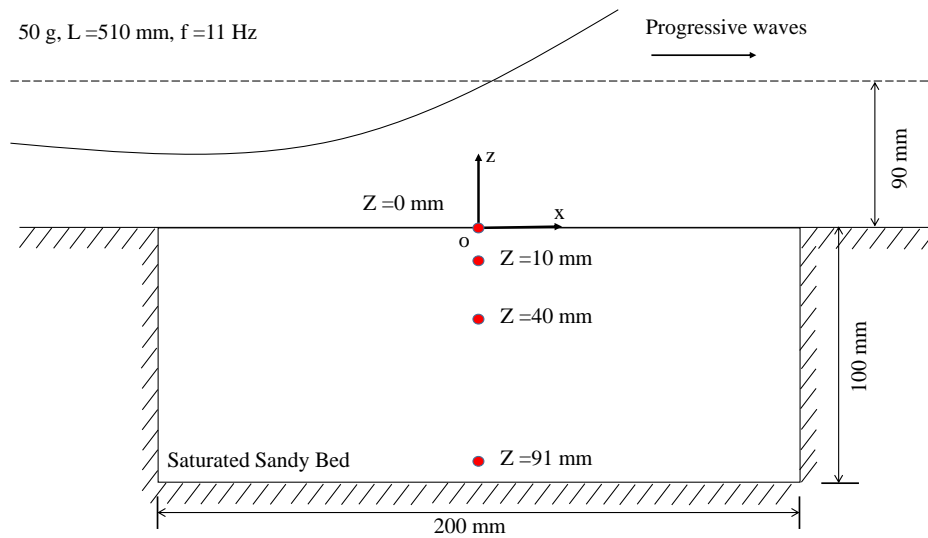


Figure 3.14 The sketch of Sassa and Sekiguchi (1999)'s centrifuge test under progressive wave loading.

Saturated Leighton Buzzard sand (British Standard sieve 100/700) was used in this test to form a soil bed with 200 mm width and 100 mm depth. It has following properties: specific gravity $G_s = 2.65$, mean grain size $D_{50} = 0.15$ mm, maximum void ratio $e_{max} = 1.07$, minimum void ratio $e_{min} = 0.64$ and relative density $D_r = 42\%$. The waves were generated

with following characteristic in centrifuge test: frequency $f = 11$ Hz, water depth $d = 90$ mm and wave length $L_w = 510$ mm, which will generate a 5.0 kPa wave induced pressure on seabed surface. This is equivalent to a wave with 4.5 m water depth, 4.55 s wave period and 1.7 m wave height in field for 1 g acceleration according to scaling principal (Sassa and Sekiguchi, 1999). The parameters of the sand for PZIII model were identified by Sassa and Sekiguchi (2001). The wave and soil parameters used in this verification are listed in Table 3.5.

Table 3.5 Parameters for verification with Sassa and Sekiguchi (1999)'s centrifuge test.

Wave characteristics	
Wave height (H)	1.7 m
Wave period (T)	4.55 s
Water depth (d)	4.5 m
Soil characteristics	
Poisson's ratio (μ_s)	0.3
Permeability (k_s)	1.5×10^{-4} m/s
Porosity (n_s)	0.445
Degree of saturation (S_r)	100 %
Relative density (D_r)	42 %
Parameters for PZIII model	
M_g	1.2124
M_f	0.75
α_f	0.1
α_g	0.1
K_{evo}	660.8 KPa
G_{eso}	770.0 kPa
β_0	0.2
β_1	2.5
p'_0	4.0 kPa
H_0	700.0
H_{U0}	1000.0 kPa
γ_u	6.0
γ_{DM}	4.0

Figure 3.15 shows the comparison of wave induced pore pressure changes in the soil bed measured by four pore pressure sensors between the numerical and centrifuge test results. It is worth noting that only the residual part of centrifuge test results is shown in the figure, indicated as the blue dashed line. It can be seen from the figure that the numerical results from presented model agree well with Sassa and Sekiguchi (1999)'s centrifuge test results. The present model is able to accurately predict the accumulation process of the excess pore

pressure over time at different depths, which indicates that the present model is capable of simulating residual soil response within the elastoplastic seabed foundation.

3.4.6 Comparison with Hsu and Jeng (1994)'s analytical solution

Another validation is performed by comparing with the analytical solution developed by Hsu and Jeng (1994) to validate the 3D numerical model as there is no 3D experimental data available. Two cases are simulated: one is the seabed with a larger soil permeability and the other one is the seabed with a smaller soil permeability. The wave characteristics and soil properties used in these two cases are listed in Table 3.6. Figure 3.16 shows the comparisons of vertical distribution of maximum wave induced pore pressure, effective stress and shear stress between the numerical simulation results from present model and Hsu and Jeng (1994)'s analytical solution. The maximum dynamic soil response is normalised by hydrodynamic wave pressure (p_0) calculated by linear wave theory and the vertical depth is normalised by the seabed thickness (h). As can be seen from the figure, the agreements between the numerical results and analytical solution are reasonably satisfactory.

Table 3.6 Parameters for validation with Hsu and Jeng (1994)'s analytical solution

Parameters	case 1	case 2
water depth d (m)	20	20
wave period T (s)	10	10
wave height H (m)	2	2
shear modulus G (N/m ²)	1×10^7	1×10^7
Poisson's ratio μ_s	0.33	0.33
permeability k_s (m/s)	1.0×10^{-2}	1.0×10^{-4}
porosity n_s	0.33	0.33
saturation S_r	0.98	0.98

3.5 Summary

In this chapter, the detailed information about the theoretical model in this thesis is presented. A one-way coupling algorithm is developed to integrate the flow model and seabed model to investigate the seabed foundation stability around breakwaters under the wave/current loading. A comprehensive set of validations of present model was performed by comparing the numerical results with a series of laboratory tests, wave flume tests, centrifuge tests and

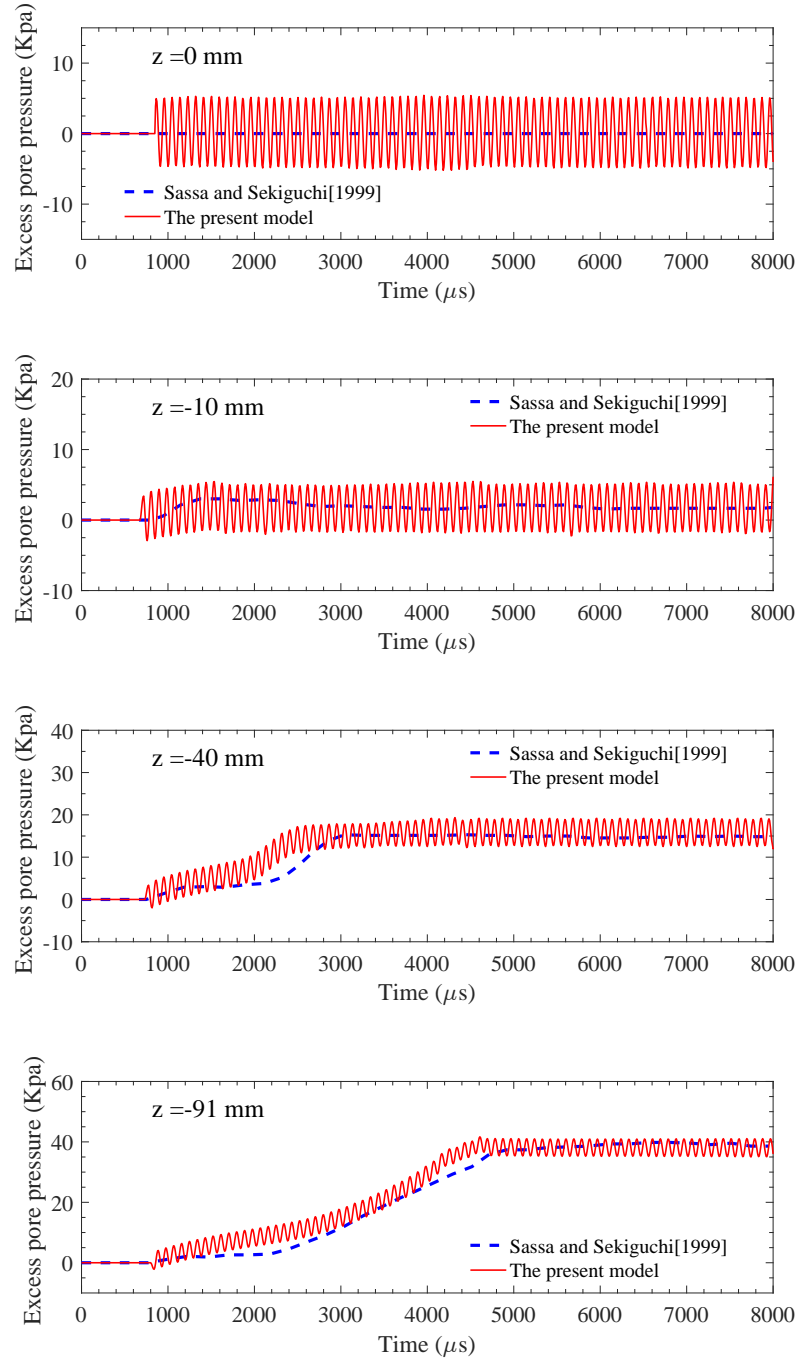
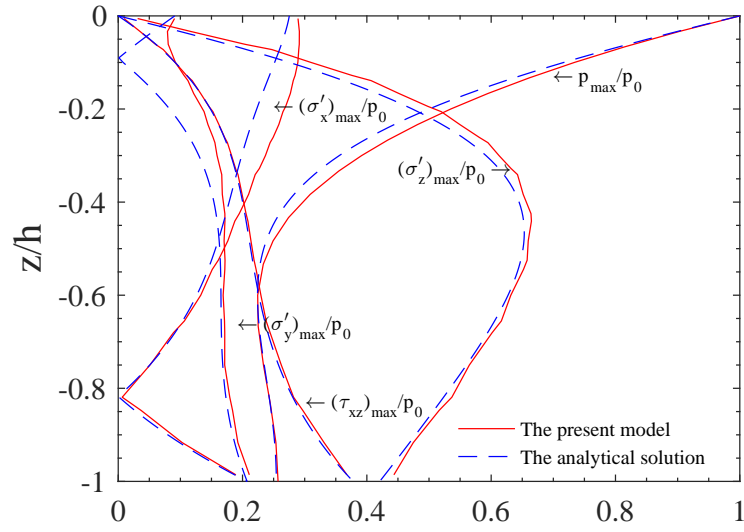
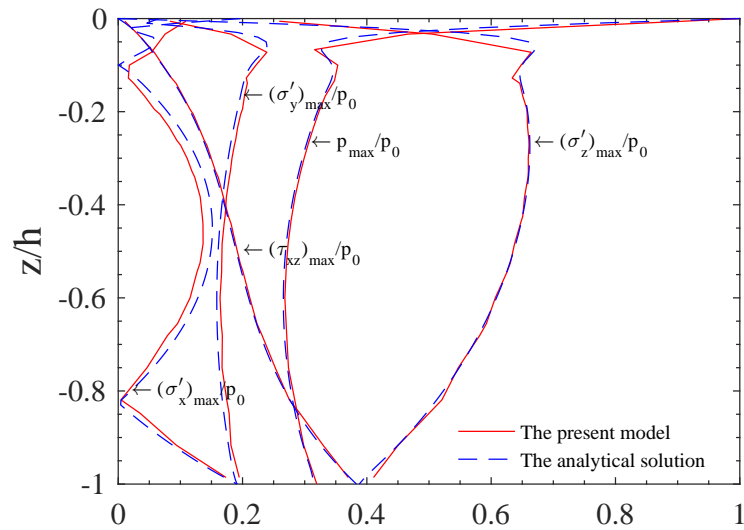


Figure 3.15 The comparison between the simulation results and Sassa and Sekiguchi (1999)'s centrifuge test results for excess pore pressure in sandy seabed.



(a) case 1



(b) case 2

Figure 3.16 The comparison between the simulation results and Hsu and Jeng (1994)'s analytical solution for vertical distribution of maximum wave induced oscillatory soil response including pore pressure, effective stress and shear stress.

analytical solution. A good agreement with the experimental results was obtained which demonstrates the capabilities of the present numerical model.

Chapter 4

2D Numerical Study: Soil responses around Submerged Breakwaters with Bragg Reflection^{1*}

4.1 Introduction

Submerged permeable breakwaters have been widely used in coastal engineering projects to protect coastline by dissipating or breaking the waves. Compared to the emerged breakwaters, submerged breakwaters have several advantages: (1) the impact on the ecological environment is less as they are very similar to natural reefs; (2) the visual impact on aesthetic appearance of coastal landscape is less as the crown of breakwater is under water surface; (3) they are less expensive; and (4) they can reflect and dissipate wave energy efficiently due to the friction effect within the porous medium. Owing to its unique advantages, submerged breakwaters have become popular as a marine structure. Stability of the submerged breakwater under natural environmental loading in ocean environments has become one of the main issues involving in design and maintenance of the structures. As reported in the literature, numerous damages of submerged breakwaters were caused by wave-induced seabed instability rather than from the construction deficiencies Sumer (2014). Therefore, it is essential to have a better understanding of the seabed responses around breakwaters under the ocean environmental loading.

^{1*}Contents in this chapter is included in the publication: Lin, C., & Jeng, D. S. (2019). Numerical study for soil responses around submerged breakwaters with Bragg reflection. *International Journal of Ocean and Coastal Engineering*; doi: 10.1142/S2529807018500057.

There are numerous factors that influence the flow field and soil responses around submerged breakwaters, such as wave characteristics, soil properties and the geometry of the breakwaters, etc. Bragg effect is defined as amplification of reflected waves by multiple breakwaters. It normally occurs when the spacing between two adjacent breakwaters is about half of the incident wavelength. This effect is formed by the constructive interference of incident and reflected waves from successive bottom undulation, which is well known in x-ray diffraction by crystalline materials (Mei et al., 2005). Bragg effect can change the wave motion and its resultant soil responses around breakwaters. On the one hand, Bragg effect is beneficial for protecting the coastlines as more waves will be reflected. On the other hand, it increases the wave height in front of the breakwaters, which might cause seabed instability. Most previous investigations have focused on single submerged permeable breakwater without considering Bragg reflection. To author's best knowledge, only Zhang et al. (2012a)'s work involved multiple submerged permeable breakwaters subject to Bragg reflection. However, their model was limited to poro-elastic soil, which is only valid for small strain condition. The plastic soil behaviours are not able to be determined by using such model.

Another factor that affects the breakwater foundation stability is the ocean currents. In natural ocean environments, waves and currents simultaneously exist and always interact with each other. The presence of currents could significantly change the hydrodynamic properties in flow field and further affect the dynamic responses within a porous seabed. However, most previous investigations of soil responses around offshore structures focused on the wave loading only without considering the effects of currents. Recently, a few works were carried out, among which, Ye and Jeng (2012) was the first to include currents in their model to study seabed responses and liquefaction. In their work, the third-order approximation of non-linear wave-current interaction was used to determine the hydrodynamic pressure acting on the surface of seabed foundation in soil model. However, their study did not consider any structure at all.

In this chapter, the integrated 2D numerical model is adopted to investigate dynamic soil responses and liquefaction potential in both poro-elastoplastic and poro-elastic seabed foundation around multiple breakwaters under combined wave and current loading. The wave-current-structures interactions will be first studied to find the strongest Bragg reflection. Then, in order to simulate the realistic nature condition, a new balance state after process of consolidation will be determined and used as the initial conditions for the following dynamic analysis. Next, the dynamic soil responses and liquefaction potential around the structures will be examined. The parametric studies will be further carried out to examine the effects

4.2 Computational domain, boundary conditions and input parameters

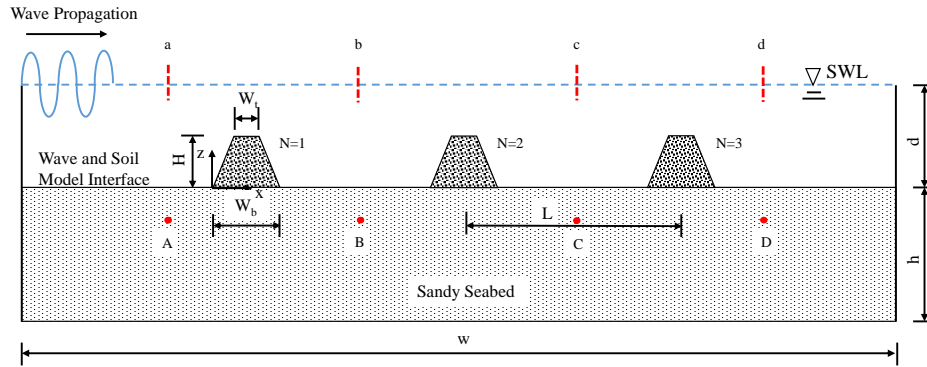


Figure 4.1 The computational domain of the 2D numerical study.

of currents, soil properties and wave characteristics on wave/current induced liquefaction potential.

4.2 Computational domain, boundary conditions and input parameters

In this study, up to three permeable breakwaters are considered. Figure 4.1 illustrates the longitudinal cross-section of the computational domain, in which the multiple breakwaters are sitting alongshore. Ocean waves with wave period $T = 8$ s, wave height $H = 3$ m and water depth $d = 15$ m are generated at the left-hand side of the computational domain and propagating from left to right. The seabed foundation has a thickness of $h = 20$ m and length of $w = 304$ m. N denotes the number of submerged permeable breakwaters which varies from 1 to 3 in the present study. Each breakwater has a bottom width of $W_b = 24$ m, crown width of $W_t = 8$ m and height of $H_b = 8$ m. The space between two adjacent breakwaters is defined as L and three sets of space ($L = 30, 40$ and 80 m) are adopted. Four monitoring points are selected in the flow field (a, b, c and d) and another four points are selected in the seabed foundation (A, B, C and D). From left to right, the four points are located in front of the first breakwater (a/A, $x = -8$ m), between the first and second breakwaters (b/B, $x = 32$ m), between the second and third breakwaters (c/C, $x = 72$ m) and behind the last breakwater (d/D, $x = 112$ m).

In the numerical simulation, the following boundary conditions are considered:

At the surfaces of seabed and breakwaters that are in contact with fluid, the pressure boundary condition is adopted. The wave induced pressures including hydrostatic pressure and

4.3 Flow field around multiple submerged breakwaters

hydrodynamic pressure is applied to these surfaces:

$$p_s(x, z; t) = p_b(x, z; t) \quad (4.1)$$

The bottom of the seabed foundation ($z = -20$ m) is treated as rigid and impermeable, in which displacements in both x - and z - direction are restrained:

$$u_s = w_s = 0 \quad \text{and} \quad \frac{\partial p_s}{\partial z} = 0 \quad (4.2)$$

Both lateral sides of seabed foundation ($x = -100$ m and $x = 204$ m) are restrained in x -direction:

$$u_s = 0 \quad (4.3)$$

The soil behaviour in the seabed foundation is simulated by the linear elastic constitutive model and the poro-elastoplastic constitutive model (Paster-Zienkiewicz Mark-III Model), respectively. The rubble mound breakwaters are treated as elastic medium in this study. The detailed parameters used in the present studies are list in Table 4.1, in which the parameters for the PZIII model are same as those used in Zienkiewicz et al. (1999), which are determined through a series of dependent laboratory tests for the Nevada loose sand.

4.3 Flow field around multiple submerged breakwaters

The construction of breakwaters will significantly change the flow pattern in the vicinity of breakwaters, which makes the hydrodynamic properties around breakwater to be complicated. This becomes even worse when multiple breakwaters are presented, which will amplify the reflected waves, known as Bragg reflection. In this section, the effects of number of breakwaters, space between breakwaters and the ocean currents on hydrodynamic properties around breakwaters will be examined first.

Figure 4.2 compares the time series of water surface elevations at three typical locations a, b and d ($x = -8$ m, 32 m, 112 m, as indicated in Figure 4.1) among cases with different number of breakwaters ($N = 1, 2$ and 3) from $t = 250$ s to $t = 300$ s. For the multiple breakwater cases, the spacing between two adjacent breakwaters is $L = 40$ m. Cases with one and two breakwaters are realised by removing second and/or third breakwaters from case with three breakwaters. As shown in the figure, the surface elevation oscillates over time at three locations. As the location goes from left to right, the oscillation amplitude decreases

4.3 Flow field around multiple submerged breakwaters

Table 4.1 The input parameters used in the 2D numerical study.

Wave characteristics	
Wave height (H)	3.0 m or various
Wave period (T)	8.0 s or various
Still water level (d)	15.0 m or various
Soil characteristics	
Young's modulus (E)	1.67×10^7 Pa
Poisson's ratio (μ_s)	0.333
Permeability (k_s)	1.0×10^{-5} m/s or various
Porosity (n_s)	0.3
Degree of saturation (S_r)	98 % or various
Relative density (D_r)	40 % and 60 %
Breakwater characteristics	
Young's modulus (E)	1.0×10^6 Pa
Poisson's ratio (μ_s)	0.33
Permeability (k_s)	8.9×10^{-2} m/s
Porosity (n_s)	0.5
Degree of saturation (S_r)	99.98 %
Parameters for PZIII model	
M_g	1.15
M_f	1.035
α_f	0.45
α_g	0.45
K_{evo}	770.0 kPa
G_{eso}	1155.0 kPa
β_0	4.2
β_1	0.2
p'_0	4.0 kPa
H_0	600.0
H_{U0}	4000.0 kPa
γ_u	2.0
γ_{DM}	0.0

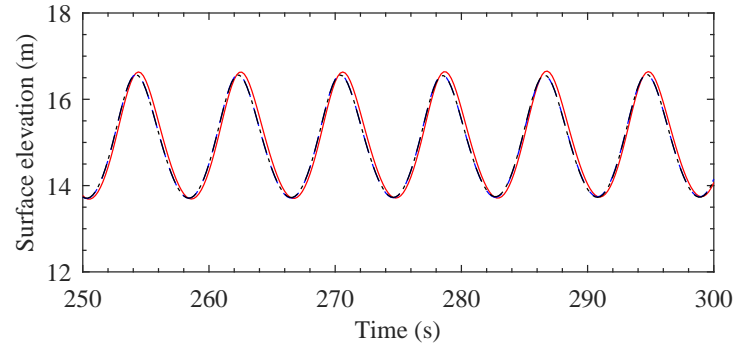
4.3 Flow field around multiple submerged breakwaters

significantly in sequence due to the blockage effect of breakwaters. At location a ($x = -8$ m), which is in front of the first breakwater, the surface elevation for three cases are almost identical. While the surface elevation at location b ($x = 32$ m) is obviously smaller in the case with one breakwater than the one with two/three breakwaters. This is because that for the latter two cases, the wave reflects back by the second/third breakwater and makes surface elevation larger. For the location behind the third breakwater (location d), the wave height becomes smaller successively in the cases with one, two and three breakwaters, which demonstrates that the multiple submerged breakwaters can dissipate the propagating waves more efficiently and better protect the coastline. The phase lag can also be observed at location d.

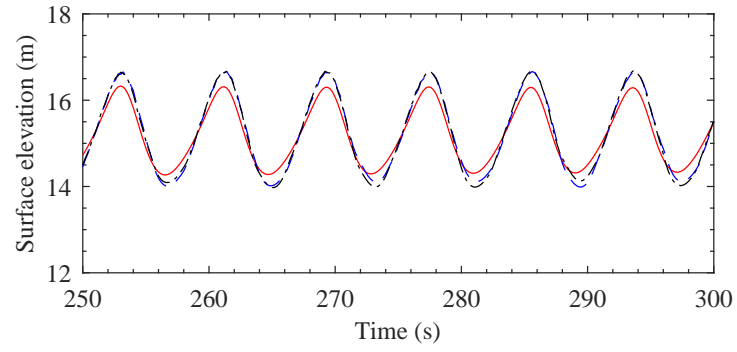
The effect of ocean currents on the surface elevation is illustrated in Figure 4.3 at location a, b, c and d. Three current conditions are considered: waves with following currents $U_0 = 1$ m/s as indicated by the red solid curve, waves with opposing currents $U_0 = -1$ m/s as indicated by the black dot dashed curve and waves without currents $U_0 = 0$ m/s as indicated by the blue dash curve. Similarly, the oscillation amplitude of the water surface gradually attenuates from location a to d due to the blockage effect of breakwater group. As can be easily seen from the figures, the presence of the currents in the flow field significantly affects the wave shapes in the vicinity of breakwaters. Under the combined influences of breakwaters and opposing currents, the oscillatory amplitude of surface elevation tends to reduce at all locations around the breakwaters. For location a, b and c, the following currents did not change the surface elevation too much, the oscillatory amplitude only decreases slightly. However, the amplitude is increased at the leeward side of the breakwater group in the following currents case compared with the waves only case. The ocean currents can also cause the phase differences. Therefore, a preliminary conclusion can be drawn that the presence of the ocean currents interacting with submerged breakwaters can significantly change the shape of the propagation waves, which might very likely to further affect the seabed stability.

Figure 4.4 depicts the effect of spacing between two adjacent breakwaters on the surface elevation at location a and d. Based on the linear wave theory, the wave length of the present wave condition applied is 81.75 m. The spacing (L) considered here are: $L = 40$ m (red solid line) which is around half of the wave length, $L = 80$ m (blue line dash line) which is around the wave length, and $L = 30$ m (black dot dash line) which is less than half of the wave length. It can be found at location a (in front of the first breakwater) that the case with $L = 40$ m has the largest wave height compared to the cases with $L = 80$ m and $L = 30$ m. At location d (behind the last breakwater), the wave height is smallest in the case with $L = 40$ m. This is coincide with that pointed out by Mei et al. (2005): the phenomenon Bragg reflection

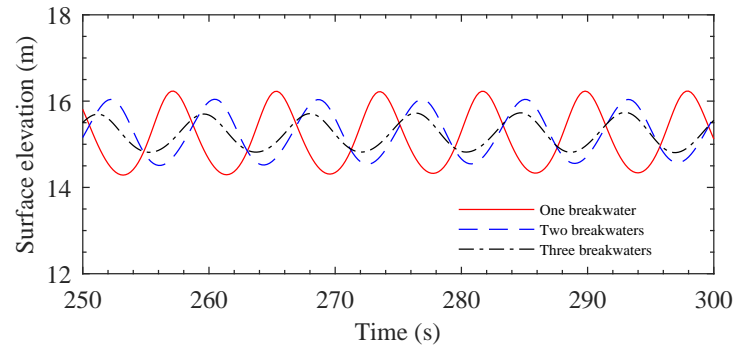
4.3 Flow field around multiple submerged breakwaters



(a) location a: $x = -8$ m



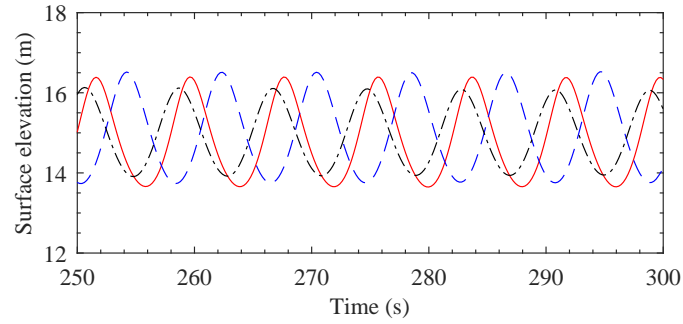
(b) location b: $x = 32$ m



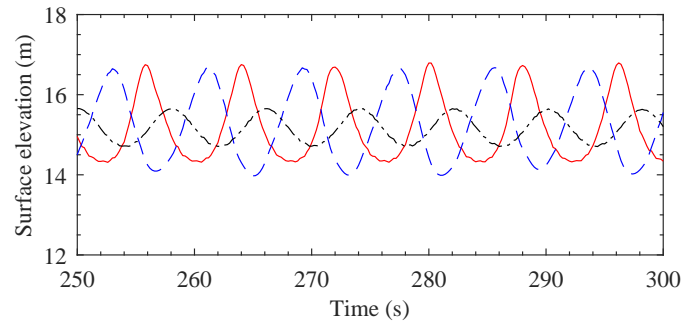
(c) location d: $x = 112$ m

Figure 4.2 Time series of surface elevation at three typical locations (a: $x = -8$ m, b: $x = 32$ m and c: $x = 112$ m) for the cases with one ($N = 1$), two ($N = 2$) and three breakwaters ($N = 3$).

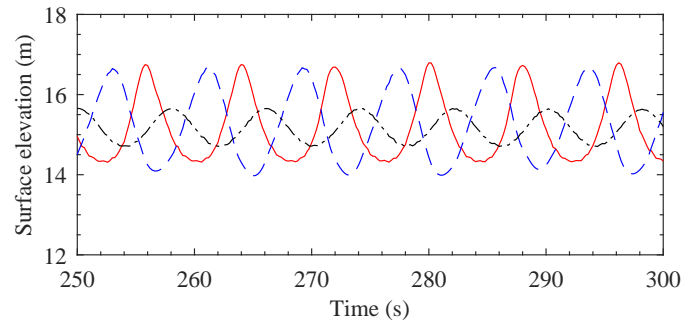
4.3 Flow field around multiple submerged breakwaters



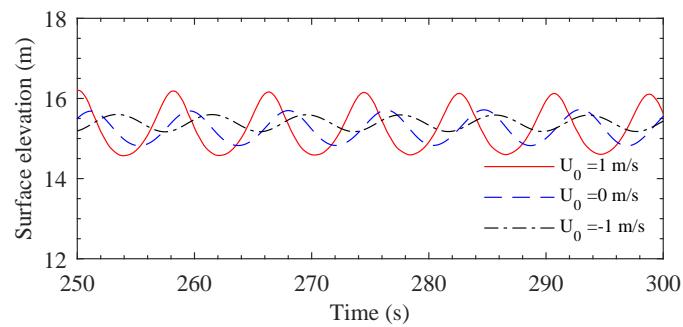
(a) location a: $x = -8$ m



(b) location b: $x = 32$ m



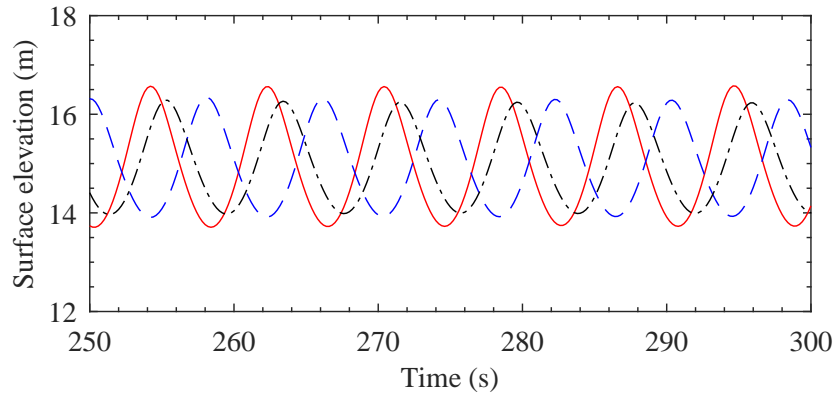
(c) location c: $x = 72$ m



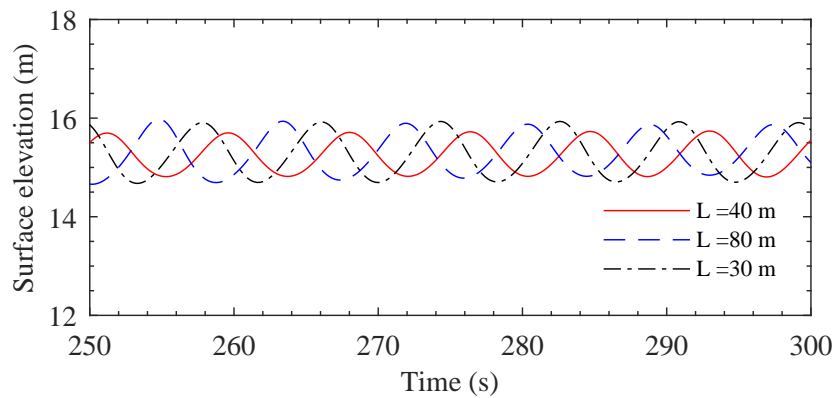
(d) location d: $x = 112$ m

Figure 4.3 Time series of surface elevation at four typical locations (a: $x = -8$ m, b: $x = 32$ m, c: $x = 72$ m and d: $x = 112$ m) for the cases under following currents ($U_0 = 1$ m/s), no currents ($U_0 = 0$ m/s) and opposing currents ($U_0 = -1$ m/s).

4.3 Flow field around multiple submerged breakwaters



(a) location a: $x = -8$ m



(b) location d: $x = 112$ m

Figure 4.4 Time series of surface elevation at two typical locations (a: $x = -8$ m and d: $x = 112$ m) for the cases with different spacing between two adjacent breakwaters ($L = 40, 80$ and 30 m).

becomes stronger when the wave length of surface wave becomes closer to the twice of distance of bottom undulation. The strongest Bragg reflection occurs in the case with $L = 40$ m whose spacing between two adjacent breakwaters is around half of the incident wave length. Different degree of Bragg reflection has different degree of influence on the flow field around the structures and the seabed foundation stability. In this study, the strongest Bragg effect is considered as it has the greatest protection to the coastline while posing the greatest threat to the stability of seabed foundation.

Figure 4.5 further examines the impact of Bragg reflection on the the distribution of horizontal velocity field around the breakwaters. The results presented are at $t = 240$ s for the cases with different spacings. The horizontal velocity field shows a positive and negative alternation and decreases with an increasing of water depth in z - direction. In the region in

4.3 Flow field around multiple submerged breakwaters

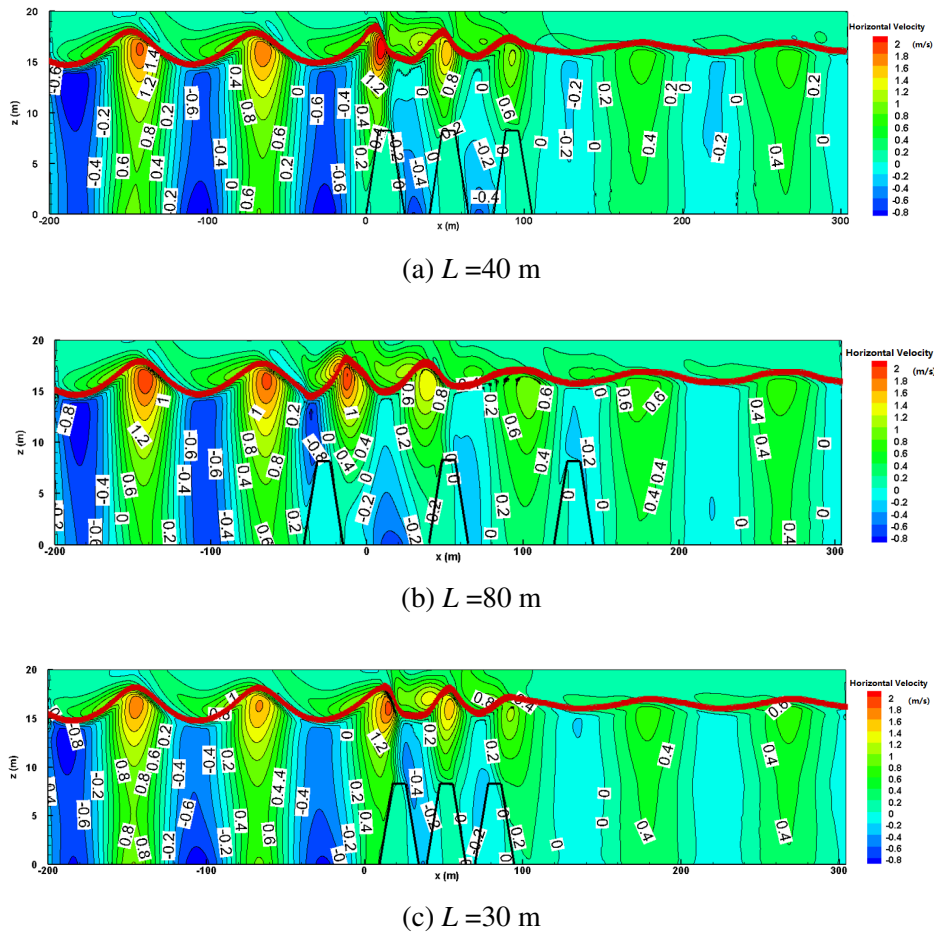


Figure 4.5 Distribution of the horizontal velocity field at $t = 240$ s for cases with different spacing between two adjacent breakwaters: (a) $L = 40$ m; (b) $L = 80$ m and (c) $L = 30$ m.

front of breakwaters, the horizontal velocity appears as negative due to the wave reflection. Owing to the blockage effect of breakwaters, the magnitude of the horizontal velocity decreases dramatically at the shoreward side of last breakwater. Comparing three cases with different value of L , the magnitudes of the horizontal velocity in the case with $L = 40$ m are larger at the seaward side but smaller at the shoreward side than the ones in case with $L = 80$ m and $L = 30$ m. This is attributed to that stronger Bragg reflection takes place in the case with $L = 40$ m, in which the wave length is twice the distance between two adjacent breakwaters.

4.4 Consolidation of the seabed foundation

In natural environments, the seabed foundation is consolidated under hydrostatic pressures from the seawater above and self-weight in the geological history. Construction of breakwaters will change the stress field in the seabed foundation around the structures. The excess pore water pressure can be generated initially and a new balance condition will be reached with the dissipation of excess pore pressure within the seabed foundation. To better simulate the wave/current-breakwaters-seabed interactions, the new balance state needs to be determined first and used as the initial condition for the later dynamic soil analysis. The consolidation process is completed when the distribution of pore pressure becomes uniform and layered, indicating the excess pore pressure has completed the dissipation process. At this stage, the seabed foundation becomes stable again under hydrostatic loading and self-gravity from breakwaters. The distributions of pore pressure (p_s), effective normal stress (σ'_z) and shear stress (τ_{xz}) within the seabed foundation and permeable breakwaters after completion of consolidation process are shown in Figure 4.6. In this case, the wave and soil parameters are adopted as the one in Table 4.1 except that the wave height is set as zero, which represent the hydrostatic pressure. The current is not considered in the consolidation process and the space between two adjacent breakwaters is 40 m.

It can be found from the figure that the construction of breakwaters has significantly affected the effective normal stress (σ'_z) and shear stress (τ_{xz}) in the region near breakwaters. The magnitude of σ'_z obviously increased under each breakwater and appeared as layered structure. This was caused by compression effect from the self-weight of each breakwater. The concentration zones of τ_{xz} appeared in the area under two sides of each breakwater. Additionally, it can be seen from the figure that shear concentration zones under the second breakwater and inside of first/last breakwaters were much smaller than the shear concentration zones under the outside of first/last breakwaters. Because soil in these area was more compacted due to the self-weight of breakwaters, the shear failure is less likely to happen in this area, but it also depends on the space between two adjacent breakwaters. It is also worth to point out that the stress field in the region far away from breakwaters has not been affected. The pore pressures (p_s) in the computational domain increased uniformly from top to bottom, indicating that no excess pore pressure exists. This final state after consolidation process will be used as initial state for dynamic analysis of seabed model.

4.4 Consolidation of the seabed foundation

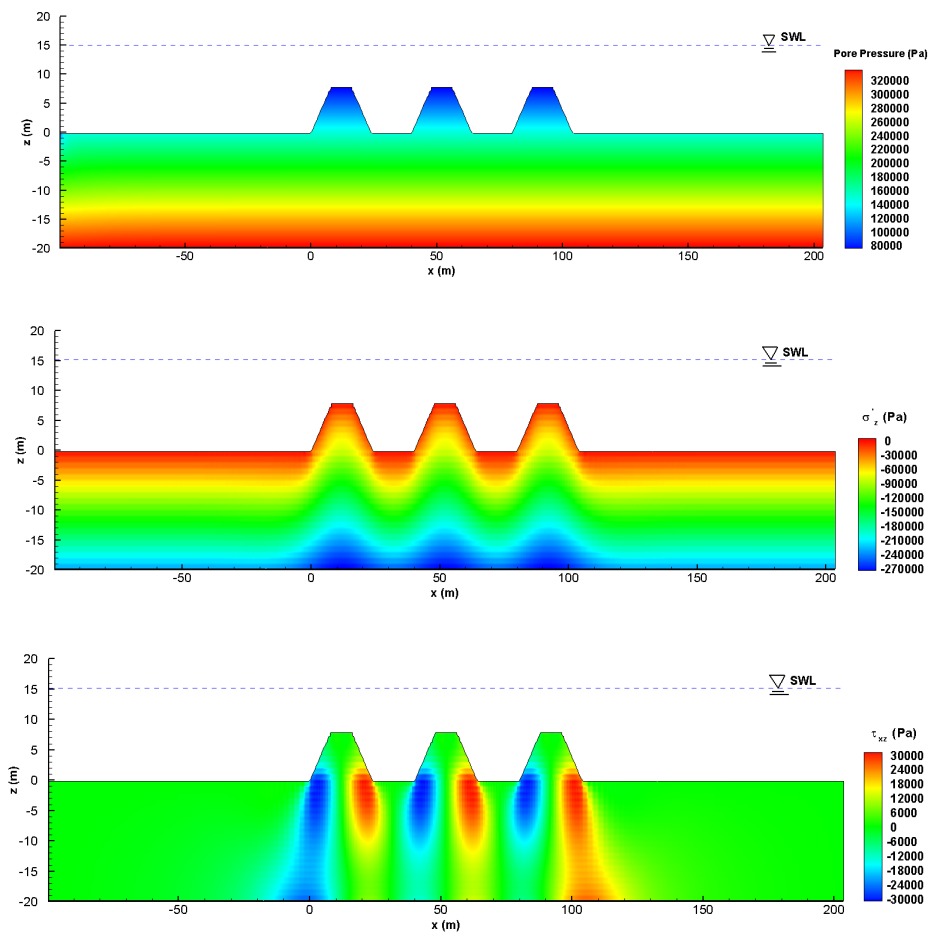


Figure 4.6 Distribution of pore pressure (p_s), effective normal stress (σ'_z) and shear stress (τ_{xz}) in the seabed foundation after the consolidation process is completed.

4.5 Wave/current induced dynamic soil responses

Effective normal stresses (σ'_z), shear stresses (τ_{xz}) and pore pressures (p_s) are important parameters that affect wave/current induced dynamic responses of seabed foundation around the structures. Figure 4.7 shows time series of σ'_z , τ_{xz} and p_s under the wave/current loading within a poro-elastoplastic seabed at two typical locations, namely A ($x = -1$ m, $z = -4$ m) and D ($x = 105$ m, $z = -4$ m), which are in front of first breakwater and behind the last breakwater, respectively. It is observed from the figure that the dynamic responses of seabed foundation consist of two components: one is oscillatory component that fluctuates with propagating wave, whose temporal average over wave cycle equals to zero, the other one is residual component that caused by the volumetric contraction of sandy soil under cyclic wave loading. p_s at both locations builds up progressively with time. However, it is not unlimited. It remains as a constant (P_{cr}) after many wave loading cycle at location A. Herein, P_{cr} is the critical value of soil liquefaction onset, defined as the initial mean normal effective stress after the pre-consolidation process has been completed:

$$\sigma'_0 = \frac{1 + \mu_s}{3} (\sigma'_{x0} + \sigma'_{z0}) \quad (4.4)$$

in which μ_s is the Poisson's ratio; σ'_{x0} and σ'_{z0} are the horizontal and vertical initial effective stresses respectively that determined through consolidation process. Along with the build-up of p_s , σ'_z and τ_{xz} decrease, and approach to zero. This is because that when p_s builds up, the contacted forces between the soil particles gradually transfer to the pore fluid, the soil tends to a status of liquid. As can be seen at location A, the residual pore pressures reached the critical value P_{cr} , for example, at $t = 240$ s in the case with $U_0 = 1$ m/s, which indicates that the soil becomes liquefied. At the same time, σ'_z and τ_{xz} both become zero. The reason of this phenomenon is that when liquefaction occurs, the soil behaves as liquid, the contacted effective stress become zero and cannot bear any shear stresses. In contrast, at location D, σ'_z and τ_{xz} still remain a relative large value, p_s did not reach critical value P_{cr} . Hence, the soil at location D has not been liquefied. This is due to the protection of multiple breakwaters, the hydrodynamic pressure at location A is much larger than the one at location D, which makes location A much easier to be liquefied. Another interesting aspect is that the oscillatory part of the pore pressure is relative small at location D, which also attributes to the breakwaters protection effects.

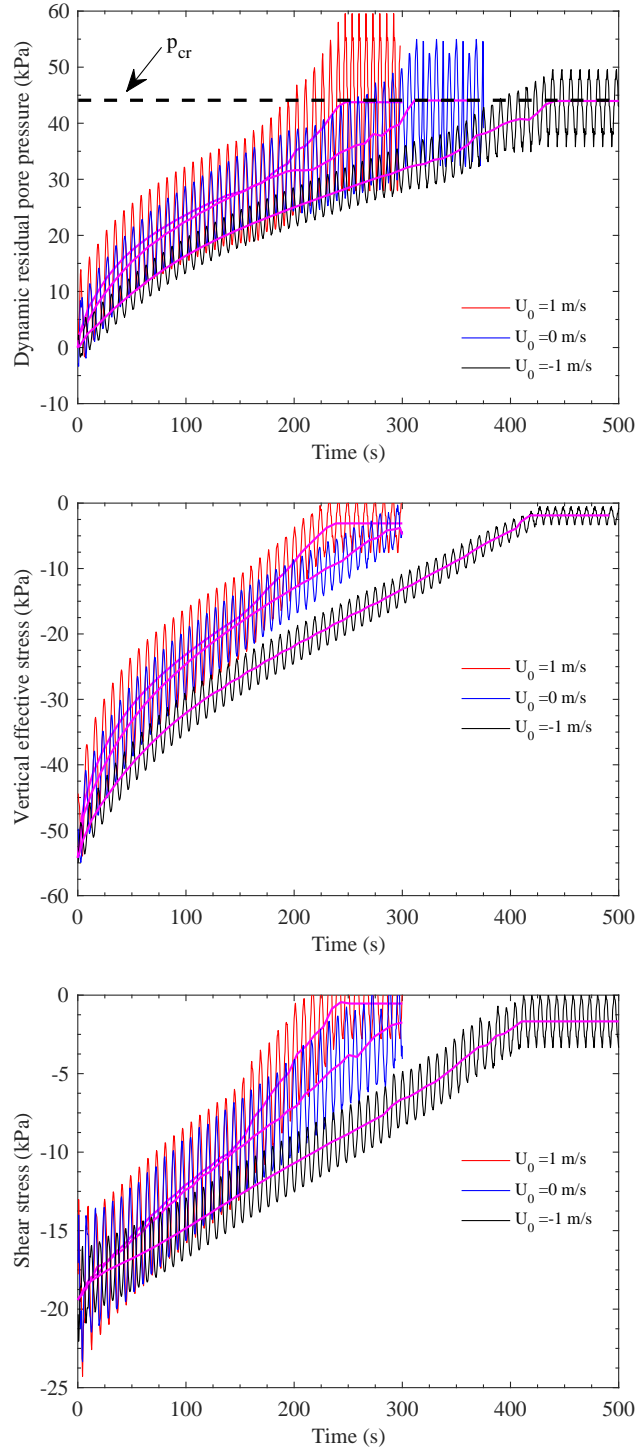
Another factor that influence the dynamic soil responses is the ocean currents. As shown in Figure 4.7, three current conditions are considered: following currents ($U_0 = 1$ m/s), without a currents ($U_0 = 0$ m/s) and opposing currents ($U_0 = -1$ m/s). It can be clearly

4.5 Wave/current induced dynamic soil responses

seen from the figures that presence of the ocean currents greatly affects the dynamic soil responses in the seabed foundation: compared to the case without currents ($U_0 = 0$ m/s), the following currents ($U_0 = 1$ m/s) aggravate the soil responses and bring forward the occurrence of soil liquefaction while the opposing currents ($U_0 = -1$ m/s) mitigate the soil responses and postpone the occurrence of soil liquefaction. For example, at location A, the soil liquefied at around 240s, 320s and 440s in the cases with following currents, without a currents and with an opposing currents, respectively. The existence of currents will change the wave characteristics. The following currents could significantly elongate the wave length, decrease wave number and increase the maximum pressure that acting on seabed. While the opposing currents have the opposite effect and make the maximum pressure acting on seabed decrease. As one-way coupling algorithm is adopted between fluid and seabed sub-model. Only the hydrodynamic pressure from fluid model will be applied on the seabed surface. Therefore, the effects of currents on soil responses are reflected in the form of hydrodynamic pressure acting on the seabed surface. The hydrodynamic pressure increases in following currents cases, resulting in a higher potential of seabed instability. As the result, a conclusion can be made that the opposing currents, to some extents, can avoid soil liquefaction while following currents have negative effects on seabed foundation stability. In addition, it can be seen from the figures that the following currents magnify the oscillatory part of soil responses while the opposing currents have opposite effects.

Figure 4.8 shows the distribution of dynamic soil responses in the (a) poro-elastoplastic seabed foundation and (b) poro-elastic seabed foundation. The dynamic responses are obtained by subtracting the full responses under the hydrostatic and hydrodynamic pressure by the initial consolidation state. For the poro-elastoplastic seabed foundation, the dynamic pore pressure (p_s) at $t = 100$ s, 200 s and 300 s is chosen as the parameter to illustrate the process of accumulation. As can be seen from Figure 4.8a, p_s is mainly distributed on two sides and underneath the breakwaters, whose value gradually increases, from less than 20 kPa at $t = 100$ s to more than 50 kPa at $t = 300$ s. At the beginning, pore water pressure accumulation occurs in the areas with maximum shear force, that is, on the two sides of the breakwaters as shown in Figure 4.6. The shear force varies periodically along with the cyclic loading and rearranges the soil particles. The soil in these areas is compacted and the pore water is pressurised which leads to the build-up. If the cyclic loading continues, the pore pressure will continue to accumulate. When it reaches the critical value, the soil will begin to liquefy. Regarding to the spatial distribution of p_s accumulation, from the location in front of first breakwater to the location behind the last breakwater, the value of residual pore pressure gradually decrease and the depth of pore pressure accumulation is also decreasing. It shows the characteristic of protection effect of multiple breakwaters on the poro-elastoplastic seabed

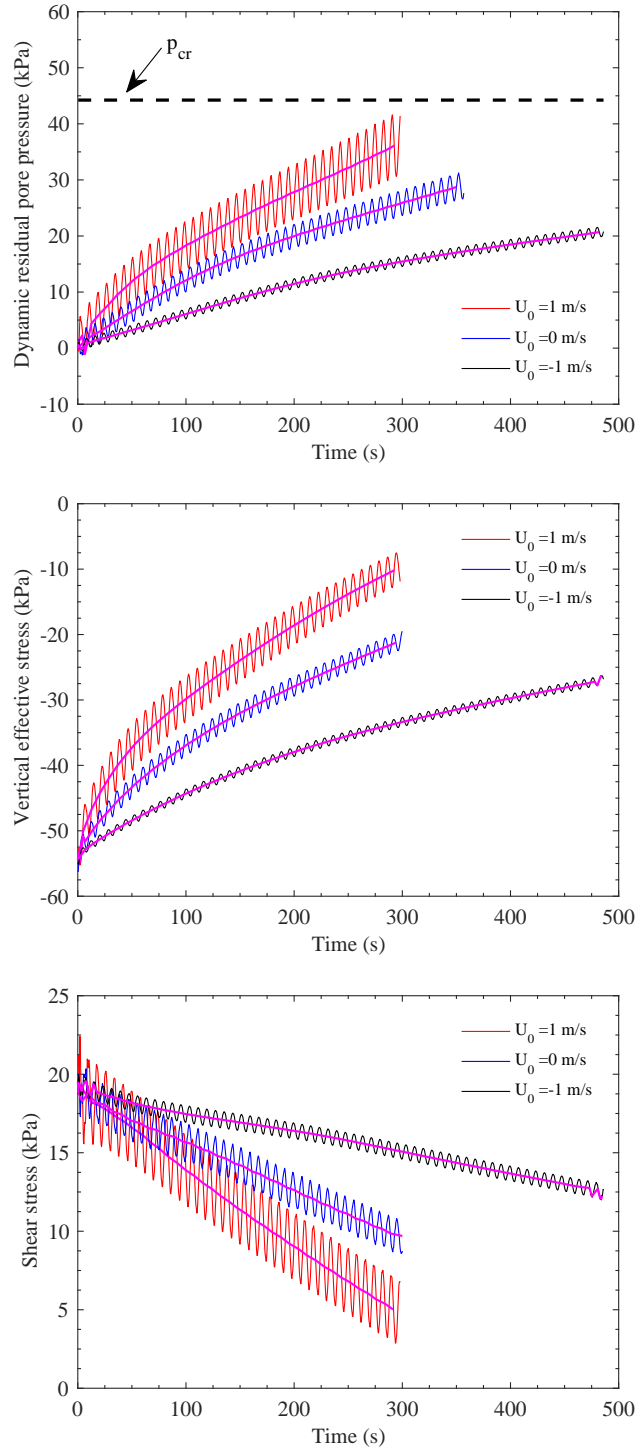
4.5 Wave/current induced dynamic soil responses



(a) location A ($x = -1$ m, $z = -4$ m) (in front of first breakwater)

Figure 4.7 Time series of wave/current induced soil responses including build-up of pore pressure (p_s) and reduction of effective normal stress (σ'_z) and shear stress (τ_{xz}) at (a) location A ($x = -1$ m, $z = -4$ m) and (b) location D ($x = 105$ m, $z = -4$ m) in a sandy seabed foundation.

4.5 Wave/current induced dynamic soil responses



(b) location D ($x = 105$ m, $z = -4$ m) (behind last breakwater)

Figure 4.7 Time series of wave/current induced soil responses including build-up of pore pressure (p_s) and reduction of effective normal stress (σ'_z) and shear stress (τ_{xz}) at (a) location A ($x = -1$ m, $z = -4$ m) and (b) location D ($x = 105$ m, $z = -4$ m) in a sandy seabed foundation(cont.).

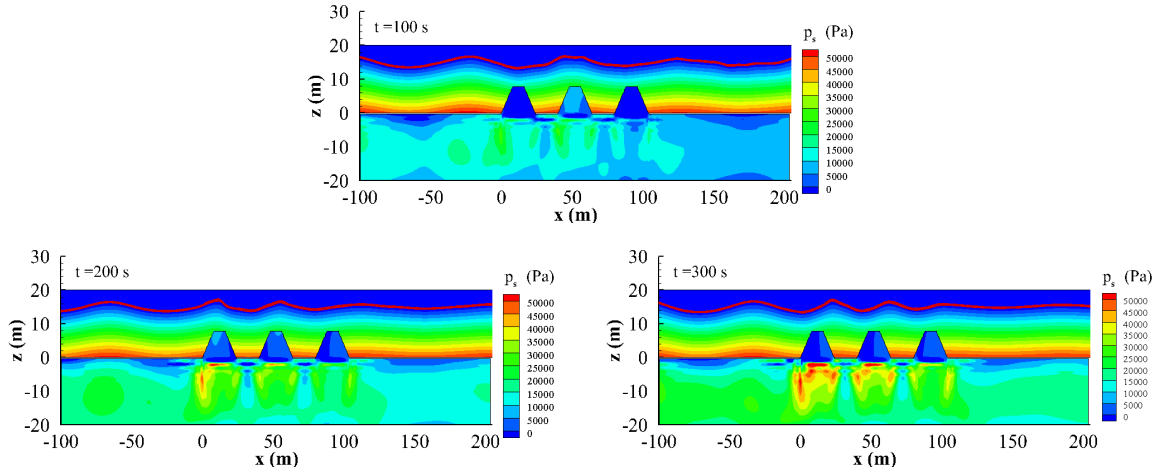
4.5 Wave/current induced dynamic soil responses

foundation. Therefore, it can be easily found that the first breakwater faces the greatest risk of potential for instability, during the practical engineering projects design, a reinforcement of the first breakwater foundation should be performed.

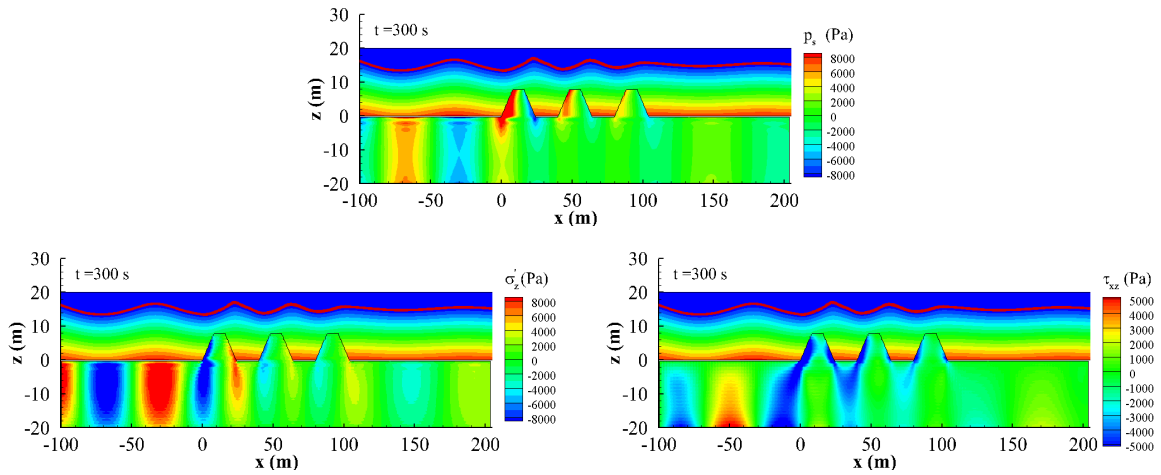
While for the poro-elastic seabed foundation, the mechanism of dynamic soil responses is totally different. Figure 4.8b shows the dynamic pore pressure (p_s), effective normal stress (σ'_z) and shear stress (τ_{xz}) at $t=300$ s in a poro-elastic seabed foundation. It can be found that the dynamic soil responses are intensively in phase with the water surface elevation, which distribute in a positive and negative alternating pattern. Under the wave troughs, p_s is positive and σ'_z is negative (i.e., in tensile), while under the wave crests, p_s is negative and σ'_z is positive (i.e., in compressive). The upward-directed transient seepage forces during the passage of a wave troughs will cause the decrease of effective normal stress. When the contact force between the soil particles disappears, momentary liquefaction happens. According to the definition of momentary liquefaction, only the seabed under wave troughs could be liquefied while the seabed under wave crests will not liquefy in the elastic seabed foundation. However, if the wave troughs are near the breakwater, like at $t=300$ s, it will still pose a great threat on the stability of the breakwater. For the region behind the last breakwater, due to the protection from multiple breakwaters, the effect of wave/current loading on the elastic seabed foundation has been significantly reduced.

Another important indicator to understand dynamic seabed responses around multiple breakwaters is soil displacement. Figure 4.9 illustrates time series of wave/current induced displacement in a poro-elastoplastic seabed foundation at $z=-4$ m. Three typical locations are selected: $x=-1$ m, 52 m and 105 m, which are in front of first breakwater, right beneath the second breakwater and behind the last breakwater, respectively. It can be observed that there is obvious lateral spreading in the loosely deposited sandy seabed at location $x=-1$ m and $x=105$ m. At $t=300$ s, the horizontal displacement reaches -13 cm at $x=-1$ m and 6 cm at $x=105$ m. While at $x=52$ m, there is no lateral spreading happens, it vibrates around 0. This is because that the soil at location $x=52$ m is relatively compacted due to gravity of the breakwater. The deformation and displacement are more difficult to happen in the denser soil. Furthermore, the multiple breakwaters have a certain extent protection for soil deformation behind breakwaters, compared between $x=-1$ m and $x=105$ m. The vertical displacement shows a different trend: there is significant vertical subsidence at all three locations with around 4.8 cm, 1.8 cm and 1.5 cm at $x=52$ m, $x=-1$ m and $x=105$ m, respectively. Similarly, due to the self-weight of breakwater, location $x=52$ m has most obvious sink. A very interesting phenomenon can be observed at $x=-1$ m: the soil keeps subsiding until around $t=220$ s, then an upward displacement appears. This is mainly because that location $x=-1$ m is just in front of first breakwater, the soil under first breakwater become liquefied at $t=220$ s,

4.5 Wave/current induced dynamic soil responses



(a) accumulation of the residual pore pressure (p_s) at $t=100, 200$ and 300 s in a poro-elastoplastic seabed foundation.



(b) dynamic pore pressure (p_s), effective normal stress (σ'_z) and shear stress (τ_{xz}) at $t=300$ s in a poro-elastic seabed foundation.

Figure 4.8 Distribution of wave/current induced dynamic soil responses in the (a) poro-elastoplastic seabed foundation and (b) poro-elastic seabed foundation.

after liquefaction happens, the soil under first breakwater cannot support the first breakwater above, the first breakwater suddenly has a large subsidence, this kind of squeezing results upward movement of surrounding soil. It may be concluded that phenomenon showing an upward movement after subsidence of soil could be used as an indirect indicator of soil liquefaction happening under the breakwater. It can also be found that the oscillatory of displacement is larger in front of breakwaters compared to the locations behind breakwaters.

Figure 4.10 shows time series of soil displacement at same locations in a poro-elastic seabed foundation. With totally different trend from the poro-elastoplastic seabed foundation, there is no permanent deformation within the poro-elastic seabed foundation. The soil only vibrates around the initial position along with the wave/current motion. However, the effect of multiple breakwaters on the soil displacement at different locations can be still observed from its vibration amplitude. The location in front of first breakwater has the largest horizontal/vertical displacement and the location behind the last breakwater has the smallest horizontal/vertical displacement.

4.6 Liquefaction in the seabed foundation

As introduced in section 2.2.4, there are two types of liquefaction mechanisms: momentary liquefaction and residual liquefaction. In general, momentary liquefaction usually occurs in relatively dense soil (i.e., poro-elastic foundation) below the wave trough; residual liquefaction normally happens in relatively loose soil (i.e., poro-elastoplastic foundation) under long term cyclic loading. When liquefaction occurs, the soil foundation loses its bearing capacity and the structures built on it will very easily collapse. Therefore, evaluation of the liquefaction potential of seabed foundation is essential for structural design and maintenance. In this section, the wave/current induced liquefaction conditions around breakwaters within the poro-elastoplastic seabed foundation and poro-elastic seabed foundation will be investigated in terms of liquefaction potential ($L_{potential}$) and liquefaction zones.

Based on the liquefaction criterion proposed by Okusa (1985) (Equation (2.18)), the liquefaction potential ($L_{potential}$) is proposed, which is defined as:

$$L_{potential} = \frac{\sigma'_{zd}}{|\sigma'_0|} \quad (4.5)$$

where σ'_{zd} and σ'_0 are the wave/current induced effective normal stress and initial mean normal effective stress, respectively. The range of the liquefaction potential is from 0 to

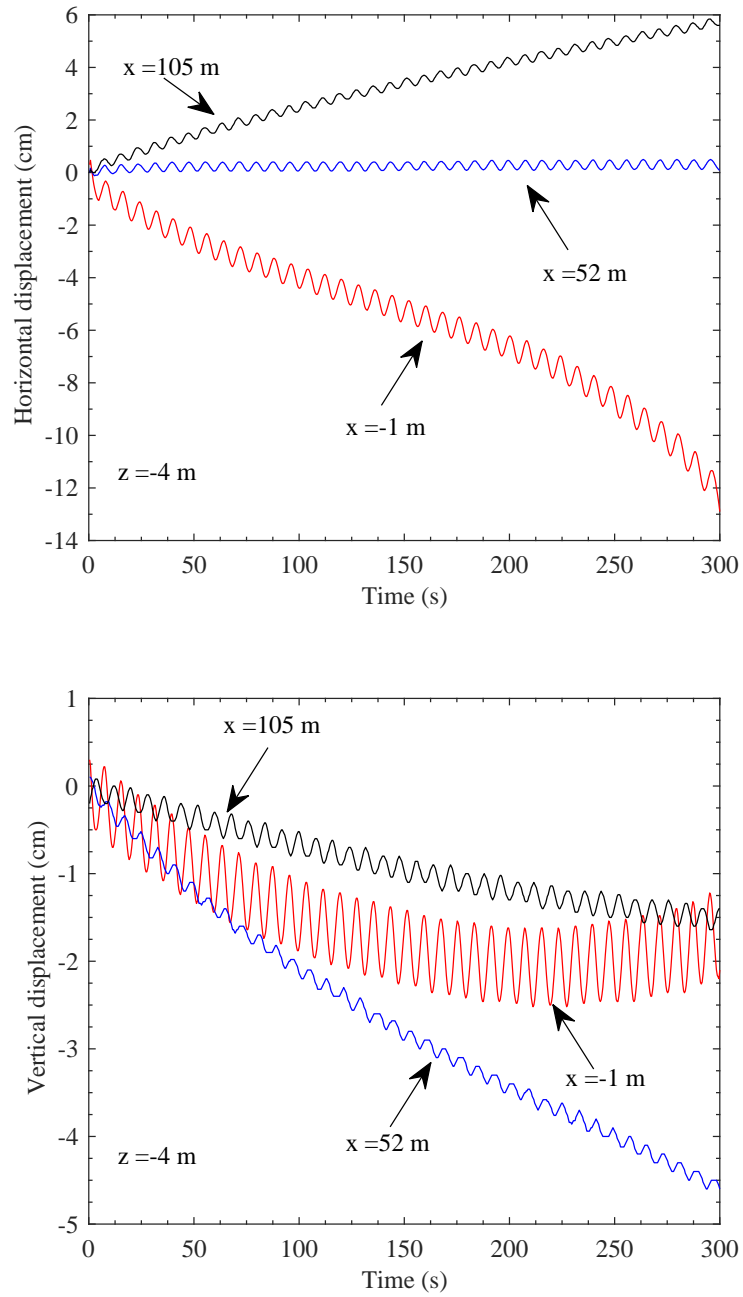


Figure 4.9 Time series of wave/current induced horizontal and vertical displacement at three typical locations ($x = -1$ m, $z = -4$ m; $x = 52$ m, $z = -4$ m; $x = 105$ m, $z = -4$ m) in a poro-elastoplastic seabed foundation.

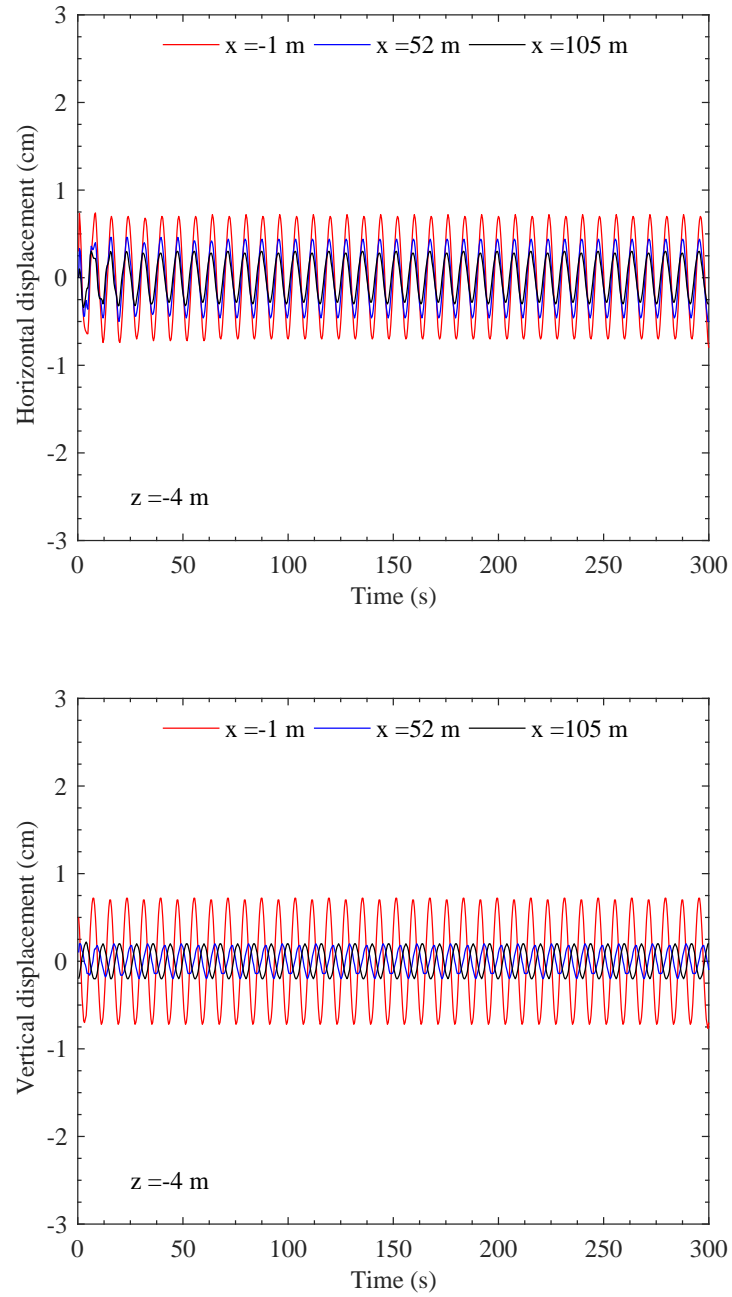


Figure 4.10 Time series of wave/current induced horizontal and vertical displacement at three typical locations ($x = -1$ m, $z = -4$ m; $x = 52$ m, $z = -4$ m; $x = 105$ m, $z = -4$ m) in a poro-elastic seabed foundation.

4.6 Liquefaction in the seabed foundation

1. The larger the value of liquefaction potential, the greater the possibility of occurrence of soil liquefaction. When $L_{potential} = 1$, the liquefaction occurs. Considering conservative evaluation, in this study, we assume that the soil is liquefied when $L_{potential}$ reaches 0.9.

Figure 4.11 shows time series of liquefaction potential ($L_{potential}$) within an poro-elastoplastic seabed foundation at four locations ($x = -1$ m, $x = 32$ m, $x = 52$ m and $x = 105$ m) from two depths ($z = -4$ m and $z = -6$ m). It can be seen from the figure that $L_{potential}$ increases over time at all locations. Different locations have different liquefaction potential: the compression effect from breakwaters makes soil at $x = 52$ m (i.e., just beneath the second breakwater) the most compacted, the pore pressure is not easy to build up here, hence $L_{potential}$ at $x = 52$ m is the smallest; $x = -1$ m is located in front of the first breakwater where there is no protection from the breakwaters, at the same time it is affected by the strong non-linear interaction among reflected waves, incident waves and ocean currents, therefore, soil at $x = -1$ m has the largest $L_{potential}$; the possibility of liquefaction at other locations from left to right gradually increases due to the protection effect from the breakwaters gradually decreases. Vertically, $L_{potential}$ decreases with the increase of soil depth, which indicates that the liquefaction is more likely to happen in the upper layer of seabed foundation.

Figure 4.12 illustrates the development of residual liquefaction areas in a poro-elastoplastic seabed foundation around one, two and three breakwaters, respectively. The green, blue and red lines represent the boundaries of liquefied area at $t = 100$ s, 200 s and 300 s, respectively. As shown in the figures, the wave/current induced liquefaction areas mostly concentrate on upper layer of seabed foundation that locates in front of breakwaters, in the gaps between breakwaters and behind breakwaters. however, the region in front of the first breakwater is most liquefied due to the most severe loading condition. From the perspective of time, it is obvious that liquefaction area grows over time in all three cases. The liquefaction area expands horizontally and vertically. Especially in the region in front of the first breakwater, the area has expanded the most, for example, at $t = 200$ s, the area is quite small, whereas the area much larger and deeper at $t = 300$ s. Combining with the results in Figure 4.8a, it can be found that the residual liquefaction in the poro-elastoplastic seabed foundation is a progressive process with the pore pressure accumulation. The residual liquefaction may have critical effect on the breakwater foundation stability.

Figure 4.13 shows the momentary liquefaction areas in a poro-elastic seabed foundation around the breakwater from $t = 17.6$ s to 20 s. In contrast to the results in Figure 4.12, the mechanism of momentary liquefaction is totally different from residual liquefaction. As can be seen from the figure, momentary liquefaction zone could only occur at the top layer of the seabed foundation under wave troughs, while the seabed under wave crests has no

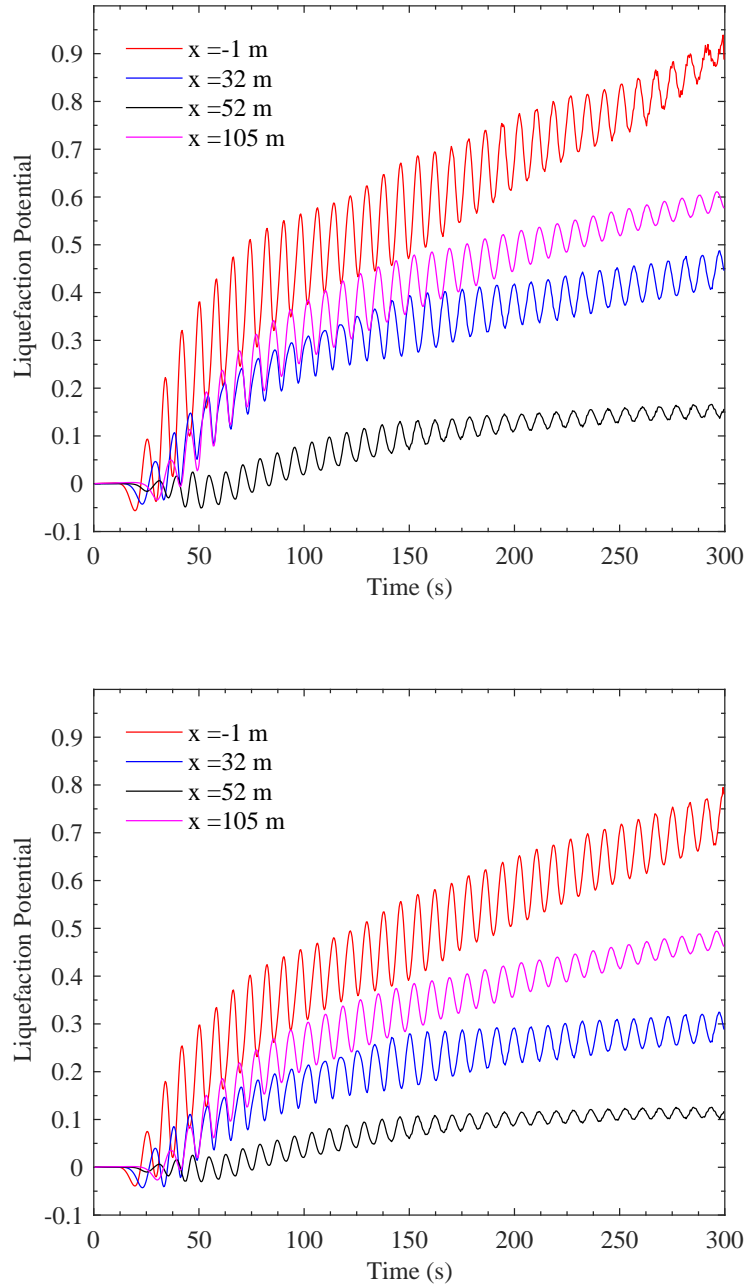


Figure 4.11 Time series of liquefaction potential ($L_{potential}$) within an poro-elastoplastic seabed foundation at typical locations ($x = -1$ m; $x = 32$ m; $x = 52$ m; $x = 105$ m) around breakwaters from two depth: (a) $z = -4$ m and (b) $z = -6$ m.

4.6 Liquefaction in the seabed foundation

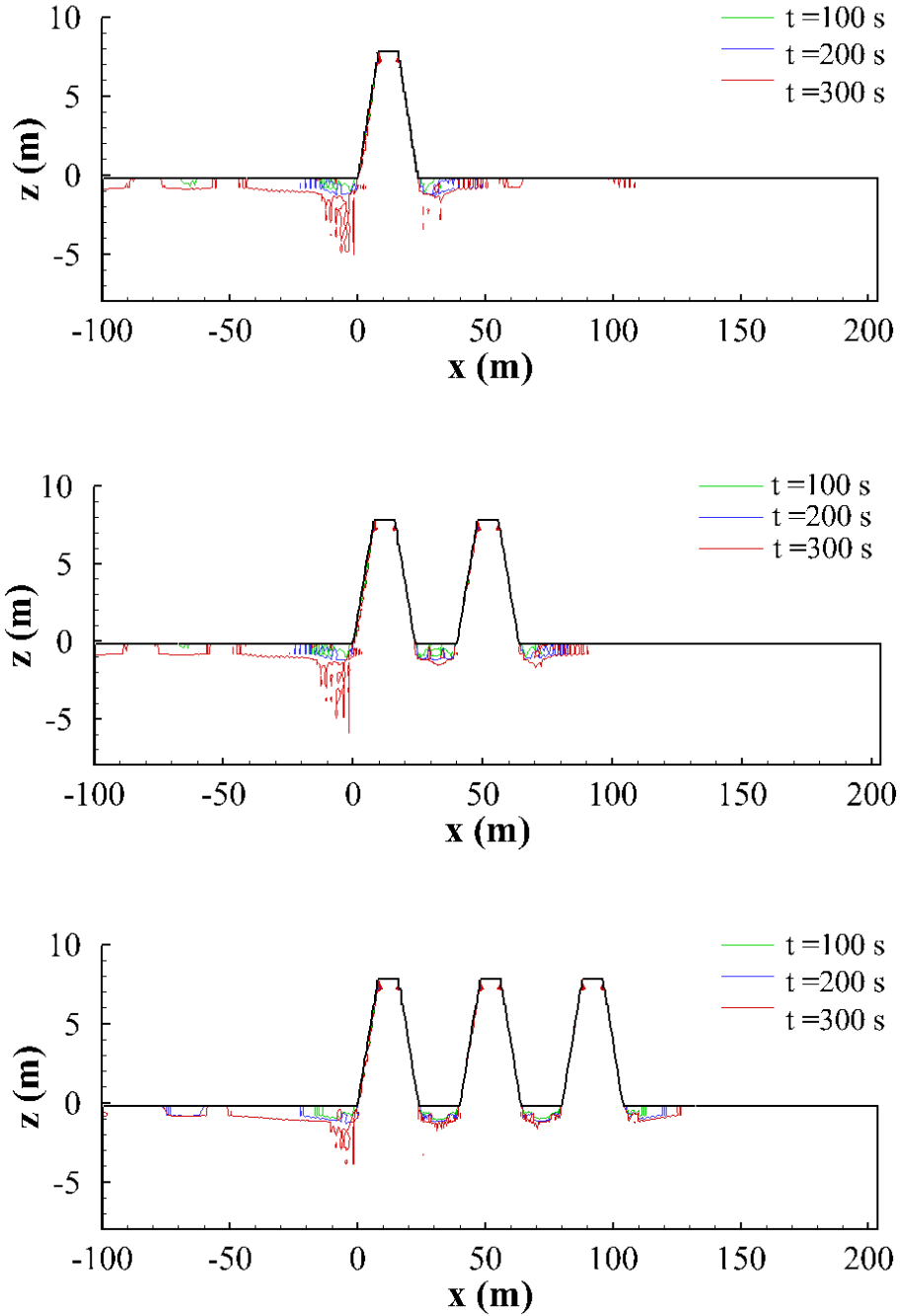


Figure 4.12 Wave/current induced liquefaction zones in a poro-elastoplastic seabed foundation at $t=100$, 200 and 300 s in the cases with one ($N=1$), two ($N=2$) and three breakwaters ($N=3$).

potential of liquefaction. The reason for this phenomenon is that the upward seepage force can be generated in the region under wave trough and seabed surface has the largest gradient which makes the effective stress in these region significant decrease, eventually causing liquefaction. For the region under wave crest, the seepage force is downward, the soil is impossible to be liquefied. Another interesting finding is that the momentary liquefaction areas move along with the wave/current motion. Compared to the residual liquefaction areas in the poro-elastoplastic seabed, the momentary liquefaction has a relatively minor effect on the stability of structure foundation. However, it still poses a threat to the structure foundation when the liquefaction zones move to the area close to the breakwater foundation (i.e., $t=20$ s), not to mention it also exacerbates the scouring condition around breakwater foundation.

4.7 Parametric study

In this section, parametric studies including the effects of currents (U_0), soil properties (soil permeability k_s , degree of saturation S_r and the relative density D_r) and wave characteristics (wave period T , wave height H and water depth d) on the vertical distribution of liquefaction potential ($L_{potential}$) in a poro-elastoplastic seabed foundation will be discussed. Four typical times are selected to illustrate the progressive process of soil liquefaction.

Figure 4.14 demonstrates the vertical distribution of liquefaction potential ($L_{potential}$) for $x=-1.5$ m at $t=20$ s, 40 s, 150 s and 250 s for various ocean current conditions, namely the following currents ($U_0=1$ m/s), waves only without currents ($U_0=0$ m/s) and opposing currents ($U_0=-1$ m/s). Spatially, $L_{potential}$ in the upper seabed is generally greater than that in the lower seabed; temporally, $L_{potential}$ at all depth of seabed increases over time until liquefaction happens. After $L_{potential}$ almost reaches 1.0, it will not increase or even decrease a little as the build-up pore pressure remains as constant in a nearly liquefied soil. It is observed from the figures that the presence of currents has valid impact on development of liquefaction potential. At $t=20$ s (the early stage), the influence is not obvious, three curves are almost overlapped. As time goes by, the impact becomes more and more obvious. It is clear that following currents ($U_0=1$ m/s) have positive effect on the development of soil liquefaction while opposing currents ($U_0=-1$ m/s) have negative effect compared to the case without ocean currents. In other words, the following currents can deteriorate the seabed foundation instability, while the opposing currents can prevent occurrence of soil liquefaction which is good for the offshore structures stability.

Soil properties and wave characteristics may vary at different sites, therefore, it is crucial to examine their effects on the breakwater foundation stability. Figure 4.15 and Figure 4.16

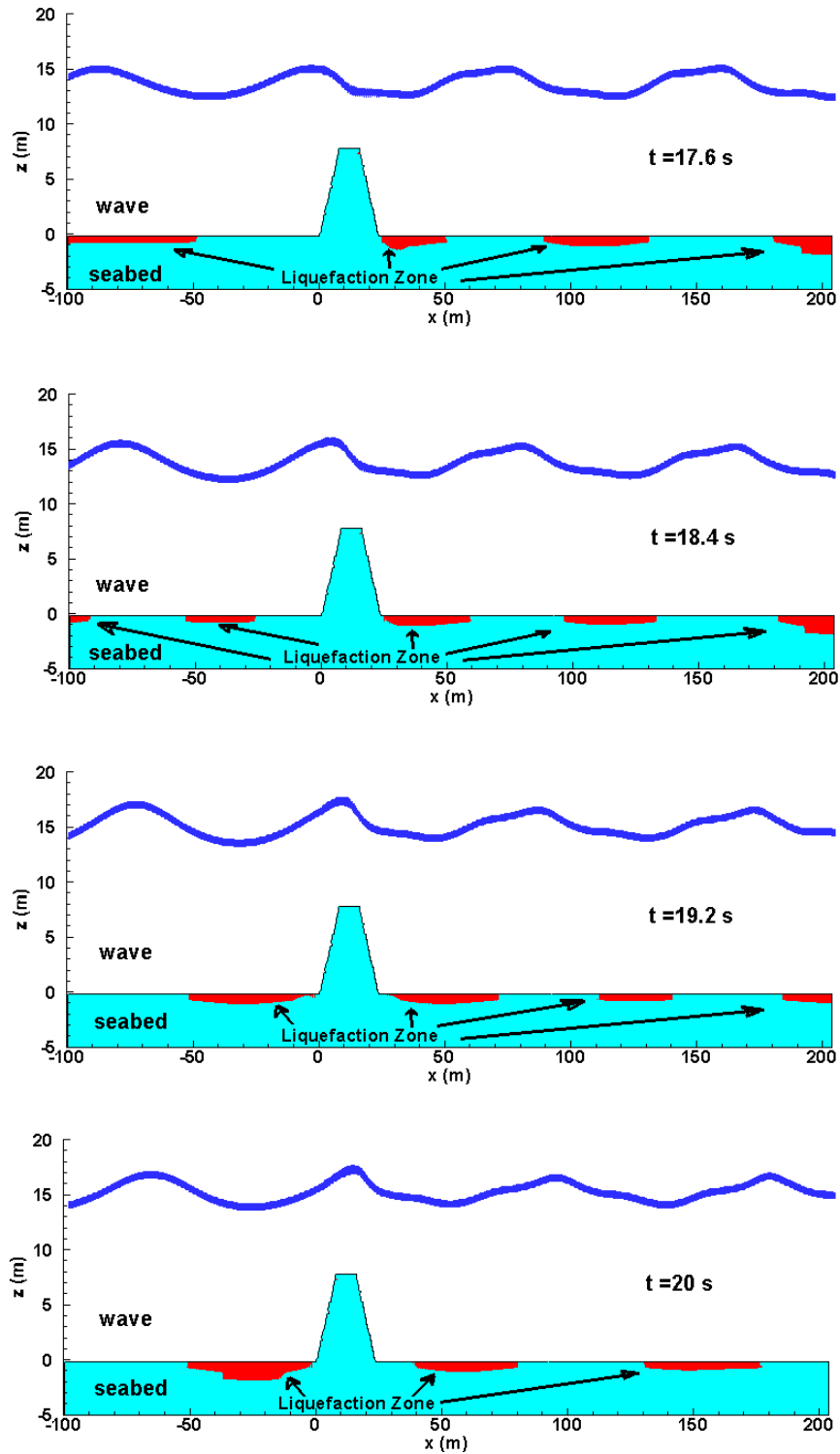


Figure 4.13 Wave/current induced liquefaction zones in a poro-elastic seabed foundation in one wave period from $t = 17.6$ s to $t = 20$ s.

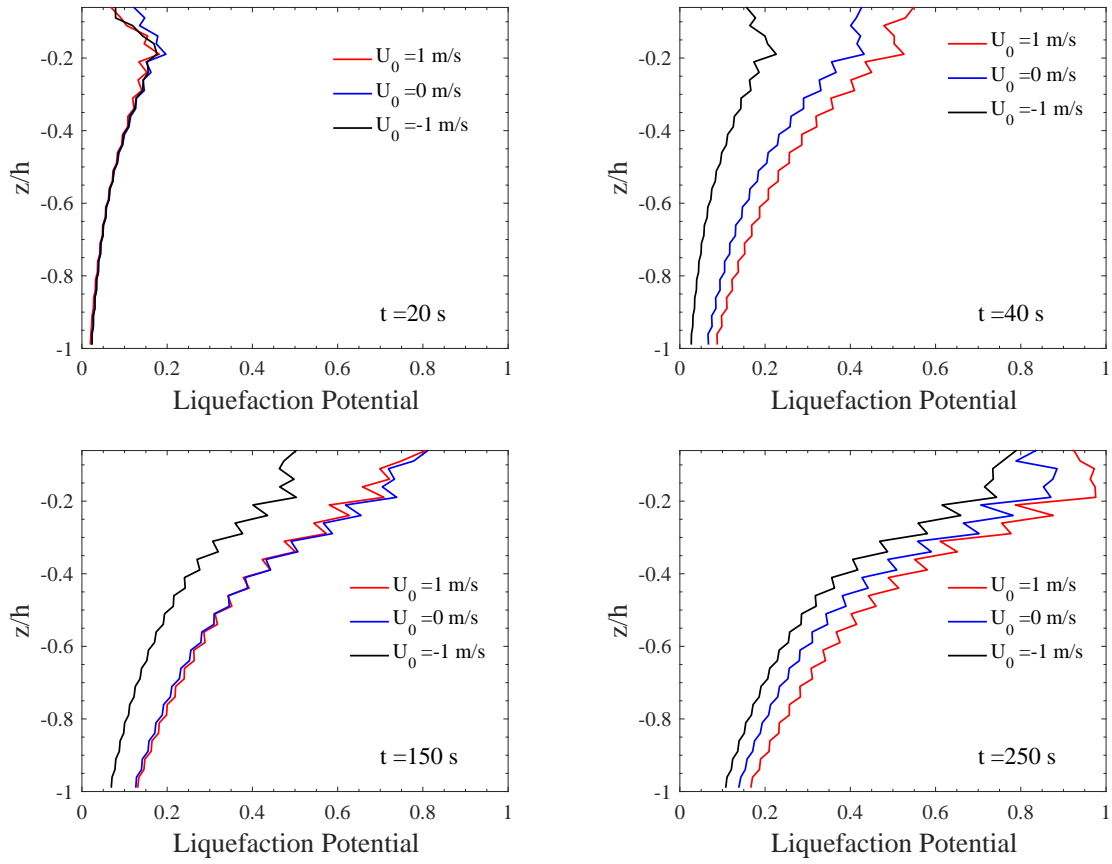


Figure 4.14 Effects of currents (U_0) on vertical distribution of liquefaction potential ($L_{potential}$) for $x = -1.5$ m at $t = 20, 40, 150$ and 250 s.

shows the effects of soil permeability (k_s) and degree of saturation (S_r) on vertical distribution of $L_{potential}$, respectively. It can be observed that the spatial and temporal distribution trends of $L_{potential}$ are found to be similar as in the previous figure. The vertical distribution of $L_{potential}$ increases as k_s decreases and S_r increases, implying that soil liquefaction is more likely to happen in a seabed foundation with small soil permeability and higher degree of saturation. Comparing these two parameters, it can be concluded that k_s is a more important parameter affecting the soil liquefaction. For example, $L_{potential}$ in a seabed with $k_s = -10^{-2}$ m/s is less than 0.2, which means it will never be liquefied, but the liquefaction occurs in the seabed with $k_s = -10^{-7}$ m/s and $k_s = -10^{-5}$ m/s at $t = 250$ s. The effect of k_s becomes less significant when k_s is small enough since $L_{potential}$ in a seabed with $k_s = -10^{-7}$ m/s is only slightly larger than that in a seabed with $k_s = -10^{-5}$ m/s. It is also worth noting that there are some slight decreases of $L_{potential}$ near the seabed surface. This is due to the fact that the build-up and dissipation of pore pressure exist simultaneously in seabed foundation. The drainage paths for the locations near the seabed surface are relatively short, the effect of pore pressure dissipation can not be ignored. If the pore pressure dissipation rate is equal to or even greater than the rate of build-up, a decrease of $L_{potential}$ can occur.

Figure 4.17 shows the vertical distribution of $L_{potential}$ in the soil with different relative density ($D_r = 40\%$ and 60%) at $t = 20, 40, 100$ and 120 s. It can be found from the figure that $L_{potential}$ increases faster and accumulates to a larger value in the soil with low D_r . For example, the seabed foundation with $D_r = 40\%$ at $x = -1.5$ m was already liquefied at 120 s, while $L_{potential}$ was less than 0.7 in the soil with $D_r = 60\%$. It implies that the residual liquefaction is more likely to happen in a seabed foundation with low relative density.

The effects of wave characteristics, including wave period (T), wave height (H) and water depth (d), are revealed in Figures 4.18, 4.19 and 4.20, respectively. As can be seen from these figures, the liquefaction potential ($L_{potential}$) is more significant in the seabed foundation under longer wave period, larger wave height and deeper water depth.

4.8 Summary

In this study, the soil responses and liquefaction around multiple submerged breakwaters under combined wave and current loading were investigated by adopting the integrated 2D numerical model. Based on the numerical results, some key conclusions are listed as following:

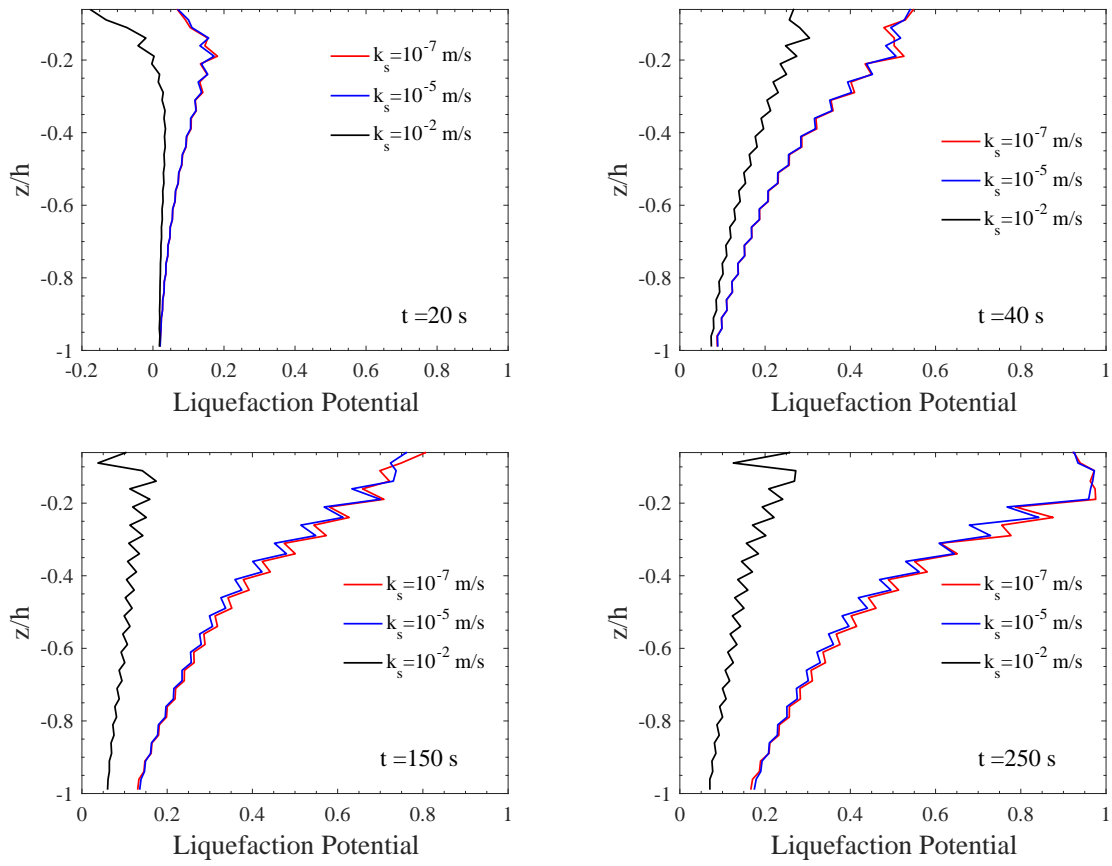


Figure 4.15 Effects of soil permeability (k_s) on vertical distribution of liquefaction potential ($L_{potential}$) for $x = -1.5$ m at $t = 20, 40, 150$ and 250 s.

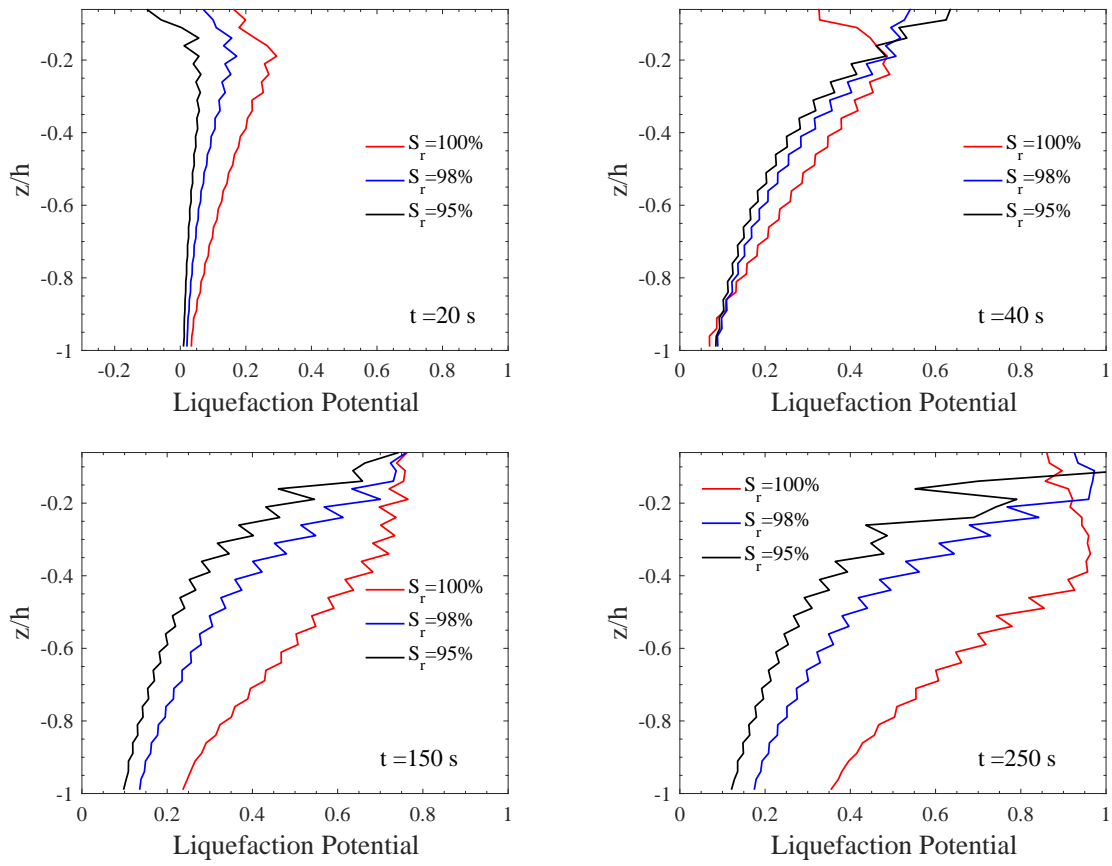


Figure 4.16 Effects of degree of saturation (S_r) on vertical distribution of liquefaction potential ($L_{potential}$) for $x=-1.5$ m at $t=20, 40, 150$ and 250 s.

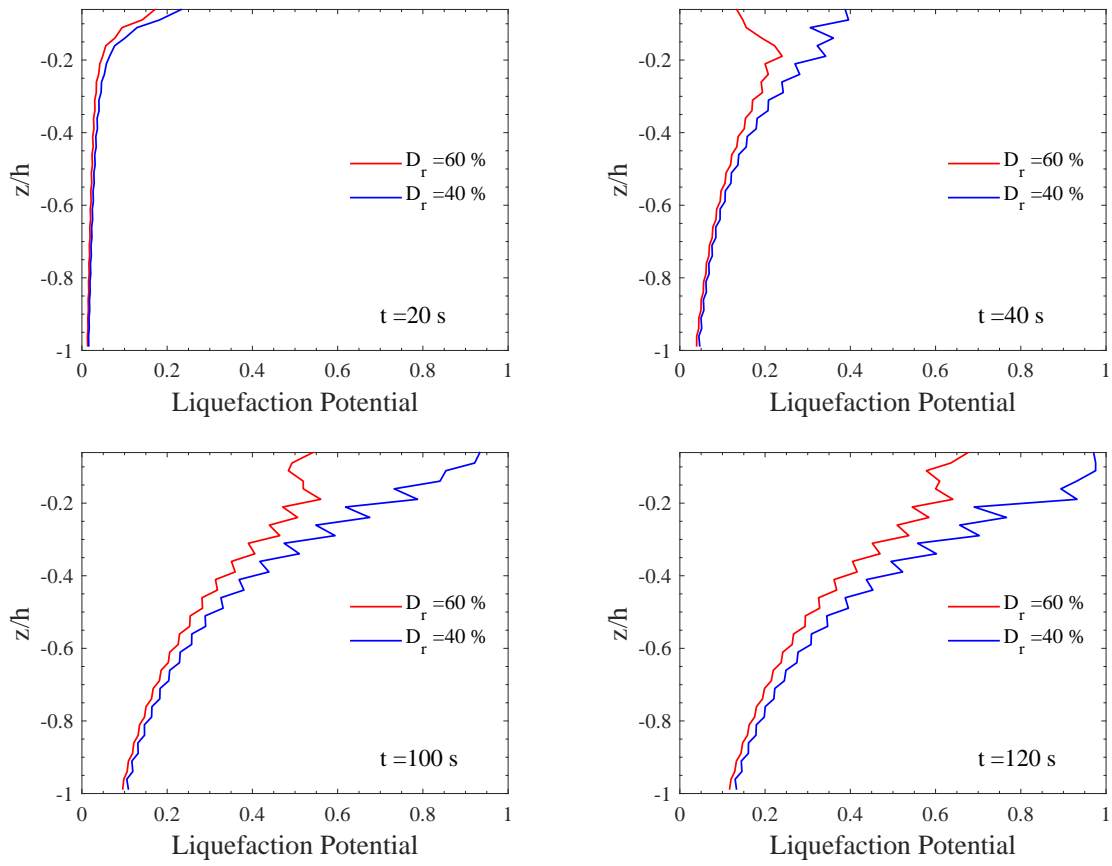


Figure 4.17 Effects of the relative density (D_r) on vertical distribution of liquefaction potential ($L_{potential}$) for $x = -1.5$ m at $t = 20, 40, 100$ and 120 s.

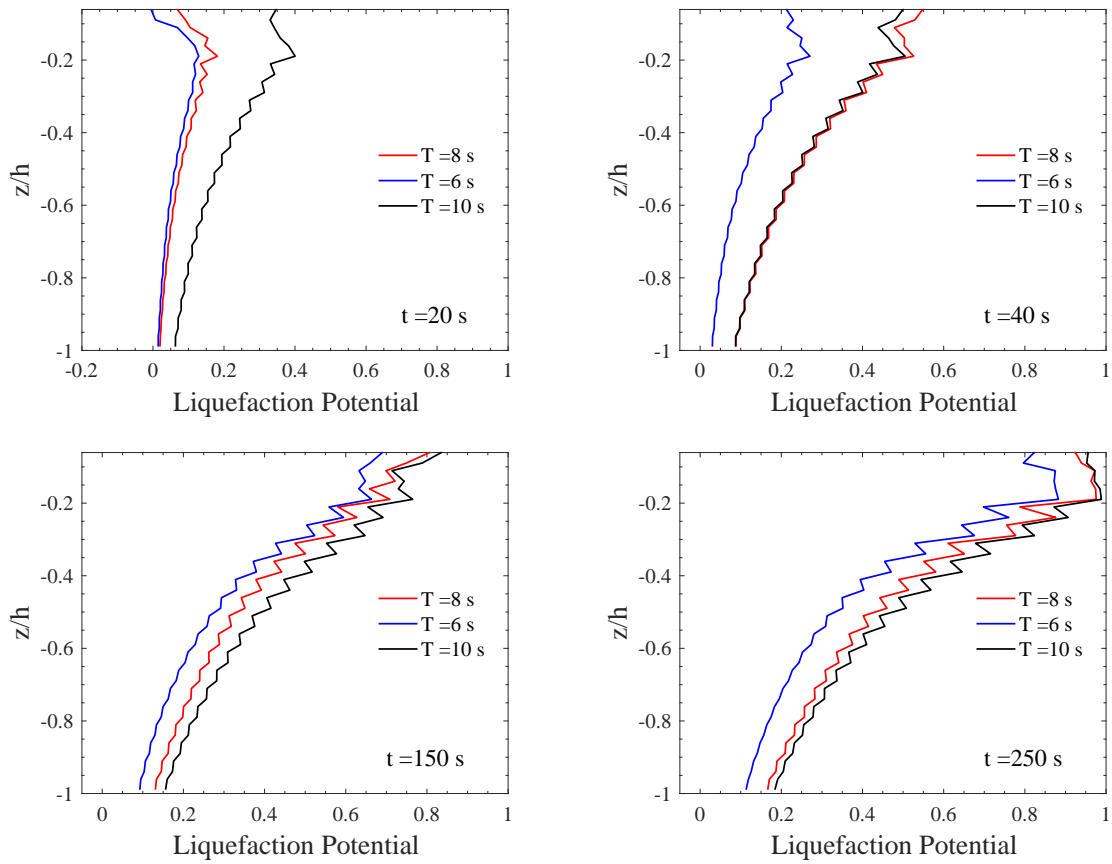


Figure 4.18 Effects of wave period (T) on vertical distribution of liquefaction potential ($L_{potential}$) for $x=-1.5$ m at $t=20$, 40, 150 and 250 s.

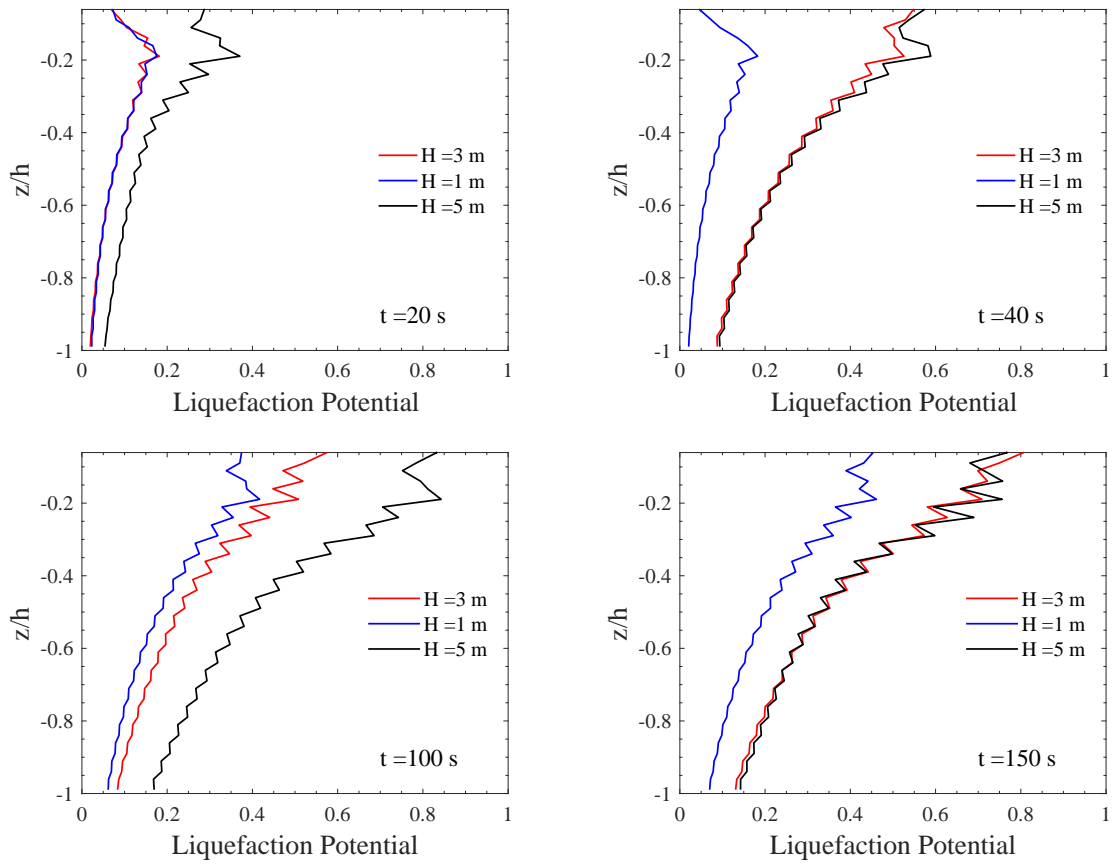


Figure 4.19 Effects of wave height (H) on vertical distribution of liquefaction potential ($L_{potential}$) for $x = -1.5$ m at $t = 20, 40, 100$ and 150 s.

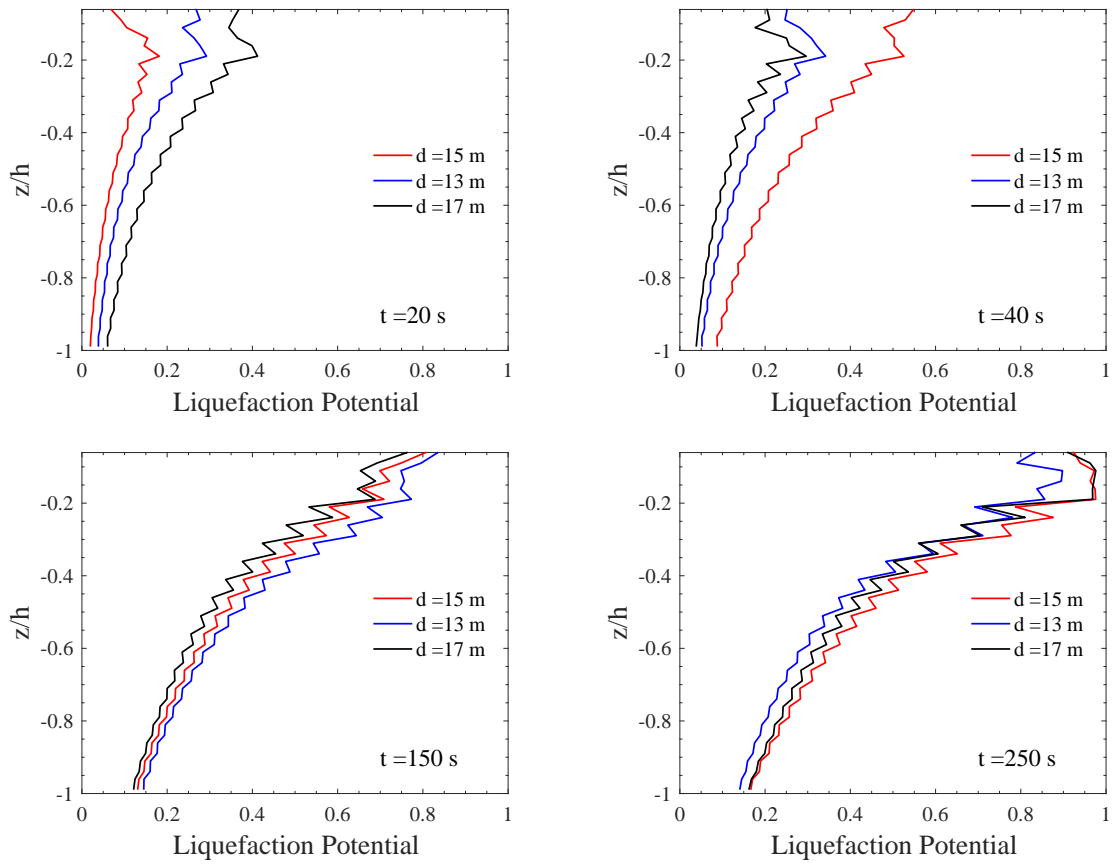


Figure 4.20 Effects of water depth (d) on vertical distribution of liquefaction potential ($L_{potential}$) for $x = -1.5$ m at $t = 20, 40, 150$ and 250 s.

- The hydrodynamic properties around multiple submerged breakwaters can be greatly affected by factors like the number of breakwaters, the ocean current conditions and the spacing between two adjacent breakwaters due to the strong non-linear wave-current-breakwaters interactions. It is also found that stronger Bragg effect is better for protecting coastline, however, it may imply more chances for the seabed foundation at seaward side of breakwater to be liquefied.
- The construction of breakwaters will considerably change the stress status in seabed foundation. Determination of the stress state after completion of consolidation process is essential for the dynamic analysis of seabed foundation and liquefaction potential evaluation.
- The pore pressure in a poro-elastoplastic foundation keeps building up to a limited value, accompanying with the reduction of effective stresses and shear stresses. Whereas, soil responses in a poro-elastic foundation variate periodically according to the water surface elevation. The ocean currents significantly affect the soil responses: the following currents aggravate the soil responses, while the opposing currents can avoid occurrence of soil liquefaction to some extent.
- The loosely deposited plastic seabed foundation has obvious lateral spreading and significant vertical subsidence under combined wave and current loading. Whereas, there is no permanent deformation within the elastic seabed foundation, it only vibrates periodically around its original position.
- The momentary liquefaction only occurs in the top seabed layer under wave troughs, which has a minor effect on structure stability. While the residual liquefaction zones gradually increase over time, which can develop to a significant level and cause critical damage to the structure foundation. The parametric studies showed that the liquefaction potential is more significant in a seabed with lower soil permeability and higher degree of saturation, and it increases as the increase of wave period, wave height and water depth. In addition, the following currents can deteriorate the seabed foundation instability, while the opposing currents can prevent occurrence of soil liquefaction.

Chapter 5

3D Numerical Study I: Seabed Foundation Stability around Breakwaters at River Mouth^{2*}

5.1 Introduction

5.1.1 Engineering background

Breakwater has been widely constructed in the offshore area to form an artificial harbour that provides a stable area for a wide range of human activities. Under the complex natural ocean loading, the assessment of the stability of the seabed foundation under the breakwater has become extremely important for the Geotechnical Engineers and Coastal Engineers. The previous scenario covered in Chapter 4 is in 2D situation, in which the research objective is the cross-section of breakwater. Hence, only the incident waves that is perpendicular to the breakwater can be taken into account. However, in the natural environment, there are situations that involve much more complicated flow-structure-seabed interactions which cannot be simulated under 2D condition. For example, Figure 5.1 is an image showing the Southport Spit at Gold Coast, Queensland. Two paralleled breakwaters are constructed at the Southport Nerang river mouth. The breakwaters are used to protect the shoreline from coastal erosion and direct the Nerang river that flows into the Pacific Ocean. At the meantime, they provide a relatively stable and peaceful navigation channel for the ships

^{2*}Contents in this chapter form the manuscript: Lin, C., & Jeng, D. S. (submitted). Numerical study for the foundation stability around breakwater heads at a river mouth. *Coastal Engineering*.



Figure 5.1 The Southport Spit, Gold Coast, QLD (Figure retrieved from <https://haveyoursay.dsdmip.qld.gov.au/the-spit>).

entering and leaving the Pacific Ocean. In this condition, the incident waves are oblique with the breakwaters, causing the reflected waves in front of breakwaters and diffracted waves behind the breakwaters. Meanwhile, the river currents coming out of the river mouth meet all components of the waves, which cause the complicated interactions, especially at the region around the breakwater heads. Therefore, in order to consider these three-dimensional effects when evaluating the seabed foundation stability, the three-dimensional numerical model has to be adopted.

In this study, the present 3D numerical model is used to simulate a case similar to the situation described above: a three-dimensional numerical study on the stability of breakwater foundation at river mouth. Two constitutive models, poro-elastic model and poro-elastoplastic model, are adopted to simulate the elastic seabed foundation and plastic seabed foundation, respectively. They are used to investigate different seabed response mechanism and liquefaction development within different types of seabed foundation. The computational domain, boundary conditions and input parameters are given first. Then, wave field characteristics involving three-dimensional wave-current-breakwater interactions such as water profiles, velocity field and hydrodynamic pressures are presented. Next, the breakwaters consolidation is done to determine the initial stress condition for the dynamic analyse of seabed foundation. Afterwards, the stability of seabed foundation around the breakwater is evaluated considering the distribution of wave/current induced dynamic soil response and the development of seabed liquefaction along with time and space. Last, some parametric studies regarding to the effect of soil properties, parameters of constitutive model

and wave characteristics on the development of liquefaction zones are presented. In the end, a brief summary of the present numerical study is given.

5.1.2 Computational domain, boundary conditions and input parameters

Figure 5.2 illustrates the computational domain of this study. As indicated in the sketch, two composite breakwaters with different lengths are built over the seabed foundation at an angle of 45 degree to the negative x - axis. The seabed foundation is considered as the porous medium, whose length (L_x), width (L_y) and thickness (L_z) are 130 m, 90 m and 15 m, respectively. Two paralleled composite breakwaters are 60 m (L_{bre1}) and 40 m (L_{bre2}) in length, respectively. The composite breakwater consists of a permeable rubble mound base with porosity (n_s) equals to 0.5 and an impermeable caisson. The cross section of the composite breakwaters can be found in Figure 5.3. To save the computational time, the mesh size and time step adopted in the seabed model is generally larger than that in the flow model. In this case, the mesh size used in the flow model is 0.5 m in x - direction, 0.8 m in y - direction and 0.4 m in z - direction. The mesh was also refined in the area near the breakwaters and free water surface with a refinement factor of 2. The initial time step for the flow model is set as 0.001 s, which will automatically adjusts itself to satisfy the Courant-Friedrichs-Lewy condition. For the seabed model, the 27-nodes hexahedral elements are adopted to discretize the seabed foundation and the breakwaters. The mesh size used in the seabed model is 3.25 m in x - direction, 3.75 m in y - direction and 1 m in z - direction. The time step for the seabed model is set as 0.5 s.

The three-view drawings of the computational domain are shown in Figure 5.4. It can be seen from the Figure 5.4a that the ocean waves propagate along the positive direction of the x - axis, interacting with the porous seabed and composite breakwaters. The river currents flow from the inland into the ocean via two breakwaters and meet the propagating waves. Five typical locations, including two points that are near to the breakwater heads (location A and B) and three points that locate in front of, between and behind the middle part of the breakwaters (location C, D and E) respectively, are selected as the references points to monitor the flow properties and seabed foundation response, such as surface elevation and dynamic pore pressure, etc. In addition, in order to specifically study the dynamic seabed foundation responses around two breakwater heads under the 3D wave/current loading, two circles with a radius of 25 m that centred in two breakwater heads respectively are selected as the study areas, as indicated by the dashed lines.

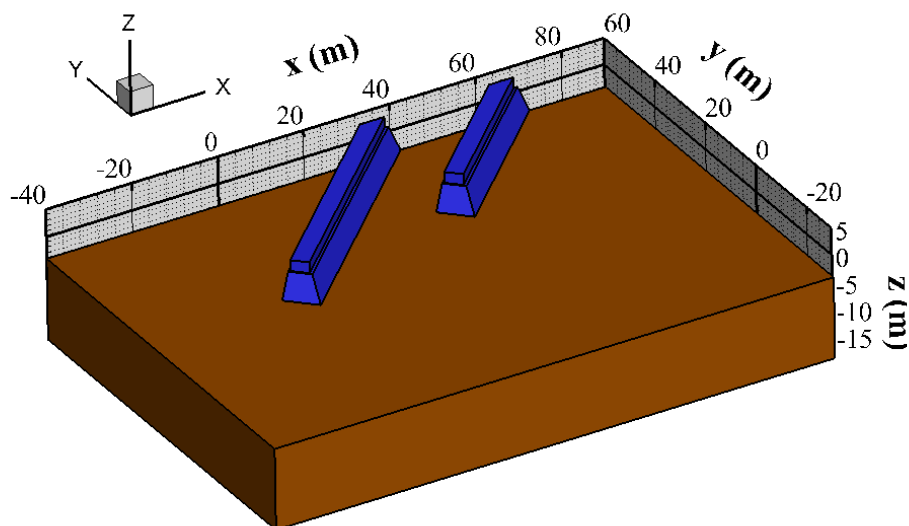


Figure 5.2 The computational domain of the 3D numerical study I.

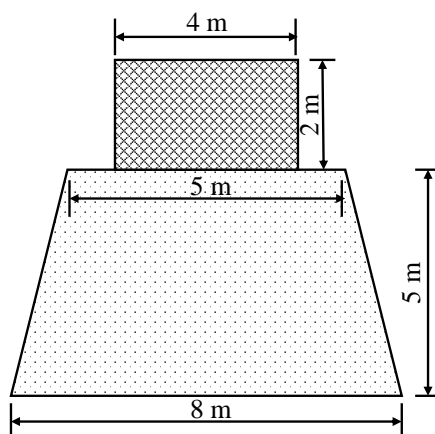


Figure 5.3 The sketch of the cross section of the composite breakwater.

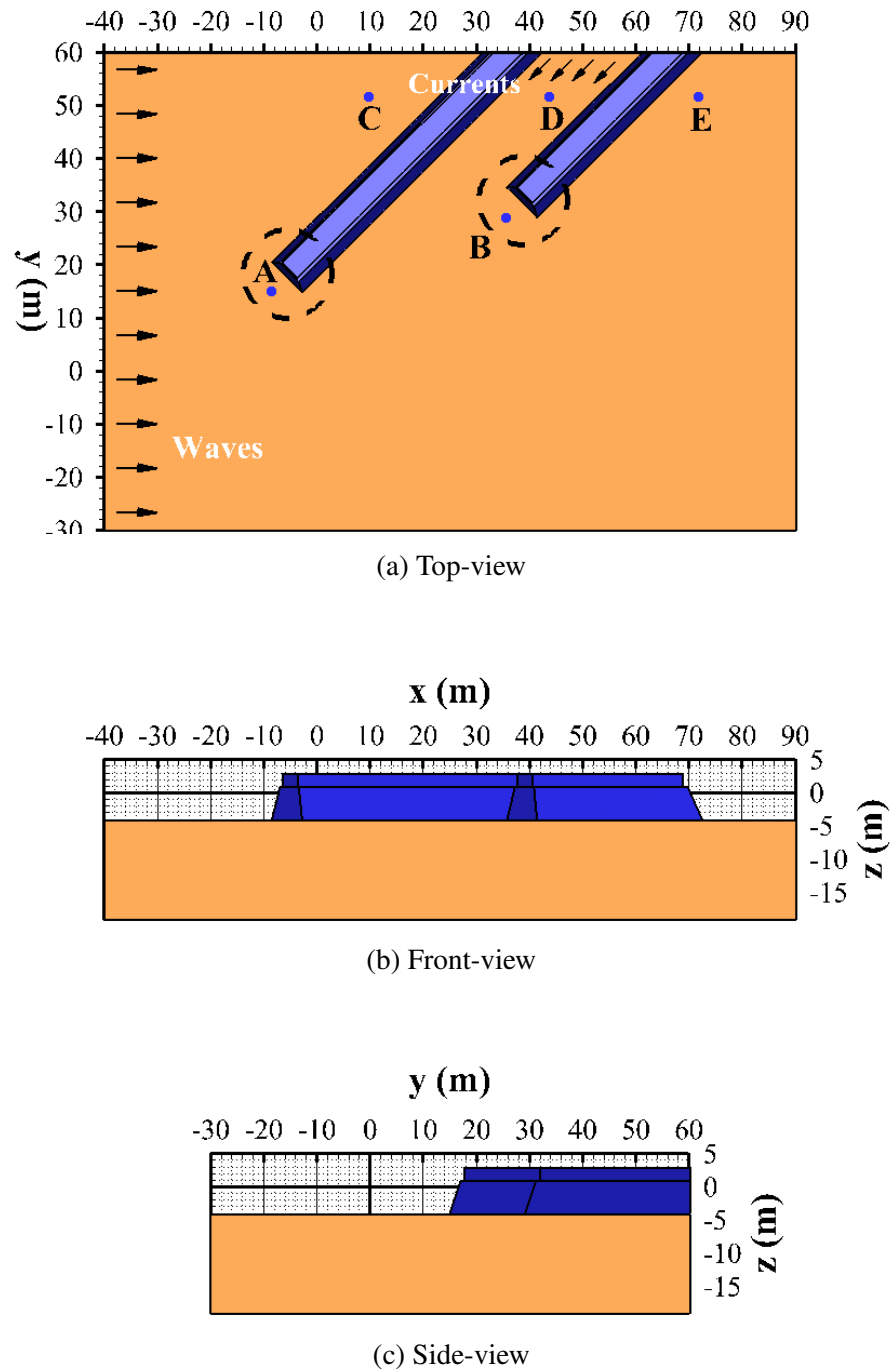


Figure 5.4 The three-view drawings of the computational domain of the 3D numerical study I.

The following boundary conditions are applied for the numerical simulation:

For all the surfaces covered with water, including all the surfaces of seabed (except the region below the breakwaters) and the breakwaters (except the surface at $y = 70$ m), the pore pressure is equivalent to the wave induced pressure obtained from flow model, which is the sum of wave induced hydrodynamic pressure and hydrostatic pressure:

$$p_s(x, y, z; t) = p_b(x, y, z; t) \quad (5.1)$$

For the bottom of the porous seabed foundation, a rigid and impermeable boundary is adopted, which means the degrees of freedom in all directions are restricted, zero displacements occur at the bottom of seabed foundation ($z = -L_z$):

$$u_s = v_s = w_s = 0 \quad \text{and} \quad \frac{\partial p_s}{\partial z} = 0 \quad (5.2)$$

For the four lateral sides of the computational domain, the degrees of freedom in x -direction are restricted for the $x = -40$ m and $x = 90$ m planes, and for the planes at $y = -30$ m and $y = 60$ m, the degrees of freedom in y -direction are restricted, therefore, the displacements are fixed in the corresponding directions:

$$u_s = 0 \quad \text{at } x = -40 \text{ m and } x = 90 \text{ m} \quad (5.3)$$

$$v_s = 0 \quad \text{at } y = -30 \text{ m and } y = 60 \text{ m} \quad (5.4)$$

The input parameters of the numerical simulations for this study are listed in Table 5.1. In this study, two constitutive models, poro-elastic model and poro-elastoplastic model (Pastor-Zienkiewicz mark III model), are adopted to analyse the three-dimensional behaviour of seabed foundation around breakwaters under combined wave and current loading. Parameters for both constitutive models are given. For PZIII model, two sets of parameters are presented, each representing the dense soil and loose soil, respectively. These two sets of parameters were obtained from Zienkiewicz et al. (1999) for Nevada sand. The difference of the predicted wave/current induced seabed foundation response between two constitutive models will be illustrated by comparing the results from two models under the same loading conditions in the later sections. The pros and cons of two different constitutive models will also be discussed.

Table 5.1 The input parameters used in the 3D numerical study I.

Wave characteristics		
Wave period (T)	6.0 s, 5.0 s or 4.0 s	
Wave height (H)	2.0 m, 1.0 m or 2.5 m	
Still water level (d)	4.0 m, 6.0 m or 8.0 m	
River currents velocity (U_0)	1.0 m/s, 0.8 m/s, 0.6 m/s or 0.0 m/s	
Breakwater characteristics		
	Caisson	Rubble mound
Young's modulus (E)	1.0×10^{10} Pa	1.0×10^8 Pa
Poisson's ratio (μ_s)	0.25	0.33
Permeability (k_s)	-	8.9×10^{-2} m/s
Porosity (n_s)	-	0.5
Seabed foundation properties		
Permeability (k_s)	10^{-5} m/s, 10^{-7} m/s or 10^{-3} m/s	
Porosity (n_s)	0.3	
Degree of saturation (S_r)	98 %, 95 % or 93 %	
Relative density (D_r)	40 % or 60 %	
Elastic parameters		
Young's modulus (E)	2.0×10^7 Pa	
Poisson's ratio (μ_s)	0.333	
Parameters for PZIII Model		
	dense sand	loose sand
M_g	1.32	1.15
M_f	1.3	1.035
α_f	0.45	0.45
α_g	0.45	0.45
K_{evo}	2000.0 kPa	770.0 kPa
G_{eso}	2600.0 kPa	1155.0 kPa
β_0	4.2	4.2
β_1	0.2	0.2
p'_0	4.0 kPa	4.0 kPa
H_0	750.0	600.0
H_{U0}	40000.0 kPa	40000.0 kPa
γ_u	2.0	2.0
γ_{DM}	4.0	0.0

5.2 Flow field around breakwaters

In this study, the flow model is based on olaFlow (Higuera, 2015), which is used to simulate the generation and propagation of waves as well as the outflow of river currents via breakwaters. The interactions between the wave/current and breakwaters have also been taken into consideration with fluid exchange between the wave/current and pore water within the breakwater rubble mound bases. In addition, the active wave absorption is adopted in olaFlow to eliminate the undesired reflected wave within a limited computational domain. The waves/currents condition is considered as: wave period (T) equals to 6 s, wave height (H) equals to 2 m, water depth (d) equals to 4 m and the velocity of currents (U_0) equals to 1 m/s along the direction of the breakwaters. Since the one-way coupling algorithm is adopted between the flow and seabed models, an accurate simulation of the wave/current-breakwater interaction in flow model is the prerequisite for correctly assessing the seabed foundation stability in the seabed model. Therefore, the properties of the flow field will be firstly examined.

5.2.1 Wave profile and surface elevation

Figure 5.5 shows the free surface around the breakwaters in one wave period (from $t = 300$ s to $t = 306$ s). The z -axis is stretched by a scale factor of 2 for better viewing. Four typical slices along the y -axis are selected ($y = 50$ m, 25 m, 0 m and -30 m) to illustrate the three-dimensional wave-current-breakwaters interaction. It can be seen from the figures that four main zones have been formed as the propagating waves approach obliquely on the breakwaters, which are the first zone in front of first breakwater with the standing waves, the second zone between two breakwaters with the diffracted waves and river currents, the third zone near to the breakwater heads with the progressive waves and the river currents and the fourth zone that behind the second breakwater. Most of the waves are reflected back by the first breakwater and interact with the subsequent incident waves, which forms the standing wave with a large wave height in the first zone. For the second and third zones, the incident waves, reflected waves, diffracted waves and the river currents exist simultaneously with a complex interaction mechanism. The three-dimensional model has the ability to simulate this kind of situation. Due to the blockage effect of the breakwaters, the water surface in the fourth zone is basically stable. It is also worth noting that, comparing the slice No.3 and No.4, a slight difference in the wave shape could be observed between two breakwaters where the river current comes out. It indicates that the currents might have an impact on the wave field transformation.

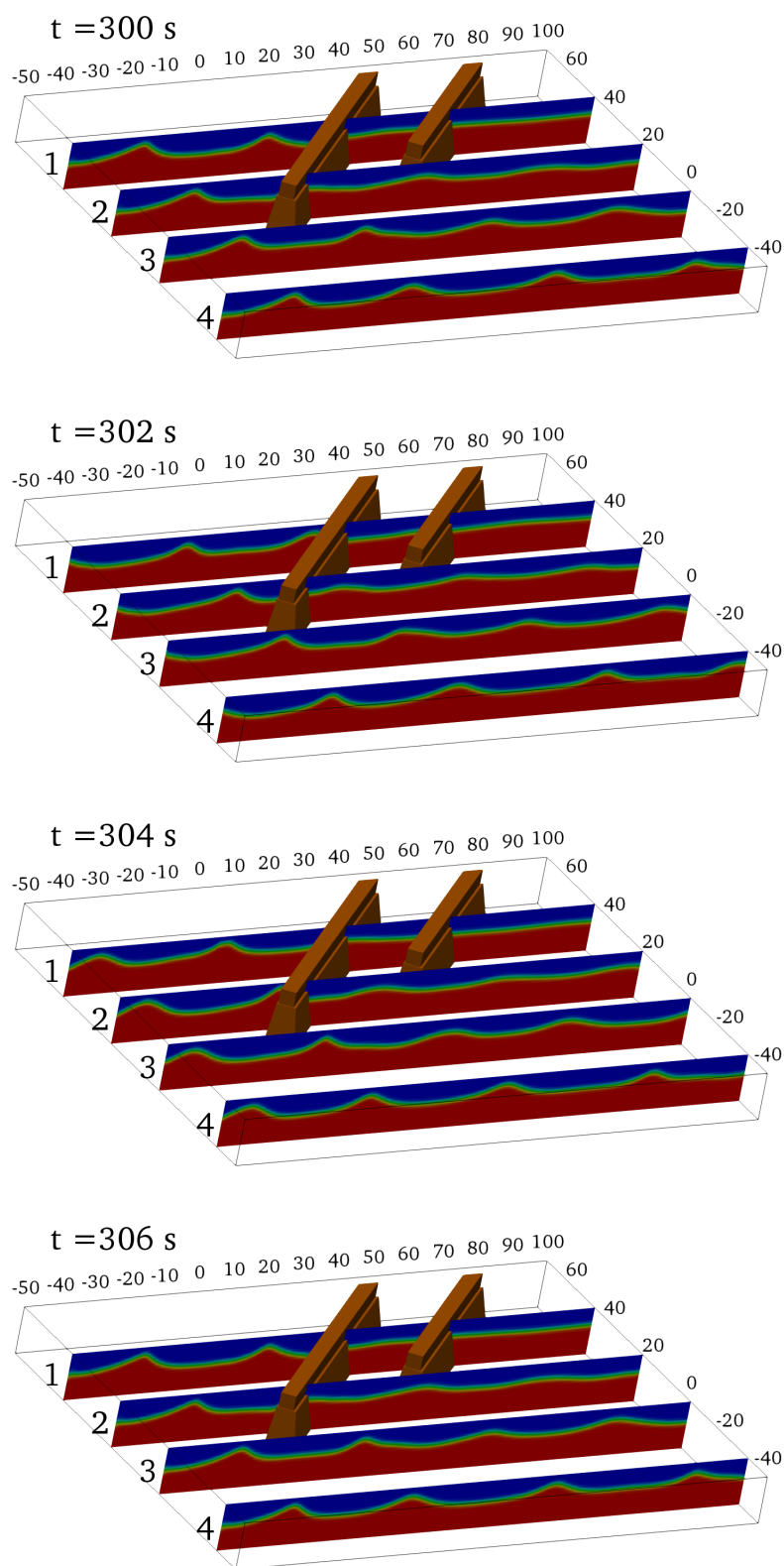
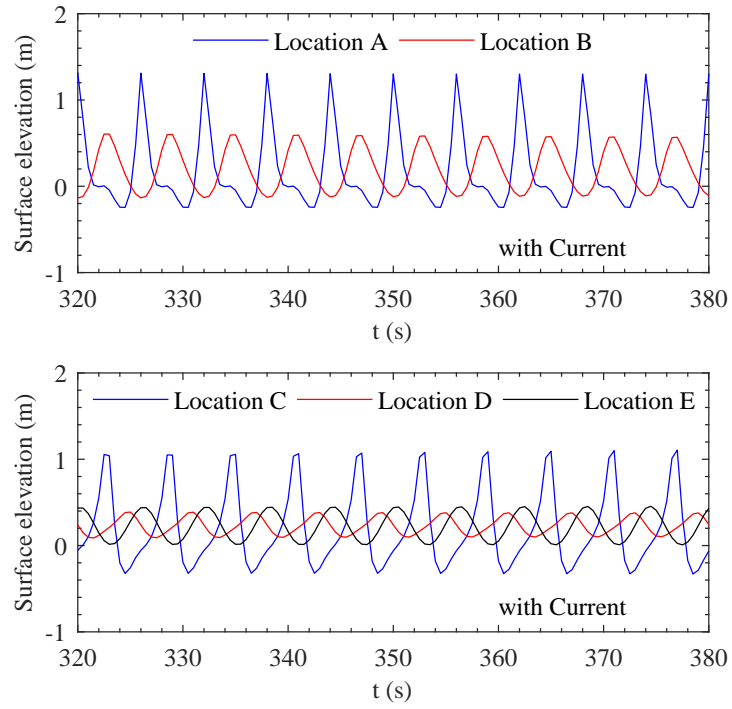


Figure 5.5 The free surface around the breakwaters at $t = 300$ s, 302 s, 304 s and 306 s.

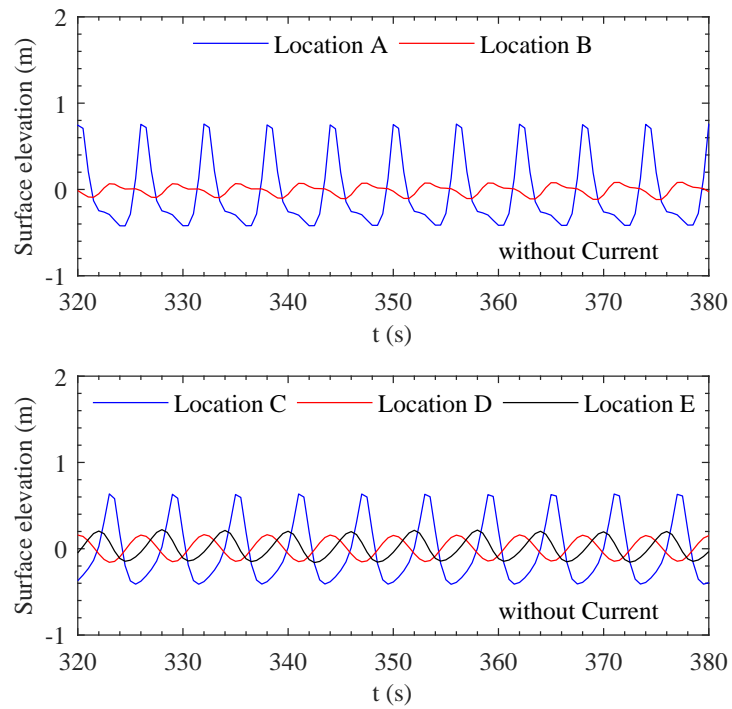
In order to have a more intuitive and quantified illustration, the time series of surface elevation at five monitored locations (A, B, C, D and E) are presented in Figure 5.6. A case removing the river currents between the breakwaters is also presented to show the impact of river currents on the surface elevation. It can be seen from the figures that for the locations near to the breakwater heads (location A and B), the surface elevation oscillation near to the first breakwater (location A) is larger than that near to the second breakwater (location B), the amplitude ratio is more than twice, especially for the case without currents, the surface elevation oscillation near to second breakwater is even smaller. What's more, the non-linearity of the wave shape at these two locations can be observed. This is due to the complex interactions among the incident, reflected, diffracted waves, currents and breakwater heads. For the locations in front of, between and behind the breakwaters (location C, D and E), the largest surface elevation oscillation occurs at location in front of the first breakwater (location C), where the momentary liquefaction is more likely to happen due to the large oscillatory amplitude. In addition, comparing Figure 5.6a and 5.6b, it can be found that the presence of the river currents makes the surface elevation oscillation increase significantly at all locations. At the same time, it increases the non-linearity of the wave shape, making the wave crest sharper. Generally, the presence of the river currents will make the flow field more complicated and severe, which has a potential to further affect the breakwater foundation stability.

5.2.2 Velocity field

Figure 5.7 and 5.8 illustrate the velocity field in y - and x - directions around breakwaters, respectively. A total of 400 s simulation time was performed in order to achieve a relative stable condition within the flow domain. Four typical moments ($t = 100$ s, 200 s, 300 s and 400 s) from the beginning to the end of simulation are selected to demonstrate the historic changes of the velocity field in the x - y plane. From Figure 5.7, the river currents come out via two breakwaters and meet the propagating waves from the left side can be clearly observed. The presence of the currents could significantly affect the wave transformation and further change the hydrodynamic pressures that acting on the surface of seabed and structures. In this study, the river currents are treated as the stable currents, whose velocity does not change with time and space. The velocity of currents is considered as one of the variables affecting the seabed foundation stability that will be discussed later in the parametric study section. Some positive values of velocity in y - direction ($U_y > 0$) have been observed in Figure 5.7, for example, the areas in front of the first breakwater and behind the first breakwater head. This is because that the breakwaters were set at an angle of 45 degree to the negative



(a) waves with river currents



(b) wave loading only

Figure 5.6 Time series of surface elevation at location A, B, C, D and E in the case: (a) with river currents and (b) without river currents.

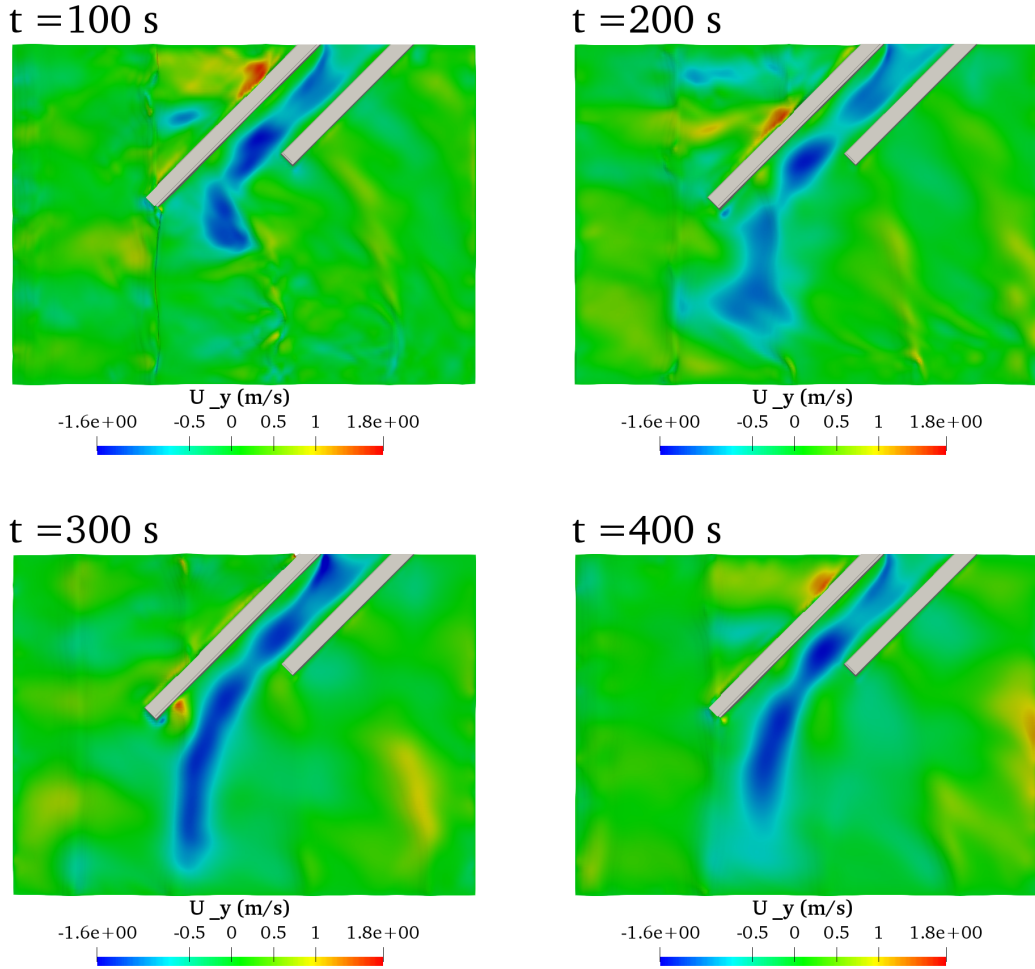


Figure 5.7 The velocity field in y - direction around breakwaters at $t = 100$ s, 200 s, 300 s and 400 s.

direction of the x - axis, when the waves encounter the front face of the first breakwater, a part of waves will travel upward along the breakwater. And the wave diffraction causes the positive U_y behind the breakwater head.

Figure 5.8 shows the x - direction velocity field (U_x) around the breakwaters. It can be clearly seen from the figure that the breakwater can significantly reduce U_x behind the breakwaters, indicating the function of the breakwaters that prevent the wave from invading the area behind the breakwaters. The diffracted wave components can be easily found at the region behind the first breakwater head and near to the second breakwater head. In addition, it can also be found that the currents along the breakwaters can reduce U_x in the nearby region.

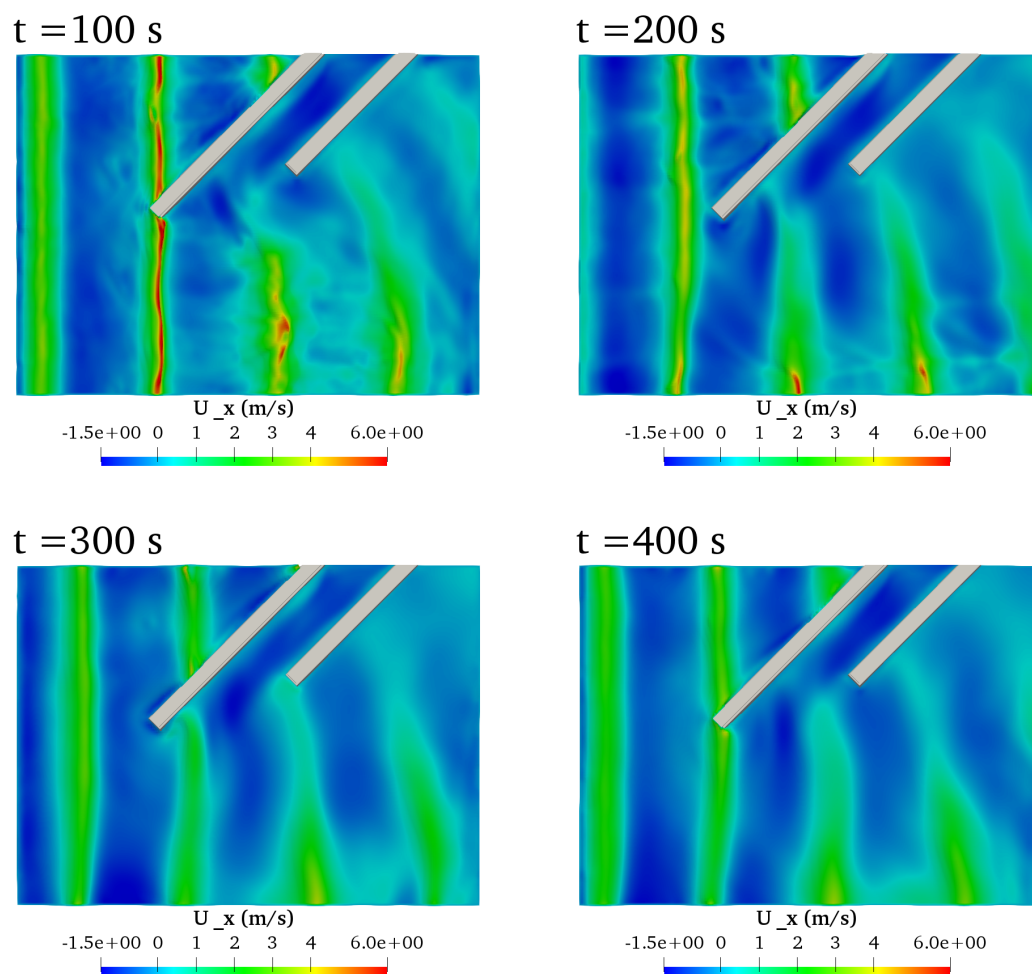


Figure 5.8 The velocity field in x - direction around breakwaters at $t = 100$ s, 200 s, 300 s and 400 s.

5.2.3 Hydrodynamic pressure

As introduced in Section 3.3, the coupling algorithm adopted between the flow model and seabed model is based on the common boundary between two sub models: the hydrodynamic pressure extracted from the flow model will be applied to the surface of seabed and structure through the data exchange port. Therefore, basically, the interaction effects of the wave-current-breakwaters is reflected in the form of hydrodynamic pressure that transmitted from flow model to the seabed model. Figure 5.9 illustrates the hydrodynamic pressure around the breakwaters extracted from the bottom of the flow model in one complete wave period from $t = 300$ s to $t = 306$ s. This wave period is at the late stage of the simulation, the flow field around the breakwaters was already in a relatively stable state. In addition, $t = 300$ s and $t = 306$ s are both the beginning of a new wave cycle. Therefore, there is no significant difference of the hydrodynamic pressure condition between $t = 300$ s and 306 s. It can be seen that the main distribution of the hydrodynamic pressure is related to the propagation of waves. The pattern of hydrodynamic pressure moves along with waves travelling and is distributed by the alternatively positive and negative variations. Due to the complicated three-dimensional wave-current-breakwater interactions, the strongest hydrodynamic pressure appears in front of the first breakwater and near to the first breakwater head, the weakest one occurs behind and between the breakwaters, which is the results of protection effects of the breakwaters. Hence, the first breakwater faces a greater risk of instability and collapse compared with the second breakwater. Meanwhile, it can be found that the hydrodynamic pressure distribution is not uniform in the three-dimensional wave/current condition due to the presence of reflected waves and diffracted waves. In particular, the hydrodynamic pressure zones formed behind the breakwaters present the more dispersed distribution feature. All these phenomena cannot be provided by the 2D model.

5.3 Consolidation of the porous seabed foundation

The seabed foundation around the breakwaters will undergo a long-term consolidation process under the hydrostatic pressure and the self-weight. The consolidation is actually a process of dissipating the excess pore pressure within the seabed foundation around breakwaters, shrinking the soil skeleton and increasing the soil bearing capacity. The state after the completion of consolidation process will be used as the initial condition for the dynamic analysis of the seabed foundation response. According to the liquefaction criteria proposed by Tsai (1995), the soil will be liquefied if the averaged dynamic effective stresses is greater than the averaged initial effective stresses. In general, after consolidation process, the initial

5.3 Consolidation of the porous seabed foundation

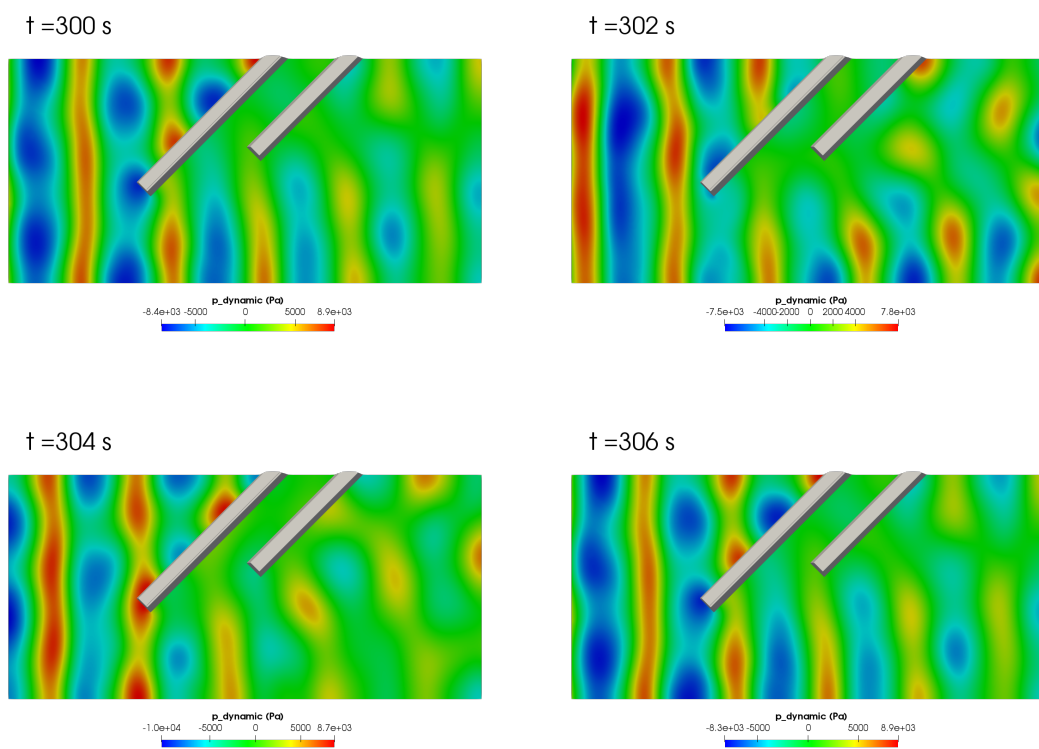


Figure 5.9 The hydrodynamic pressure acting on the seabed surface around breakwaters at $t = 300$ s, 302 s, 304 s and 306 s.

5.4 Dynamic soil response in the seabed foundation

effective stress below the breakwaters increases, which an overestimation of liquefaction can be assessed in the region below the breakwaters when the consolidation has not been taken into consideration. Therefore, when studying the dynamic responses and evaluating the stability (i.e., liquefaction phenomenon) of seabed foundation around breakwaters, it is necessary to consider the consolidation process.

Figure 5.10 illustrates the distribution of pore pressure, effective stresses (σ'_x , σ'_y and σ'_z) and shear stresses (τ_{xy} , τ_{yz} and τ_{zx}) on a typical plane ($y = 30$ m) after the completion of consolidation process. It can be seen from the first figure that the pore pressure layered uniformly from top to the bottom, which indicates that there is no excess pore pressure left and the consolidation process has been completed. It can be also found from the figures that the stress state in the region below or near to the breakwaters has been significantly affected. Due to the compression effect of the breakwater gravity, the effective stresses all obviously increase under each breakwater and appear as the layered structure, especially the effective normal stress, the magnitude reaches up to 800 kPa. For the shear stresses, τ_{xy} and τ_{zx} concentrate at two side of each breakwater while τ_{yz} appears as a whole region at the bottom of the seabed just below two breakwaters. Comparing the three shear stresses, τ_{zx} is the dominant stress whose magnitude can reach up to 250 kPa, while the magnitude of τ_{xy} is very small which is less than 700 Pa.

5.4 Dynamic soil response in the seabed foundation

Once the pre-consolidation process has been completed, the consolidation state will be used as the initial stress state for the dynamic analysis of seabed response under the wave/current loading. The dynamic response of seabed foundation around the breakwaters plays an important role in the stability of the structures. When the waves propagate on the seabed surface, a complex change of pore pressure, effective stress and displacement within the seabed foundation is caused by the cyclic wave loading, especially for the present study, which involves the three-dimensional seabed-breakwaters-waves-current interactions, the situation becomes more complicated. The extreme situation of the wave/current induced dynamic response is the soil liquefaction. When the soil liquefaction occurs, the seabed loses its ability to carry any load, which leads to the instability failure of the upper structures. Therefore, a clear understanding of the wave/current induced dynamic seabed response mechanism is the precondition for assessing the foundation stability. For the wave/current induced liquefaction within the porous seabed foundation, a detailed discussion will be covered in later section.

5.4 Dynamic soil response in the seabed foundation

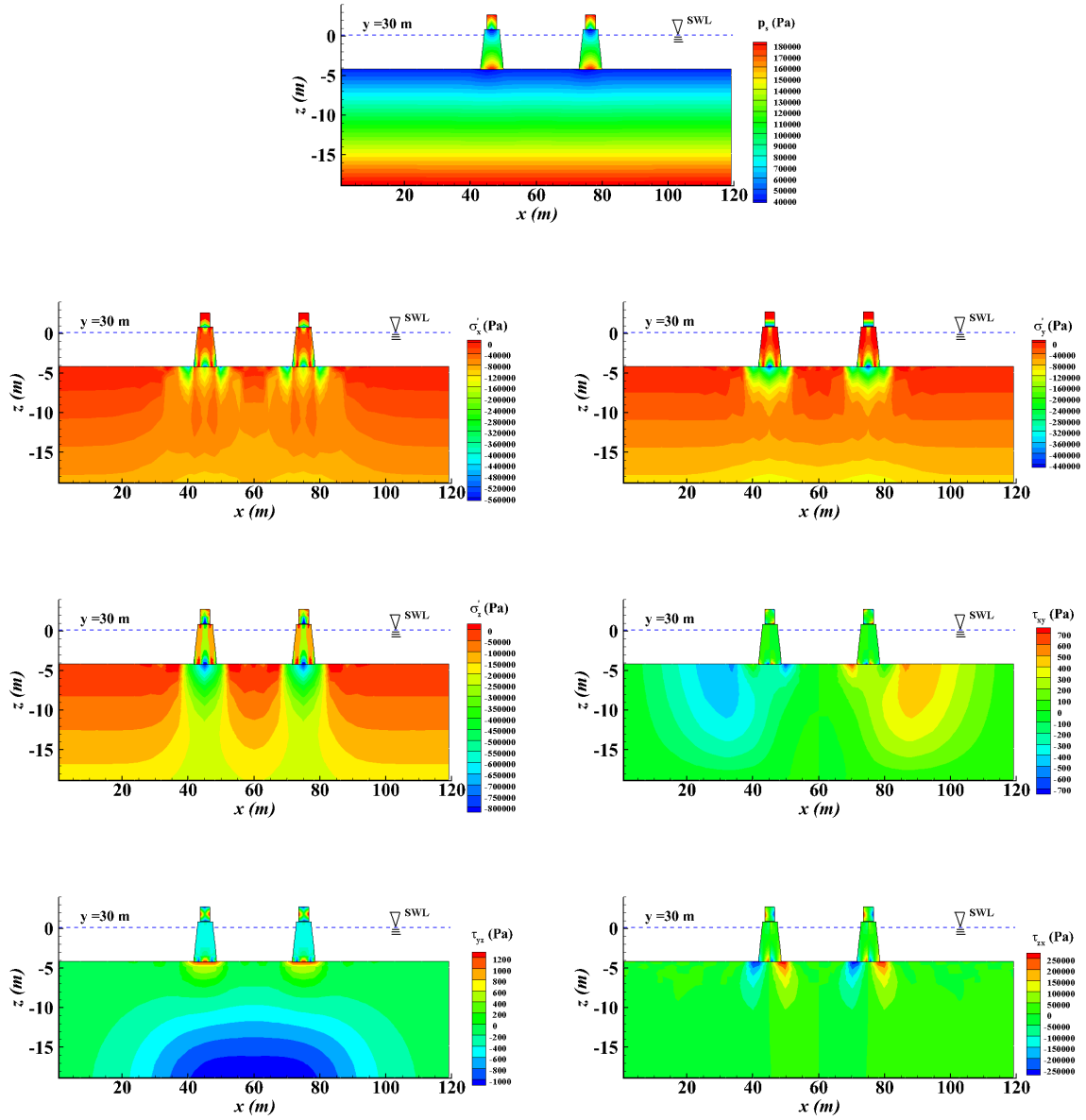


Figure 5.10 Distribution of pore pressure (p_s), effective stresses (σ'_x , σ'_y and σ'_z) and shear stresses (τ_{xy} , τ_{yz} and τ_{zx}) on plane $y=30$ m after consolidation process.

5.4 Dynamic soil response in the seabed foundation

In this section, the 3D seabed model with both poro-elastic and poro-elastoplastic constitutive models is adopted to investigate the dynamic response of the seabed foundation around breakwaters under the combined wave and current loading on the basis of completion of the seabed consolidation process. The results predicted using the different constitutive models under the same condition will be compared to further understand the different mechanisms of dynamic soil response. As reviewed in Chapter 2, two mechanisms of dynamic soil response have been observed in the laboratory experiments and field measurements: oscillatory mechanism and residual mechanism. The oscillatory soil response is generated by the oscillatory excess pore pressure and accompanied by the pore pressure amplitude damping and phase lag. The distribution of the periodical oscillatory soil response is directly related to the shapes of free surface. This mechanism is mainly dominated by the elastic properties of the soil, which can be simulated using the poro-elastic constitutive model. While the residual soil response is mainly due to the plastic soil behaviour. It is usually accompanied by the build-up of pore pressure and reduction of the effective stress, which are caused by the contraction of relative loose soil skeleton with poor drainage condition under the long-term cyclic shear stress within the soil. The residual mechanism can be simulated using the poro-elastoplastic constitutive model. This section will analyse the wave/current induced oscillatory and residual dynamic soil response in the elastic and plastic seabed foundation respectively from the perspective of time distribution and spatial distribution.

5.4.1 Time series of dynamic soil responses

Figure 5.11 to 5.13 demonstrate the time series of dynamic soil response, including pore pressure (p_s), effective stress (σ'_x , σ'_y and σ'_z) and shear stress (τ_{xy} , τ_{yz} and τ_{zx}), at three typical locations: location A ($x = -10$ m, $y = 15$ m, $z = -6$ m) which is near to the first breakwater head; location C ($x = 10$ m, $y = 52$ m, $z = -6$ m) which is in front of first breakwater and location D ($x = 45$ m, $y = 52$ m, $z = -6$ m) which is between two breakwaters. Both the residual soil response (red line) and oscillatory soil response (blue line) are presented in these figures. The difference between the residual soil response predicted by the poro-elastoplastic model and the oscillatory soil response predicted by poro-elastic model is obvious. The residual soil response consists of two parts: one is the periodic oscillatory part as a result of wave/current loading; and the other one is the residual part resulting from the continual cyclic loading, which is usually accompanied by the build-up of pore pressure/shear stress and the reduction of effective stress. While the oscillatory soil response only has the oscillatory component. Therefore, for different kind of soils, with different expected results, it is very important to use a more appropriate constitutive model for the simulation.

5.4 Dynamic soil response in the seabed foundation

In Figure 5.11 (location A which is near to the breakwater head), it can be found that the residual pore pressure (red line) continues to increase until it remains at a stable value after $t = 260$ s. The accumulative amount of pore pressure reaches 25 kPa. While the oscillatory pore pressure (blue line) only oscillates around the initial value. For the residual effective stresses, they reduce from the initial compressive state and approach zero after around $t = 260$ s. According to the definition of soil liquefaction, location A ($x = -10$ m, $y = 15$ m, $z = -6$ m) has been liquefied at $t = 260$ s after the effective stress become zero. σ'_z has the largest initial value which is at around 23 kPa compared to σ'_x and σ'_y at around 11 kPa. Also, since the wave is propagating along the x - direction, the oscillatory component of σ'_y is quit small. Similar to the oscillatory pore pressure, the oscillatory effective stresses only vibrate around the initial values. For the shear stress, the dominant factor is τ_{zx} . τ_{xy} and τ_{yz} have relative small amplitude and basically oscillate near zero. The residual τ_{zx} has increased at the beginning then decreased to zero as approaching to the soil liquefaction. This kind of trend also reflects the mechanism of residual soil response: at the initial stage, the shear force gradually increased due to the cyclic wave/current loading, making the soil skeleton compressed. However, when the soil is liquefied, the soil loses its strength and appears as a liquid state, hence the shear stress disappears. Meanwhile, the oscillatory τ_{zx} predicted by the poro-elastic model has no such trend, only oscillating around zero which represents the feature of an elastic seabed foundation.

The dynamic soil response at $x = 10$ m, $y = 52$ m, $z = -6$ m (location C which is in front of the breakwater) are present in Figure 5.12. This point is nearly approaching the liquefaction state at the end of simulation. However, for location D ($x = 45$ m, $y = 52$ m, $z = -6$ m; between the two breakwaters) shown in Figure 5.13, due to the protection effect from breakwaters, it is far from the liquefaction status. The non-linearity of the soil response at this point is also more obvious. With the pore pressure build-up and effective stress reduction, the seabed foundation at this point is becoming more and more unstable undoubtedly. However, it has not been liquefied since the effective stress still remains a relative large value, for example, σ'_z remains over 14 kPa after $t = 400$ s. Also, τ_{zx} keeps accumulating without an attenuation appears. The above analysis explains the historic curves of dynamic soil response at different locations around breakwaters, compares the differences between two mechanism obtained from two constitutive models, gives the relationship between the variables, and concludes that location A was first liquefied.

Figure 5.14 and 5.15 show the wave/current induced displacement, including x - direction displacement (u_s), y - direction displacement (v_s) and z - direction displacement (w_s), at location A, C and D within the poro-elastoplastic seabed foundation and poro-elastic seabed foundation, respectively. It can be seen from Figure 5.14 that each location sways in the

5.4 Dynamic soil response in the seabed foundation

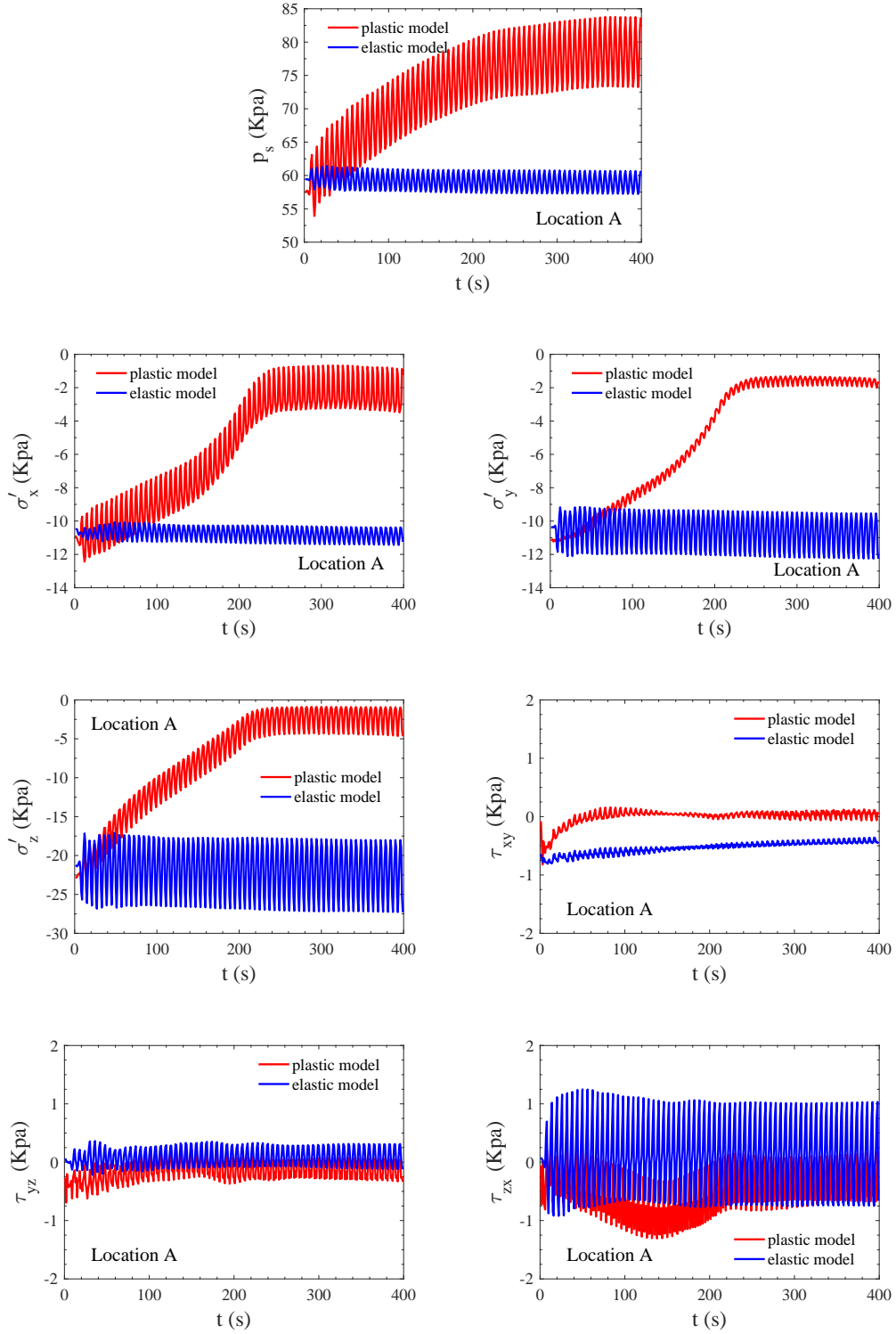


Figure 5.11 Time series of the dynamic soil responses, including pore pressure (p_s), effective stresses (σ'_x , σ'_y and σ'_z) and shear stresses (τ_{xy} , τ_{yz} and τ_{zx}) at location A ($x = -10$ m, $y = 15$ m, $z = -6$ m) near to first breakwater head.

5.4 Dynamic soil response in the seabed foundation

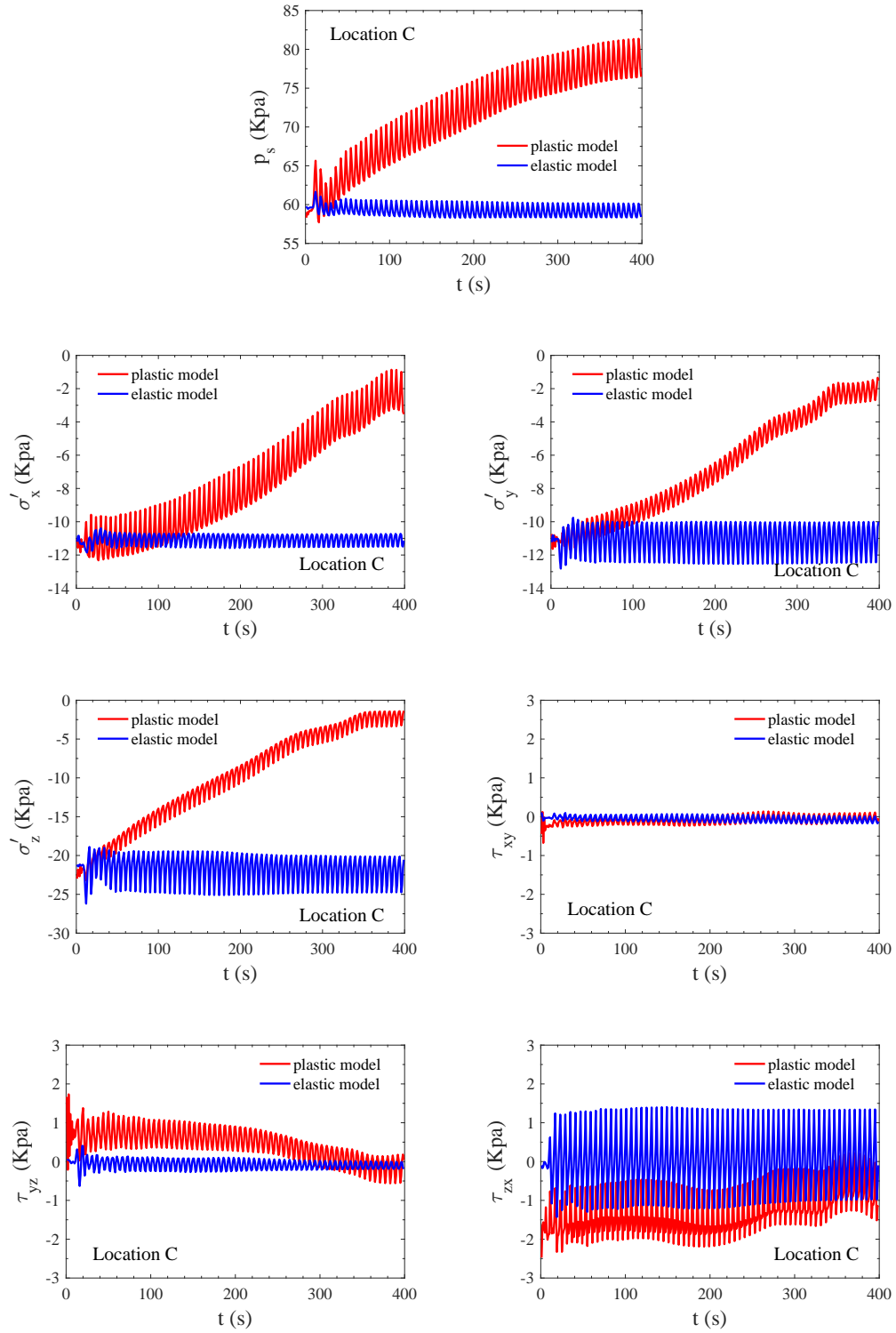


Figure 5.12 Time series of the dynamic soil responses, including pore pressure (p_s), effective stresses (σ'_x , σ'_y and σ'_z) and shear stresses (τ_{xy} , τ_{yz} and τ_{zx}) at location C ($x=10$ m, $y=52$ m, $z=-6$ m) in front of first breakwater.

5.4 Dynamic soil response in the seabed foundation

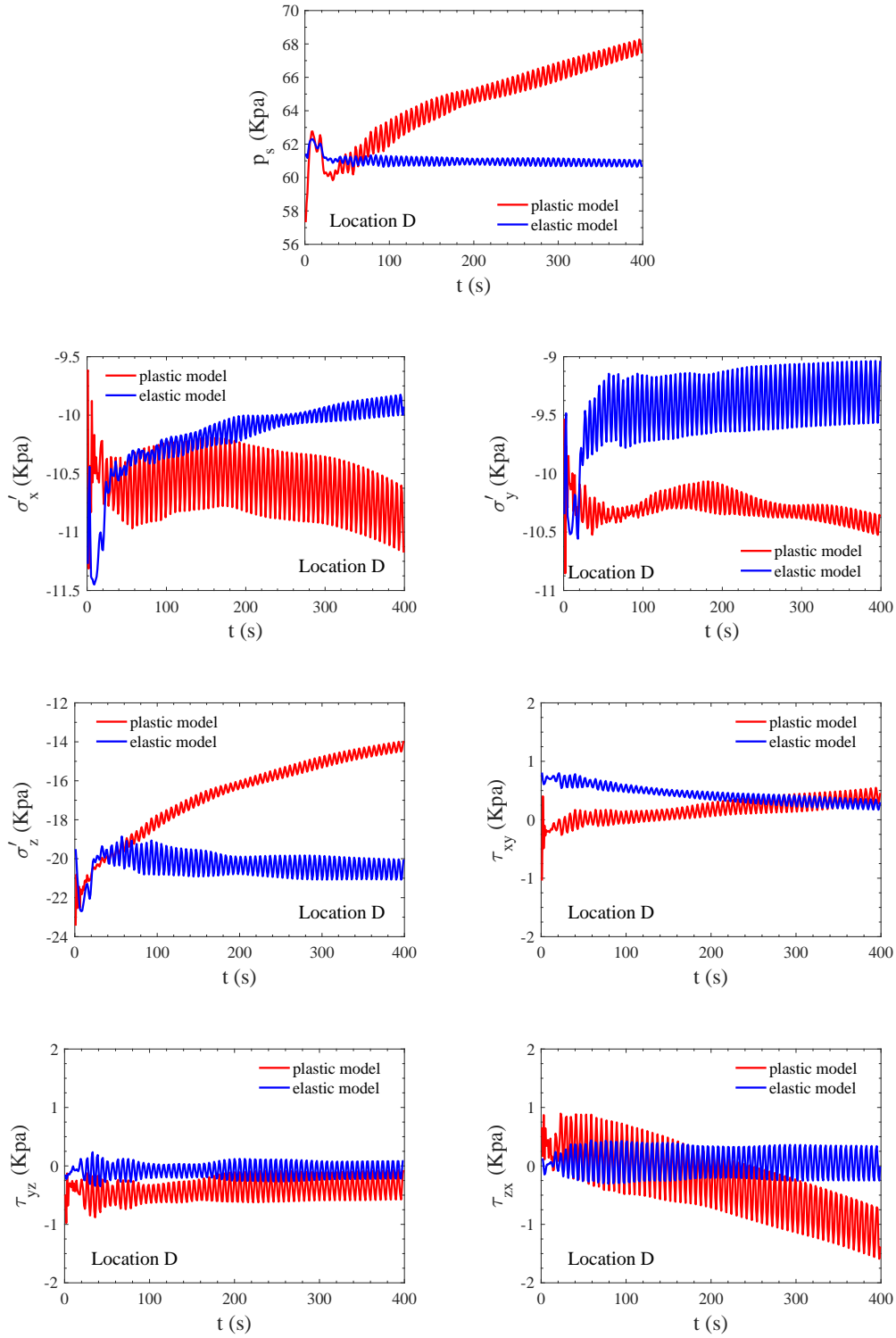


Figure 5.13 Time series of the dynamic soil responses, including pore pressure (p_s), effective stresses (σ'_x , σ'_y and σ'_z) and shear stresses (τ_{xy} , τ_{yz} and τ_{zx}) at location D ($x = 45$ m, $y = 52$ m, $z = -6$ m) between two breakwaters.

5.4 Dynamic soil response in the seabed foundation

corresponding direction as the cyclic loading acting on the seabed surface. The displacement in the z — direction is obviously the dominant one, whose magnitude is about 40 mm at location A, 25 mm at location C and 10 mm at location D. It also can be observed that, at point in front of first breakwater head (location A), there is a clear accumulative displacement to the positive x — direction (u_s) and negative z — direction (w_s), the accumulation of u_s and w_s can both reach up to 40 mm. The similar trend could be found at location C which is located in front of the first breakwater. It indicates that the first breakwater has settled downwards and tilted rightwards permanently under the wave/current loading, which has huge impacts on its stability. At location D, due the protection from the breakwater, the vibration magnitude at this location decreases significantly. Additionally, there is accumulated displacement towards up and right at location D. The possible reason is that due to the subsidence of the first breakwater to the lower right direction, the soil between two breakwaters is squeezed which may cause the upward and rightward displacement. For the y — direction displacement (v_s) at these three locations, the amplitude is small and there is almost no accumulated value.

The displacements at the same locations occurs within a poro-elastic seabed foundation are shown in Figure 5.15. Compared with the results in the poro-elastoplastic seabed foundation, the displacement response mechanism in the poro-elastic seabed foundation is totally different. First of all, it can be clearly seen that there is no accumulative displacement in the elastic seabed, each point only vibrate at its original position. It shows that the elastic seabed foundation does not undergo any permanent deformation. Secondly, the displacement response in the poro-elastic seabed foundation is much weaker than that in the poro-elastoplastic seabed foundation, the amplitude ratio of displacement in elastic and plastic seabed foundation is only 10 %. Since the settlement and tilt could happen to the breakwater that built on the poro-elastoplastic seabed foundation, which is considered as a negative factor for the stability of the breakwater, the poro-elastoplastic model is more advanced than the poro-elastic model when assessing the breakwater foundation stability for certain kinds of soils.

5.4.2 Spatial distribution of dynamic soil responses

Figure 5.16 shows the spatial distribution of wave induced oscillatory pore pressure (p_s) and stress field (effective stresses: σ'_x ; σ'_y ; σ'_z and shear stresses: τ_{xy} ; τ_{yz} ; τ_{zx}) within an elastic seabed foundation around the breakwaters at $t = 300$ s predicted by the poro-elastic model. It can be seen from the pore pressure distribution that the propagating wave trough reaches to the front of the first breakwater at $t = 300$ s, which causes a large negative pore pressure in this region. The negative pore pressure creates the corresponding upward-directed seepage

5.4 Dynamic soil response in the seabed foundation

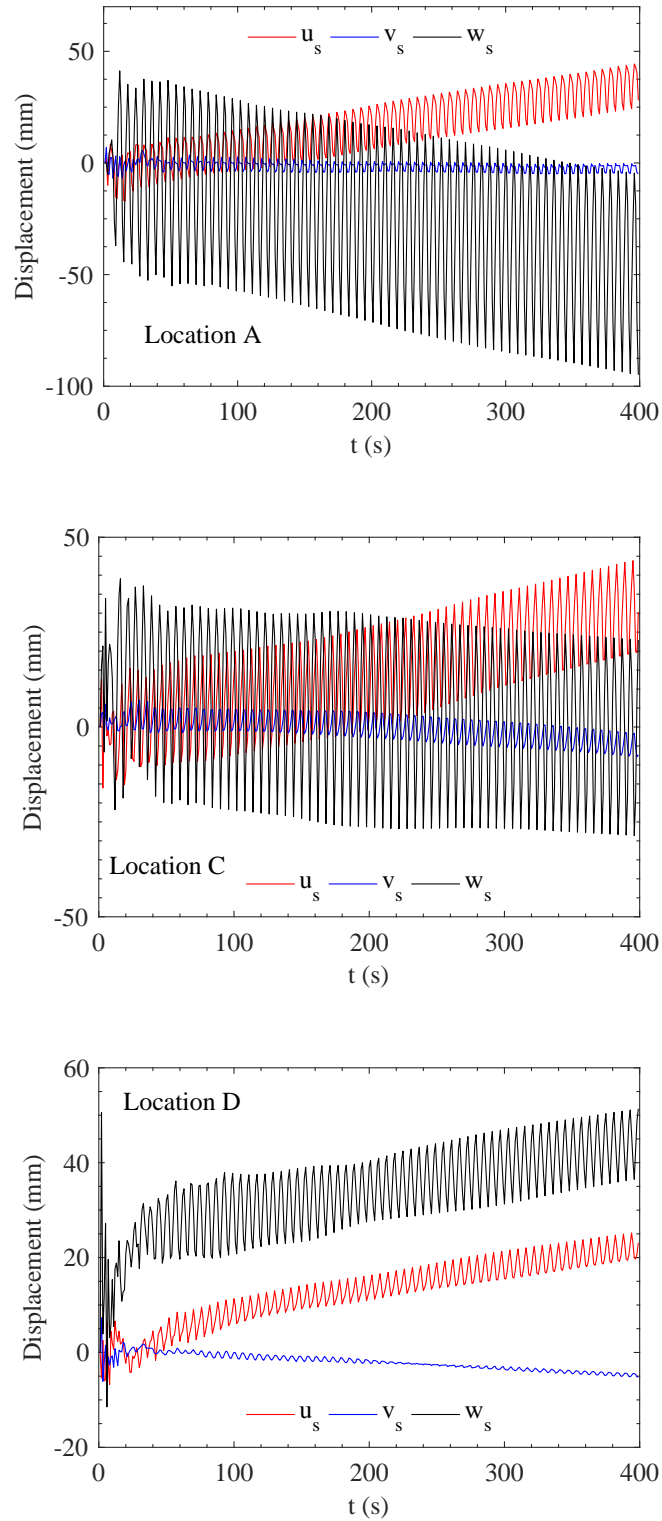


Figure 5.14 Time series of displacements in x - direction (u_s), y - direction (v_s) and z - direction (w_s) at location A ($x = -10$ m, $y = 15$ m, $z = -6$ m), C ($x = 10$ m, $y = 52$ m, $z = -6$ m) and D ($x = 45$ m, $y = 52$ m, $z = -6$ m) within the poro-elastoplastic seabed foundation.

5.4 Dynamic soil response in the seabed foundation

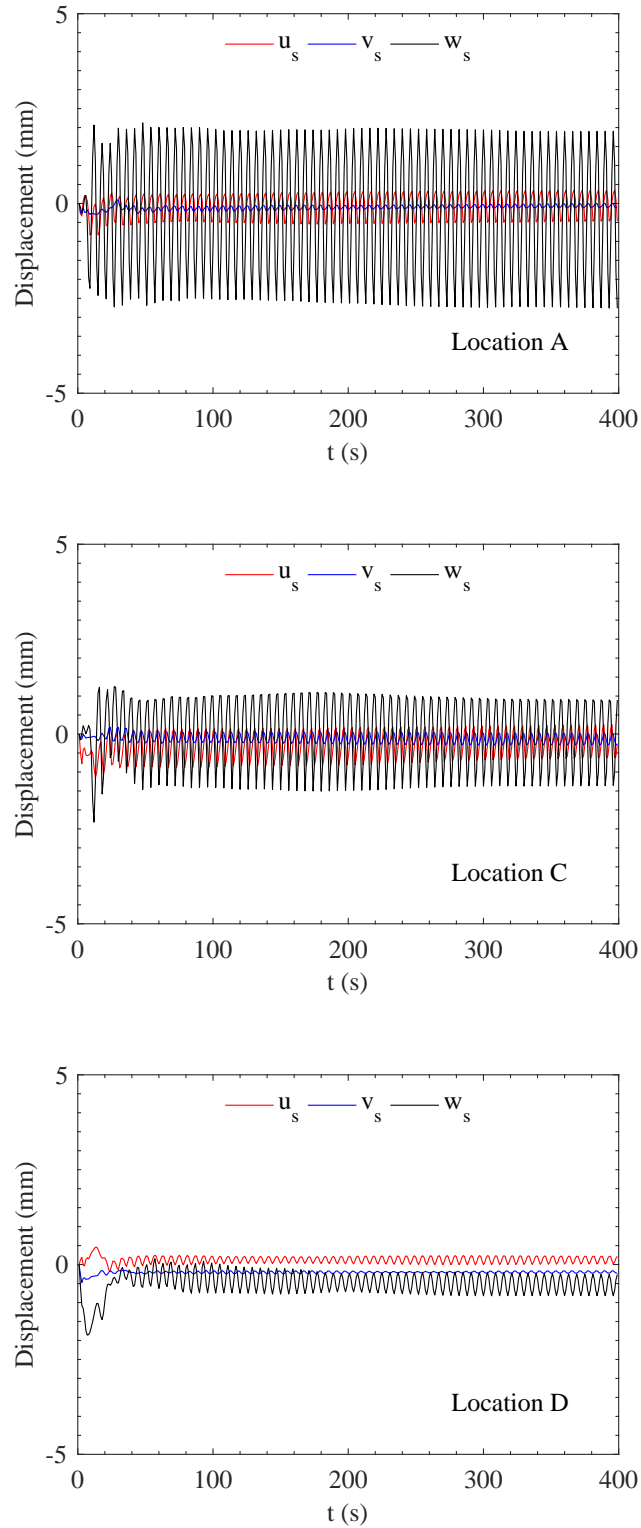


Figure 5.15 Time series of displacements in x - direction (u_s), y - direction (v_s) and z - direction (w_s) at location A ($x=-10$ m, $y=15$ m, $z=-6$ m), C ($x=10$ m, $y=52$ m, $z=-6$ m) and D ($x=45$ m, $y=52$ m, $z=-6$ m) within the poro-elastic seabed foundation.

5.4 Dynamic soil response in the seabed foundation

force in the soil, causing the pore fluid to move upwards, thereby weakening the contact force between the soil skeleton. The stability of seabed foundation in this region is reduced. When the seepage force is greater than the initial effective stress, the momentary liquefaction happens. If the momentary liquefaction zone is just below the breakwater, it poses a threat to the stability of the breakwater. From another point of view, the same conclusion can be drawn based on the spatial distribution of the dynamic effective stress of seabed foundation around the breakwaters. As can be seen from the figures, the dynamic effective stresses are presented by the alternatively positive and negative variations within the seabed foundation due to the wave loading. In the soil under the wave trough, a large positive effective stress is shown, indicating that the soil in this area is being in tension. When the tensile dynamic effective stress is greater than the initial effective stress, the momentary liquefaction occurs. For the areas under the wave crest, as the pore pressure is positive, the seepage force is downward-directed, the dynamic effective stress is in compression, the momentary soil liquefaction is unlikely to happen.

The wave induced shear stresses (τ_{xy} , τ_{yz} and τ_{zx}) mainly locate at the lower part of seabed foundation and they appear on the two side of each breakwater. Comparing all the shear stresses, it can be found that τ_{zx} is the dominant one, whose magnitude reaches up to 5 kPa. The wave induced cyclic shear stress could also be one of the failure factor for the stability of breakwaters. Another phenomenon that is easy to be observed is that the amplitude of dynamic response in the areas in front of and near to the breakwaters is greater than that behind the breakwaters. This is due to the reflection and diffraction effects of the breakwater on the wave transformation. It proves that the breakwaters can effectively block the wave and protect the seabed foundation behind the breakwaters.

Different from the transient/oscillatory soil response, the residual soil response predicted by the poro-elastoplastic model is usually manifested as the build-up of pore water pressure within the seabed foundation. The process of pore pressure build-up involves the permanent deformation of the seabed foundation, which cannot be solved properly by poro-elastic model. Figure 5.17 shows the accumulation of the residual pore pressure within the poro-elastoplastic seabed foundation under the long-term cyclic wave/current loading from $t = 50$ s to $t = 350$ s. It can be clearly seen from the figures that the wave/current induced pore pressure (p_s) at location in front of the first breakwater (the upper slice) and near to the first breakwater head (the lower slice) is increasing and accumulating significantly, from less than 8 kPa at $t = 50$ s to over 28 kPa at $t = 350$ s. The reasons why the pore pressure built up at these two locations are: the wave height increases significantly in front of the first breakwater due to the interaction of the incident wave and reflected wave; and for the location near to the first breakwater head, there is always a cyclic shear stress concentration zone that constantly

5.4 Dynamic soil response in the seabed foundation

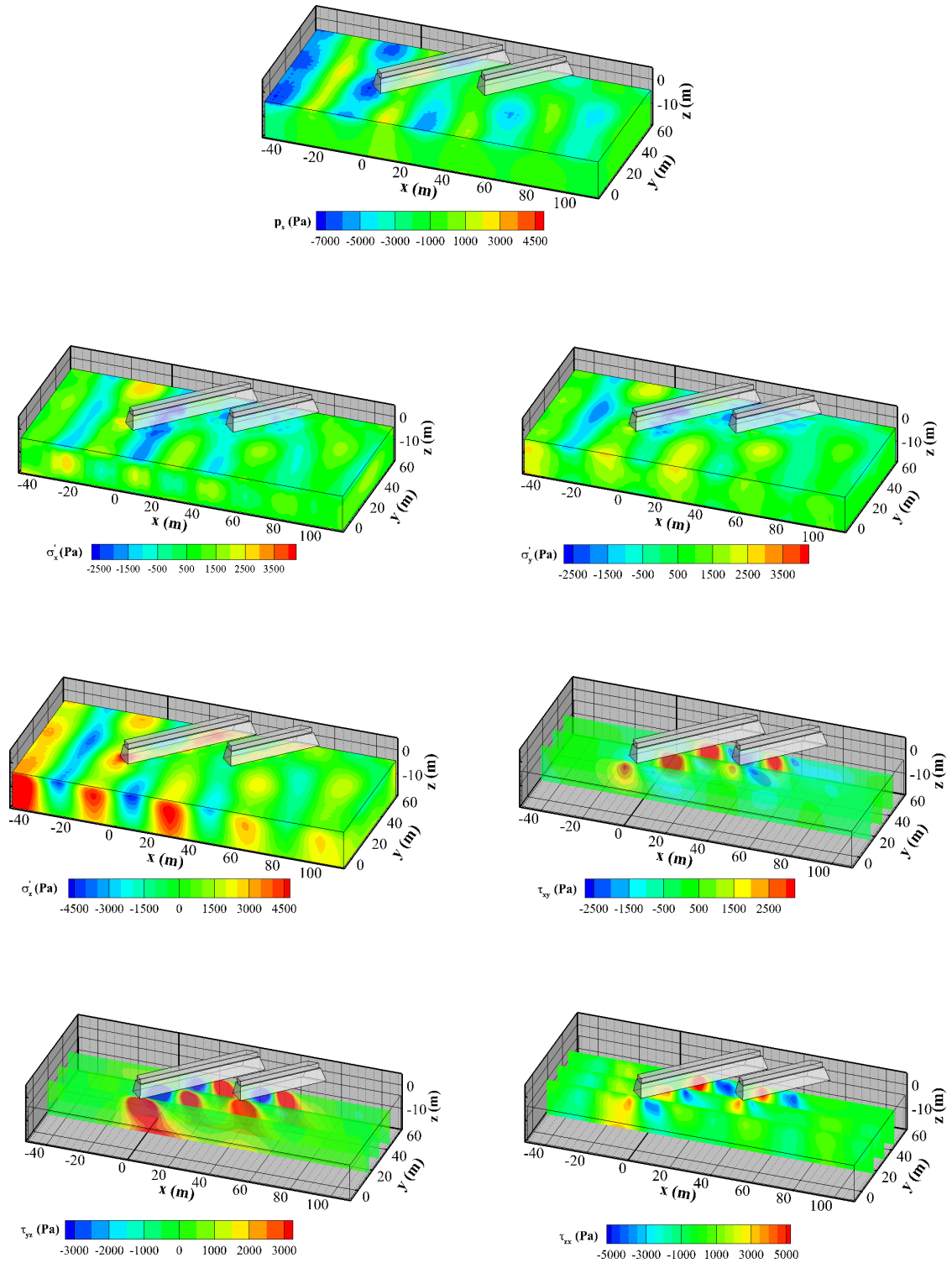


Figure 5.16 Spatial distribution of oscillatory pore pressure (p_s) and stress field (effective stresses: σ'_x ; σ'_y ; σ'_z and shear stresses: τ_{xy} ; τ_{yz} ; τ_{zx}) within an elastic seabed foundation around the breakwaters at $t = 300$ s.

5.4 Dynamic soil response in the seabed foundation

pressurise the soil skeleton. It can also be found that the accumulation of the pore pressure in front of the breakwater is more rapid, intense and obvious than that near to the breakwater head, which indicates that the area in front of the breakwater is more likely to be liquefied. Since these potential liquefaction zones are close to the breakwater foundation, they may pose greater threats to the breakwater stability.

Figure 5.18 illustrates the vertical distribution of the maximum dynamic oscillatory pore pressure within the poro-elastic seabed foundation and the residual dynamic pore pressure at $t = 400$ s within the poro-elastoplastic seabed foundation at location A, location C and location D. The dynamic pore pressure is nondimensionalised by dividing the dynamic wave pressure (p_0) determined by linear wave theory to a first-order. It can be seen from the figures that the difference in outcome of dynamic pore pressure response mechanisms in the two kinds of seabed can be huge. The residual pore pressure at $t = 400$ s along the depth of the plastic seabed is generally much larger than the maximum oscillatory pore pressure, whose simulation time is also 400 s, in elastic seabed. The largest value in the plastic seabed at location A can reach nearly 5 times p_0 , while the largest value in elastic seabed is only half of p_0 . In addition, the vertical distribution trend of dynamic pore pressure in the elastic seabed foundation is that the largest value appears in the upper seabed, and as the depth increases, the dynamic pore pressure gradually decreases. While in the plastic seabed, the largest dynamic pore pressure occurs in the middle part of the seabed and the dynamic pore pressure in the upper and lower seabed is relative small. These kinds of distributions are determined by the mechanisms of dynamic pore pressure response in two kinds of seabed: in elastic seabed, the dynamic pore pressure response is caused by the vertical attenuation of the pore water pressure and phase lag, so the closer to the seabed surface where the dynamic wave pressure is applied, the greater the dynamic pore water pressure; while in the plastic seabed, the dynamic pore pressure at one location is related to the rate of accumulation and the rate of dissipation. The upper seabed has a fast dissipation rate and the lower seabed has a slow accumulation rate, both of them are not prone to generate large dynamic pore pressure. What's more, comparing the results predicted at different locations, it can be found that the breakwaters have huge impact on the vertical distribution of dynamic pore pressure in both seabed foundations. The point near to the first breakwater head (location A) has the strongest response while the point between two breakwaters (location D) has the weakest response. What's more, since location D is between two breakwaters, the non-linearity of the dynamic pore pressure distribution could be observed due to the interaction of different components of waves, currents and breakwaters.

The dynamic pore pressure distribution around two breakwater heads should be the most complex, meanwhile because of the persistence of the cyclic shear stress, the possibility of

5.4 Dynamic soil response in the seabed foundation

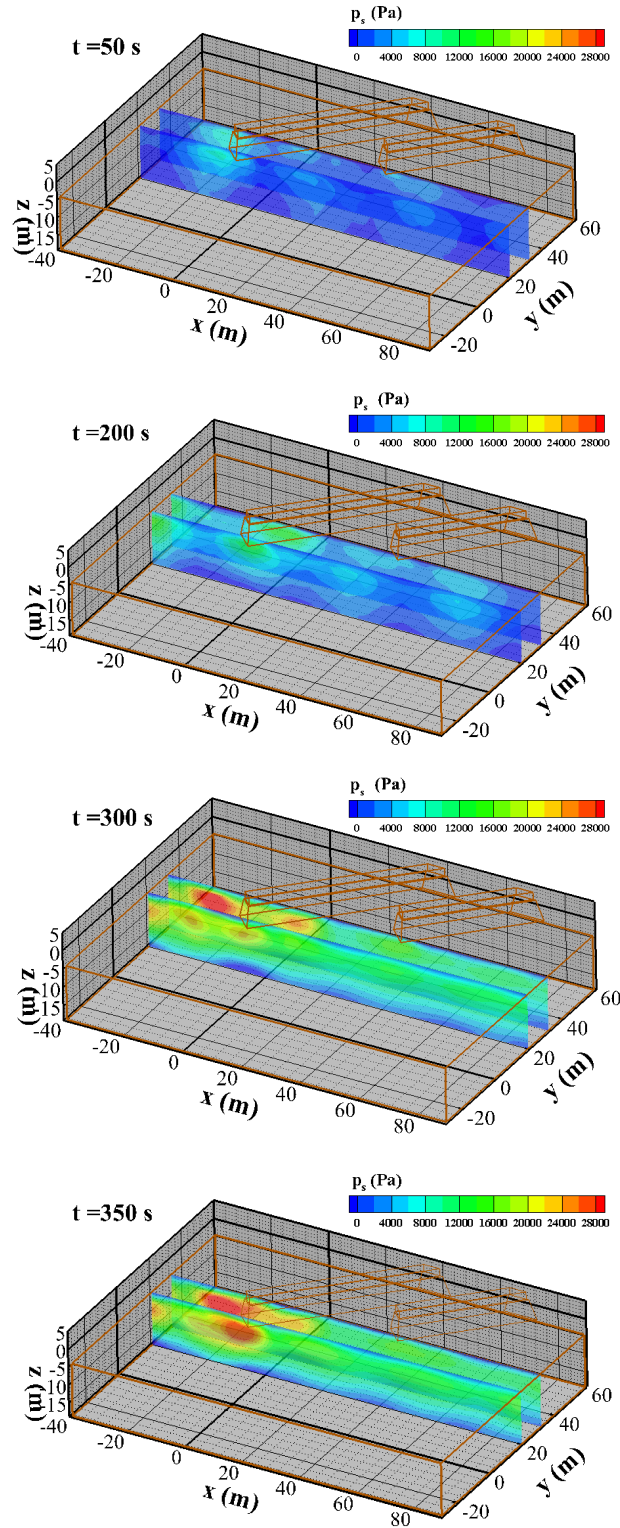


Figure 5.17 Accumulation of the residual pore pressure within a poro-elastoplastic seabed foundation at $t = 50$ s, 200 s, 300 s and 350 s.

5.4 Dynamic soil response in the seabed foundation

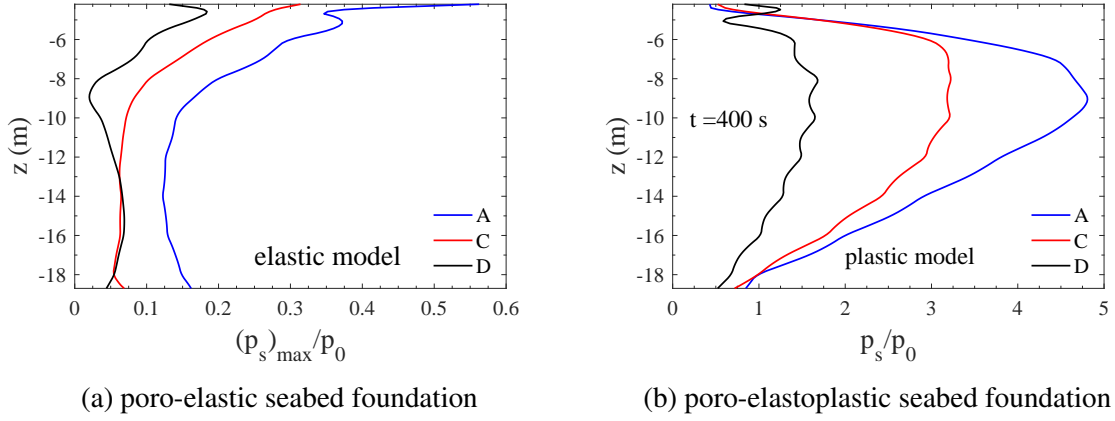


Figure 5.18 Vertical distribution of (a) the maximum dynamic oscillatory pore pressure within the poro-elastic seabed foundation; and (b) the residual dynamic pore pressure at $t = 400$ s within the poro-elastoplastic seabed foundation at location A, C and D.

instability of the breakwater heads is high. Figure 5.19 demonstrates the distribution of the dynamic pore pressure on a circular area around two breakwater heads at $t = 375$ s. These circles, as shown in Figure 5.19a, reach out from the centre of the breakwater heads ((-5.67, 17.67, -6) and (38.47, 31.81, -6)) with a radius of 10 m, whose vertical depth is 2 m from the seabed surface ($z = -6$ m). Likewise, both residual and oscillatory dynamic pore pressure are presented in the figure, indicated by the red solid line and blue dashed line, respectively. It can be seen from the figures that two mechanism of dynamic pore pressure response differently. For the oscillatory dynamic pore pressure (the blue dashed lines), at $t = 375$ s, the largest value appears at point right in front of two breakwater heads (point a: 225 degree), which is around twice p_0 . Approaching two sides of the breakwater heads clockwise and counter-clockwise from point a to point b, the oscillatory dynamic pore pressure gradually decreased until to the point b that located just beneath the breakwater heads whose dynamic pore pressure is basically zero. For the residual dynamic pore pressure, the accumulated pore pressure around the first breakwater head (i.e., around three times p_0) is significantly larger than the value around the second breakwater head (i.e., around p_0). This is due to the protection effect from the first breakwater since the second breakwater head is located behind the first breakwater. The larger residual dynamic pore pressure mainly distributes on the left and right sides of the each breakwater head. In the area near to point b, the residual dynamic pore pressure gradually decreases. There is even a negative value in the range of 20 to 75 degree, which indicates that the dissipation rate is greater than the accumulation rate in this range, so it is unlikely that the soil liquefaction occurs here. It can be concluded from this

figure that the liquefaction is more likely to happen at two sides of the breakwater head in the poro-elastoplastic seabed, which may cause the tilt of the breakwater heads.

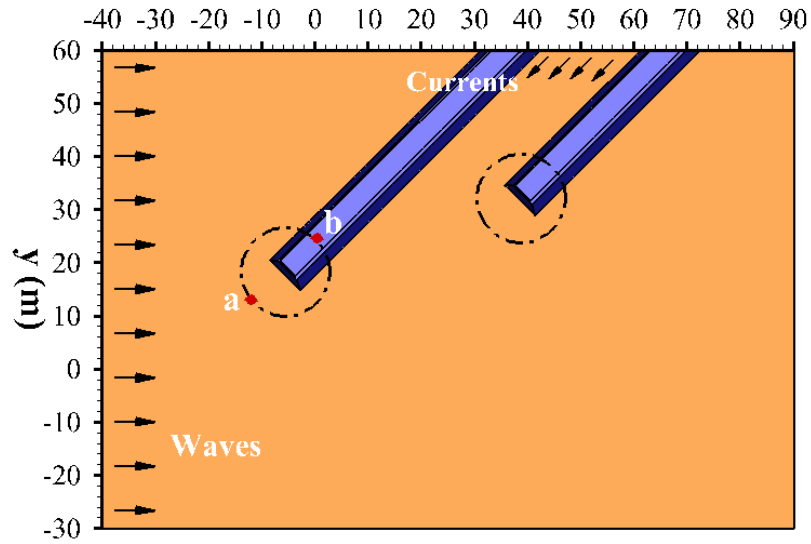
5.5 Soil liquefaction in the seabed foundation

The previous section mainly focus on the dynamic response mechanism and spatial/temporal distribution characteristics within the seabed foundation around the breakwaters, including the pore pressure, effective stresses, shear stresses, displacement. Based on these results, the instability mechanism of the seabed foundation will be further understood by studying the liquefaction conditions around the breakwaters. In this section, the liquefaction phenomenon around the breakwaters at river mouth will be investigated. According to the different liquefaction criteria, the liquefaction characteristics of two liquefaction mechanisms (i.e., momentary liquefaction and residual liquefaction) in the poro-elastic and poro-elastoplastic seabed foundation will be discussed and compared in section 5.5.1 and 5.5.2, respectively.

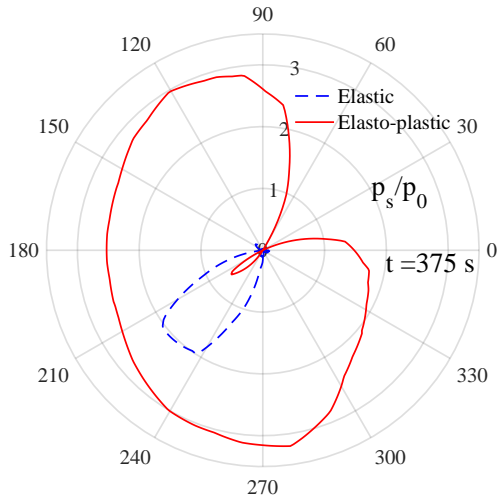
5.5.1 Momentary liquefaction

Based on the liquefaction criteria proposed by Tsai (1995) (Equation (2.19)), replacing the left-hand side term by the stress status that determined by consolidation process, the momentary liquefaction zones predicted by poro-elastic model can be obtained. Figure 5.20 shows the momentary liquefaction zones within an elastic seabed foundation around the breakwaters in a typical wave period from $t = 300$ s to $t = 306$ s, which is the same wave period chosen to demonstrate the hydrodynamic pressure shown in Figure 5.9. The red zones represent where the momentary liquefaction occurs. It can be seen in the figures that the momentary liquefaction mainly occurs on the seabed surface where the pore pressure gradient is large. The liquefaction depth in the elastic seabed foundation is quite small, which is less than 0.5 m. Comparing the distribution of hydrodynamic pressure shown in Figure 5.9 and the distribution of Momentary liquefaction zones shown in Figure 5.20, it can be found that the momentary liquefaction zones can only occur in the region where the hydrodynamic pressure is negative (i.e., under the wave troughs), where the upward seepage force is generated in these regions. For the areas where the hydrodynamic pressure is positive (i.e., under the wave crests), the vertical seepage force is downward, the soil in these areas will not be liquefied. Due to the interactions of the wave/current and breakwaters, the liquefaction zones behind the breakwaters are significantly reduced, however, there are still a few scattered pieces caused by the diffracted waves. The liquefaction zones are moving

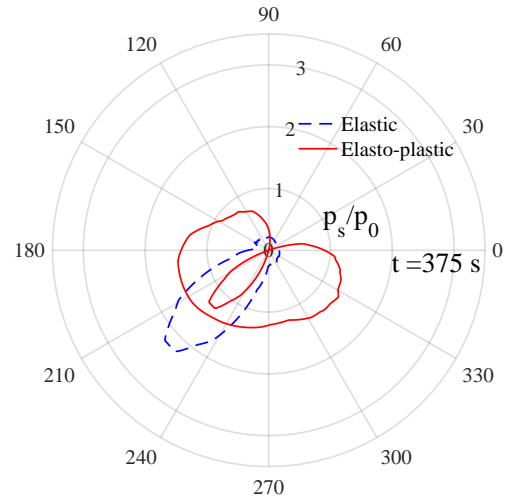
5.5 Soil liquefaction in the seabed foundation



(a) sketch for explanation



(b) first breakwater head



(c) the second breakwater head

Figure 5.19 Distribution of the dynamic pore pressure on a circular area around two breakwater heads at $t = 375$ s.

as the movement of the wave trough. When the liquefaction zones move to the region near to the breakwater foundation, the stability of the breakwater will be greatly affected. For example, at $t = 300$ s, a large liquefied area appears around the first breakwater head, which is likely to cause the breakwater head instability or even collapse.

5.5.2 Residual liquefaction

The residual liquefaction zones predicted by the poro-elastoplastic model are presented based on the liquefaction criteria proposed by Jeng and Seymour (1997b) (Equation (2.21)). Similarly, the left-hand side term of the criteria should be replaced by the stress state obtained after the consolidation process. The development mechanism of residual liquefaction zones in the plastic seabed foundation is quite different from the momentary liquefaction in the elastic seabed foundation. Figure 5.21 shows the development of residual liquefaction zones within a plastic seabed foundation at $t = 50$ s (green lines), $t = 200$ s (blue lines) and $t = 350$ s (red lines) around the breakwaters. Three slices are selected to have a better illustration of the liquefaction status at different locations: $y = -25$ m which is at the area far away from the breakwaters where is dominant by the progressive wave; $y = 20$ m which is beneath the first breakwater head; and $y = 50$ m which is below the two breakwaters. The lines in the figure represent the boundary lines of the residual liquefaction zones at a certain time, the area inside the lines is liquefied while outside the lines is not liquefied.

From Figure 5.21, at the early stage ($t = 50$ s), there is only a small range of liquefied areas in front of the first breakwater that appear at the upper part of seabed foundation as indicated by the green lines. It indicates that the seabed foundation in front of the breakwater will liquefy in the very first place since the reflected waves make the hydrodynamic pressure condition in this area the most intense. As time goes on, the initial liquefaction zones gradually expand laterally and vertically. At $t = 200$ s, even the area far away from the breakwater begins to liquefy as indicated by the blue lines. At $t = 300$ s (red line), the liquefaction zones have further developed downward and horizontally, some areas in front of the breakwaters have been connected to form the larger liquefaction layer. If the wave/current loading continues, the liquefaction boundary line will continue to develop downward. The explanation of this kind of progressive liquefaction from its development mechanism is: at the initial stage, the cyclic shear stress is largest at the region between the wave crest and wave trough where the first liquefaction occurs. As the wave propagating, the regions with the largest shear force start moving, causing these initial liquefaction zones extend laterally and downward, eventually, they are connected together.

5.5 Soil liquefaction in the seabed foundation

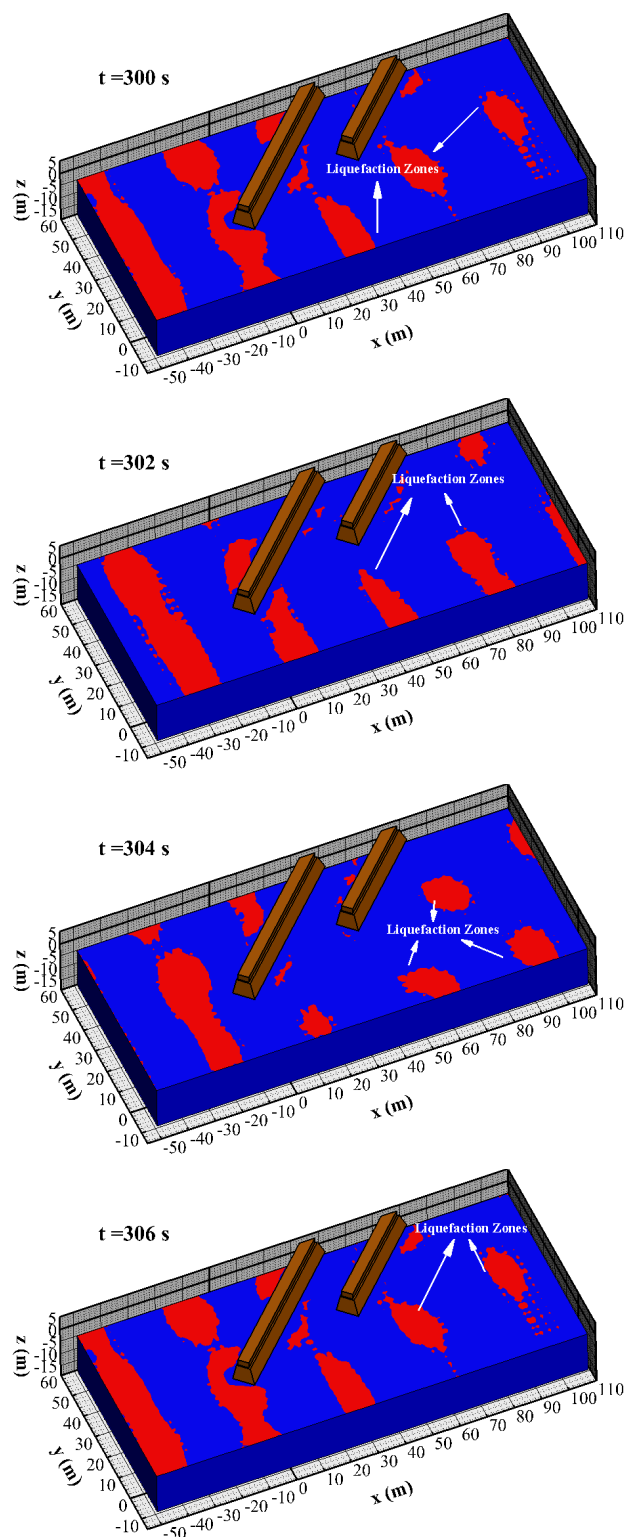


Figure 5.20 The predicted momentary liquefaction zones around the breakwaters in a typical wave period from $t = 300$ s to $t = 306$ s, based on Tsai (1995)'s liquefaction criteria.

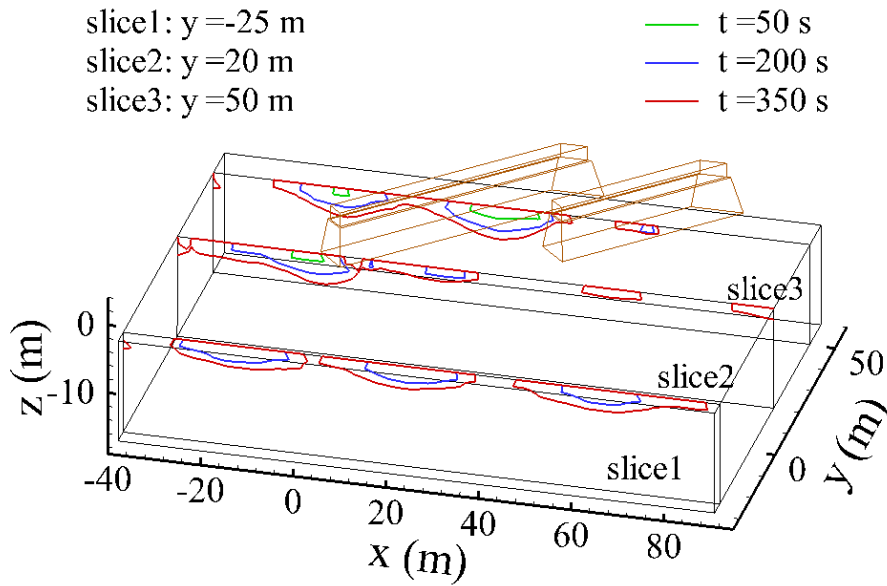


Figure 5.21 The predicted residual liquefaction zones around breakwaters from $t = 50$ s to $t = 350$ s based on Jeng and Seymour (1997b)'s liquefaction criteria.

The effect of the breakwaters on the development of the residual liquefaction zones in the plastic seabed foundation can also be seen from the figure. The most severe liquefaction is located in front of the first breakwater while there is no liquefaction occurs behind the second breakwater, which again shows that the breakwaters can effectively protect the soil behind them. Meanwhile, comparing the stability of two breakwaters, the first one is facing a greater threat of collapse and failure while the second one is relatively safe. Therefore, during the engineering construction process, it is better to reinforce the foundation around the first breakwater. It can be also seen from the slice 2 that located under the first breakwater head, the diffracted waves still cause the soil to be liquefied behind the breakwater head, however, the liquefaction areas are much smaller. In contrast to the momentary liquefaction, the residual liquefaction happened in the plastic seabed foundation has the larger liquefaction zones and deeper liquefaction depth, which will pose a greater threat on the stability of the breakwater built on it.

As mentioned earlier, the residual liquefaction within the poro-elastoplastic seabed foundation does not occur instantaneously. As the excess pore water pressure increases with the cyclic wave/current loading, the stability of the seabed foundation gradually decreases until the excess pore water pressure reaches the mean initial effective stress value, the residual liquefaction happens. In order to describe this kind of process of gradual reduction in seabed stability, a variable, liquefaction potential ($L_{potential}$), has been introduced to assess the

5.5 Soil liquefaction in the seabed foundation

possibility of occurrence of residual liquefaction. Based on the liquefaction criteria proposed by Jeng and Seymour (1997b) (Equation (2.21)), $L_{potential}$ in this Chapter is defined as:

$$L_{potential} = \frac{p_{excess}}{\frac{1}{3}(|\sigma'_{x0}| + |\sigma'_{y0}| + |\sigma'_{z0}|)} \quad (5.5)$$

in which p_{excess} is the dynamic residual pore pressure caused by the cyclic wave/current loading; σ'_{x0} , σ'_{y0} and σ'_{z0} are the initial effective stresses in x –, y – and z – direction, respectively, which is determined after the consolidation process. When $L_{potential}$ is equal or greater than 1, the residual soil liquefaction happens.

Figure 5.22 shows the time series of residual liquefaction potential at typical five locations (A, B, C, D and E) within the plastic seabed foundation around the breakwaters under the combined wave and current loading. It can be found that the residual liquefaction potential $L_{potential}$ gradually increases from zero during the 400 s simulation time. Similar to the dynamic response of residual pore pressure, $L_{potential}$ also has the oscillatory component and residual component. Due to the complex three-dimensional wave/current loading, the increasing rate and the accumulated value vary from location to location indicating that the stability of the different locations in the seabed foundation around the breakwaters is different. Location A, B and C, which are near to the two breakwater heads and in front of the first breakwater, have a faster increasing rate and larger accumulated value of liquefaction potential. All these locations have been liquefied as time goes on. Especially for location A and C, as indicated in blue line and green line, $L_{potential}$ reaches 1 at around $t = 100$ s and $t = 160$ s, respectively, indicating that residual liquefaction has occurred. Location B have also been liquefied at the end of the simulation. However, due to the protection of the breakwaters, $L_{potential}$ at the point located between two breakwaters (D) and behind the breakwaters (E) only reaches around 0.8 and 0.65, respectively. It is far away from 1 which demonstrates that there is no liquefaction occurs at point D and E, whereas it still can be seen from the development trend that the stability of the seabed foundation at these two locations is decreasing, especially at point D.

Figure 5.23 shows the vertical distribution of $L_{potential}$ at five reference points (A, B, C, D and E) within the poro-elastoplastic seabed foundation and poro-elastic seabed foundation at $t = 350$ s. In the poro-elastoplastic seabed foundation, the liquefaction potential is zero on the bottom of seabed, which means there is no excess pore pressure build-up at the seabed bottom. Along the upward-direction of the seabed depth, the liquefaction potential gradually increases until $L_{potential}$ reaches a maximum value at the seabed surface. It is found that liquefaction occurs at location A and C as $L_{potential}$ exceeds the critical value for the

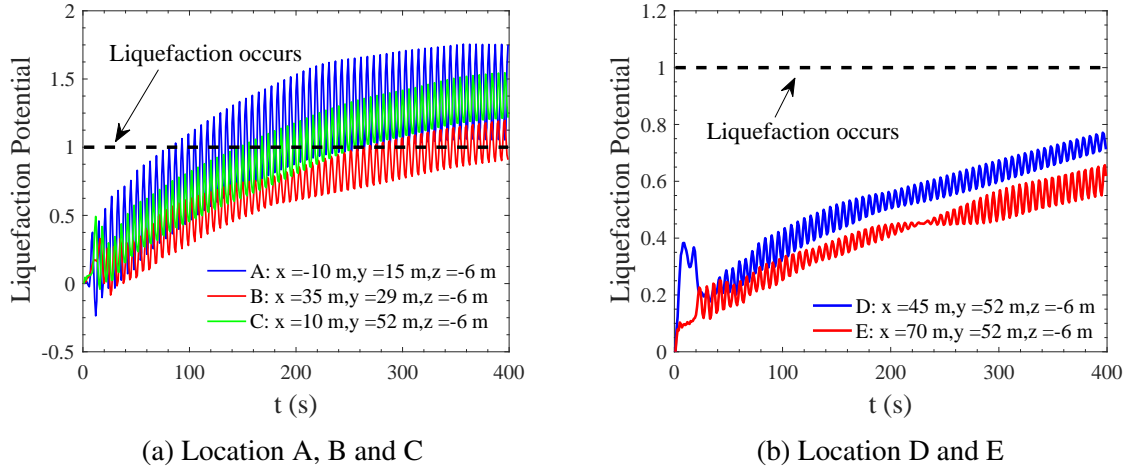


Figure 5.22 Time series of residual liquefaction potential at location A, B, C, D and E within the poro-elastoplastic seabed foundation around the breakwaters under combined wave and current loading.

liquefaction ($L_{potential} = 1$) and the liquefaction depths for location A and C at $t = 350$ s reach almost 30 % and 10 % of the seabed thickness, respectively. While location B, D and E are not liquefied at $t = 350$ s. In contrast, in the poro-elastic seabed foundation at $t = 350$ s, the liquefaction potential at all locations within the lower 70 % seabed is zero, showing that no liquefaction happened there. The liquefaction potential only begin to change on the upper layer of seabed. Only $L_{potential}$ at point A has exceeded 1, indicating that point A is under the wave trough at this moment and the momentary liquefaction occurred here. For location B, C and D, $L_{potential}$ is negative, which means that these locations are under the wave crest at $t = 350$ s, these locations are under compressive and liquefaction is impossible. Although location E is under the wave trough, it does not liquefy since it is located behind the breakwaters. From this figure, it can be seen again that the liquefaction development and distribution trends in the elastic seabed foundation and plastic seabed foundation are totally different. Under the same wave/current loading condition, the residual liquefaction phenomenon in the plastic seabed foundation usually is more serious.

5.6 Parametric study

The soil properties and fluid parameters can significantly affect the numerical simulation results. In this section, the parametric analyses based on the poro-elastoplastic seabed model are carried out. The effects of soil properties, including the soil permeability (k_s) and degree

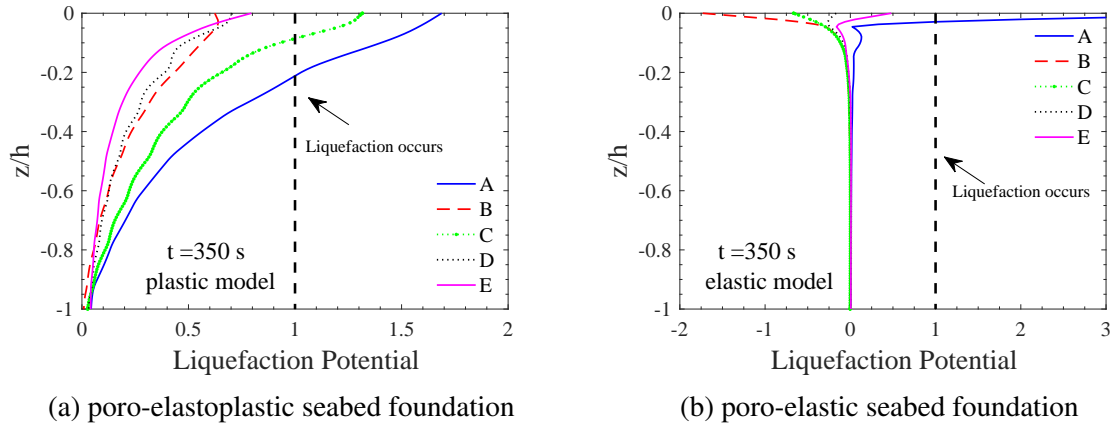


Figure 5.23 Vertical distribution of the wave/current induced liquefaction potential at location A, B, C, D and E within (a) poro-elastoplastic seabed foundation; and (b) poro-elastic seabed foundation at $t = 350$ s.

of saturation (S_r), and the wave characteristics, including the wave Height (H) and wave period (T), on the predicted residual liquefaction zones at $t = 300$ s are presented. On top of that, the influences of the PZIII model parameters and different velocity of the river currents on the development of the residual liquefaction areas are also considered.

5.6.1 Effect of soil properties

Among the seabed parameters, the influence of the soil permeability (k_s) and degree of saturation (S_r) on the response of seabed foundation cannot be ignored. k_s is an important parameter to measure the accumulation rate of pore pressure. It reflects the ability of soil drainage that the larger k_s is, the better the soil drainage capacity is, and vice versa. Figure 5.24 shows the residual liquefaction development of the seabed foundation at $t = 300$ s with different soil permeability ($k_s = 10^{-7}$ m/s, $k_s = 10^{-5}$ m/s and $k_s = 10^{-3}$ m/s). Three slides are selected to present the predicted liquefaction zones, which are $y = 0$ m, $y = 25$ m and $y = 50$ m, respectively. It can be easily found from the figure that the soil with lower permeability is much easier to be liquefied than the soil with higher permeability. For example, after the 300 s of cyclic loading, the seabed with $k_s = 10^{-7}$ m/s has the largest liquefaction zones, while the seabed with $k_s = 10^{-3}$ m/s was barely liquefied and some part of surface of seabed with $k_s = 10^{-5}$ m/s was liquefied, but the liquefaction areas had not yet been connected into a layer. This is because the seabed foundation with a lower permeability has a lower dissipation rate of excess pore pressure which causes the higher excess pore pressure build-up rate. While in the seabed foundation with a large permeability, the soil has a strong drainage capacity, the

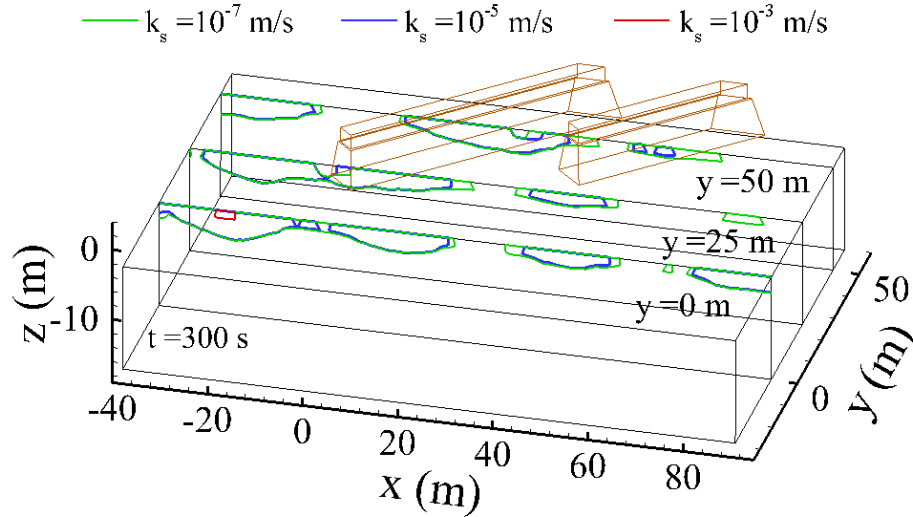


Figure 5.24 The development of residual liquefaction zones at $t = 300$ s showed in three typical slides ($y = 0$ m, $y = 25$ m and $y = 50$ m) with different soil permeability ($k_s = 10^{-7}$ m/s, $k_s = 10^{-5}$ m/s and $k_s = 10^{-3}$ m/s).

excess pore pressure has “escaped” from the pore of the soil skeleton before the accumulation of the pore pressure. This results in the fact that the seabed with large permeability is not easy to be liquefied while the seabed with small permeability is more likely to lose its stability and eventually to be liquefied.

In addition to k_s , the soil degree of saturation (S_r) is another factor affecting the dynamic seabed response. Figure 5.25 illustrates the development of residual liquefaction zones within the poro-elastoplastic seabed foundation at $t = 300$ s with different soil degree of saturation ($S_r = 98\%$, $S_r = 95\%$ and $S_r = 93\%$). As indicated by the figure, the effect of S_r on the residual liquefaction area is very small. The boundary lines of the residual liquefaction zones at $t = 300$ s for different degree of saturation are almost same, only a very slight difference can be observed that the seabed with lower degree of saturation has slightly larger liquefaction areas. Comparing three slides at different locations, another noteworthy finding is that the breakwater is able to protect the region behind it effectively.

Quite a number of model parameters are involved in the poro-elastoplastic constitutive model PZIII. These parameters should be determined experimentally through the laboratory test. In this study, two sets of the PZIII model parameters that listed in Table 5.1 are adopted to examine the effect of model parameters on the numerical simulation results of the soil response. These two sets of parameters were obtained by Zienkiewicz et al. (1999)

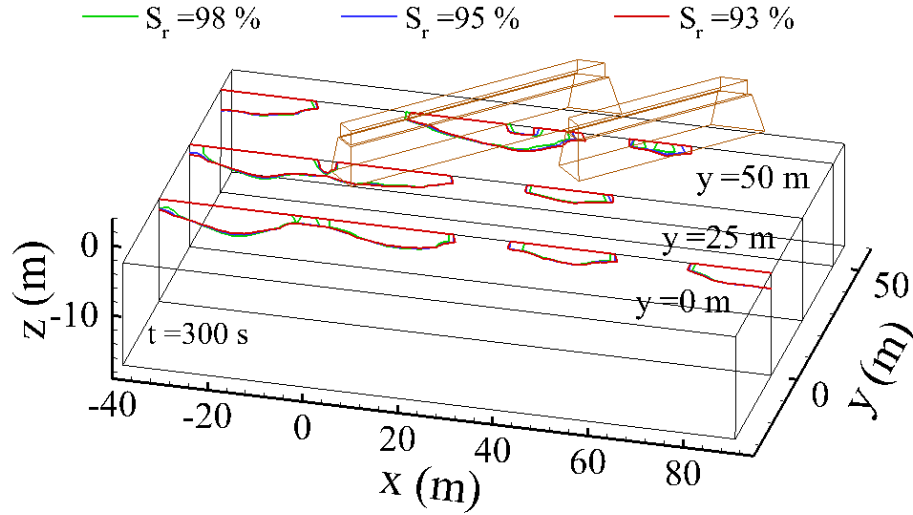


Figure 5.25 The development of residual liquefaction zones at $t = 300$ s showed in three typical slides ($y = 0$ m, $y = 25$ m and $y = 50$ m) with different soil degree of saturation ($S_r = 98$ %, $S_r = 95$ % and $S_r = 93$ %).

from the experimental results of CIUC (Isotropically Consolidated followed by Undrained Compression) tests for the Nevada sand, representing the loosely packed sand with a soil relative density of $D_r = 40$ % and the densely packed sand with a relative density of $D_r = 60$ %, respectively. Figure 5.26 demonstrates the residual liquefaction zones that developed within the two kinds of sand at $t = 300$ s. The numerical results prove that the residual liquefaction in the loose sand with small D_r is more severe. This is due to the fact that the loose sand has a relative large porosity, which is more likely to deform under the cyclic loading. The deformation will further cause the larger accumulation of pore pressure. A further novel finding is that, when analysing parametric study of different soil parameters, the external loading applied to the seabed model is same, the locations of the occurrence of liquefaction are always same but with different liquefaction ranges. Since the results are presented at $t = 300$ s, It reveals the progressive feature of residual liquefaction.

5.6.2 Effect of fluid characteristics

As two important factors, wave height (H) and wave period (T) can greatly affect the dynamic soil response within the seabed foundation. In this section, the influence of different H and T on the development of residual liquefaction will be examined. Figure 5.27 displaces the

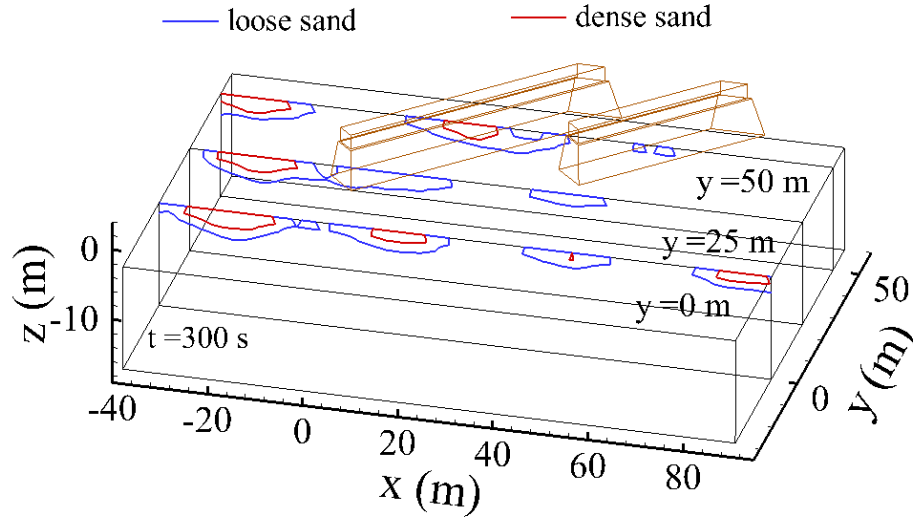


Figure 5.26 The development of residual liquefaction zones at $t = 300$ s showed in three typical slides ($y = 0$ m, $y = 25$ m and $y = 50$ m) within the loosely packed seabed foundation and densely packed seabed foundation.

effect of H on the liquefaction ranges at $t = 300$ s. Three wave height values were used: $H = 1$ m, $H = 2$ m and $H = 2.5$ m. It can be observed from the figure that the larger the wave height, the larger the residual liquefaction zones, since the large wave height can induce large hydrodynamic pressure that acting on the seabed surface.

Wave period also has a certain impact on the dynamic soil response within the seabed foundation. Figure 5.28 illustrates the effect of wave period ($T = 6$ s, $T = 5$ s and $T = 4$ s) on the residual liquefaction zones in the seabed foundation. From the numerical results in the figure, the ranges of residual liquefaction are positively correlated with wave period.

Furthermore, another parametric analysis for the effect of velocity of the river currents (U_0) that flows into the ocean through the breakwaters on the seabed response has also been conducted. Four conditions have been considered: $U_0 = 0$ m/s (wave loading only), $U_0 = 1$ m/s, $U_0 = 0.8$ m/s and $U_0 = 0.6$ m/s. The numerical simulation results have been shown in Figure 5.29. It is suggested by the figure that since the river currents only appear around the breakwaters, its scope of influence on the seabed stability is limited. Even the influence of the present conditions considered in this study is not very significant, the affected regions are located in critical areas which are near breakwater foundation (between two breakwaters and near the breakwater heads). For example, in slide $y = 0$ m, for the range between $x = 0$ m and $x = 30$ m which is just in front of the opening of two breakwaters, the presence of the river

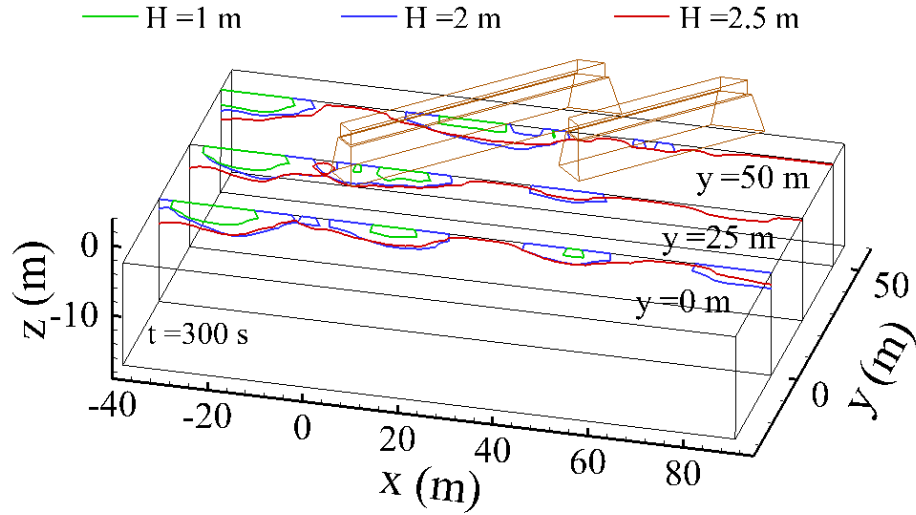


Figure 5.27 The development of residual liquefaction zones at $t = 300$ s showed in three typical slides ($y = 0$ m, $y = 25$ m and $y = 50$ m) with different wave height ($H = 1$ m, $H = 2$ m and $H = 2.5$ m).

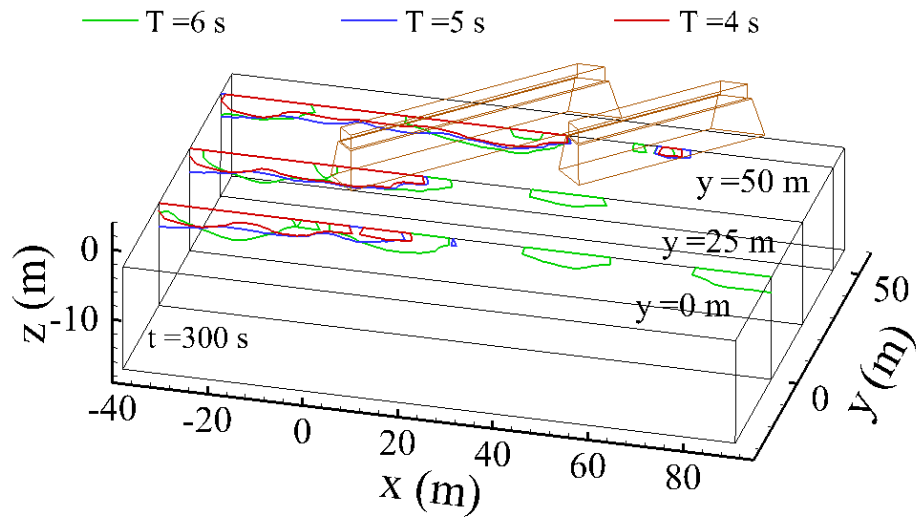


Figure 5.28 The development of residual liquefaction zones at $t = 300$ s showed in three typical slides ($y = 0$ m, $y = 25$ m and $y = 50$ m) with different wave period ($T = 6$ s, $T = 5$ s and $T = 4$ s).

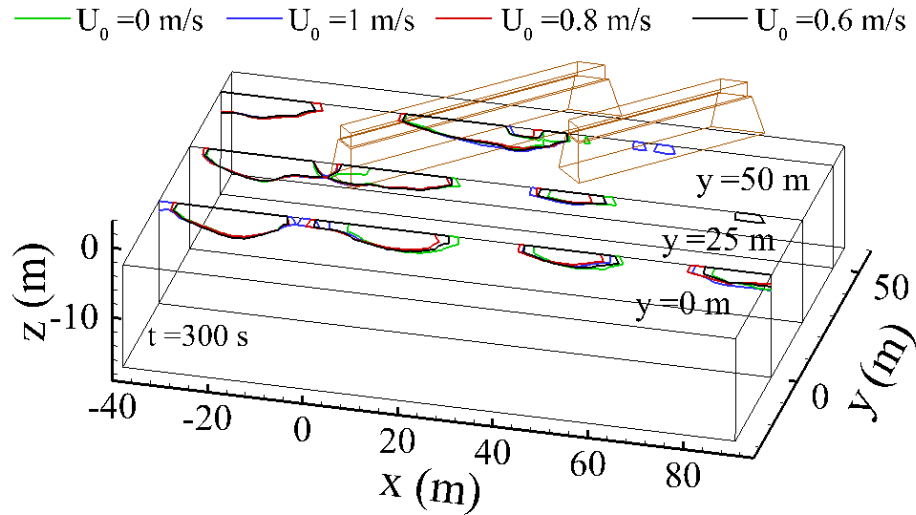


Figure 5.29 The development of residual liquefaction zones at $t = 300$ s showed in three typical slides ($y = 0$ m, $y = 25$ m and $y = 50$ m) with different river currents velocity ($U_0 = 0$ m/s, $U_0 = 1$ m/s, $U_0 = 0.8$ m/s and $U_0 = 0.6$ m/s).

currents can exacerbate the liquefaction conditions, and the liquefaction zones increases with the increase of river currents velocity. Meanwhile, a slight shift of liquefaction area along the direction of river currents can be observed. It can be concluded that the river currents at the river mouth around the breakwaters will increase the possibility of instability of the breakwater foundation.

5.7 Summary

In this chapter, a 3D integrated numerical model has been used to investigate the foundation stability of the breakwaters at a river mouth. The flow field around the breakwaters were firstly examined, followed by the determination of stress state after consolidation process. Based on two different soil mechanisms, the time and space distribution of dynamic foundation responses under the cyclic loading were studied and compared using two constitutive models. Then, both momentary liquefaction and residual liquefaction that occur within the elastic foundation and plastic foundation respectively were examined. The parametric studies on different conditions were also carried out. Based on the predicted results from the 3D numerical model, some conclusions can be drawn as follows:

- This study includes a complicated interaction process between the waves, river currents, seabed foundation and breakwaters. The present 3D integrated numerical model is capable of simulating this kind of complicated scenarios which cannot be simulated using the 2D model.
- The wave/current induced dynamic soil responses predicted by the elastic and plastic constitutive models show that the mechanism of oscillatory soil response and residual soil response are completely different. From the perspective of time distribution, the oscillatory soil response only oscillates around the initial value while the residual soil response is usually accompanied by the build-up of pore pressure and the reduction of effective stress. From the perspective of space distribution, the oscillatory soil response shows a periodic distribution which is directly related to the shapes of free surface while the residual soil response shows a progressive build-up trend around the breakwaters.
- The numerical results also illustrate the different mechanisms of liquefaction. The momentary liquefaction mainly occurs on the seabed surface where the pore pressure gradient is large. In contrast, the residual liquefaction initially occurs at the seabed surface due to the accumulation of pore pressure. The liquefaction zones will be extended laterally and vertically along with time. Under the same external loading, the residual liquefaction within the plastic foundation usually is more serious than the momentary liquefaction within the elastic foundation.
- The presence of the structure significantly changes the dynamic foundation response. The liquefaction conditions at different locations around the structure are quite different.
- The parametric studies indicate that the development of the residual liquefaction is more serious within the loosely deposited poro-elastoplastic seabed foundation with poor drainage conditions under large wave height and wave period. The presence of the river currents can also exacerbate the liquefaction conditions, and the liquefaction zones increases with the increase of river currents velocity.

Chapter 6

3D Numerical Study II: Seabed Foundation Stability around Offshore Detached Breakwaters^{3*}

6.1 Introduction

There are many forms of breakwaters with different main functions in the coastal environment. In the last chapter, the foundation stability around breakwaters at river mouth was studied. Beyond that, the shore-parallel detached breakwater is another very common type of coastal structure. Unlike the multiple longitudinally paralleled breakwaters described in Chapter 4, which the waves pass through each breakwater successively, the shore-parallel breakwaters in this chapter are juxtaposed in a straight line whose distance to the coastline is same. This situation can also only be simulated by 3D numerical model. There are several types of shore-parallel breakwater existed, from which detached breakwater is the most common one. It is usually constructed as part of coastal management facilities to protect the shoreline from wave action. The breakwater, in general, can be classified as emerged, submerged or even floated. Among them, the emerged breakwater can provide a better shelter from the wave actions compared to other types of breakwater. However, it has disadvantages, for example, it has a relatively large impact on aesthetic viewing of the environment than the submerged breakwater. Figure 6.1 shows an example of shore-parallel detached breakwaters at Sea Palling that locate at north-east of Norwich, Norfolk. It can be seen

^{3*}Contents in this chapter form the manuscript: Lin, C., & Jeng, D. S. (in preparation). Wave/current induced soil response and liquefaction around offshore detached breakwaters. *Ocean Engineering*.

that the segmented breakwaters are utilised in this coastline management scheme, which can partly provide wave shelter for a certain part of coastline. The construction of these breakwaters makes significant hydrodynamic impact on the fluid field in the vicinity and further induce the complicated hydrodynamic loading on the seabed foundation. Hence, it is necessary to perform the foundation stability assessment around the shore-paralleled breakwaters.



Figure 6.1 The shore-paralleled detached breakwater at Sea Palling, Norfolk (Figure retrieved from <http://pcwww.liv.ac.uk/civilCRG/leacoast/studyarea.htm>).

In this study, the proposed 3D numerical model is used to examine the seabed foundation stability around paralleled detached breakwater along the shoreline. This chapter is organised as following parts: first and foremost, the problem set-up for the numerical simulation will be

introduced; then, the flow field around the structures will be investigated; next, the stress state after consolidation process will be presented; then, the seabed foundation stability will be assessed by studying the liquefaction potential and liquefaction zones for various wave and soil parameters within two types of seabed foundation: poro-elastoplastic seabed foundation and poro-elastic seabed foundation; finally, a summary will be given.

6.2 Problem set-up

Three paralleled breakwaters sitting on a porous seabed foundation are considered in this study. Figure 6.2 demonstrates the configuration of the computational domain for the present study. The seabed foundation is $95 \text{ m} \times 80 \text{ m} \times 12 \text{ m}$ ($L_x \times L_y \times L_z$) in dimension. Three paralleled breakwaters are located on the middle of the seabed foundation. The length of the breakwaters (L_B) on two sides is 10 m and for the middle breakwater L_B equals to 20 m. The width of the breakwaters (W_B) is 5 m and the height of the breakwaters (H_B) is 5.6 m. The length of the gap (L_G) between the breakwaters is 20 m.

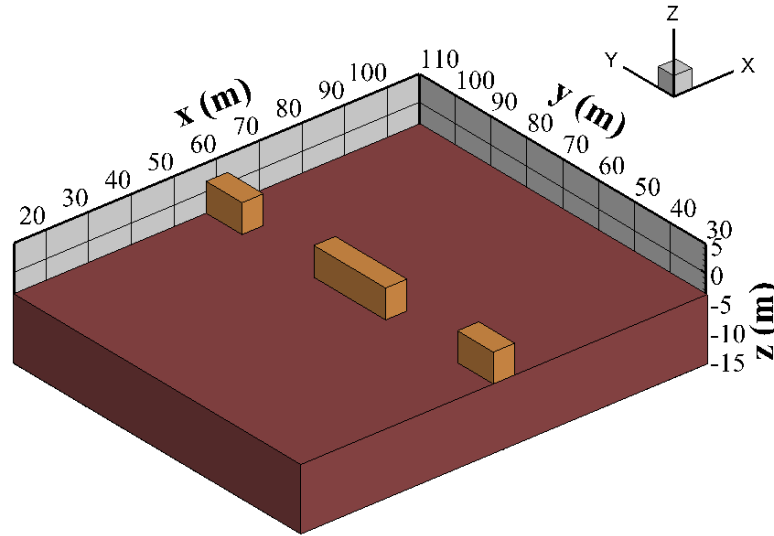


Figure 6.2 The computational domain of the 3D numerical study II.

Figure 6.3 illustrates the three-view drawings of the computational domain. The waves are generated at the left boundary and propagate to the right to meet the breakwaters. Currents that travel in the area in front of the breakwaters that are perpendicular to the incident waves (in negative y -axis direction) are to simulate the longshore currents, which commonly exist at any beaches in the near shore zones that travel parallel to shoreline. Three main

zones in the computational domain can be identified in this study that contain different wave/current components, where zone I is in front of the breakwaters including incident waves, reflected waves and longshore currents, zone II is between the breakwaters including only the incident waves and zone III is behind the breakwaters including part of the incident waves and diffracted waves. Due to the different wave/current impacts, the soil behaviours are different from zone to zone. Hence, four reference points (A, B, C and D) are selected in corresponding zones to monitor the hydrodynamic process caused by wave/current-structure interactions and soil behaviour within the seabed foundation.

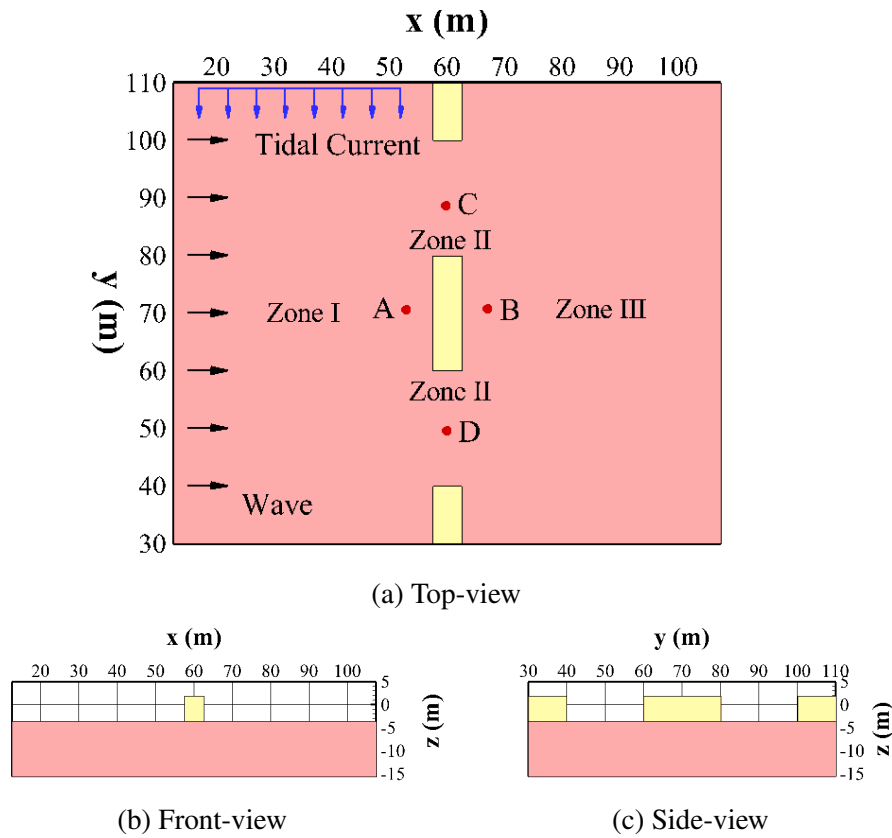


Figure 6.3 The three-view drawings of the computational domain of the 3D numerical study II.

Three breakwaters are treated as the porous medium that follow the linear elastic theory, whereas the seabed foundation is considered as two different types of porous medium, which is simulated by the elastic and plastic constitutive modes, respectively. The stability (i.e., liquefaction potential) of two different types of breakwater foundation will be examined under the same wave/current loading with different parameters setting. The input parameters of the wave characteristics, properties of the breakwaters and porous seabed foundation are listed in Table 6.1.

Table 6.1 The input parameters used in the 3D numerical study II.

Wave characteristics		
Wave period (T)	4.5 s, 4.0 s or 3.5 s	
Wave height (H)	2.4 m, 2.05 m or 1.7 m	
Still water level (d)	3.6 m, 4.6 m or 5.6 m	
Longshore current velocity (U_0)	0.6 m/s, 0.3 m/s or 0.0 m/s	
Breakwater characteristics		
Young's modulus (E)	2.48×10^9 Pa	
Poisson's ratio (μ_s)	0.24	
Permeability (k_s)	1.0×10^{-3} m/s	
Porosity (n_s)	0.49	
Seabed foundation properties		
Permeability (k_s)	10^{-6} m/s, 10^{-4} m/s or 10^{-8} m/s	
Porosity (n_s)	0.425	
Degree of saturation (S_r)	99 %, 98 % or 97 %	
Relative density (D_r)	40 % or 60 %	
Elastic parameters		
Young's modulus (E)	1.35×10^7 Pa	
Poisson's ratio (μ_s)	0.35	
Parameters for PZIII Model		
	dense sand	loose sand
M_g	1.32	1.15
M_f	1.3	1.035
α_f	0.45	0.45
α_g	0.45	0.45
K_{evo}	2000.0 kPa	770.0 kPa
G_{eso}	2600.0 kPa	1155.0 kPa
β_0	4.2	4.2
β_1	0.2	0.2
p'_0	4.0 kPa	4.0 kPa
H_0	750.0	600.0
H_{U0}	40000.0 kPa	40000.0 kPa
γ_u	2.0	2.0
γ_{DM}	4.0	0.0

6.3 Flow field around breakwaters

Figure 6.4 shows the time series of water surface elevation at location A, B, C and D in different zones for case with longshore currents and case without longshore currents. The longshore currents commonly exist in the nearshore zone that move parallel to the shoreline. It can be observed from the figure that the wave height at location A in zone I is greater than the wave height at other locations due to the superposition of the incident and reflected waves. Since there are only diffracted waves at location B in zone III, the wave height is the smallest. The wave height at location C and D is between the largest and smallest value. The free surface elevation at location C and D are completely coincident and have same wave height in the case where no longshore currents exist. This is because location C and D are symmetrical between the breakwaters and only the incident waves are involved. However, the presence of the longshore currents can change this situation, they make the wave crest at location D more sharp and a deviation of free water surface elevation between location C and D can be observed. The longshore currents in zone I also have an impact on the fluid field in the vicinity by altering the progressive waves around the structures. For example, at location A and B, the presence of the longshore currents at right angles to the progressive waves make the wave height larger at location A and B, which will further affect the dynamic soil response within the seabed foundation and structure stability.

6.4 Stress state after consolidation process

Similar to previous studies, the new effective stress state within the seabed foundation after the consolidation process under the hydrostatic pressure and self-weight of breakwaters is determined first before been applied as the initial condition in the dynamic analysis of wave/current-seabed-breakwater interactions. Figure 6.5 displays the distribution of the pore pressure (p_s), effective stresses (σ'_x , σ'_y and σ'_z) and shear stresses (τ_{xy} , τ_{yz} and τ_{xz}) within the seabed foundation after consolidation process. When the structure is built on the seabed foundation, the self-weight of the structure is initially transferred to the pore water, resulting in the generation of excess pore pressure. As time goes by, the self-weight of the structure gradually transfers from pore water to the soil particle, showing as the dissipation of the pore pressure and increase of the effective stresses. In Figure 6.5, the pore pressure is uniformly distributed and appears as layered, indicating that there is no excess pore pressure and the consolidation process has been completed. The figure also demonstrates that the breakwaters can significantly affect the stress field of the surrounding soil. σ'_x , σ'_y and σ'_z all increase

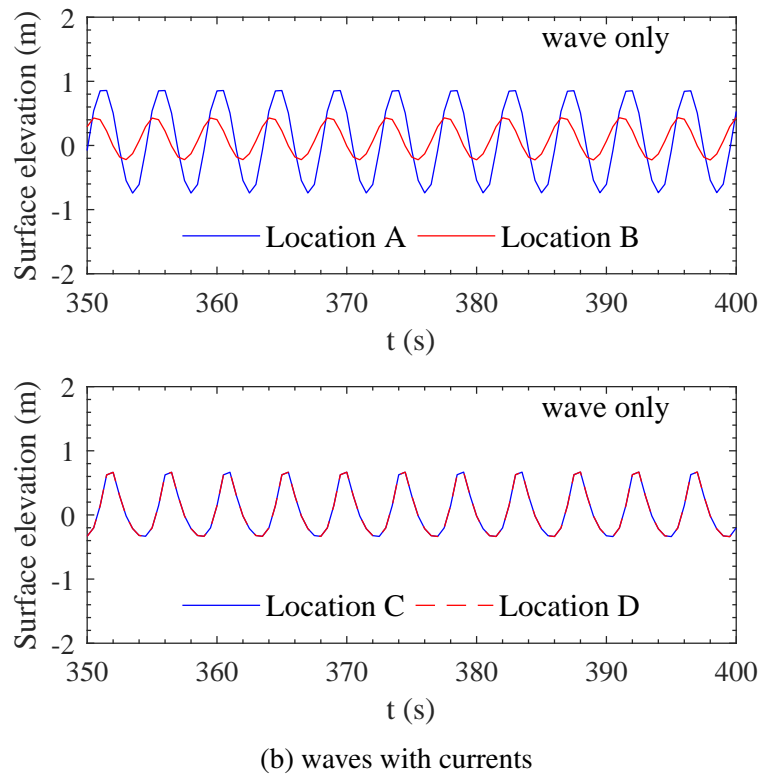
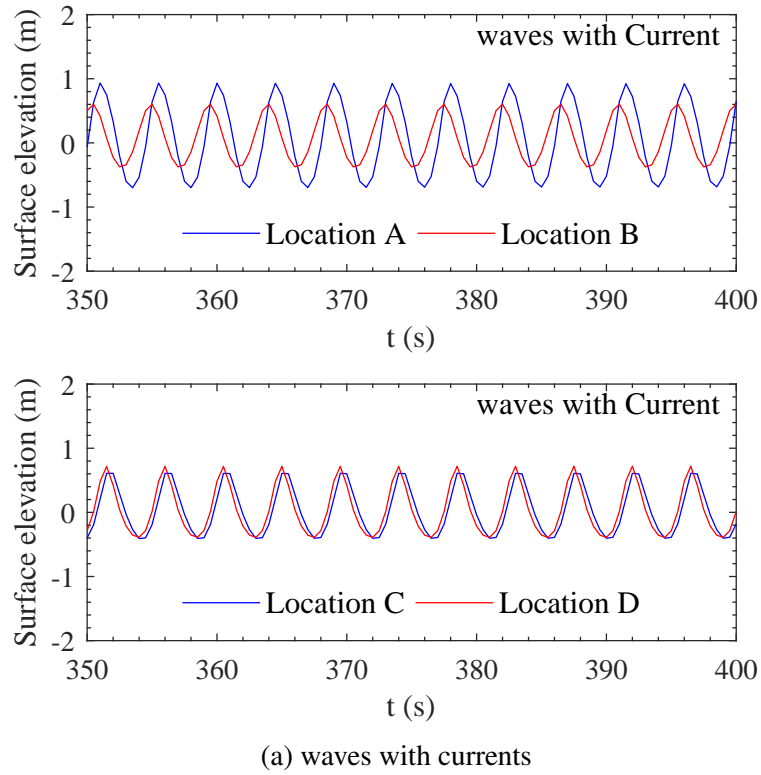


Figure 6.4 Time series of surface elevation at location A, B, C and D in the case: (a) with currents; and (b) without currents.

significantly in the region under or near three breakwaters due to the compression effect of breakwaters, especially σ'_z whose maximum value reached 120 kPa. According to the liquefaction criteria described in section 2.2.4, the increase of initial effective stress will cause the threshold of liquefaction to increase, which indicates that ignoring the consolidation process would overestimate the liquefaction potential within the seabed foundation. The concentration zones of τ_{xy} and τ_{yz} appear at the bottom corner of three breakwaters. Whereas, τ_{xz} distributes in the whole zone under the breakwaters and its magnitude is the largest which can reach up to 35 kPa. It is found that the stress state only in the region under or near the structures has been affected. In the region far away from the breakwaters, the distribution of the effective stresses has not been affected, showing uniformly layered pattern as the condition when there are no structures.

6.5 Liquefaction potential in the seabed foundation

In order to investigate the effects of various parameters on the stability of the seabed foundation around shore-paralleled detached breakwaters under combined wave and current loading, the vertical distribution of the liquefaction potential with specific parameter setting will be discussed for two different types of seabed foundations in this section, namely the poro-elastoplastic seabed foundation and the poro-elastic seabed foundation. The liquefaction potential in the poro-elastoplastic seabed foundation after many wave cycles (i.e., $t=350$ s) is presented to illustrate the foundation stability condition since the foundation stability continuously decreases with the build-up of pore pressure. Equation (5.5), based on the liquefaction criteria proposed by Jeng and Seymour (1997b), is used to calculate the liquefaction potential in the poro-elastoplastic seabed foundation. Differently, the liquefaction potential in the poro-elastic seabed foundation is periodic without accumulation, hence, the maximum value is selected, which is calculated based on the liquefaction criteria proposed by Okusa (1985).

6.5.1 Effect of seabed properties

Among the soil parameters, the soil permeability (k_s) and degree of saturation (S_r) usually will affect the soil response around the structures under the wave/current loading and further affect the structure foundation stability. k_s is an important parameter for measuring the drainage capacity of the soil, which has a great impact on the pore water pressure accumulation rate. When k_s is large, the drainage performance of the soil is good and the pore water pressure

6.5 Liquefaction potential in the seabed foundation

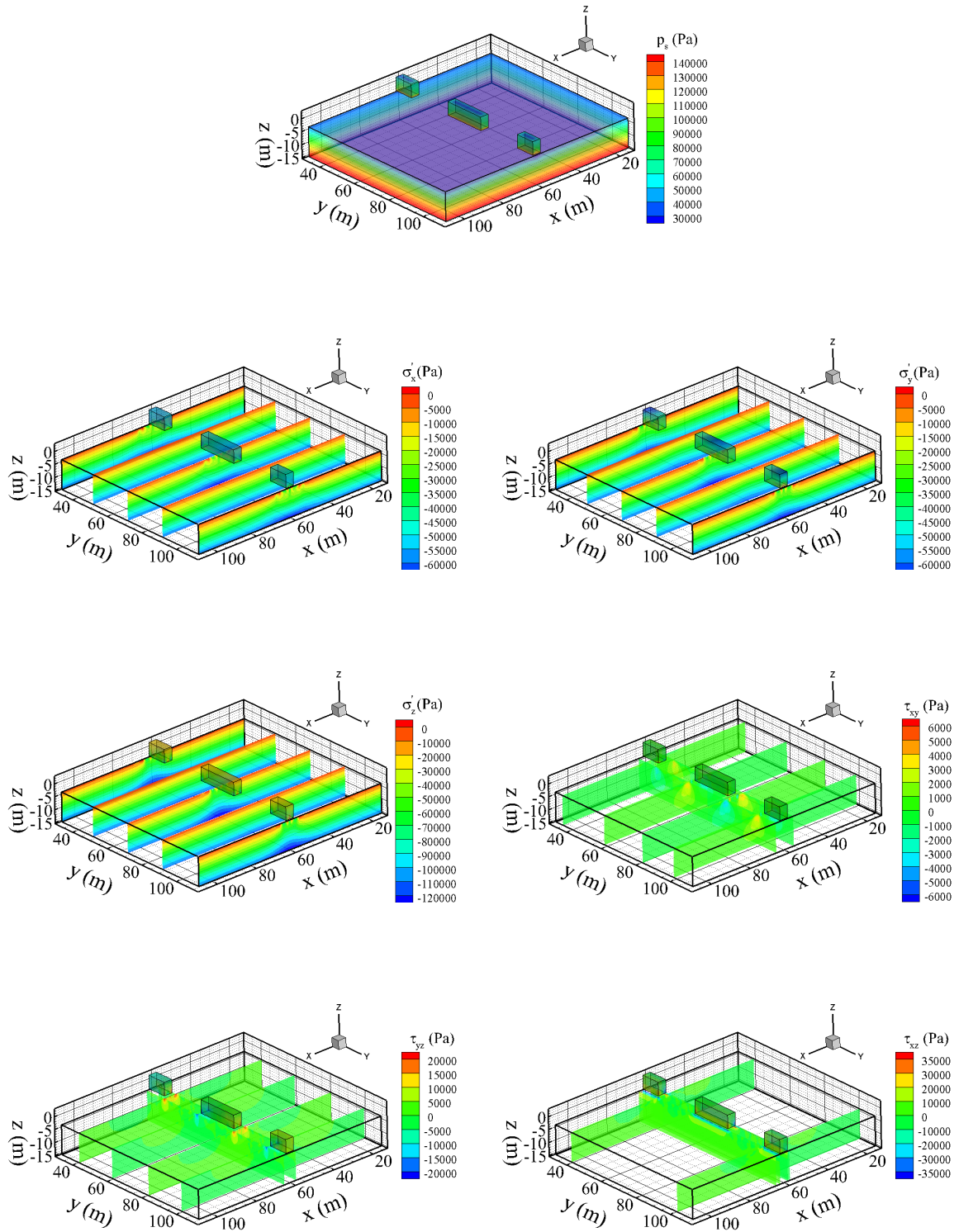


Figure 6.5 The distribution of pore pressure (p_s), effective stresses (σ'_x , σ'_y and σ'_z) and shear stresses (τ_{xy} , τ_{yz} and τ_{xz}) after consolidation process.

6.5 Liquefaction potential in the seabed foundation

build-up rate is low; otherwise, the drainage capacity is bad and the pore water pressure build-up rate is high. S_r is another soil parameter that might affect the seabed foundation response. It is common to find air within the seabed soil. Jeng (2013) pointed out that most seabed foundations have degrees of saturation close to fully saturated, however, the full saturation condition is rare in field or laboratory experiments, except for an ideal condition.

Figure 6.6 and Figure 6.7 illustrate the effect of soil permeability (k_s) and degree of saturation (S_r) on the vertical distribution of liquefaction potential ($L_{potential}$) in the poro-elastoplastic seabed foundation at location A, B, C and D at $t = 350$ s, respectively. The figures show that k_s has a more significant impact on the foundation stability compared to S_r . As been displayed by Figure 6.6, the liquefaction condition is more severe in the seabed foundation with low k_s . An interesting finding is that $L_{potential}$ increases as k_s decreases from 10^{-4} m/s to 10^{-8} m/s, however, the effect of k_s on the foundation stability becomes less sensitive as it reaches 10^{-6} m/s and continues to decrease. This might indicate that the soil liquefaction does not deteriorate indefinitely with the decrease of k_s . When k_s is low to a certain extent, the liquefaction condition reaches its worst case.

For the influence of degree of saturation (S_r), there are no significant differences between different cases, which indicates that S_r has little effect on the stability of poro-elastoplastic seabed foundation. Therefore, it can be concluded that in the poro-elastoplastic seabed foundation, the key influence factor among the soil properties on the foundation stability is the soil permeability (k_s).

Comparing among the different locations, location A has the deepest liquefaction depth (L_{depth}). While the locations between the breakwaters (i.e., location C and D) have the smallest L_{depth} compared to other locations. For example, in the case of seabed foundation with $k_s = 10^{-4}$ m/s, L_{depth} at location A reaches over 20 % of foundation thickness. Due to the protection from the middle breakwater, location B only has a L_{depth} of 5 % of foundation thickness. Whereas, there is no liquefaction happened at location C and D and $L_{potential}$ at these locations is nearly identical. One of the possible reasons for location C and D having the smallest $L_{potential}$ is that the soil at location C and D is relatively compact due to the compression of the breakwaters. Therefore, the build-up rate of pore pressure is slow here. The effect of location on $L_{potential}$ in the poro-elastic soil is not the same as in poro-elastoplastic soil, which will be mentioned later. It is also found from the figures that the liquefaction potential is smallest at seabed bottom ($L_{potential} = 0$) and gradually increases along the depth to the seabed surface.

Figure 6.8 and Figure 6.9 reveal the influence of k_s and S_r on the vertical distribution of maximum liquefaction potential ($L_{potential_{max}}$) at location A, B, C and D in a poro-elastic

6.5 Liquefaction potential in the seabed foundation

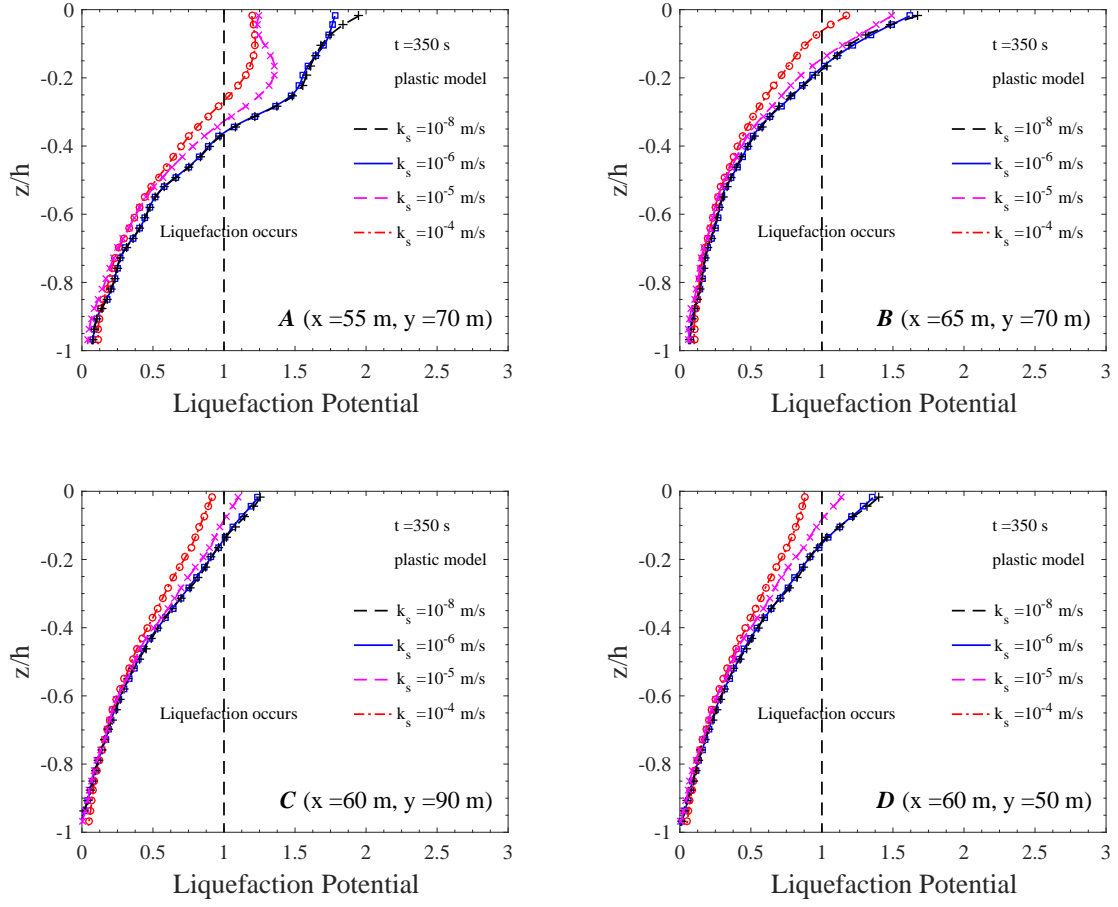


Figure 6.6 Vertical distribution of the liquefaction potential ($L_{potential}$) for various soil permeability ($k_s = 10^{-4}$ m/s, $k_s = 10^{-5}$ m/s, $k_s = 10^{-6}$ m/s and $k_s = 10^{-8}$ m/s) at location A ($x = 55$ m, $y = 70$ m), B ($x = 65$ m, $y = 70$ m), C ($x = 60$ m, $y = 90$ m) and D ($x = 60$ m, $y = 50$ m) within the poro-elastoplastic seabed foundation at $t = 350$ s.

6.5 Liquefaction potential in the seabed foundation

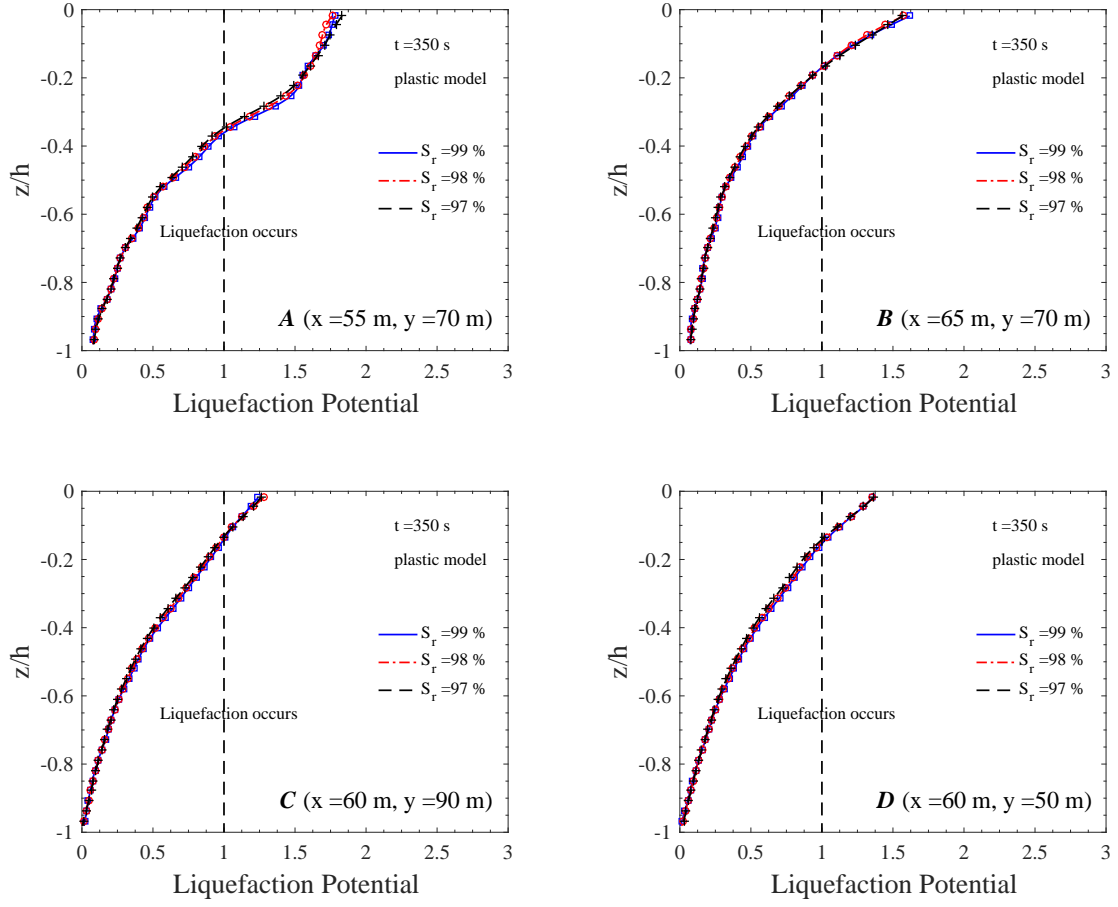


Figure 6.7 Vertical distribution of the liquefaction potential ($L_{potential}$) for various degree of saturation ($S_r = 99\%$, $S_r = 98\%$ and $S_r = 97\%$) at location A ($x = 55 \text{ m}$, $y = 70 \text{ m}$), B ($x = 65 \text{ m}$, $y = 70 \text{ m}$), C ($x = 60 \text{ m}$, $y = 90 \text{ m}$) and D ($x = 60 \text{ m}$, $y = 50 \text{ m}$) within the poro-elastoplastic seabed foundation at $t = 350$ s.

6.5 Liquefaction potential in the seabed foundation

seabed foundation. It can be clearly found that the liquefaction potential in the poro-elastic seabed foundation is much smaller than that in the poro-elastoplastic seabed foundation under the same wave/current loading, the value of $L_{potential}$ of the former foundation is only about 10 % of the latter foundation. For example, in the case of seabed with $k_s = 10^{-4}$ m/s, $L_{potential_{max}}$ is less than 0.25, indicating that the poro-elastic seabed foundation is not liquefied under such condition. A similar vertical distribution trend can be observed: the closer to the seabed surface, the greater the liquefaction potential value. Figure 6.8 depicts that $L_{potential_{max}}$ increases as k_s decreases, implying that the breakwaters built on a seabed with lower permeability may fail easier than that with higher permeability. Different from that in poro-elastoplastic seabed foundation, S_r has quite an impact on the stability of poro-elastic seabed foundation, as presented in Figure 6.9. It is observed that $L_{potential_{max}}$ increases as S_r decreases, and $L_{potential_{max}}$ reduces swiftly as S_r becomes 100 %. In summary, compared to the poro-elastoplastic seabed foundation, the liquefaction has minor effects on the structure stability in a poro-elastic seabed foundation. However, the liquefaction could still deteriorate the scouring around offshore structures and affect the stability of coastal structures.

Two sets of PZIII constitutive model parameters, representing the loose deposited poro-elastoplastic seabed foundation with relative density (D_r) equals to 40 % and the dense deposited poro-elastoplastic seabed foundation with D_r equals to 60 %, are used to study the foundation stability around the breakwaters. Figure 6.10 shows the vertical distribution of $L_{potential}$ in these two types of seabed foundation at $t = 350$ s. It can be seen from the figure that L_{depth} in loose sand is almost twice as deep as in dense sand at each location. For instance, L_{depth} at location behind the middle breakwater (i.e., location B ($x = 65$ m, $y = 70$ m)) reaches nearly 10 % and 20 % of the seabed thickness in dense foundation and loose foundation, respectively. This suggests that severe liquefaction is more likely to occur in loose seabed foundation with small D_r because loose sand is easier to be contracted under cyclic loading and causes greater pore pressure accumulation.

6.5.2 Effect of wave characteristics

Figures 6.11 and 6.12 represent the vertical distribution of $L_{potential}$ and $L_{potential_{max}}$ for various combination of waves and longshore currents ($U_0 = -0.6$ m/s, $U_0 = 0$ m/s and $U_0 = 0.3$ m/s) at location A, B, C and D in poro-elastoplastic seabed foundation and poro-elastic seabed foundation, respectively. As illustrated in the figures, the presence of the perpendicular longshore currents increase the liquefaction potential along the depth of seabed foundation and it becomes larger as the magnitude of velocity becomes larger. Additionally, the relative difference in liquefaction potential for different current velocity is more obvious near the

6.5 Liquefaction potential in the seabed foundation

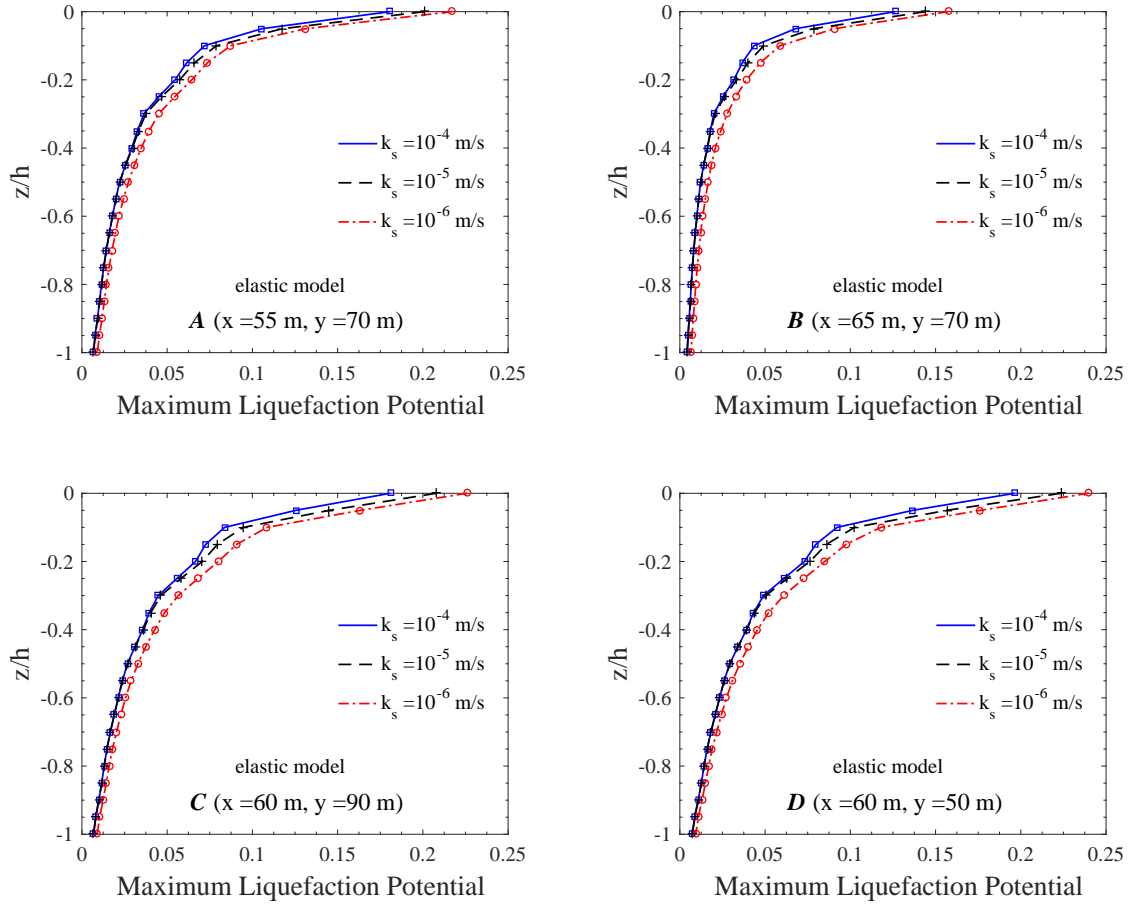


Figure 6.8 Vertical distribution of the maximum liquefaction potential ($L_{potential}$) for various soil permeability ($k_s = 10^{-4}$ m/s, $k_s = 10^{-5}$ m/s and $k_s = 10^{-6}$ m/s) at location A ($x=55$ m, $y=70$ m), B ($x=65$ m, $y=70$ m), C ($x=60$ m, $y=90$ m) and D ($x=60$ m, $y=50$ m) within the poro-elastic seabed foundation.

6.5 Liquefaction potential in the seabed foundation

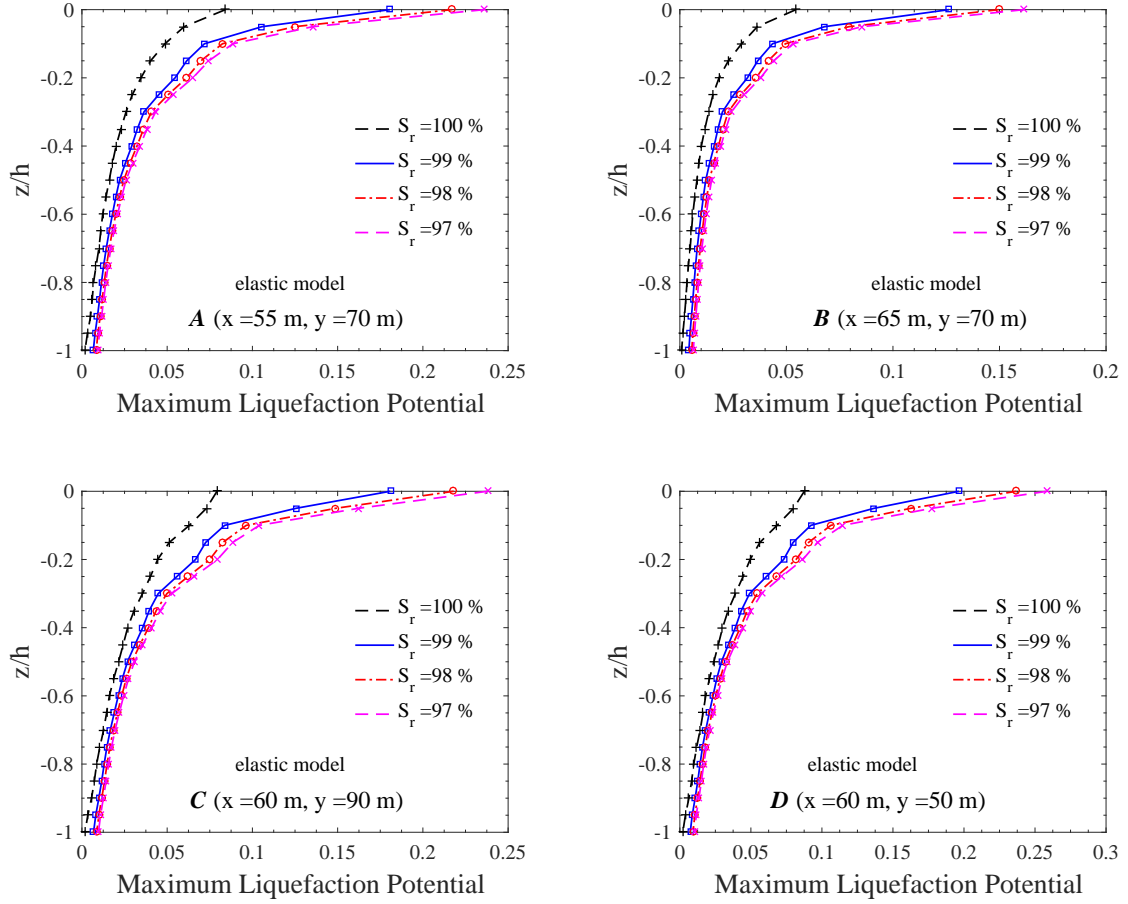


Figure 6.9 Vertical distribution of the maximum liquefaction potential ($L_{potential}$) for various degree of saturation ($S_r = 99\%$, $S_r = 98\%$ and $S_r = 97\%$) at location A ($x=55 \text{ m}$, $y=70 \text{ m}$), B ($x=65 \text{ m}$, $y=70 \text{ m}$), C ($x=60 \text{ m}$, $y=90 \text{ m}$) and D ($x=60 \text{ m}$, $y=50 \text{ m}$) within the poro-elastic seabed foundation.

6.5 Liquefaction potential in the seabed foundation

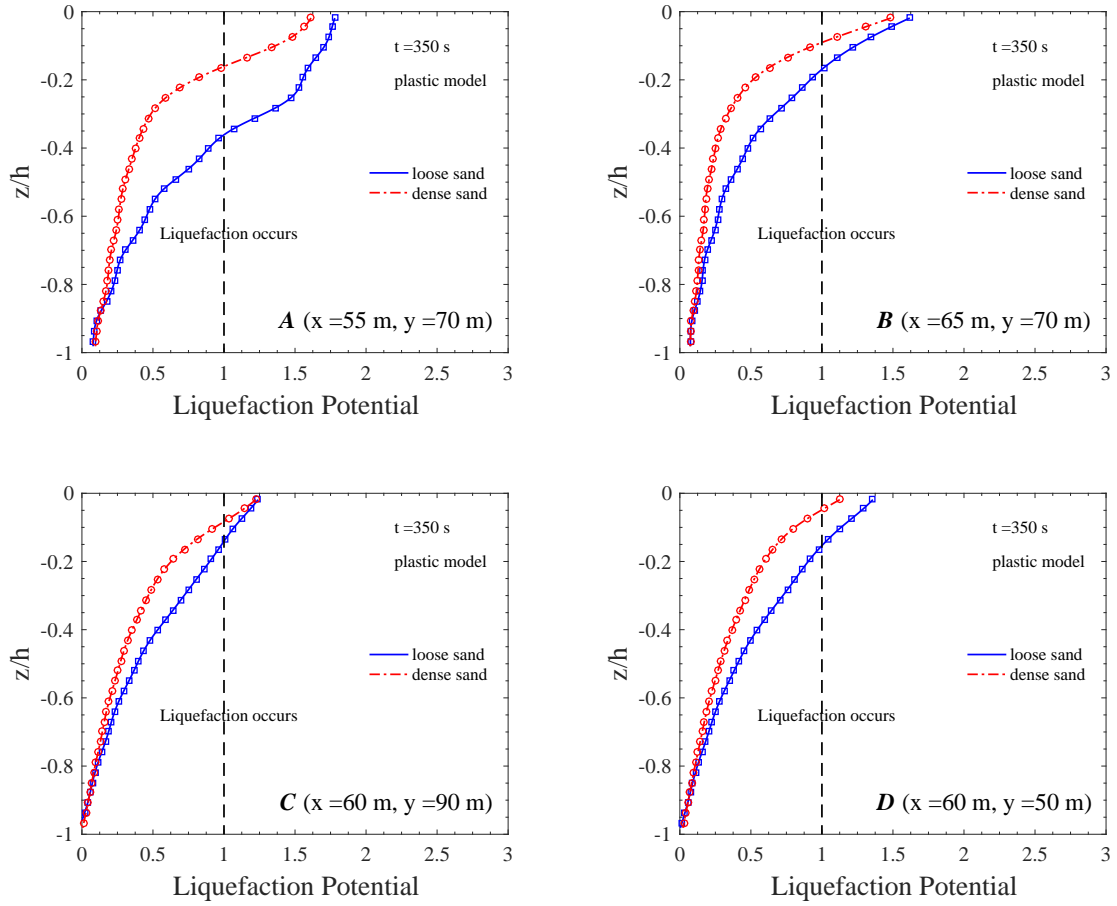


Figure 6.10 Vertical distribution of the liquefaction potential ($L_{potential}$) at location A ($x=55$ m, $y=70$ m), B ($x=65$ m, $y=70$ m), C ($x=60$ m, $y=90$ m) and D ($x=60$ m, $y=50$ m) within the loosely deposited poro-elastoplastic seabed foundation and densely deposited poro-elastoplastic seabed foundation at $t=350$ s.

6.6 Liquefaction zones in the seabed foundation

seabed surface. Therefore, it can be concluded that the effect of wave-current interaction is more significant in the upper seabed layer with stronger longshore currents and the current has little effect on the stability in the deeper seabed.

Among the fluid parameters, in addition to the ocean currents, wave height (H) and wave period (T) can also affect the stability of the foundation. As illustrated in Figures 6.13 and 6.14, the vertical distribution of liquefaction potential ($L_{potential}$) in the poro-elastoplastic seabed foundation increases as the increase of H and T . It implies that waves with larger height and longer period can pose more threats on foundation stability around the structures than a smaller height and shorter period wave under the same soil condition. As an example, at location A which is in front of the middle breakwater, the liquefaction depth (L_{depth}) is about 25 % of foundation thickness for $H = 1.7$ m, and reaches 35 % of foundation thickness for $H = 2.4$ m; and the difference of L_{depth} between the case with $T = 3.5$ s and $T = 4.5$ can reach up to 20 %. This may be explained by the fact that the wave steepness (H/L) becomes larger for a larger H and the relative water depth (d/L) becomes smaller for a longer T in the same water depth.

The vertical distributions of the maximum liquefaction potential ($L_{potential_{max}}$) for various wave height (H) and wave period (T) in a poro-elastic seabed foundation are shown in Figures 6.15 and 6.16, respectively. Similar influence relationship can be observed: $L_{potential_{max}}$ increases as H and T increase. However, the liquefaction potential predicted by the elastic model is much smaller than that predicted by the plastic model.

6.6 Liquefaction zones in the seabed foundation

Given the fact that the soil liquefaction is more severe in the poro-elastoplastic seabed foundation, this section will focus on the residual liquefaction zones predicted by the poro-elastoplastic model. According to the liquefaction criteria proposed by Jeng and Seymour (1997b), the liquefaction zones and liquefaction depth around breakwaters can be obtained. Figure 6.17 displays the residual liquefaction zones around breakwaters within a loosely packed poro-elastoplastic seabed foundation from $t = 250$ s to $t = 350$ s. Three typical locations are selected: $x = 54$ m which is located in front of the paralleled breakwaters, $x = 60$ m which is just beneath the paralleled breakwaters and $x = 66$ m which is behind the breakwaters. It can be observed from the figure that the liquefaction zones are still expanding in this late stage, however, the rate of expansion is slowing down. Another finding is that the soil in front of the paralleled breakwaters is most severely liquefied. While the liquefaction of soil behind the breakwaters is relatively less severe due to the protection from the breakwaters,

6.6 Liquefaction zones in the seabed foundation

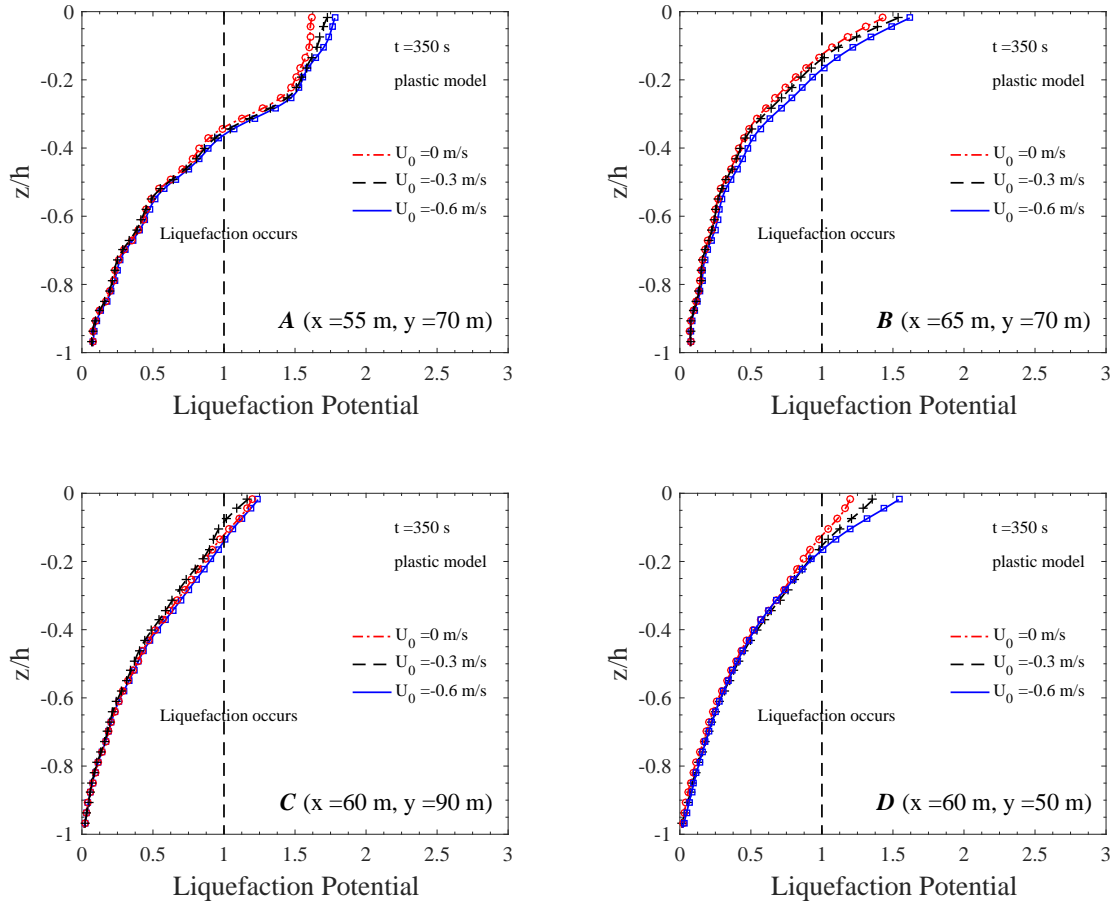


Figure 6.11 Vertical distribution of the liquefaction potential ($L_{potential}$) for various longshore currents conditions ($U_0 = -0.6$ m/s, $U_0 = 0$ m/s and $U_0 = -0.3$ m/s) at location A ($x = 55$ m, $y = 70$ m), B ($x = 65$ m, $y = 70$ m), C ($x = 60$ m, $y = 90$ m) and D ($x = 60$ m, $y = 50$ m) within the poro-elastoplastic seabed foundation at $t = 350$ s.

6.6 Liquefaction zones in the seabed foundation

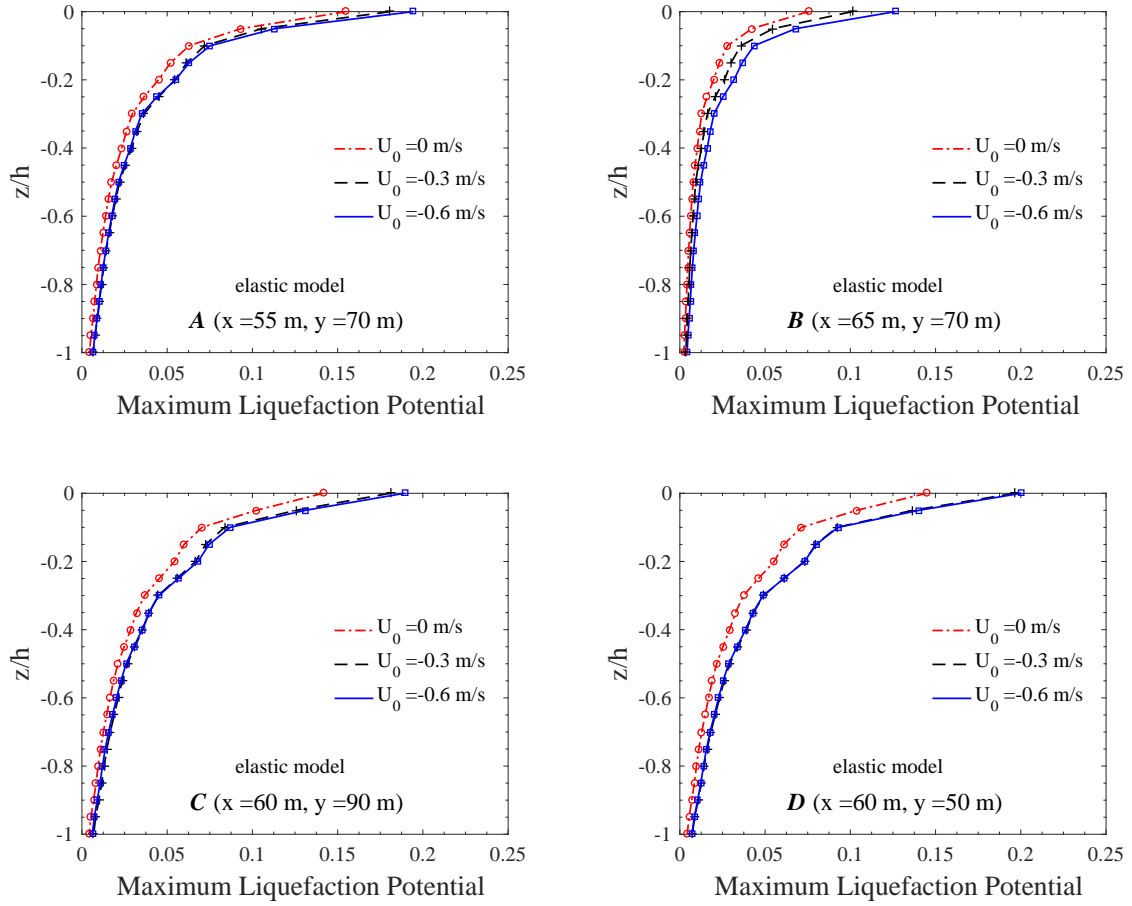


Figure 6.12 Vertical distribution of the maximum liquefaction potential ($L_{potential}$) for various longshore currents conditions ($U_0 = -0.6 \text{ m/s}$, $U_0 = 0 \text{ m/s}$ and $U_0 = -0.3 \text{ m/s}$) at location A ($x = 55 \text{ m}$, $y = 70 \text{ m}$), B ($x = 65 \text{ m}$, $y = 70 \text{ m}$), C ($x = 60 \text{ m}$, $y = 90 \text{ m}$) and D ($x = 60 \text{ m}$, $y = 50 \text{ m}$) within the poro-elastic seabed foundation.

6.6 Liquefaction zones in the seabed foundation

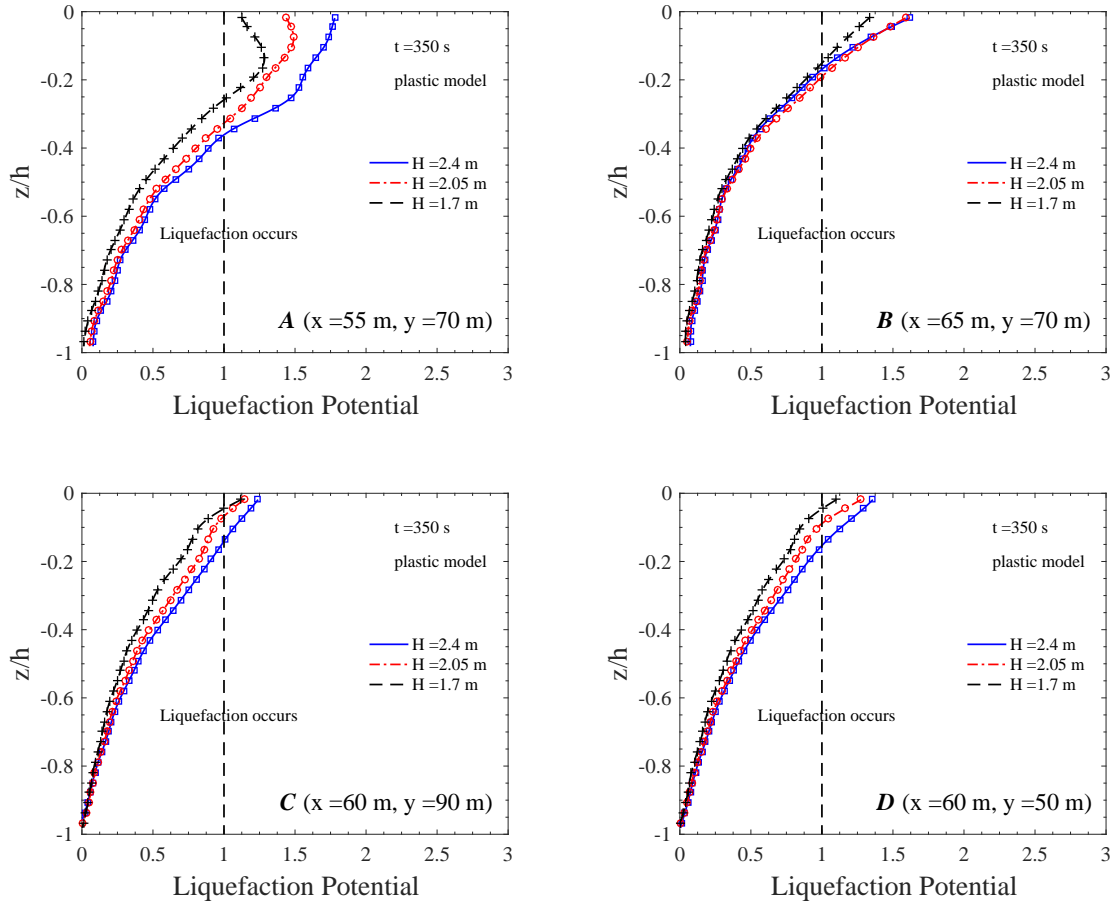


Figure 6.13 Vertical distribution of the liquefaction potential ($L_{potential}$) for various wave height ($H = 2.4$ m, $H = 2.05$ m and $H = 1.7$ m) at location A ($x = 55$ m, $y = 70$ m), B ($x = 65$ m, $y = 70$ m), C ($x = 60$ m, $y = 90$ m) and D ($x = 60$ m, $y = 50$ m) within the poro-elastoplastic seabed foundation at $t = 350$ s.

6.6 Liquefaction zones in the seabed foundation

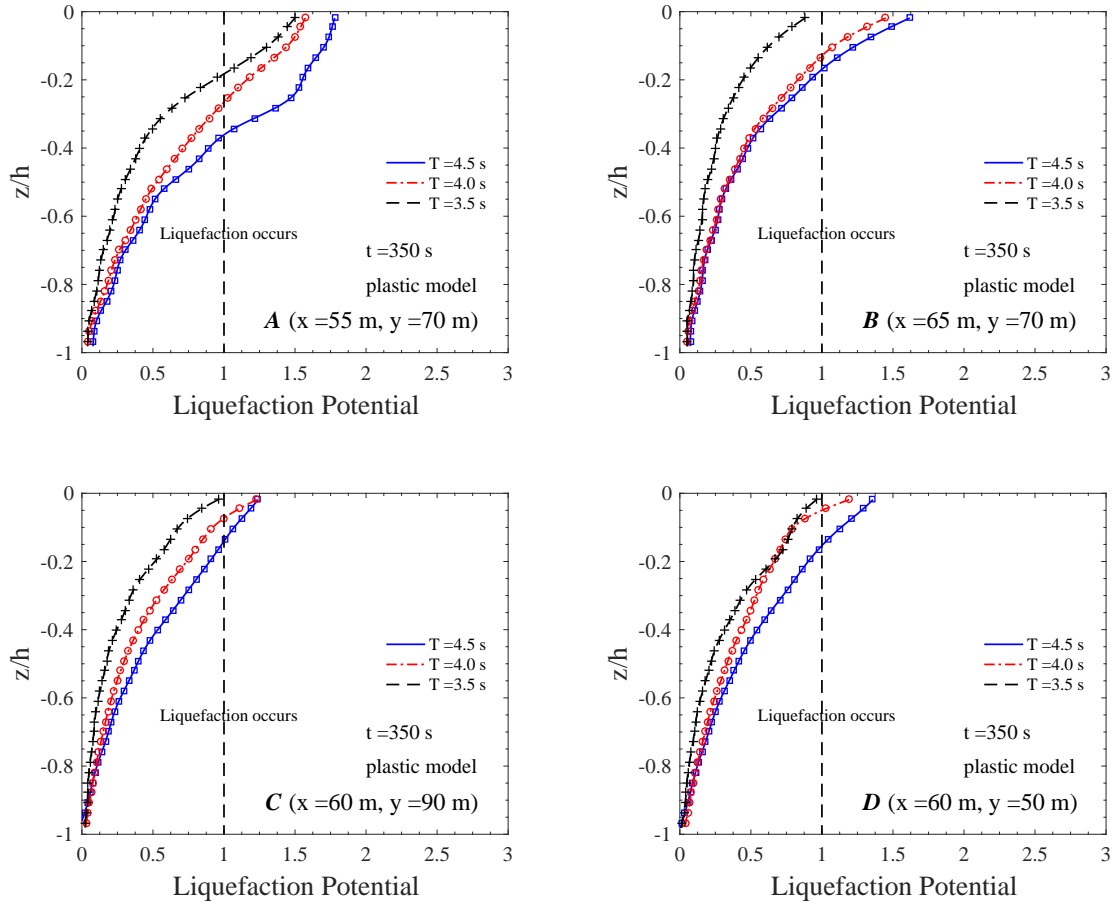


Figure 6.14 Vertical distribution of the liquefaction potential ($L_{potential}$) for various wave period ($T = 4.5$ s, $T = 4.0$ s and $T = 3.5$ s) at location A ($x = 55$ m, $y = 70$ m), B ($x = 65$ m, $y = 70$ m), C ($x = 60$ m, $y = 90$ m) and D ($x = 60$ m, $y = 50$ m) within the poro-elastoplastic seabed foundation at $t = 350$ s.

6.6 Liquefaction zones in the seabed foundation

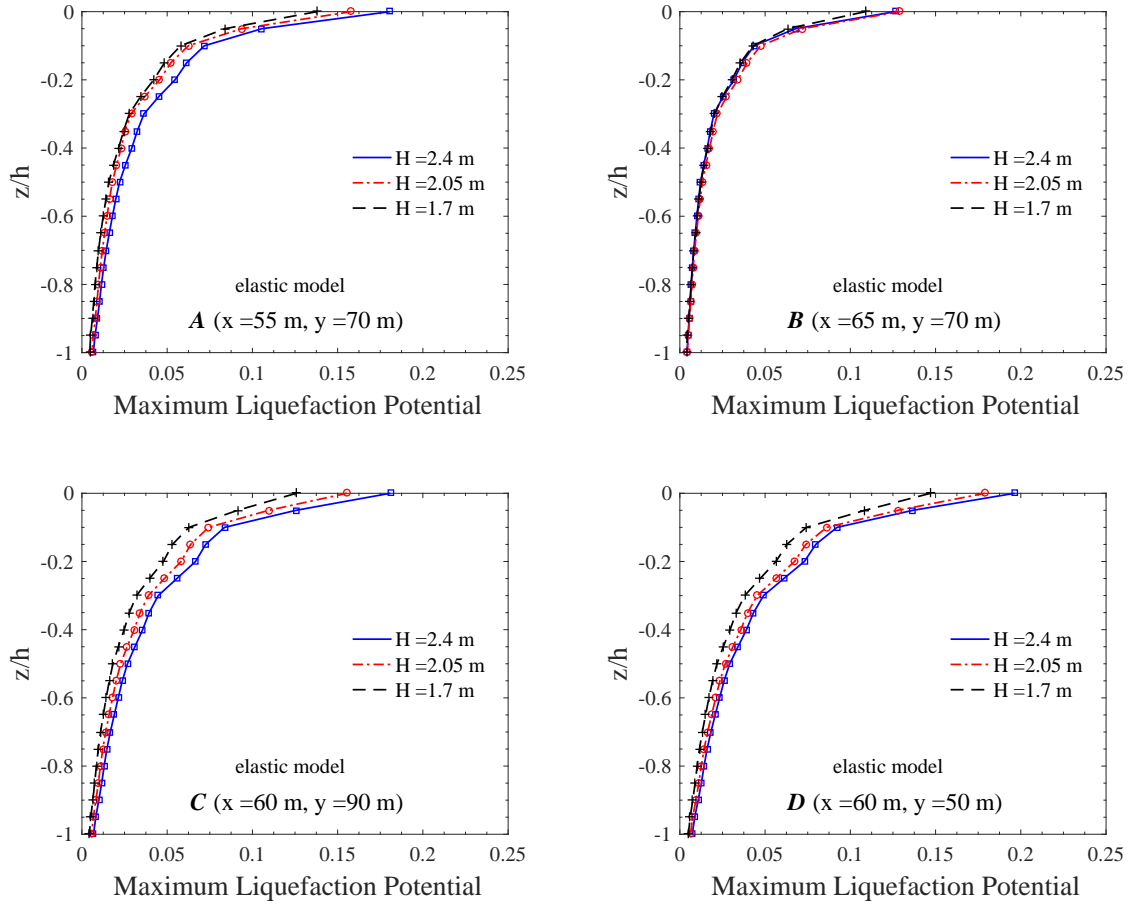


Figure 6.15 Vertical distribution of the maximum liquefaction potential ($L_{potential}$) for various wave height ($H = 2.4$ m, $H = 2.05$ m and $H = 1.7$ m) at location A ($x = 55$ m, $y = 70$ m), B ($x = 65$ m, $y = 70$ m), C ($x = 60$ m, $y = 90$ m) and D ($x = 60$ m, $y = 50$ m) within the poro-elastic seabed foundation.

6.6 Liquefaction zones in the seabed foundation

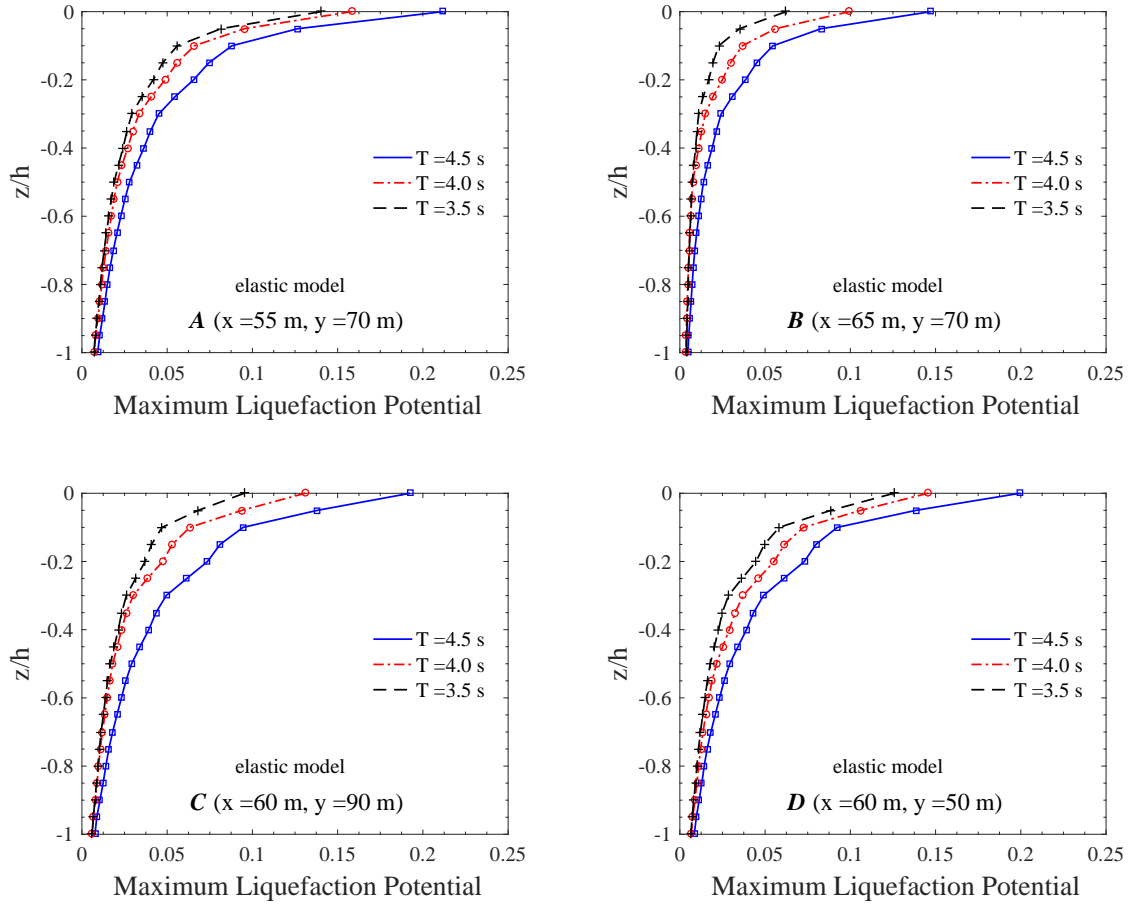


Figure 6.16 Vertical distribution of the maximum liquefaction potential ($L_{potential}$) for various wave period ($T = 4.5$ s, $T = 4.0$ s and $T = 3.5$ s) at location A ($x = 55$ m, $y = 70$ m), B ($x = 65$ m, $y = 70$ m), C ($x = 60$ m, $y = 90$ m) and D ($x = 60$ m, $y = 50$ m) within the poro-elastic seabed foundation.

6.6 Liquefaction zones in the seabed foundation

only small areas of liquefaction appeared which concentrate on the gap region between breakwaters. For example, at $t = 350$ s, the largest liquefaction depth in the slice of $x = 54$ m is around 30 % of foundation thickness and less than 20 % in the slice of $x = 66$ m.

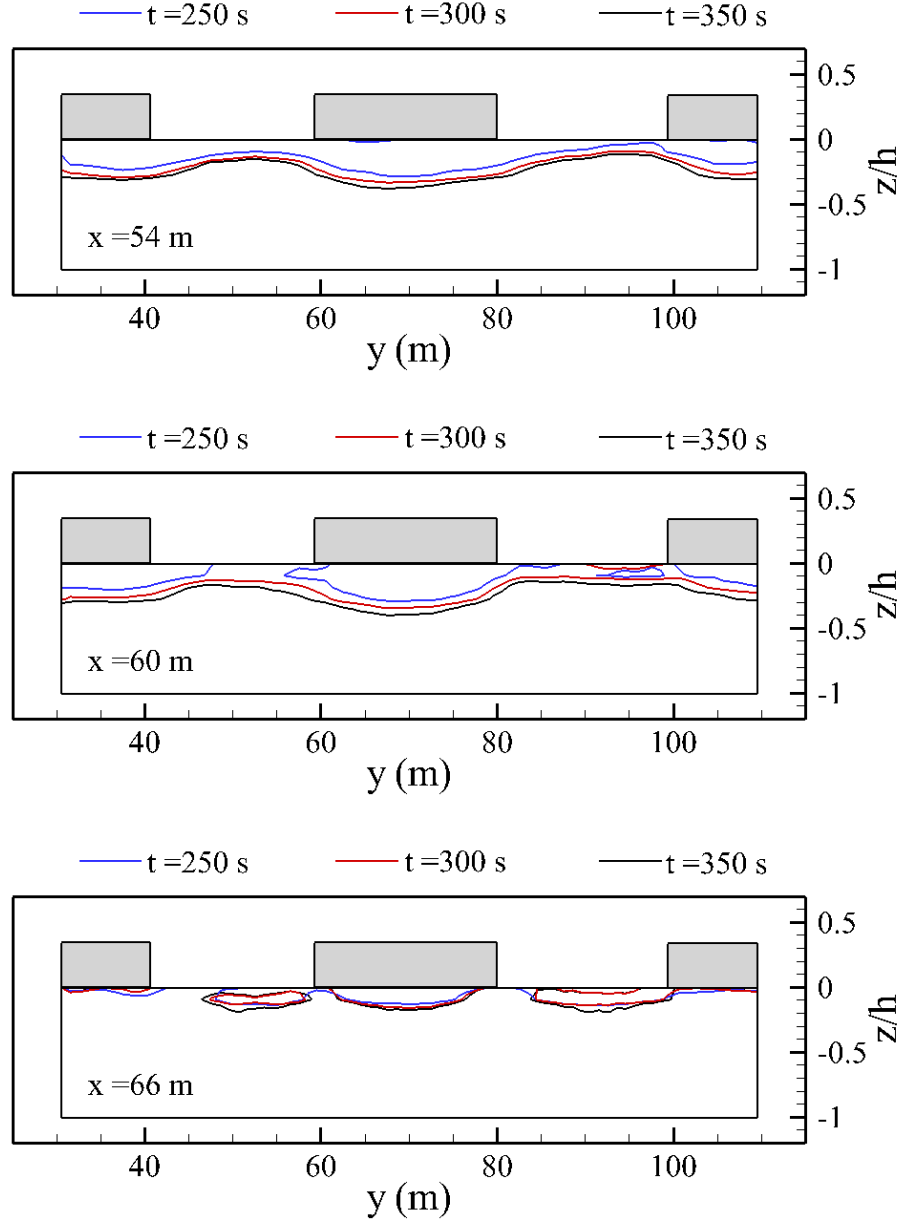


Figure 6.17 Liquefaction zones within a loosely packed poro-elastoplastic seabed foundation around breakwaters at $t = 250, 300$ and 350 s for three typical slices: $x = 54, 60$ and 66 m.

Figure 6.18 illustrates the liquefaction depth (L_{depth}) within a densely packed poro-elastoplastic seabed foundation at $t = 300$ s. The 3D effect of wave/current loading around the

structures can be clearly observed from the figure. From the figure, the largest L_{depth} occurs in front of the middle breakwater, which is over 2 m. This is because the strong non-linear interactions between the incident waves, reflected waves and longshore current makes this area more active comparing to other regions. The segmented coast-paralleled breakwaters can partly provide shelter area behind the breakwater, however, due to that the waves can pass through the gaps between the breakwaters and the existence of diffracted waves, there will still be a certain degree of liquefaction behind the breakwaters. As shown in the figure, the liquefaction zones behind the breakwaters are relatively shallow and distributed dispersively.

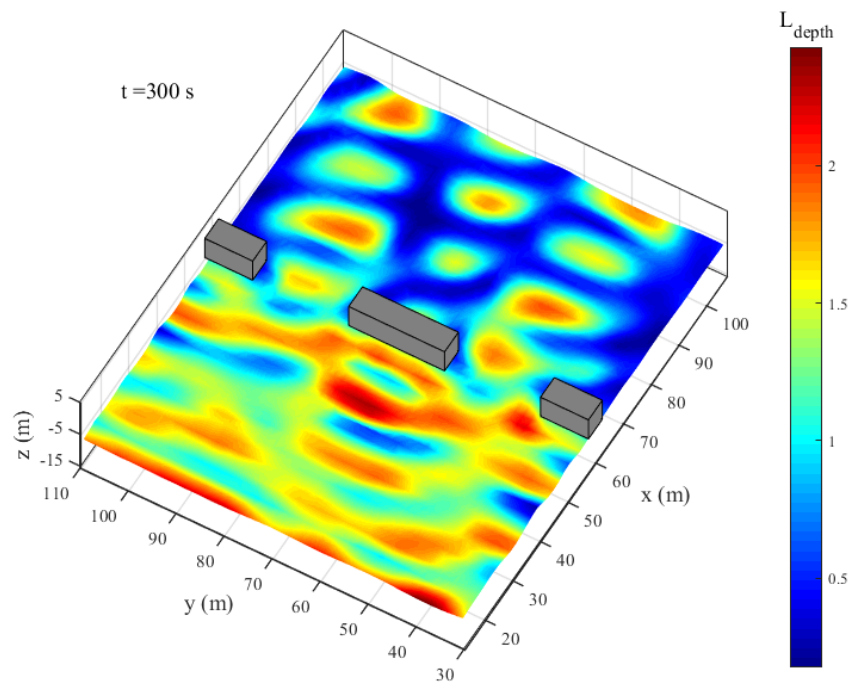


Figure 6.18 Liquefaction depth within a densely packed seabed foundation at $t = 300$ s.

6.7 Summary

In this chapter, the dynamic behaviour of seabed foundation around shore-paralleled detached breakwaters under combined cyclic wave and longshore currents loading is investigated by adopting the 3D integrated numerical model, in which the VARANS equations are used for governing the flow inside and outside the porous breakwater, while the $u - p$ approximation is used for linking the soil-pore fluid interactions. The liquefaction potential and liquefaction

zones around the structures within both poro-elastic seabed foundation and poro-elastoplastic seabed foundation have been examined for various wave/soil parameters. Based on the analyses of the numerical results, some conclusions can be drawn:

- The presence of the longshore currents can constantly alter the wave propagation and have an impact on the hydrodynamic process and soil behaviour around the structure. From the numerical results, it is concluded that the longshore currents make the wave height larger in the vicinity and increase the liquefaction potential along the depth of seabed foundation, and it becomes larger as the magnitude of currents velocity becomes larger.
- The stress status of porous seabed foundation after the consolidation process is determined first and applied as the initial condition in the dynamic analysis of wave/current-seabed-breakwater interactions. It is found that the construction of breakwaters can significantly increase the effective stress and shear stress in the nearby region. The increase of initial effective stress for the dynamic analysis makes the liquefaction more difficult to occur, which indicates that ignoring the consolidation process would overestimate the liquefaction potential within the seabed foundation.
- Numerical results show that, under the same wave/current loading, the liquefaction potential within the poro-elastic seabed foundation is much smaller than that in the poro-elastoplastic seabed foundation. It reveals that the residual liquefaction within a poro-elastoplastic foundation has critical effect on structure stability. Since the plastic soil is common in natural environment, it becomes particularly important to study the liquefaction in poro-elastoplastic seabed foundation.
- Based on parametric studies, the liquefaction potential is larger in a loosely deposited seabed foundation with poor drainage conditions under large wave height and long wave period.

Chapter 7

Conclusions and Future Works

7.1 Conclusions

The main objective of this thesis is to numerically assess the seabed foundation stability around breakwaters by investigating the soil response and liquefaction potential that involved in fluid-seabed-structure interactions. To do this, the 2D and 3D integrated numerical models that consist of flow sub-model, seabed sub-model and the integration module between two sub-models have been developed in this thesis. The flow model employed for modelling wave-current-structure interactions was developed within the framework of open-source CFD toolbox OpenFOAM®. The VARANS equations were adopted as the governing equations for simulating the two incompressible phases (i.e., water and air) inside and outside of the porous structures, in which the linear, non-linear and unsteady flow within the porous media were considered. The VOF method was adopted to track the free surface elevation which is an Eulerian approach. The effects of random, non-linear and diffusive turbulence and vortexes generated in the vicinity of breakwaters were also considered by solving the Volume-Averaged $k - \varepsilon$ turbulence model.

The seabed model was based on 2D finite element program, DIANA-SWANDYNE II, and its extended 3D version, DYNE3WAC. The Biot's dynamic equations, $u - p$ approximations, were the governing equations for the interactions between solid skeleton and pore fluid in a porous seabed, in which the relative displacements of pore fluid to soil particles are ignored and the acceleration of pore fluid and solid particles is included. Two constitutive models were incorporated into the seabed model: one is linear poro-elastic model governed by Hooke's law which is used to predict the transient/oscillatory soil response within the poro-elastic seabed foundation; and the other one is PZIII model based on generalised plasticity

theory which is used to predict the residual soil response within the poro-elastoplastic seabed foundation. A one-way coupling algorithm was developed between the flow sub-model and seabed sub-model through the pressure continuity on the common faces including the surface of seabed and structures for the integration of numerical model. A comprehensive set of validations has been performed by comparing with laboratory data and analytical solutions to prove the reliability of the integrated numerical model.

By adopting the integrated numerical models, one 2D numerical study and two 3D numerical studies have been conducted: the soil response and liquefaction potential around multiple breakwaters with Bragg reflection (2D case); seabed foundation stability around breakwaters at river mouth (3D case); and seabed foundation stability around coast-paralleled detached breakwaters (3D case). Some specific key findings drawn from these numerical studies were concluded as follows:

- The hydrodynamic properties in the vicinity of breakwaters are significantly affected by the strong non-linear wave-current-structure interactions which can further induce the seabed foundation instability. The 2D model is only able to investigate the middle cross-section of breakwater under perpendicular incident waves, If a more complicated interaction is involved, for example, the incident waves, reflected waves, diffracted waves, oblique current stream and complex breakwater configurations, the 3D integrated model has to be used for simulating such scenarios.
- The pre-assessed consolidation process of breakwater under hydrostatic pressure and self-weight of the structure is essential in the assessment of breakwater foundation stability since the construction of breakwaters can dramatically increase the effective stresses and shear stresses within the seabed foundation near to the structure. The newly estimated stress state after the completion of consolidation process will be applied as initial condition in the later dynamic analyses of soil responses. It was found that ignoring the pre-consolidation process can cause great overestimation of liquefaction potential within the seabed foundation, since it increases the initial effective stresses which raises the liquefaction threshold.
- The presence of the currents in the fluid domain has non-negligible effects on the dynamic soil responses and liquefaction potential in the seabed foundation: the following currents aggravate the soil responses and increase the liquefaction potential, while the opposing currents mitigate the soil responses and avoid the occurrence of liquefaction to some extent. It was also found that such influence increases with the increasing of currents velocity. Additionally, other forms of current stream, such as the

river currents (in 3D numerical study I) and longshore currents (in 3D numerical study II) that interact with waves obliquely, also have impact on the dynamic behaviour of seabed foundation.

- The numerical results predicted by the poro-elastic and poro-elastoplastic constitutive models showed that the mechanism of oscillatory soil response and residual soil response, and the associated momentary liquefaction and residual liquefaction are completely different. It was found that, under the same wave/current loading, the liquefaction potential within the poro-elastic seabed foundation is much smaller than that within the poro-elastoplastic seabed foundation. The residual liquefaction related to the soil volume contraction and pore pressure build-up is much easier to occur and can cause more severe damage to the structure foundation stability than the momentary liquefaction whose impact is minor and limited. Hence, it can be concluded that the residual liquefaction is the critical factor for the structure stability. Since the poro-elastoplastic soil is common in natural environment, it becomes particularly important to study the residual liquefaction around the structures.
- Parametric studies indicated that the wave characteristics and soil properties have significant effect on the breakwater foundation stability under cyclic wave loading. The liquefaction potential is larger in a loosely deposited seabed foundation with poor drainage conditions under large wave height and long wave period.

7.2 Future works

There are plenty of improvements that can be done in the future in order to achieve better results. Some of the open issues that deserve further research are presented as follows:

- In this thesis, the wave loading was limited to regular waves (i.e., Stokes waves and Cnoidal waves) that were given in terms of a wave frequency, a wave height and the phase factor. However, in a realistic marine environment, the waves are far from being regular as the wind blow over the open ocean, and it is very difficult to keep track of an individual wave for more than a few periods. Therefore, the random waves system appearing irregular water surface elevation around the marine structures is desired. Dissimilar to the regular waves, the random waves can induce the different soil response and cause the structure foundation instability. In addition, the interaction between random waves and currents can also bring difference on the assessment of foundation stability.

- The poro-elastoplastic constitutive model PZIII adopted in the seabed model in this thesis is an advanced constitutive model to describe both the oscillatory and residual components of soil response simultaneously under the cyclic wave loading. However, PZIII model is not able to describe the mechanical behaviour of soil under tensile stress or zero stress, which makes it not suitable for modelling the sequence of post-liquefaction soil behaviour. In this thesis, only the liquefaction potential is included without considering the post-liquefaction behaviour. In other words, this study focus on the soil behaviour up to the onset of liquefaction. To predict the process of post-liquefaction, the model proposed by Sassa et al. (2001) and Liu et al. (2009) should be used. However, their models were based on one-dimensional approach, which is only valid for the wave-seabed interactions without a structure. To author's best knowledge, there is no reference available in the literature for the post-liquefaction with a structure (i.e., 2D or 3D cases). Therefore, further development of the numerical model is desired to describe post-liquefaction soil behaviour in the future.
- The integration method in this thesis is a one-way coupling algorithm, in which only the hydrodynamic pressure extracted from the flow sub-model will be applied on the surface of the seabed and structure in the seabed sub-model. This integration method is relatively simple as it ignores the shear effect of fluid on the surface of seabed and structure, and it also does not consider the effect of motion of soil and structure on the fluid domain. As a consequence, in order to achieve the more realistic simulation, the integration algorithm between two sub-models needs further development.
- In this thesis, the marine structure considered is the breakwaters. However, the 2D and 3D integrated numerical model can also be applied to simulate other marine structures such as pipelines and pile foundations by changing the computational geometry and adjusting the structure boundary conditions.

References

- Biot, M. A. (1941). General theory of three-dimensional consolidation. *Journal of Applied Physics*, 26(2):155–164.
- Biot, M. A. (1955). Theory of elasticity and consolidation for a porous anisotropic solid. *Journal of Applied Physics*, 26(2):182–185.
- Biot, M. A. (1956a). Theory of deformation of a porous viscoelastic anisotropic solid. *Journal of Applied Physics*, 27(5):459–467.
- Biot, M. A. (1956b). Theory of propagation of elastic waves in a fluid-saturated porous solid, Part I: Low frequency range. *Journal of Acoustic Society, American*, 28(2):168–177.
- Biot, M. A. (1956c). Theory of propagation of elastic waves in a fluid-saturated porous solid, Part II: High frequency range. *Journal of Acoustic Society, American*, 28(2):179–191.
- Biot, M. A. (1962). Mechanics of deformation and acoustic propagation in porous media. *Journal of Applied Physics*, 33(4):1482–1498.
- Burcharth, H. F. and Andersen, O. K. (1995). On the one-dimensional steady and unsteady porous flow equations. *Coastal Engineering*, 24(3-4):233–257.
- Chan, A. H. C. (1988). *A unified finite element solution to static and dynamic problems of geomechanics*. PhD thesis, University of Wales, Swansea Wales.
- Chen, T. W., Huang, L. H., and Song, C. H. (1997). Dynamic response of poroelastic bed to nonlinear water waves. *Journal of Engineering Mechanics, ASCE*, 123(10):1041–1049.
- Cheng, L., Sumer, B. M., and Fredsøe, J. (2001). Solution of pore pressure build up due to progressive waves. *International Journal for Numerical and Analytical Methods in Geomechanics*, 25:885–907.
- del Campo, J. M. and Vicente, N. (2011). Failures of harbour walls at malaga and barcelona. *Bulletin of Engineering Geology and the Environment*, 70(1):1–6.
- del Jesus, M. (2011). *Three-dimensional interaction of water waves with maritime structures*. PhD thesis, University of Cantabria, Santander, Spain.
- Drucker, D. C. (1957). Soil mechanics and work-hardening theories of plasticity. *Trans. ASCE*, 122:338–346.

- Drucker, D. C. and Prager, W. (1952). Soil mechanics and plastic analysis or limit design. *Quarterly of Applied Mathematics*, 10(2):157–165.
- Dunn, S. L., Vun, P. L., Chan, A. H. C., and Damgaard, J. S. (2006). Numerical modeling of wave-induced liquefaction around pipelines. *Journal of Waterway, Port, Coastal, and Ocean Engineering*, ASCE, 132(4):276–288.
- Engelund, F. (1953). *On the laminar and turbulent flows of ground water through homogeneous sand*. Transactions of the Danish Academy of Technical Sciences. No. 3.
- Foo, C. S. X., Liao, C., and Chen, J. J. (2019). Two-dimensional numerical study of seabed response around a buried pipeline under wave and current loading. *Journal of Marine Science and Engineering*, 7(3):66.
- Gatmiri, B. (1990). A simplified finite element analysis of wave-induced effective stress and pore pressures in permeable sea beds. *Géotechnique*, 40(1):15–30.
- Gatmiri, B. (1992). Response of cross-anisotropic seabed to ocean waves. *Journal of Geotechnical Engineering*, ASCE, 118(9):1295–1314.
- Guo, Z., Jeng, D.-S., and Guo, W. (2014). Simplified approximation of wave-induced liquefaction in a shallow porous seabed. *International Journal for Geomechanics*, ASCE, 14(4):06014008.
- Higuera, P. (2015). *Application of computational fluid dynamics to wave action on structures*. Phd thesis, University of Cantabria, Santander, Spain.
- Higuera, P., Lara, J. L., and Losada, I. J. (2013). Realistic wave generation and active wave absorption for Navier–Stokes models: Application to OpenFOAM®. *Coastal Engineering*, 71:102–118.
- Higuera, P., Lara, J. L., and Losada, I. J. (2014a). Three-dimensional interaction of waves and porous coastal structures using OpenFOAM®. Part I: Formulation and validation. *Coastal Engineering*, 83:243–258.
- Higuera, P., Lara, J. L., and Losada, I. J. (2014b). Three-dimensional interaction of waves and porous coastal structures using OpenFOAM®. Part II: Application. *Coastal Engineering*, 83:259–270.
- Hirt, C. W. and Nichols, B. D. (1981). Volume of fluid (VOF) method for the dynamics of free boundaries. *Journal of Computational Physics*, 39(1):201–225.
- Hsieh, P. C., Huang, L. H., and Wang, T. W. (2001). Dynamic response of soft poroelastic bed to linear water waves – A boundary layer approximation. *International Journal for Numerical and Analytical Methods in Geomechanics*, 25(7):651–674.
- Hsu, J. R. C. and Jeng, D.-S. (1994). Wave-induced soil response in an unsaturated anisotropic seabed of finite thickness. *International Journal for Numerical and Analytical Methods in Geomechanics*, 18(11):785–807.
- Hsu, J. R. C., Jeng, D.-S., and Lee, C. P. (1995). Oscillatory soil response and liquefaction in an unsaturated layered seabed. *International Journal for Numerical and Analytical Methods in Geomechanics*, 19(12):825–849.

- Hsu, J. R. C., Jeng, D.-S., and Tsai, C. P. (1993). Short-crested wave-induced soil response in a porous seabed of infinite thickness. *International Journal for Numerical and Analytical Methods in Geomechanics*, 17(8):553–576.
- Hsu, T. J., Sakakiyama, T., and Liu, P. L.-F. (2002). A numerical model for wave motions and turbulence flows in front of a composite breakwater. *Coastal Engineering*, 46(1):25–50.
- Huang, L. H. and Chwang, A. T. (1990). Trapping and absorption of sound waves. II: A sphere covered with a porous layer. *Wave Motion*, 12(5):401–414.
- Huang, L. H. and Song, C. H. (1993). Dynamic response of poro-plastic bed to water waves. *Journal of Hydraulics Engineering, ASCE*, 119(9):1003–1020.
- Hughes, B. A. and Stewart, R. W. (1961). Interaction between gravity waves and a shear flow. *Journal of Fluid Mechanics*, 10(3):385–400.
- Jeng, D.-S. (1996a). Wave-induced liquefaction potential at the tip of a breakwater. *Applied Ocean Research*, 18(5):229–241.
- Jeng, D.-S. (1996b). Wave-induced liquefaction potential in a cross-anisotropic seabed. *Journal of the Chinese Institute of Engineering*, 19(1):59–70.
- Jeng, D.-S. (1998). Wave-induced seabed response in a cross-anisotropic seabed in front of a breakwater: An analytical solution. *Ocean Engineering*, 25(1):49–67.
- Jeng, D.-S. (2003). Wave-induced sea floor dynamics. *Applied Mechanics Reviews*, 56(4):407–429.
- Jeng, D.-S. (2013). *Porous Models for Wave-seabed Interactions*. Springer, Berlin Heidelberg, Germany.
- Jeng, D.-S. and Cha, D. H. (2003). Effects of dynamic soil behavior and wave non-linearity on the wave-induced pore pressure and effective stresses in porous seabed. *Ocean Engineering*, 30(16):2065–2089.
- Jeng, D.-S., Cha, D. H., Lin, Y. S., and Hu, P. S. (2000). Analysis on pore pressure in an anisotropic seabed in the vicinity of a caisson. *Applied Ocean Research*, 22(6):317–329.
- Jeng, D.-S., Cha, D. H., Lin, Y. S., and Hu, P. S. (2001). Wave-induced pore pressure around a composite breakwater. *Ocean Engineering*, 28(10):1413–1432.
- Jeng, D.-S., Cheng, L., and Lin, Y. S. (1998). Numerical study for wave-seabed interaction in gibson soil. In *The 8th Biennial Computational Techniques and Application Conference*, pages 321–328, Adelaide, Australia.
- Jeng, D.-S. and Lin, Y. S. (1996). Finite element modelling for water waves–soil interaction. *Soil Dynamics and Earthquake Engineering*, 15(5):283–300.
- Jeng, D.-S. and Lin, Y. S. (1997). Non-linear wave-induced response of porous seabed: A finite element analysis. *International Journal for Numerical and Analytical Methods in Geomechanics*, 21(1):15–42.

- Jeng, D.-S. and Ou, J. (2010). 3-D models for wave-induced pore pressure near breakwater heads. *Acta Mechanica*, 215(1-4):85–104.
- Jeng, D.-S. and Rahman, M. S. (2000). Effective stresses in a porous seabed of finite thickness: Inertia effects. *Canadian Geotechnical Journal*, 37(6):1383–1392.
- Jeng, D.-S. and Rahman, M. S. (2001). Wave-induced oscillatory soil response: Difference between quasi-static and dynamic solutions. In *Computer Methods and Advances in Geomechanics*, volume 2, pages 1103–1106. A. A. Balkema.
- Jeng, D.-S., Rahman, M. S., and Lee, T. L. (1999). Effects of inertia forces on wave-induced seabed response. *International Journal of Offshore and Polar Engineering*, 9(4):307–313.
- Jeng, D.-S. and Seymour, B. R. (1997a). Response in seabed of finite depth with variable permeability. *Journal of Geotechnical and Geoenvironmental Engineering, ASCE*, 123(10):902–911.
- Jeng, D.-S. and Seymour, B. R. (1997b). Wave-induced pore pressure and effective stresses in a porous seabed with variable permeability. *Journal of Offshore Mechanics and Arctic Engineering, ASME*, 119(4):226–233.
- Jeng, D.-S. and Seymour, B. R. (2007). A simplified analytical approximation for pore-water pressure build-up in a porous seabed. *Journal of Waterway, Port, Coastal, and Ocean Engineering, ASCE*, 133(4):309–312.
- Jeng, D.-S., Seymour, B. R., and Li, J. (2007). A new approximation for pore pressure accumulation in marine sediment due to water wave. *International Journal for Numerical and Analytical Methods in Geomechanics*, 31(1):53–69.
- Jeng, D.-S. and Zhao, H. (2015). Two-dimensional model for pore pressure accumulations in marine sediments. *Journal of the Waterway, Port, Coastal and Ocean Engineering, ASCE*, 141:04014042.
- Katona, M. G. and Zienkiewicz, O. C. (1985). A unified set of single step algorithms. Part 3: The Beta- m method, a generalisation of the newmark scheme. *International Journal for Numerical Methods in Engineering*, 21(7):1345–1359.
- Kumagai, T. and Foda, M. A. (2002). Analytical model for response of seabed beneath composite breakwater to wave. *Journal of Waterway, Port, Coastal, and Ocean Engineering, ASCE*, 128(2):62–71.
- Lara, J. L., Garcia, N., and Losada, I. J. (2006). Rans modeling applied to random wave interaction with submerged permeable structures. *Coastal Engineering*, 53(5-6):395–417.
- Le Méhauté, B. (1976). *An introduction to hydrodynamics and water waves*. Springer-Verlag, New York.
- Li, X., Zhang, J., and Zhang, H. (2002). Instability of wave propagation in saturated poroelastoplastic media. *International Journal for Numerical and Analytical Methods in Geomechanics*, 26(6):563–578.

- Liao, C., Jeng, D.-S., and Zhang, L. L. (2015a). Analytical approximation for dynamic soil response of a porous seabed under combined wave and current loading. *Journal of Coastal Research*, 31(5):1120–1128.
- Liao, C., Tong, D., Jeng, D.-S., and Zhao, H. (2018). Numerical study for wave-induced oscillatory pore pressures and liquefaction around impermeable slope breakwater heads. *Ocean Engineering*, 157:364–375.
- Liao, C., Zhao, H., and Jeng, D.-S. (2015b). Poro-elastoplastic model for wave-induced liquefaction. *Journal of Offshore Mechanics and Arctic Engineering, ASME*, 137(4):042001.
- Lin, P. and Liu, P. L.-F. (1999). Internal wave-maker for Navier–Stokes equations models. *Journal of Waterway, Port, Coastal, and Ocean Engineering, ASCE*, 125(4):207–415.
- Lin, Y. S. and Jeng, D.-S. (1996). Response of poro-elastic seabed to a 3-D wave system: A finite element analysis. *Coastal Engineering in Japan*, 39(2):165–183.
- Lin, Y. S. and Jeng, D.-S. (1997). The effect of variable permeability on the wave-induced seabed response. *Ocean Engineering*, 24(7):623–643.
- Lin, Y. S. and Jeng, D.-S. (2000). Effects of variable shear modulus on wave-induced seabed response. *Journal of the Chinese Institute of Engineers*, 24(1):109–115.
- Liu, B., Jeng, D.-S., and Zhang, J.-S. (2014). Dynamic response of a porous seabed of finite depth due to combined wave and current loadings: Inertial forces. *Journal of Coastal Research*, 30(4):765–776.
- Liu, P. L. F. (1973). Damping of water waves over porous bed. *Journal of the Hydraulics Division, ASCE*, 99(12):2263–2271.
- Liu, P. L.-F. (1977). On gravity waves propagated over a layered permeable bed. *Coastal Engineering*, 1:135–148.
- Liu, X. F. and García, M. H. (2006). Numerical simulation of sea bed response under waves with coupled solver of Biot consolidation equations and free surface water flow. In *The Seventh ISOPE Pacific/Asia Offshore Mechanics Symposium*. International Society of Offshore and Polar Engineers.
- Liu, X. F., García, M. H., and Muscari, R. (2007). Numerical investigation of seabed response under waves with free-surface water flow. *International Journal of Offshore and Polar Engineering*, 17(02).
- Liu, Z., Jeng, D.-S., Chan, A. H. C., and Luan, M. T. (2009). Wave-induced progressive liquefaction in a poro-elastoplastic seabed: A two-layered model. *International Journal for Numerical and Analytical Methods in Geomechanics*, 33(5):591–610.
- Longuet-Higgins, M. S. and Stewart, R. W. (1960). Changes in the form of short gravity waves on long waves and tidal currents. *Journal of Fluid Mechanics*, 8(4):565–583.
- Longuet-Higgins, M. S. and Stewart, R. W. (1961). The changes in amplitude of short gravity waves on steady non-uniform currents. *Journal of Fluid Mechanics*, 10(4):529–549.

- Longuet-Higgins, M. S. and Stewart, R. W. (1964). Radiation stresses in water waves; a physical discussion, with applications. *Deep-Sea Res*, 11(4):529–562.
- Lundgren, H., Lindhardt, J. H. C., and Romold, C. J. (1989). Stability of breakwaters on porous foundation. In *Proceeding of 12th International Conference on Soil Mechanics and Foundation Engineering*, volume 1, pages 451–454.
- Madga, W. (1990). On one-dimensional model of pore pressure generation in a highly saturated sandbed due to cyclic loading acting on a sand surface. I: Theoretical description and numerical approach. Technical report, Internal Report No. 5, SFB-205, TP A13, Kusteningenieurwesen, University Hannover.
- Madsen, O. S. (1978). Wave-induced pore pressures and effective stresses in a porous bed. *Géotechnique*, 28(4):377–393.
- Mase, H., Sakai, T., and Sakamoto, M. (1994). Wave-induced porewater pressure and effective stresses around breakwater. *Ocean Engineering*, 21(4):361–379.
- McDougal, W. G., Tsai, Y. T., Liu, P. L.-F., and Clukey, E. C. (1989). Wave-induced pore water pressure accumulation in marine soils. *Journal of Offshore Mechanics and Arctic Engineering, ASME*, 111(1):1–11.
- Mei, C. C. and Foda, M. A. (1981). Wave-induced response in a fluid-filled poro-elastic solid with a free surface – A boundary layer theory. *Geophysical Journal of the Royal Astronomical Society*, 66(3):597–631.
- Mei, C. C., Stiassnie, M., and Yue, D. K.-P. (2005). *Theory and applications of ocean surface waves*. World Scientific, New York.
- Mizutani, N., Mostafa, A. M., and Iwata, K. (1998). Nonlinear regular wave, submerged breakwater and seabed dynamic interaction. *Coastal Engineering*, 33(2-3):177–202.
- Møshagen, H. and Tørum, A. (1975). Wave induced pressures in permeable seabeds. *Journal of Waterways, Harbors and Coastal Engineering Division, ASCE*, 101(1):49–57.
- Mostafa, A. M., Mizutani, N., and Iwata, K. (1999). Nonlinear wave, composite breakwater and seabed dynamic interaction. *Journal of Waterway, Port, Coastal, and Ocean Engineering, ASCE*, 125(2):88–97.
- Mynett, A. E. and Mei, C. C. (1982). Wave-induced stresses in a saturated poroelastic seabed beneath a rectangular caisson. *Géotechnique*, 32(3):235–248.
- Nago, H., Maeno, S., Matsumoto, T., and Hachiman, Y. (1993). Liquefaction and densification of loosely deposited sand bed under water pressure variation. In *Proceeding of the 3rd International Offshore and Polar Engineering Conference*, volume 1, pages 578–584.
- Nakamura, H., Onishi, R., and Minamide, H. (1973). On the seepage in the seabed due to waves. In *Proceedings of 20th Coastal Engineering Conference, J.S.C.E*, pages 421–428.
- Newmark, N. M. (1959). A method of computation for structural dynamics. *Journal of Engineering Mechanics Division, ASCE*, 85(3):67–94.

- Nova, R. and Wood, D. M. (1982). A constitutive model for soil under monotonic and cyclic loading. *Soil mechanics-transient and cyclic loading*, pages 343–373.
- Oh, Y. H., Jeng, D.-S., Teo, H. T., and Cha, D. H. (2002). Effects of wave non-linearity on the wave-induced seabed response. In *The 12th (2002) International Offshore and Polar Engineering Conference (ISOPE02)*, pages 738–744.
- Okusa, S. (1985). Wave-induced stress in unsaturated submarine sediments. *Géotechnique*, 35(4):517–532.
- Ou, J. (2009). *Three-dimensional numerical modelling of interaction between soil and pore fluid*. PhD thesis, University of Birmingham.
- Oumeraci, H. (1994). Review and analysis of vertical breakwater failures—lessons learned. *Coastal Engineering*, 22(1-2):3–29.
- Pastor, M., Zienkiewicz, O. C., and Chan, A. H. C. (1990). Generalized plasticity and the modelling of soil behaviour. *International Journal for Numerical and Analytical Methods in Geomechanics*, 14(3):151–190.
- Phillips, O. M. (1966). *The dynamics of the upper ocean*. Cambridge University Press.
- Putnam, J. A. (1949). Loss of wave energy due to percolation in a permeable sea bottom. *Transactions, American Geophysical Union*, 30(3):349–356.
- Puzrin, A. M., Alonso, E. E., and Pinyol, N. M. (2010). Caisson failure induced by liquefaction: Barcelona harbour, Spain. In *Geomechanics of failures*, pages 85–148. Springer, Dordrecht.
- Qi, W. G. and Gao, F. P. (2014a). Physical modelling of local scour development around a large-diameter monopile in combined waves and current. *Coastal Engineering*, 83:72–81.
- Qi, W. G. and Gao, F. P. (2014b). Responses of sandy seabed under combined waves and current: Turbulent boundary layer and pore-water pressure. *Physical Modelling in Geotechnics—Gaudin & White (Eds)*, pages 561–567.
- Qi, W. G., Li, C. F., Jeng, D.-S., Gao, F. P., and Liang, Z. D. (2019). Combined wave-current induced excess pore-pressure in a sandy seabed: Flume observations and comparisons with analytical solution. *Coastal Engineering*, 147:89–98.
- Rahman, M. S., El-Zahaby, K., and Booker, J. (1994). A semi-analytical method for the wave-induced seabed response. *International Journal for Numerical and Analytical Methods in Geomechanics*, 18(4):213–236.
- Raman-Nair, W. and Sabin, G. C. W. (1991). Wave-induced failure of poro-plastic seabed slopes: A boundary element study. *Proceedings of the Institution of Civil Engineers*, 91(4):771–794.
- Roscoe, K. H., Schofield, A. N., and Wroth, C. P. (1958). On the yielding of soils. *Géotechnique*, 8(1):22–53.

- Sakai, T., Hattori, A., and Hatanaka, K. (1991). Wave-induced transient pore-water pressure and seabed instability in the surf zone. In *Proceeding of International Conference on Geotechnical Engineering for Coastal Development-Theory and Practice on soft Ground*, volume 1, pages 627–632, Yokohama, Japan.
- Sakai, T., Mase, H., and Matsumoto, A. (1988). Effects of inertia and gravity on seabed response to ocean waves. *Modelling Soil-Water-Structure Interactions* (ed. Kolkman, et al.), pages 61–66.
- Sassa, S. and Sekiguchi, H. (1999). Wave-induced liquefaction of beds of sand in a centrifuge. *Géotechnique*, 49(5):621–638.
- Sassa, S. and Sekiguchi, H. (2001). Analysis of wave-induced liquefaction of sand beds. *Géotechnique*, 51(2):115–126.
- Sassa, S., Sekiguchi, H., and Miyamamoto, J. (2001). Analysis of progressive liquefaction as moving-boundary problem. *Géotechnique*, 51(10):847–857.
- Seed, H. B. and Rahman, M. S. (1978). Wave-induced pore pressure in relation to ocean floor stability of cohesionless soils. *Marine Geotechnology*, 3(2):123–150.
- Sekiguchi, H., Kita, K., and Okamoto, O. (1995). Response of poro-elastoplastic beds to standing waves. *soils and Foundations*, 35(3):31–42.
- Seymour, B. R., Jeng, D.-S., and Hsu, J. R. C. (1996). Transient soil response in a porous seabed with variable permeability. *Ocean Engineering*, 23(1):27–46.
- Sleath, J. F. A. (1970). Wave-induced pressures in beds of sand. *Journal of Hydraulics Division, ASCE*, 96(2):367–378.
- Stoker, J. J. (1957). *Water waves*. Interscience Publishers, Inc., New York.
- Sumer, B. M. (2014). *Liquefaction around marine structures*. World Scientific, New Jersey.
- Sumer, B. M. and Cheng, N. S. (1999). A random-walk model for pore pressure accumulation in marine soils. In *The 9th International Offshore and Polar Engineering Conference (ISOPE99)*, volume 1, pages 521–528.
- Sumer, B. M. and Fredsøe, J. (1997). *Wave scour around structures*, volume 4, pages 191–248. World Scientific.
- Sumer, B. M. and Fredsøe, J. (2002). *The Mechanics of scour in the marine environment*. World Scientific.
- Sumer, B. M., Whitehouse, R. J. S., and Tørum, A. (2001). Scour around coastal structures: A summary of recent research. *Coastal Engineering*, 44(2):153–190.
- Thomas, S. D. (1989). A finite element model for the analysis of wave induced stresses, displacements and pore pressure in an unsaturated seabed. I: Theory. *Computers and Geotechnics*, 8(1):1–38.

- Thomas, S. D. (1995). A finite element model for the analysis of wave induced stresses, displacements and pore pressure in an unsaturated seabed. II: Model verification. *Computers and Geotechnics*, 17(1):107–132.
- Tong, D., Liao, C., Chen, J., and Zhang, Q. (2019). Numerical simulation of a sandy seabed response to water surface waves propagating on current. *Journal of Marine Science and Engineering*, 6(3):88.
- Tsai, C. P. (1995). Wave-induced liquefaction potential in a porous seabed in front of a breakwater. *Ocean Engineering*, 22(1):1–18.
- Tsai, C. P. and Lee, T. L. (1995). Standing wave induced pore pressure in a porous seabed. *Ocean Engineering*, 22(6):505–517.
- Tsai, C. P., Lee, T. L., and Hsu, J. R. C. (2000). Effects of wave nonlinearity on the standing wave-induced seabed response. *International Journal for Numerical and Analytical Methods in Geomechanics*, 24(11):869–892.
- Tsai, Y. T., McDougal, W. G., and Sollitt, C. K. (1990). Response of finite depth seabed to waves and caisson motion. *Journal of Waterways, Port and Coastal and Ocean Engineering*, ASCE, 116(1):1–20.
- Ulker, M. B. C. and Rahman, M. S. (2009). Response of saturated and nearly saturated porous media: Different formulations and their applicability. *International Journal for Numerical and Analytical Methods in Geomechanics*, 33(5):633–664.
- Ulker, M. B. C., Rahman, M. S., and Guddati, M. N. (2010). Wave-induced dynamic response and instability of seabed around caisson breakwater. *Ocean Engineering*, 37(17–18):1522–1545.
- Ulker, M. B. C., Rahman, M. S., and Guddati, M. N. (2012). Breaking wave-induced response and instability of seabed around caisson breakwater. *International Journal for Numerical and Analytical Methods in Geomechanics*, 36(3):362–390.
- Ulker, M. B. C., Rahman, M. S., and Jeng, D.-S. (2009). Wave-induced response of seabed: Various formulations and their applicability. *Applied Ocean Research*, 31(1):12–24.
- Umeyama, M. (2010). Coupled PIV and PTV measurements of particle velocities and trajectories for surface waves following a steady current. *Journal of Waterway, Port, Coastal and Ocean Engineering*, ASCE, 137(2):85–94.
- Wang, J. G., Zhang, B., and Nogami, T. (2004). Wave-induced seabed response analysis by radial point interpolation meshless method. *Ocean Engineering*, 31(2):21–42.
- Wen, F., Jeng, D.-S., and Wang, J. H. (2012). Numerical modeling of response of a saturated porous seabed around an offshore pipeline considering non-linear wave and current interactions. *Applied Ocean Research*, 35:25–37.
- Wen, F. and Wang, J. H. (2013). Response of layered seabed under wave and current loading. *Journal of Coastal Research*, 31(4):907–919.

- Yamamoto, T. (1981). Wave-induced pore pressures and effective stresses in inhomogeneous seabed foundations. *Ocean Engineering*, 8(1):1–16.
- Yamamoto, T., Koning, H., Sellmeijer, H., and Hijum, E. V. (1978). On the response of a poro-elastic bed to water waves. *Journal of Fluid Mechanics*, 87(1):193–206.
- Ye, J. and Jeng, D.-S. (2012). Response of seabed to natural loading-waves and currents. *Journal of Engineering Mechanics, ASCE*, 138(6):601–613.
- Ye, J., Jeng, D.-S., Chan, A. H. C., Wang, R., and Zhu, Q. C. (2017). 3D integrated numerical model for fluid-structure seabed interaction (FSSI): Loosely deposited seabed foundation. *Soil Dynamics and Earthquake Engineering*, 92:239–252.
- Ye, J., Jeng, D.-S., Liu, P. L.-F., Chan, A. H. C., Wang, R., and Zhu, C. (2014). Breaking wave-induced response of composite breakwater and liquefaction in seabed foundation. *Coastal Engineering*, 85:72–86.
- Ye, J., Jeng, D.-S., Wang, R., and Zhu, C. (2015). Numerical simulation of the wave-induced dynamic response of poro-elastoplastic seabed foundations and a composite breakwater. *Applied Mathematical Modelling*, 39(1):322–347.
- Yuhi, M. and Ishida, H. (1998). Analytical solution for wave-induced seabed response in a soil-water two-phase mixture. *Coastal Engineering Journal*, 40(4):367–381.
- Zen, K. and Yamazaki, H. (1990a). Mechanism of wave-induced liquefaction and densification in seabed. *Soils and Foundations*, 30(4):90–104.
- Zen, K. and Yamazaki, H. (1990b). Oscillatory pore pressure and liquefaction in seabed induced by ocean waves. *Soils and Foundations*, 30(4):147–161.
- Zen, K. and Yamazaki, H. (1991). Field observation and analysis of wave-induced liquefaction in seabed. *Soils and Foundations*, 31(4):161–179.
- Zhang, J. S., Jeng, D.-S., and Liu, P. L.-F. (2011). Numerical study for waves propagating over a porous seabed around a submerged permeable breakwater PORO-WSSI II model. *Ocean Engineering*, 38(7):954–966.
- Zhang, J. S., Jeng, D.-S., Liu, P. L.-F., Zhang, C., and Zhang, Y. (2012a). Response of a porous seabed to water waves over permeable submerged breakwaters with Bragg reflection. *Ocean Engineering*, 43:1–12.
- Zhang, J.-S., Zhang, Y., Jeng, D.-S., Liu, P. L.-F., and Zhang, C. (2014a). Numerical simulation of wave-current interaction. *Ocean Engineering*, 75:157–164.
- Zhang, J.-S., Zhang, Y., Zhang, C., and Jeng, D.-S. (2013a). Numerical modeling of seabed response to the combined wave-current loading. *Journal of Offshore Mechanics and Arctic Engineering, ASME*, 135(3):031102.
- Zhang, J.-S., Zheng, J. H., Jeng, D.-S., and Wang, G. (2012b). Numerical simulation of solitary wave induced flow motion around a permeable submerged breakwater. *Journal of Applied Mathematics*, page 508754.

- Zhang, Y., Jeng, D.-S., Gao, F. P., and Zhang, J.-S. (2013b). An analytical solution for response of a porous seabed to combined wave and current loading. *Ocean Engineering*, 57:240–247.
- Zhang, Y., Jeng, D.-S., Liao, C., Zhao, H., Zhang, J. S., et al. (2014b). Numerical modelling of poro-elastoplastic seabed under combined waves and currents. In *The Eleventh ISOPE Pacific/Asia Offshore Mechanics Symposium*. International Society of Offshore and Polar Engineers.
- Zhang, Y., Jeng, D.-S., Zhao, H., and Zhang, J.-S. (2016). Numerical modelling of pore pressure accumulations in marine sediments around submerged breakwaters under combined wave and current loadings. *Journal of Coastal Research*, 32(46):1092–1104.
- Zhang, Y., Zhang, J. S., Zhang, H., Zhao, H., and Jeng, D.-S. (2012c). Three-dimensional model for wave-induced dynamic soil response around breakwaters. In *The Twenty-second International Offshore and Polar Engineering Conference*. International Society of Offshore and Polar Engineers.
- Zhao, H. and Jeng, D.-S. (2015). Numerical study of wave-induced soil response in a sloping seabed in the vicinity of a breakwater. *Applied Ocean Research*, 51:204–221.
- Zhao, H., Jeng, D.-S., Zhang, J. S., Liao, C., Zhang, H. J., and Zhu, J. F. (2017). Numerical study on loosely deposited foundation behavior around a composite breakwater subject to ocean wave impact. *Engineering Geology*, 227:121–138.
- Zhao, H., Jeng, D.-S., Zhang, Y., Zhang, J.-S., Zhang, H. J., and Zhang, C. (2013). Three-dimensional numerical model for wave-induced seabed response in the vicinity of breakwater heads. *Geomechanics and Engineering*, 5(6):595–611.
- Zhao, H., Liang, Z. D., Jeng, D.-S., Zhu, J. F., Guo, Z., and Chen, W. Y. (2018). Numerical investigation of dynamic soil response around a submerged rubble mound breakwater. *Ocean Engineering*, 156:406–423.
- Zhou, X. L., Wang, J. H., Zhang, J., and Jeng, D.-S. (2014). Wave and current induced soil response around a submarine pipeline in an anisotropic seabed and liquefaction. *Ocean Engineering*, 75(112–127).
- Zienkiewicz, O. C., Chan, A. H. C., Pastor, M., Schrefler, B. A., and Shiomi, T. (1999). *Computational Geomechanics with Special Reference to Earthquake Engineering*. John Wiley and Sons, England.
- Zienkiewicz, O. C., Chang, C. T., and Bettess, P. (1980). Drained, undrained, consolidating and dynamic behaviour assumptions in soils. *Géotechnique*, 30(4):385–395.
- Zienkiewicz, O. C. and Morz, Z. (1984). Generalized plasticity formulation and applications to geomechanics. *Mechanics of Engineering Materials*, 44(3):655–680.